The Pennsylvania State University
The Graduate School
Department of Materials Science and Engineering

MODELING GROWTH AND DISSOLUTION OF INCLUSIONS DURING FUSION WELDING OF STEELS

A Thesis in

Materials Science and Engineering

by

Tao Hong

Submitted in Partial Fulfillment
of the Requirements
for the Degree of

Doctor of Philosophy

May 2003

The thesis of TAO HONG
was reviewed and approved* by the following:

Tarasankar DebRoy
Professor of Materials Science and Engineering
Thesis Advisor, Chair of Committee

Zi-Kui Liu
Assistant Professor of Materials Science and Engineering

Panagiotis Michaleris
Assistant Professor of Mechanical Engineering

Long-Qing Chen
Professor of Materials Science and Engineering

Gary L. Messing
Professor of Ceramic Science and Engineering
Head of the Department of Materials Science and Engineering

*Signatures are on file with the Graduate School.

Abstract

The ultimate objectives of welding are to obtain perfect structural continuity and sound mechanical properties of welded materials. However, flaws and defects, such as inclusions, pores, and cracks, are often present in the weld metal. It is well known from previous research that the characteristics of these flaws, especially of inclusions, in the weld metals are critical factors to determine the structure, properties and performance of weldments. Therefore, extensive research efforts have been made to understand the formation and growth of inclusions in the molten liquid and solid metal. Previous research of inclusion focused mainly on characterization of inclusions in the weld metals, and thermodynamics and kinetics of inclusion nucleation and growth. Synthesis of the knowledge for better understanding the inclusion behavior in the weld pool was mostly overlooked. Particularly, the special features of thermal history that the inclusion experiences in the weld pool due to heat transfer and fluid flow were not taken into account by most researchers.

To get a comprehensive understanding of inclusion characteristics in the weld metal, the research in the present thesis applied computational modeling to study inclusion behavior considering thermodynamics and kinetics of nucleation, growth and dissolution of inclusion along its trajectory in the weld pool. The trajectory and thermal cycle of inclusion in the weld pool are calculated from the heat transfer and fluid flow model developed at Penn State. The objective of this research is to predict the characteristics of inclusions, such as composition, size distribution, and number density in the weld metal. The information and knowledge will be useful for further understanding of relationship between inclusion characteristics, weld metal properties, and control of welding parameters.

To synthesize the knowledge of thermodynamics and kinetics of nucleation, growth and dissolution of inclusion in the liquid metal, a set of time-temperature-transformation (TTT) diagrams are constructed to represent the effects of time and temperature on the growth and dissolution behavior of individual inclusions. Fourteen

types of inclusions are considered in this research, of them 6 are oxides, 3 are nitrides, 2 are sulfides and 3 are complex oxides. Apart from the stability of various inclusions in a given composition of steel, the TTT diagrams provide important kinetic information of diffusion controlled growth and dissolution. The TTT diagrams show that alloy composition dramatically affects the relative stability of inclusions. Although Al_2O_3 and $MnO{\cdot}Al_2O_3$ are always the most stable inclusions in the weld pool, other inclusions can be the premier compositions of impurities when the alloy composition changes. The non-isothermal behavior of growth and dissolution of inclusions is predicted from their isothermal behavior by constructing continuous-cooling-transformation (CCT) diagrams for growth and continuous-heating-transformation (CHT) diagrams for dissolution using Scheil additive rule. This approach offers a tool to better understand the effects of temperature and time on the growth and dissolution of inclusions in liquid steels under non-isothermal conditions.

A well verified fluid flow and heat transfer model developed at Penn State is used to calculate the temperature and velocity fields in the weld pool for different welding processes, such as gas tungsten arc (GTA) welding and submerged arc (SA) welding. Due to the usage of high currents during welding, the nature of fluid flow and heat transfer in the liquid is turbulent in most case. A turbulent model considering enhanced viscosity and thermal conductivity (k-ε model) is applied to calculate the temperature and velocity fields. The calculations show that there is vigorous circulation of metal in the weld pool. The comparison between calculated and experimentally observed length, depth and cross-section area of weld pool verifies the model. The heat transfer and fluid flow model helps to understand not only the fundamentals of the physical phenomena during welding, but also the basis to further study thermodynamics and kinetics of nucleation, growth and dissolution of inclusions.

The calculations of particle tracking of thousands of inclusions show that most inclusions experience complex gyrations and thermal cycles before they are trapped on the solid region in the weldment. The calculated result shows that the temperature versus time plots of the inclusion particles display several characteristic temperature peaks in

many cases. However, about one third of the particles experience continuous cooling behavior without any temperature peak.

The inclusions experience both growth and dissolution during their lifetime in the weld pool. Thermal cycles of thousand of inclusions nucleated in the liquid region are tracked and their growth and dissolution are calculated to estimate the final size distribution and number density of inclusions statistically by combining the thermodynamics and kinetics of inclusion growth and dissolution.

The calculations show that welding conditions affect the average residence time of the particles in the weld pool and their final size distributions. The residence time decreases with higher welding speeds and lower welding powers. The inclusions are coarser at low welding speeds and high welding powers. Good agreement between the computed and the experimentally observed inclusion size distribution indicates that the inclusion behavior in the weld pool can be understood from the fundamentals of transport phenomena and transformation kinetics.

The collision and coalescence model is applied to modify the calculated number density of single kind of inclusions. With the increase of time, the number densities of smaller inclusions become lower. Small size particles collide and coalescent with each other to form bigger particles. Therefore, the number densities of inclusion of bigger size become higher. The collision and coalescence are important mechanisms for inclusion coarsening.

TABLE OF CONTENTS

List of Figures

Chapter 1:

Chapter 2:

Chapter 3

Chapter 4

Chapter 5

Chapter 6

Appendix

ACKNOWLEDGEMENTS

First, I would like to thank my advisor, Dr. Tarasankar DebRoy, for his patient and innovative guidance throughout this research. I would also like to thank Dr. Longqing Chen, Dr. Zi-kui Liu, Dr. Pan Michiliaris and Dr. Kwadwo Osseo-Asare for their valuable time and advices while serving as the committee members of my candidacy examination, comprehensive examination and Ph.D. thesis defense.

Many thanks to Dr. Kamlesh Mundra, Dr. Todd Palmer, Dr. Walther Pitschneder and Dr. Zhishang Yang for their outstanding research and great help as the teammates and friends in Dr. DebRoy's research group. I am very grateful to Dr. Stan David and Dr. Suresh Babu of Oak Ridge National Lab, and Dr. Harry Bhadeshia of Cambridge University for their interests and helpful discussion on this research topic. Thanks to Dr. Hailiang Zhao, Mr. Mario Pastor, Wei Zhang, and Sarangapany Sista for the help and informative discussion during my study at Penn State.

I would like to give my deep gratitude to my wife, Qun Xue, for all her understanding, cooperation and support in both my academic and personal life.

I would like to acknowledge the financial support of the US Department of Energy, Office of Basic Energy Science, Division of Materials Science.

CHAPTER 1

INTRODUCTION

1.1 General Introduction of Welding Processes

Although metals have been in service of mankind since the early ages of civilization, welding technologies was only widely used in the manufacturing of metal products from 20th century. Welding is playing a critical role in the modern industry. It is used extensively in the fabrication of automobiles, aircrafts, buildings and bridges, integrated circuits, pipes and containers, and thousands of other products. According to a survey, welding is used in more than 60% of the manufactured products that make up the GNP of United States.[1]

By the definition given by International Standard Organization (ISO),[2] "Welding is an operation in which continuity is obtained between parts for assembly by various means." The objectives of welding are to achieve structural continuity and sound mechanical properties. To achieve these objectives, many types of welding processes were carried out in the manufacturing industries from last century. In these welding processes, various energy sources are used, including electric arc, laser beam, electron beam, ultrasonic wave, and mechanical force etc. Pressure may or may not be applied. Filler or intermediate materials may or may not be added. The melting of materials under the heat sources may or may not take place (fusion or non-fusion welding).

In fusion welding, a heat source moves along a joint seam of two parts. The material under the heat source is heated to the temperature above the melting point and a

liquid weld pool is formed. After the heat source moves away, the molten zone cools down and solidifies to form the fusion zone (FZ). Due to the heat conduction, the material close to the fusion zone, which is called heat affected zone (HAZ), is also heated but does not reach the melting point. Many important physical processes occur during fusion welding. Due to the high heat input interacting with the material surface, the materials are always heated and melted very rapidly. The high temperature region established at the weld pool surface in welding leads to several physical phenomena at and above the liquid vapor interface. For instance, the dissolution of gaseous species, such as nitrogen, oxygen, and hydrogen, the vaporization of alloying elements, the formation of plasma above the molten zone, and the interaction and heat exchange between molten metal and surrounding atmosphere take place during welding. In the weld pool, the molten metal undergoes vigorous recirculatory motion driven primarily by various forces, such as buoyancy, electromagnetic and surface tension forces. Oxide, nitride, sulfide and carbide inclusions may form in the weld pool and undergo growth and dissolution depending on their thermal histories. During heating and cooling, HAZ undergoes considerable changes in microstructure and grain evolutions. In the recent decades, significant advances have been achieved in both understanding of the physical processes in welding and in welding techniques.[3-5]

1.2 Importance of Inclusions in the Weldments

All welded products have one thing in common: certain impurities or inclusions exist in the weldments.[6-10] Figure 1.1 shows a typical micrographic image of the inclusions embedded and distributed through submerged arc (SA) welding of low alloy steel[11]. It was taken from the carbon extraction replica specimen. The most commonly observed inclusions in the steel welds are oxide, nitride and sulfide inclusions. Inclusion formation is almost unavoidable during steel welding because of the existence of oxygen, nitrogen and sulfur in the weld metal. For example, in gas metal arc (GMA) welding, oxygen is deliberately introduced through the shielding gas to improve bead morphology

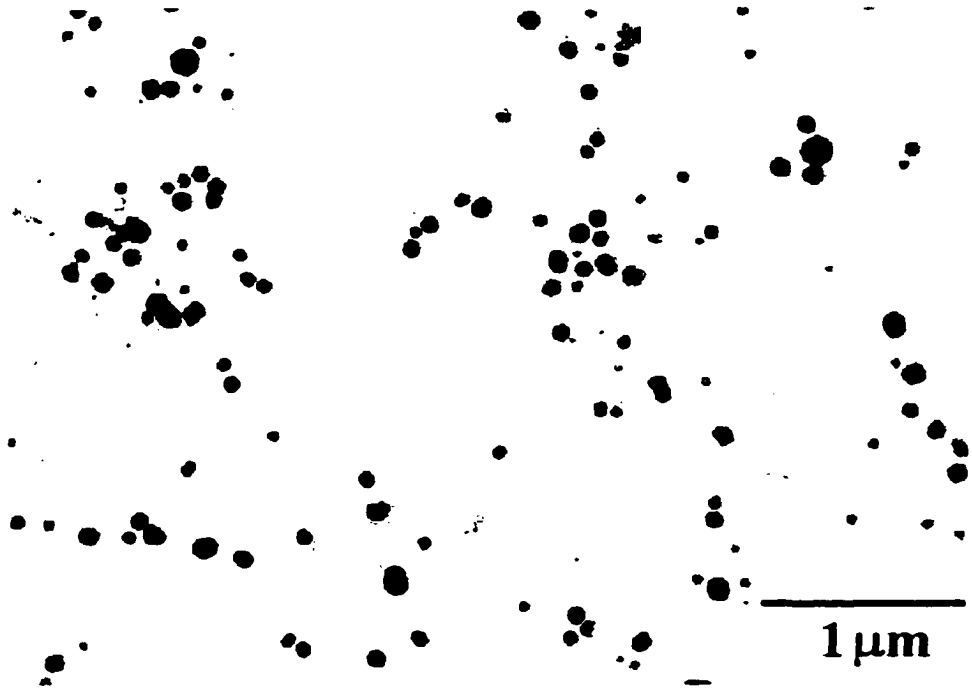

Figure 1.1 Bright-field electron micrograph showing a typical inclusion distribution in low alloy steel submerged arc welding.[11] Metal composition: C0.06-S0.009-P0.016-Si0.32-Mn1.38-Ti0.008-Cu0.02-N0.01-O0.036 wt%, electrode type of AWS E7016.

and arc stability. In submerged arc (SA) welding, the flux is the main source of oxygen. The moisture at the metal surface is also one source of oxygen. The oxidation reactions always proceed very quickly because of the high temperatures in the weld pool.

The composition, size distribution and number density of inclusions depend on many factors such as various welding processing parameters, the compositions of base metal and the flux, etc. The existence of inclusions has both positive and negative effects on the product quality. Some major effects of inclusions on weldment structures and properties are outlined in this chapter.

Generally speaking, the presence of inclusions in the weldment is detrimental to the weld metal properties. However, in many instances, the inclusions can improve the toughness by promoting the formation of acicular ferrite which is characterized by high toughness.[4,12] Dowling et al[12] investigated the effect of inclusions on the nucleation of acicular ferrite. The SEM (Figure 1.2) showed a round shape inclusion surrounded by the acicular ferrite growing from the inclusion radiantly. They concluded that acicular ferrite might nucleate in the strain field around inclusions. Inclusions nucleate acicular ferrite by acting as inert substrates according to the classical theory of heterogeneous nucleation. However, not all types of inclusions and all size ranges are favorable for promoting the formation of acicular ferrite.[4,5] Barbaro et al.[4] concluded that oxide inclusions are likely to be more effective than sulfide and nitride precipitates in controlling acicular ferrite formation and grain coarsening even in the heat-affected zone (HAZ). The oxide inclusions containing γ-Al_2O_3, titanium oxide (Ti_xO_y) and galaxite ($MnO{\cdot}Al_2O_3$) with diameters larger than 0.4 μm are often found to be effective nucleation sites for acicular ferrite.[4] Therefore, predicting the composition and size distribution of inclusions in weld metal is important to understand the optimization of microstructure and mechanical properties of weldment.

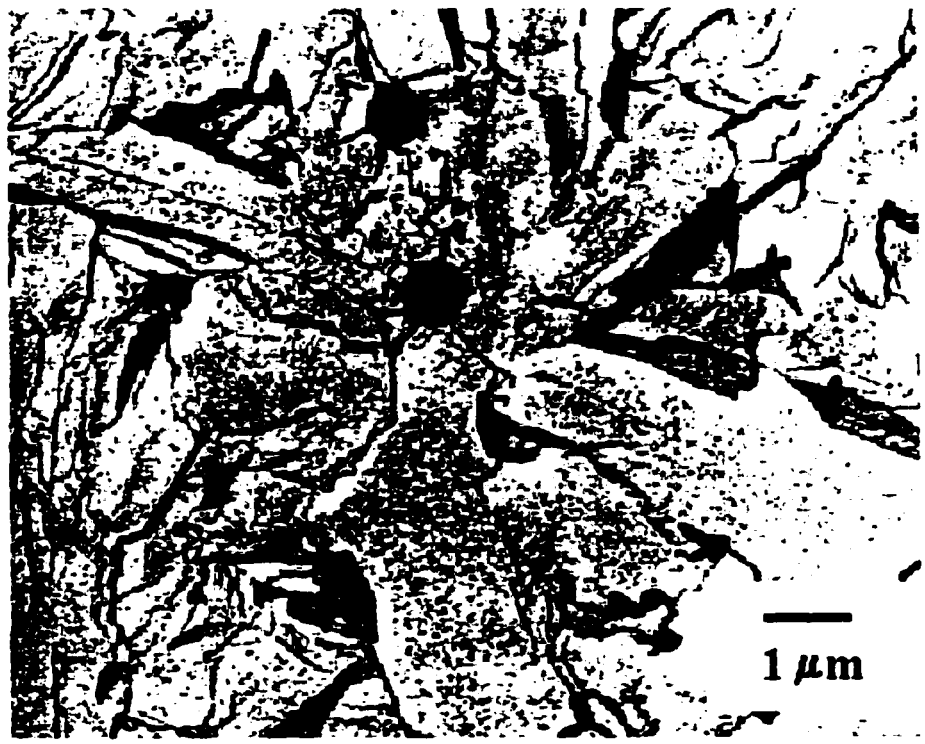

Figure 1.2 Extraction replica submerged arc welded sample showing round shape inclusion and acicular ferrite.[12] Weld metal composition: C0.051-Mn1.37-P0.012-S0.005-Si0.26-NI0.1-Cr0.37-Mo0.35-V0.0190-Nb0.034-Al0.011-Ti0.029-O0.04-N0.0066 wt%.

On the other side, the existence of a large volume fraction of inclusions in the weldments may initiate premature ductile fracture, promote stress oriented cracking, reduce machinability, and degrade fatigue property of the weld metal. Takahashi et al[13,14] studied the cracking susceptibility of pipes containing inclusions. The effect of inclusions is illustrated[13] in Figure 1.3. They found that a small non-metallic inclusion induced an incipient crack in the HAZ.

Pickering[15] did a series of experiments to study the influence of volume fraction of inclusions on the ductile fracture in different steels. It was found[15] that the total ductility expressed by fracture strain decreases strongly with the increasing volume fraction of inclusions as shown in Figure 1.4. Nordburg et al[16] studied the effect of defect size on the fatigue properties. The defect represented various types of inclusions as well as pores. They presented their experimental and theoretical results as shown in Figure 1.5. It is observed that the fatigue limit of steel reduce strongly with the increase of inclusion size affects. For high strength steels, the reduction of fatigue limit with increasing inclusion size is more profound.

It is concluded from the previous work that nature of inclusions formed during welding is an important factor in affecting the structure and properties of weldment. To achieve good mechanical properties of weldments, the welding parameters and weld metal composition must be carefully selected to attain desirable inclusion characteristics.

1.3 Research of Inclusions in the Weld Pool

Although the effects of inclusions on weld-metal structure and properties have been recognized for a long time, no systematic studies on inclusion formation in weld metals have been made until recent years. This section reviews some notable previous research work on inclusion in liquid metals.

Figure 1.3 Inclusion initiates cracking in HAZ of line pipe seam welding.[13] Pipe steel composition: C0.044-Si0.29-Mn1.22-P0.004-Ni0.27-Mo0.14-Al0.022-Ti0.011-Nb0.048-N0.0016-O0.0014 wt%.

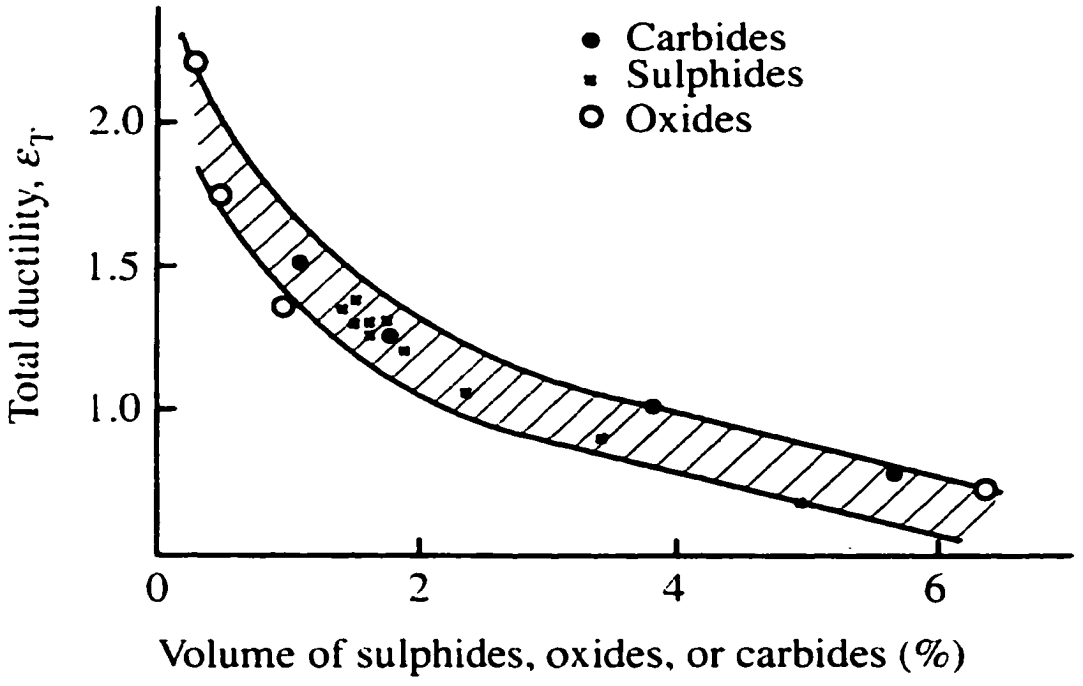

Figure 1.4 Influence of inclusion volume fraction on ductility of tool steel (not welded samples).[15]

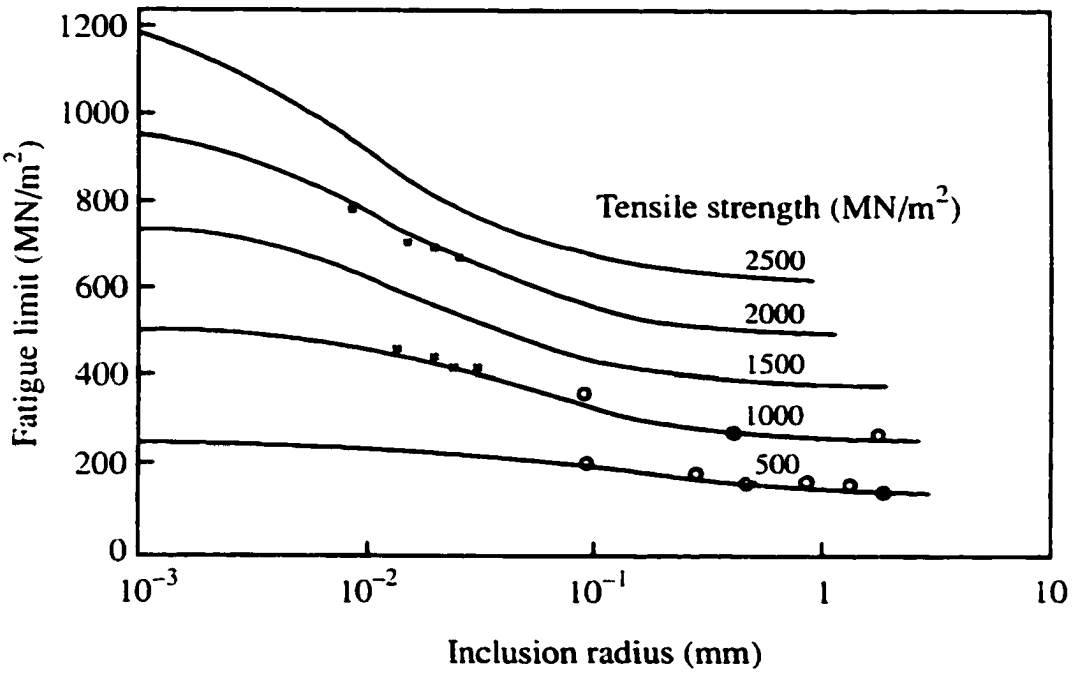

Figure 1.5 Influence of size of all inclusions on fatigue property[16] of high-strength steel (not welded samples). Solid lines: theoretical results, circles and crosses: experimental results.

Most previous studies on inclusions considered the thermodynamics of inclusion formation. Frost et al.[8] used the available equilibrium data for oxide dissolution to predict the sequence of precipitation of various oxide inclusions during the solidification process. Turpin and Elliott[17] calculated the nucleation of oxides in steel from thermodynamic considerations. Hsieh et al.[18] predicted the sequential oxide inclusion formation in low alloy steel welds. They found that change in weld metal composition would change the formation sequence dramatically. Thermodynamics can predict which of several possible phases could nucleate in the steel melt, however, it cannot predict kinetic factors such as nucleation rate and the number density of the nuclei in the melt. Furthermore, no further study on the size and space distribution of inclusions was developed to understand the inclusion behavior in the whole weldment.

Kluken and Grong[9] studied mechanisms of inclusion formation in Al-Ti-Si-Mn steel weld metals and precipitate stability in weld metals. They also showed that welding parameters have a significant effect on the size distribution of oxide inclusions. However, in their theoretical investigation, the effects of cooling history and element concentrations were not taken into account. Babu et al.[9,10] have assumed that the number density of inclusions was greatly determined by the nucleation rate of the first forming oxide. Therefore, by relating the time spent in the temperature range of the first-forming oxide, the effect of the weld-metal cooling rate on the inclusion number density can be described. However, this method considered monotonous cooling of the liquid steel region. It is known[3] that the inclusions may experience temperature excursions including both heating and cooling because of fluid flow in the weld pool.

In previous work, although several aspects of inclusion nucleation, growth and dissolution in liquid steels have been studied, such as the thermodynamic stability and diffusion controlled growth and dissolution rates of inclusions, synthesis of the accumulated knowledge of these component processes was largely overlooked. Currently no unified approach is available for understanding the growth and dissolution behavior of inclusions in liquid steels. One goal of this thesis is to synthesize our current

knowledge of stability and growth/dissolution kinetics of inclusions in liquid steels in a form that allows a clear understanding of their growth and dissolution behavior. In particular, a formalism will be presented that describes the effects of time and temperature on the diffusion controlled growth and dissolution of inclusions in steels of known compositions, by constructing time-temperature-transformation (TTT) diagrams. Apart from the stability of various inclusions in a given composition of steel, the diagrams provide important kinetic information about diffusion controlled growth and dissolution of inclusions.

TTT diagrams are only restricted to isothermal conditions, however, because of the fast heating and cooling rates inclusions experience, non-isothermal conditions must be taken into account. TTT diagrams can be readily extended to non-isothermal conditions for inclusion growth and dissolution. Scheil additive rule,[19] a well known approach, can be used to calculate the continuous cooling transformation (CCT) diagrams for the growth and continuous heating transformation (CHT) diagrams for the dissolution from the corresponding TTT diagrams. The approach and calculated results presented in the thesis reveal the effects of time and temperature on the inclusion growth kinetics during continuous cooling and inclusion dissolution kinetics during continuous heating.

Understanding the thermal histories and corresponding growth/dissolution of a large number of inclusions is a prerequisite for the understanding of the size distribution, composition, and other properties of inclusions in the weld pool for a given welding condition. In recent years, significant advances have been made in the calculation of fluid flow and heat transfer in the weld pool and these calculations can provide significant insight about the welding process that cannot be achieved otherwise. However, very little effort has been made to combine these new powerful capabilities to understand fusion zone microstructures and inclusion growth. Previous research showed that molten liquid undergoes vigorous circulation resulting from buoyancy, surface tension, and when electric current is used, electromagnetic forces inside the weld pool.[20,21] As an inclusion is transported by convective currents in the weld pool, it will grow or dissolve along its

path depending on the temperature it experiences.[22,23] At any given instant, its velocity and temperature depend on the velocity and temperature fields prevailing in the location because the inclusions are small enough to neglect the drag effect in the liquid.

To address the phenomena, a technique is developed to calculate the size distribution of inclusions considering fluid flow as well as the thermodynamics and diffusion controlled kinetics of inclusion growth and dissolution. In this method, the temperature histories and loci of a large amount of inclusions are calculated under different welding parameters to study the effect of welding parameters on inclusion size distribution. Such an approach is extended to study inclusion formation over a wide range of welding processes such as gas tungsten arc welding (GTA) and submerged arc (SA) welding. Such an approach is preferred over the conventional analytical equation of heat transfer to understand the details of the inclusion formation. Moreover, the calculated result of number density was modified to account for the coarsening of inclusions due to collision and coalescence between inclusions.[24,25] The calculated results were compared with the experimentally determined results.

1.4 Simulation of Inclusion Behaviors in the Weld Pool

As previously discussed, characteristics of inclusions are the critical factors to determine the microstructure and mechanical properties of weld metal. Although the characteristics of inclusions, such as composition, number density, and size distribution etc., can be measured using optical micrograph, EDS and SEM with the help of image analysis and date processing software, it is almost impossible to measure them *in situ*. Thus, the measured result itself is only the integrated final result of the inclusion behavior prior to and during solidification. It cannot offer the significant insight about inclusion behavior during welding.

Due to the difficulties in the experimental measurements, mathematical modeling has become an essential way to study the inclusion behavior considering the fluid flow

and heat transfer in the weld pool. Modeling can provide quantitative fundamental understanding which cannot be obtained by any other ways. In Chapter 2, the fundamental thermodynamics and kinetics of inclusion nucleation, growth and dissolution in the weld pool are discussed. Principles involved in the heat transfer and fluid flow models and some major previous work are carefully reviewed.

1.5 Statement of Objectives

The overall objective of this research is to develop a comprehensive model to quantitatively understand the inclusion behavior in the weld pool of low alloy steel welding. More specifically, the objectives are:

A. To construct the time-temperature-transformation and continuous-cooling (heating)-transformation diagrams for the growth and dissolution of inclusions

Both thermodynamics and kinetics are considered to construct the time-temperature-transformation (TTT) diagrams of inclusion growth and dissolution. Continuous-cooling(heating)-transformation (CCT or CHT) diagrams for inclusion growth and CHT diagrams for inclusion dissolution are constructed from the corresponding TTT diagrams to predict the non-isothermal behavior of inclusion in liquid steels.

B. To understand the temperature history of inclusions in the weld pool.

A heat transfer and fluid flow model is used to calculate the temperature and velocity fields in the weld pool. The temperature gyrations of a large number of inclusions are calculated based on the calculated temperature and velocity fields. The statistical properties of inclusion behavior in the weld pool are investigated to predict the characteristics of inclusions.

C. To develop a comprehensive computational model to predict the size distribution, composition and number density of inclusions

Incorporating heat transfer and fluid flow model in the weld pool with thermodynamics and kinetics calculation of inclusion nucleation, growth and dissolution, a comprehensive model is developed to predict the composition, size distribution, and number density of inclusion.

D. To verify the model prediction with the available experimental results

The calculated composition, size distribution and number density of inclusions are compared with experimental results to verify the model.

1.6 Layout of Thesis

The thesis consists of 6 chapters. In Chapter 1, the need for understanding the behavior of inclusions during welding and the motivation for the proposed research are briefly described. The objectives of the research described in this thesis are identified.

The available literature is critically reviewed in Chapter 2. In this chapter, recent progress in computer modeling of transport phenomena in the welding processes are also discussed. The previous research on the thermodynamics and kinetics of inclusion nucleation, growth and dissolution is presented. The existing models about inclusions are presented and discussed.

In Chapter 3, the details of the construction of TTT diagrams for the nucleation, growth and dissolution of inclusions are presented. The calculated results are discussed.

The effects of alloying elements, time, and temperature on the stability of inclusions are studied. The predicted results of stability of inclusions are compared with experimental data of inclusion compositions.

In Chapter 4, the details on how to calculate CCT and CHT diagrams from the corresponding TTT diagrams are presented. The calculated CCT and CHT diagrams for different kinds of inclusions are presented to study non-isothermal growth and dissolution of inclusions during heating and cooling in the weld pool.

In Chapter 5, the techniques to calculate temperature and velocity fields in the weld pool are discussed. The particle tracking approach to calculate the trajectories and thermal cycles of inclusions are discussed.

In Chapter 6, the predicted results of composition, size distribution and number density of inclusions obtained from the comprehensively synthesized model are presented and compared with experimental results.

The conclusions of this research are presented in Chapter 7. The suggestions for future work are also documented in this chapter.

A detailed documentation of the developed FORTRAN source code and user's manual of the program are appended as Appendix.

References:

1. D. J. Abson: *Welding in the World*, **27**, 76-101 (1989).
2. International Standard Organization: Standard for Welding Technologies, Volume 6, Version 8 (1988)
3. T. DebRoy and S. A. David: *Reviews of Modern Physics*, **67**, 85-112 (1995).
4. F. J. Barbaro, P. Krauklis, and K. E. Easterling: *Mater. Sci. Tech.*, **5**, 1057-68 (1989).
5. J. W. Christian: *The Theory of Transformations in Metals and Alloy - Part I: Equilibrium and General Kinetic Theory*, 2nd ed., Pergamon Press, Oxford, (1981)
6. O. Kluken and O. Grong: *Metall. Trans. A*, **20A**, 1335-49 (1989).
7. S. S. Babu, S. A. David, and T. DebRoy: *Sci. Tech. Weld. Join.*, **1**, 17-27 (1996).
8. G. Frost and D. G. Brothers: *Scripta Metallurgica et Materialia*, **32**, 1061-66 (1995).
9. S. S. Babu, S. A. David, J. M. Vitek, K. Mundra, and T. DebRoy: *Mater. Sci. Tech.*, **11**, 186-199 (1995).
10. S. S. Babu, S. A. David, J. M. Vitek, K. Mundra, and T. DebRoy: *Trends in Welding Research*, Proceedings of the 4th International Conference, 1995, Gatlinburg, TN.
11. S. A. Court and G. Pollard: *Metallography*, **22**, 219-43 (1989).
12. J. M. Dowling, J. M. Corbett and H. W. Kerr: *Metall. Trans. A*, **17A**, 1611-23 (1986).
13. A. Takahashi, T. Hara, and H. Ogawa: *ISIJ International*, **36**, 229-234 (1996).
14. A. Takahashi and H. Ogawa: *ISIJ International*, 1996, **36**, 334-340 (1996).
15. F. B. Pickering: *Proceeding of Climax Molybdenum Comp. Conf.*, Kyoto, Japan (1971).
16. H. Nordberg: Internal report (IM-1450), Swedish Institute For Metal Research, (1980).
17. M. L. Turpin and J. F. Elliot: *J. Iron Steel Inst.*, **204**, 217-225 (1966)
18. K. C. Hsieh, S. S. Babu, J. M. Vitek, and S. A. David: *Mater. Sci. Engi.*, **A215**, 84-91 (1996).
19. E. Scheil: *Arch. Eisenhuttenwesen*, **12**, 565-567 (1935).
20. K. Mundra, T. DebRoy, and K. M. Kelkar: *Numerical Heat Transfer*, **29**, 115-129 (1996).
21. S. Kumar and S. C. Bhaduri: *Metall. Mater. Trans. B*, **25B**, 435-441 (1994).
22. T. Hong, W. Pitscheneder, and T. DebRoy: *Sci. Tech. Weld. Join.*, **3**, 33-41 (1998).
23. T. Hong, T. DebRoy, S. S. Babu, and S. A. David:. *Metall. Mater. Trans. B*, **31B**, 161-169 (2000).

24. U. Lindborg and K. Torssell: *Trans. Metallurgical Society of AIME*, **242**, 94-102 (1968)

25. R. K. Iyengar and W. O. Philbrook: *Metall. Trans*, **3**, 1823-30 (1972).

CHAPTER 2

BACKGROUND AND LITERATURE REVIEW

The purpose of this chapter is to critically review the literature and introduce the background knowledge necessary for the study reported in this thesis. The subject matters are classified into three sections: (1) Thermodynamics and kinetics fundamentals of inclusion nucleation, growth and dissolution, (2) Transport phenomena in weld processes, and (3) Inclusion behaviors in the weld pool.

2.1 Fundamentals of Thermodynamics and Kinetics of Inclusion Nucleation, Growth, and Dissolution

Oxide, nitride, and sulfide inclusions are commonly present in steel weldments. The effect of inclusions on weldment structure and properties was discussed in Chapter 1. In general, the presence of inclusions is detrimental to weld properties. However, under a given set of conditions, certain types of inclusion in some specific size ranges are known to promote the formation of acicular ferrite, which in turn improves the weldment toughness. Although the importance of inclusions has been recognized for a long time, it is only in recent years that systematic studies of inclusions in the weld metal have started.

The studies of inclusions in the weld metals can stem from the studies of inclusions in the ladle deoxidation and refining of steels.[1-5]

The extensive studies of inclusion nucleation and growth during ladle steel deoxidation and refining have demonstrated that inclusion characteristics are determined by thermodynamics and kinetics of oxidation reaction.[2-5] The rates of oxidation reactions are controlled by the concentrations of alloying elements in the steel, the reaction temperature, and the liquid steel bath conditions. Similarly, during welding, the processing variables, such as heat input, shielding gas, welding speed, base metal composition etc., affect inclusion behavior significantly. Although the principles of inclusion nucleation and growth used in steel ladle deoxidization and refining can be extended to weld metal condition, some unique features of welding must be considered because of the existence of much higher temperatures and larger heating or cooling rates.

In the weld pool, non-metallic elements, such as oxygen, nitrogen and sulfur, are dissolved in the liquid metal and react with the alloying elements to form inclusions. The formation of an inclusion involves various events such as nucleation, growth and dissolution, collision, coalescence, and coarsening. To have a complete scope of understanding on inclusion behavior, all of these events are considered in this thesis.

2.1.1 Dissolution of Gaseous Elements in the Weld Pool

The dissolution of oxygen and nitrogen invariably takes place during welding. For example, in gas metal arc (GMA) welding, nitrogen, oxygen or carbon dioxide is deliberately introduced through the shielding gas to improve bead morphology and arc stability.[6] In submerged arc (SA) welding, the flux is the main source of oxygen.[6] The moisture in the air or at the surface of the weld pool is also a source of oxygen.[6] The presence of sulfur in the steel is also very common, although normally at small concentration (<0.04%).[7] Therefore, most steels have certain concentrations of oxygen,

nitrogen, and sulfur. To understand the fundamentals of gas dissociation and dissolution in the liquid steel is the first step to study inclusion formation in the weld pool.

Many investigations conducted in Penn State about dissolution of oxygen, hydrogen and nitrogen from air or shielding gas to weld metals have been reported.[8-10] Here, nitrogen is discussed as an example specie. Typically, the nitrogen concentration in liquid iron is calculated using Sieverts' Law, which is presented as equations (2.1) and (2.2) for the iron-nitrogen system. Sieverts' Law predicts the equilibrium nitrogen concentration in liquid iron at a constant temperature is proportional to the square root of the partial pressure of diatomic nitrogen:[11]

$$\frac{1}{2}N_2(g) \rightarrow \underline{N}(wt.\%) \tag{2.1}$$

$$\underline{N}(wt.\%) = K_{eq}\sqrt{P_{N_2}} = \sqrt{P_{N_2}}\, e^{-\frac{\Delta G_1^{\circ}}{RT}} \tag{2.2}$$

where ΔG_1° is the standard free energy change for the reaction (2.1), $\underline{N}$ (wt.%) is the nitrogen concentration in solution at equilibrium with the diatomic nitrogen gas. K_{eq} is the equilibrium constant of this reaction. P_{N_2} is the partial pressure of N_2, and T is the temperature of iron. Palmer et al.[12] developed a model to explain the difference between predicted results from Sievert's law and experimental results as shown in Figure 2.1. In Figure 2.1, y-coordinate is the concentration of nitrogen in arc-welded iron. Palmer concluded that the nitrogen dissolution in the weld metal is affected by the events that take place in three regions: the plasma phase, the plasma-metal interface, and the liquid weld pool. The concentrations of various nitrogen-bearing species in the welding arc during GTA welding were determined. It is necessary to calculate these values from fundamentals of thermodynamics since the plasma temperatures are significantly higher than those of the metal in metals processing operations, for which the current thermodynamic database is not suitable. Calculations showed that neutral monatomic and diatomic species dominate regions near the surface of the weld pool. However, ionic and atomic species dominate regions away from the weld pool surface. The high

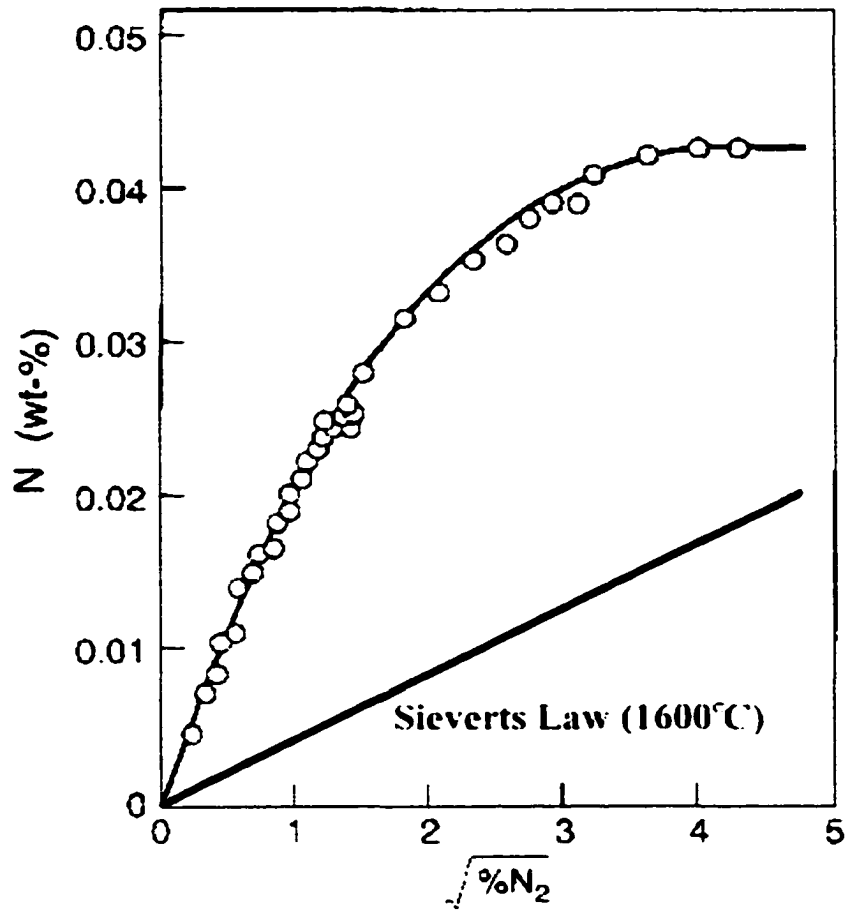

Figure 2.1. Nitrogen concentration in an arc melted iron sample plotted as a function f the square root of the nitrogen partial pressure.[11]

electron temperatures in plasma phase produce monatomic nitrogen partial pressures high enough to cause dramatic increases in the amount of nitrogen absorbed in the weld metal compared with predicted nitrogen concentration from Sievert's law.

Additions of oxygen into nitrogen-containing plasma, like the addition of air into the welding arc, affect the species density distribution of nitrogen containing species in the welding arc.[12] Calculations showed a significant increase in the monatomic nitrogen number density with the addition of oxygen to the shielding gas. Palmer's research provides a conclusive scientific basis to explain the experimentally observed enhancement in nitrogen concentrations with the addition of oxygen to the arc.

Palmer[12] developed a model to calculate the nitrogen concentration in the weld metal during GTA welding of steel. This model was based, in part, on the calculations of the turbulent, quasi-steady-state velocity and temperature fields in the weld pool using the model developed at Penn State which will be discussed later. Calculations of residual nitrogen concentration in the weld pool were based on the nitrogen concentration distribution in the weld metal at the time of solidification. Nitrogen concentrations on the weld pool surface were calculated as a function of both the monatomic nitrogen partial pressure and the weld pool surface temperatures. Once absorbed at the weld pool surface, nitrogen is then transported to the weldment interior predominantly by convection. Figure 2.2 shows the comparisons between experimentally measured nitrogen concentrations and modeled results for several mass transport enhancement factors at electron temperatures of arc plasma between 3250 and 3000 K for a travel speed of 0.847 cm/sec and nitrogen supersaturation levels of (a) 50% and (b) 75% greater than the nitrogen equilibrium concentration.[12] It is observed that the agreements between experimental and calculated results are good, especially when the mass transport enhancement factors is around 10.

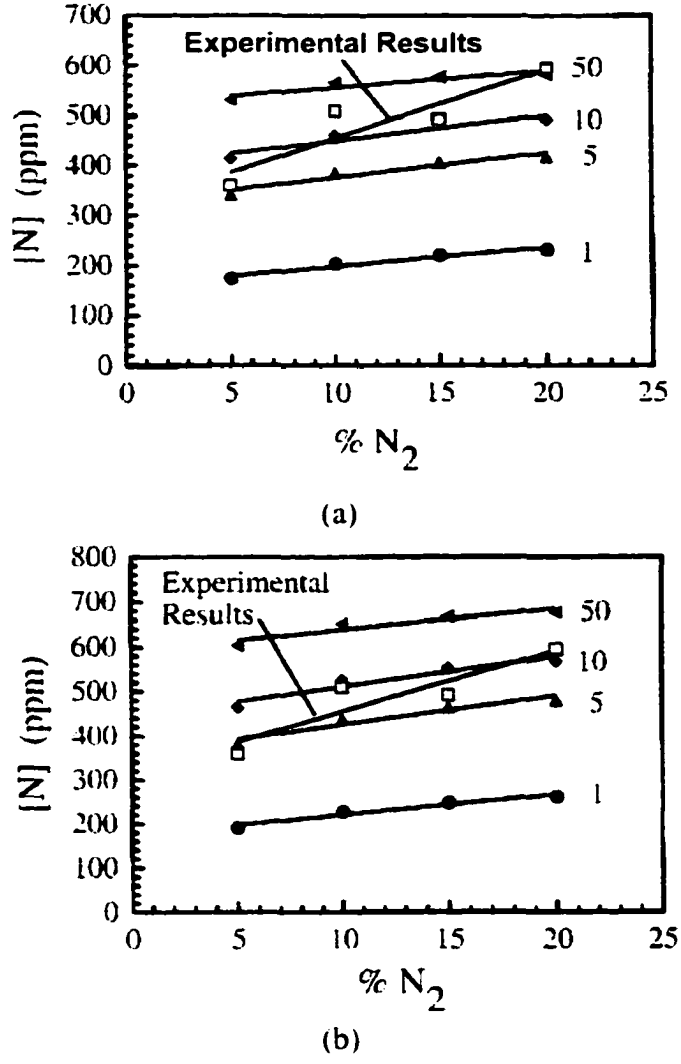

Figure 2.2. Comparison between experimental nitrogen concentrations and modeled results for several mass transport enhancement factors (1, 5, 10, and 50 in the figures) at electron temperatures between 3250 and 3000 K for a travel speed of 0.847 cm/sec and nitrogen supersaturation levels of (a) 50% and (b) 75% greater than the nitrogen equilibrium concentration.[12] The lines of experimental results were regressed from the measured data points marked with □.

This model makes it possible to calculate the concentration of nitrogen in the weld pool which is different with the nominal nitrogen concentration in the alloy taking into account many influencing factors. The same model can be used to estimate the oxygen concentration in the liquid metal with some modification. The conclusion from this model verifies our later assumption that ionic and atomic species dominate regions away from the weld pool surface when nucleation and growth rates of inclusions are calculated.

2.1.2 Thermodynamics and Kinetics of Inclusion Nucleation

When an inclusion nucleus forms in liquid steel without the aid of foreign materials, the nucleation is homogeneous. When a third phase is involved to aid the inclusion nucleation, the nucleation is heterogeneous. In the starting stage of homogeneous nucleation, a large driving force is required due to the relatively large surface energy to the total Gibbs energy for a small particle. Therefore, the supersaturation of constituent elements of inclusion must exist around the nucleation positions. The supersaturation is due to the undercooling or the presence of extra elements.

In the following discussion, alumina is used as the example to pursue the understanding of inclusion nucleation. The formation reaction expressed in equation (2.3) is assumed to take place in the melt:

$$2\underline{Al} + 3\underline{O} = Al_2O_3\,(\text{solid}) \qquad (2.3)$$

where $\underline{Al}$ and $\underline{O}$ are the concentrations of Al and O in liquid steel. Assuming the activity of Al_2O_3 is unity, the thermodynamic driving force of this reaction for one mole alumina is given by:

$$\Delta G = \Delta G^0 - RT \ln(a_{Al}^2 a_O^3) \qquad (2.4)$$

where ΔG^0 is the standard free energy change for reaction (2.3), T is temperature, R is gas constant, a_{Al} and a_O are the activities of Al and O in liquid steel, respectively, and the activity of Al_2O_3 is assumed to be unity. In equation (2.4), surface tension is disregarded as the driving force of homogeneous nucleation. When alumina is precipitated homogeneously from a melt, only small particles form initially. For small particles, surface energy plays an important role on the free energy change of precipitation. Therefore, the total driving force for one particle, ΔG_t, considering surface tension and assuming spherical shape of nuclei is expressed by[13]:

$$\Delta G_t = \frac{\Delta G}{V_m}\frac{4\pi r^3}{3} + \sigma_{il} 4\pi r^2 \qquad (2.5)$$

where ΔG is defined in equation (2.4), σ_{il} is the interfacial tension between melt and particle, r is the inclusion radius, and V_m is the molar volume of inclusion. The plot of ΔG_t versus r is presented in Figure 2.3. It is noticed that, at a specific value r^*, the total driving force of nucleation reaches the maximum. Thus, a particle with radius r^* or greater can grow while a particle smaller than r^* tends to dissolve. r* is defined as the critical radius of nucleation of inclusion in given liquid metal.

To determine r^*, the equation $\frac{\partial \Delta G_t}{\partial r} = 0$ must be satisfied. This gives the expression of r^* and ΔG^*_{hom}:

$$r^* = -\frac{2\sigma_{il} V_m}{\Delta G} = \frac{2\sigma_{il} V_m}{RT \ln(a_O^3 a_{Al}^2) - \Delta G^0} \qquad (2.6)$$

$$\Delta G^*_{hom} = \frac{4\pi\sigma_{il} r^{*2}}{3} \qquad (2.7)$$

The critical radius, r^*, for different inclusions can be estimated from above equation. For instance,[2] the interfacial tension for Al_2O_3 particle, σ_{il}, in liquid steel is around 1.5 J/m^2, ΔG^0 at 1873 K is 476 kJ/mol, $V_m = 32\times10^{-6}$ m^3/mol. Assuming $a_{Al} = 0.08$ and $a_O = 0.002$, r^* is estimated to be 8.95×10^{-10} m, or 8.95Å. This is a very small radius comparing with the normal size of inclusion, which is in the order of micrometer. In later discussion, it is

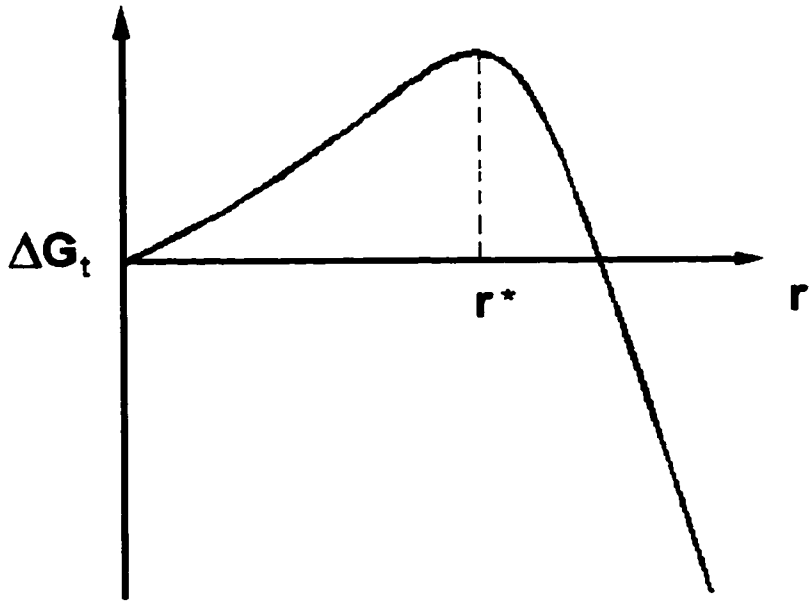

Figure 2.3 Free energy of nuclei as a function of radius.

concluded that the time necessary for an inclusion to grow to r* is insignificant comparing with total growth time, so incubation time is neglected when considering the growth behavior of inclusions.

The above discussions assume homogeneous nucleation. Due to the existence of slag, liquid-solid interface and other solid phases in the weld pool, the nature of inclusion nucleation is always heterogeneous.[13] Figure 2.4 shows the schematic figure of an nucleus and surrounding solid and liquid regions in heterogeneous nucleation. The following equation can be derived from force balance at point O:[13]

$$\Delta G^{*} = \frac{\sigma_{il}}{3}(A_{il} - A_{sl}\cos\theta) \tag{2.8}$$

where ΔG^{*} is the balanced surface tension working as the driving force of heterogeneous nucleation, σ_{il} is the interfacial tension between the inclusion and liquid as shown in Figure 2.4, A_{sl} is the interfacial area between the solid and inclusion, A_{il} is the interfacial area between the liquid and inclusion, θ is the contact angle between inclusion and solid phase shown in Figure 2.4. Assuming the inclusion is one part of the sphere of radius r*, equation (2.8) can be rewritten as[2]:

$$\Delta G^{*} = \frac{2\pi\sigma_{il}r^{*2}}{3}(1 - \cos\theta - \cos\theta\frac{\sin^{2}\theta}{2}) = \Delta G^{*}_{hom}f(\theta) \tag{2.9}$$

where:

$$f(\theta) = \frac{1}{2}(1 - \cos\theta - \cos\theta\frac{\sin^{2}\theta}{2}) = \frac{1}{4}(2 + \cos\theta)(1 - \cos\theta)^{2} \tag{2.10}$$

and ΔG^{*}_{hom} is given by equation (2.7).

For most inclusions in the liquid steel, θ is found to be around 50-70°. Therefore, $f(\theta)$ is far less than 1 and the free energy change of heterogeneous nucleation is much smaller than that of homogeneous nucleation, which makes the heterogeneous nucleation rate much higher.

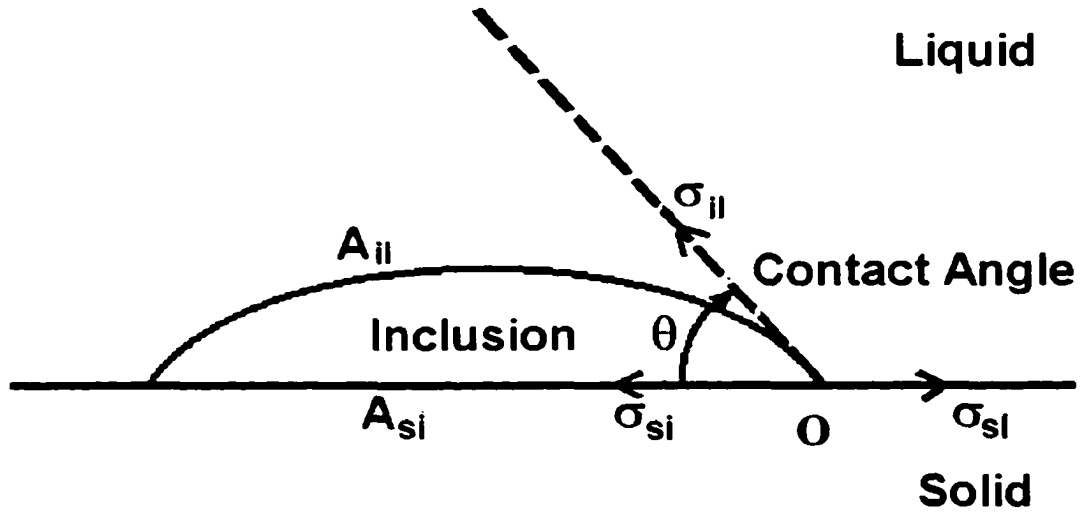

Figure 2.4. A nucleus and surrounding regions during heterogeneous nucleation. A_{il} is the area between inclusion and liquid; A_{si} is the area between inclusion and solid, σ_{il} is the interfacial tension between inclusion and liquid, σ_{si} is that between inclusion and solid, σ_{sl} is that between solid and liquid, θ is contact angle.

2.1.3 Thermodynamics and Kinetics of Inclusion Growth

After the inclusion nucleus forms, it will experience growth or dissolution in its life cycle in the weld pool. The growth of inclusion involves the diffusion of non-metallic elements (such as O, N, or S) and deoxidizing elements (such as Al, Si, Mn, Cr, etc.) from the liquid melt towards the inclusion nuclei and the formation reaction at the inclusion/liquid interface. Many previous study showed that the inclusion formation reactions at the inclusion/liquid interface are much faster than diffusion rates of elements in the liquid steel. Diffusion is the dominant factor to determine the growth and dissolution rates. Element diffusion is driven by the concentration gradient ahead of the inclusion/liquid interface. Figure 2.5 shows the schematic profiles of element concentrations ahead of inclusion interface during growth. In the figure, M and Q stand for the metallic and non-metallic elements of the considered inclusion, C represents the element concentrations in which the superscript p, i and b stand for the element concentrations in the particle, at the interface between the liquid and the inclusion, and in the bulk liquid, respectively.

The thermodynamic potential for the formation of various inclusions in liquid steel can be compared by considering their free energy changes in the inclusion formation reaction. The free energy change ΔG associated with the inclusion formation reaction, $x\underline{M} + y\underline{Q} = M_xQ_y$, at the interface is given by:

$$\Delta G = \Delta G^{0} - RT\ln(a_M^{x} a_Q^{y}) \qquad (2.11)$$

where ΔG^{0} is the standard free energy for the reaction, M is the metallic elements of the inclusion, such as Al, Ti, Si, Mn, and Q is the non-metallic elements of the inclusion, such as O, S, N, T is the temperature, a_M and a_o are the activities of M, Q, respectively, and x and y are stoichiometric coefficients. The activity of M_xQ_y in the liquid is assumed to be unity. The underlined symbols $\underline{M}$, and $\underline{Q}$ indicate that the elements M and Q are dissolved in the liquid steel. The standard free energies of formation, ΔG^{0}, of various

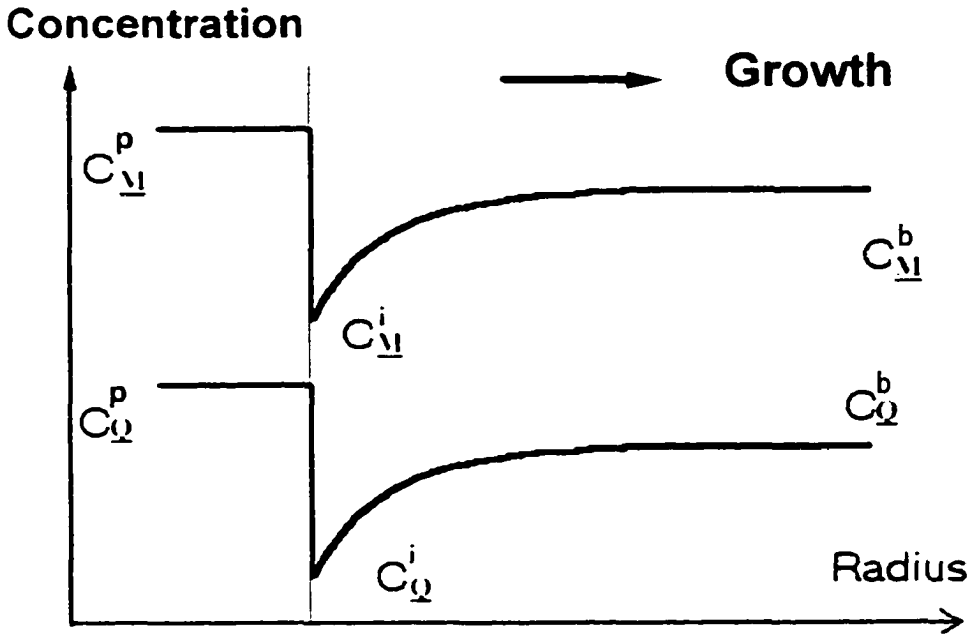

Figure 2.5. Schematic illustration of the concentration profile ahead of inclusion and liquid interface in the case of growth

inclusions can be obtained from thermodynamic database or literature. The free energy changes for the formation reaction of inclusions are highly sensitive to the element concentrations and temperature. Hence, the stability of various inclusions is functions of temperature and particular steel composition.

Babu et al.[14] calculated the free energy changes for the formation of different oxide inclusions as shown in Figure 2.6 in an alloy system which composition is shown in Table 2.1. The more negative the free energy change value is, the more likely the formation reaction will happen. If the free energy change is positive, the reaction will not take place thermodynamically. The calculated results showed that Ti_3O_5 is the most stable oxide below 2080K in this particular alloy. However, above 2200K, Al_2O_3 becomes the most stable oxide. The calculation also showed that the formations of TiO and MnO are not possible above 2100K because the free energy changes for the inclusion formation are positive, which implies the reactions are not feasible thermodynamically. They also calculated the free energy change for the formation of some complex oxides, such as $MnO{\cdot}Al_2O_3$.

Table 2.1 Composition of the alloy used in reference[14]

Elements	C	Cr	Ni	Al	Ti	Mn	N	O	S
Concentrations (wt%)	0.01	0.01	-	0.027	0.028	1.56	0.005	0.032	0.002

Deoxidation diagram for a particular inclusion at equilibrium with liquid iron at a given temperature is a powerful tool to illustrate the equilibrium behavior of inclusions. Babu et al.[17] calculated the deoxidation diagrams for equilibrium concentrations of Al, Ti, Si and Mn in liquid iron at 1809K, as shown in Figure 2.7. The alloy composition is listed in Table 2.1. For reaction (2.11), if the experimentally determined activities of M and Q (a_M and a_Q) lie to the left of the deoxidation line, the formation of corresponding inclusion is not possible. For example as Al_2O_3, beyond 0.1 wt% Al, the deoxidation curve changes its slope from negative to positive. Al_2O_3 formation is suppressed and as a

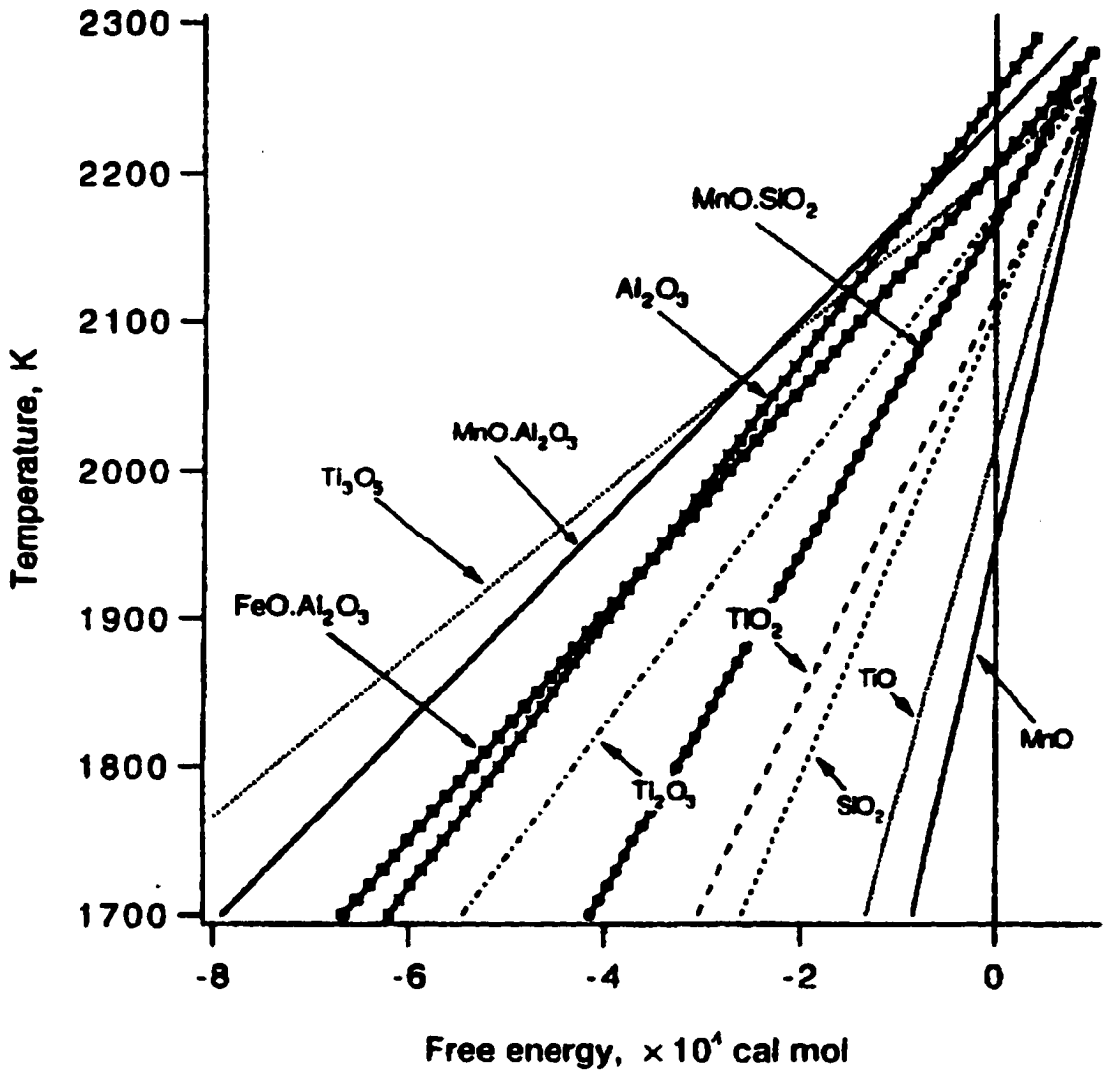

Figure 2.6 Comparison of free energy of formation of various oxides as a function of temperature.[14]

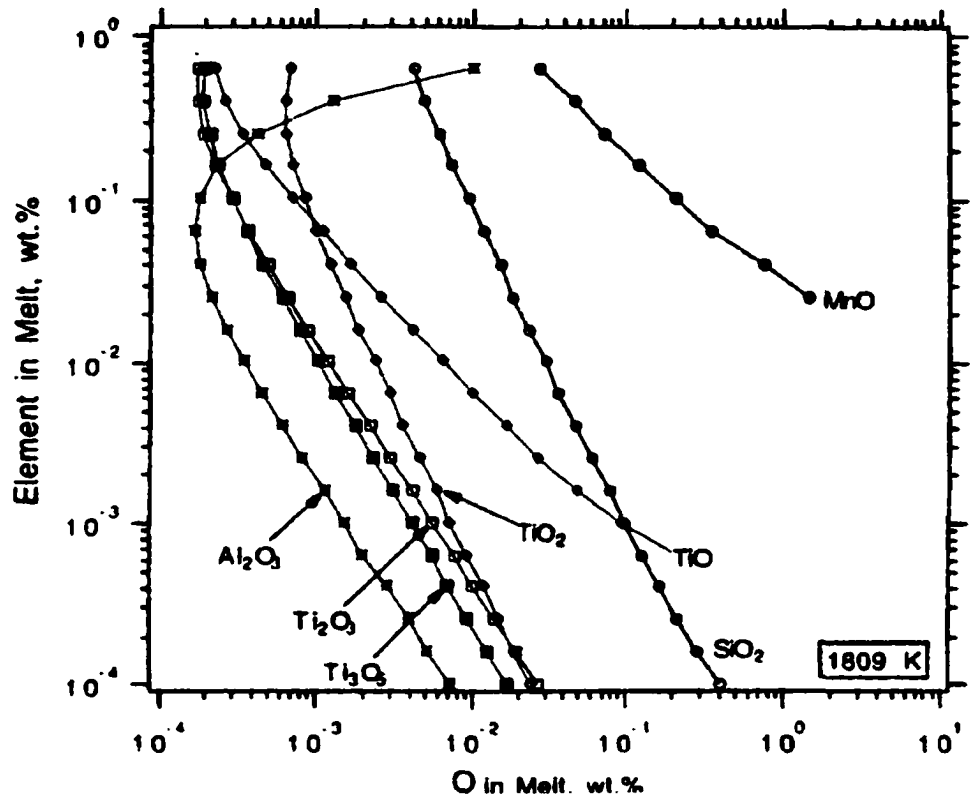

Figure 2.7 Deoxidation diagram[14] of equilibrium concentration of Al, Ti (All oxidation states), Si, and Mn (wt%) in liquid iron at 1809K.

result, increasing amount of oxygen is necessary for the possible reaction as the aluminum concentration increases. The plots also show that the oxidation state of titanium is highly sensitive to the concentrations of Ti and O (sharp slope of Ti/O curves). For example, at low oxygen concentrations, the formation of TiO is preferred over the formation of TiO_2.

Since inclusion growth is similar to precipitate growth in a supersaturated solid solution, it is possible to extend the treatment of Zener[15] for diffusion-controlled growth of precipitates in solid solutions to inclusion growth in liquid steel. Zener studied the growth of spherical precipitate and made the following assumptions:

1. The growth rate was solely limited by the diffusion of elements in liquid;
2. There was no precipitate initially;
3. The effect of surface tension upon the equilibrium concentration was neglected;

Therefore, the results would be only valid after the precipitate particles have attained a size large compared to the critical size of a nucleus. Zener defined a variables named dimensionless supersaturation of the considered elements, c*, which is given by:

$$c^* = (c^b - c^i)/(c^p - c^i) \tag{2.12}$$

where c^i, c^b and c^p is the element concentrations at the interface of inclusion/liquid, in the bulk liquid and in the inclusion particle, respectively. He derived the following equation of precipitate radius, r, as a function of c* and growth time:

$$r = \sqrt{2Dc^*t} \tag{2.13}$$

where t is the growth time. Another variable, which is defined as parabolic thickening rate and designated as α, can be given by:

$$\alpha = \sqrt{2Dc^*} \tag{2.14}$$

where D is the diffusion coefficient of the element of inclusion. D is a function of temperature and c* is a function of temperature and alloy composition. Again, the equations show that the growth rate of inclusion is a function of temperature and steel composition.

In some previous research, the mechanism of inclusion growth has been investigated by examining how the inclusion radius changes with time. Kluken and Grong concluded[16] inclusions grow by Ostwald ripening at lower temperatures which are slightly above the liquidus temperature of steel. The mean particle diameter of inclusions as function of time can be expressed by Wagner equation:

$$\bar{d}_t^3 - \bar{d}_0^3 = \frac{64D\gamma V_m C_\alpha(\infty)}{9RT} t = Ct \qquad (2.15)$$

where C is a constant and $\bar{d}_0$ is the initial mean diameter of inclusions and is assumed to be very small. They[16] did experiments to determine C empirically. However, Wagner equation was derived isothermal condition and inclusions experience growth and dissolution at all temperature range above melting point of alloy. Therefore, the final size of an inclusion is the combined effect of growth and dissolution resulting from their thermal histories. Inclusion coarsening resulting from collision and coalescence also contributes to the final inclusion size distribution. It is difficult to judge the growth mechanism solely from examining the pattern of size change with time.

2.1.4 Thermodynamics and Kinetics of Inclusion Dissolution

As show in Figure 2.8, when the interfacial concentrations of constituent elements of inclusion are bigger than that in the liquid bulk, the concentration flux will be established from the interface to the liquid, the inclusion will dissolve. To evaluate the flux of solute away from the precipitate during inclusion dissolution, Aaron[17] and Whelan[18] assumed spherical particle and diffusion controlled dissolution and derived the concentration profile in Figure 2.8 for $x \geq r$ using stationary-interface approximation:

$$c(x,t) = \frac{(c^i - c^b)r}{x} \operatorname{erfc}\left(\frac{x-r}{2\sqrt{Dt}}\right) \qquad (2.16)$$

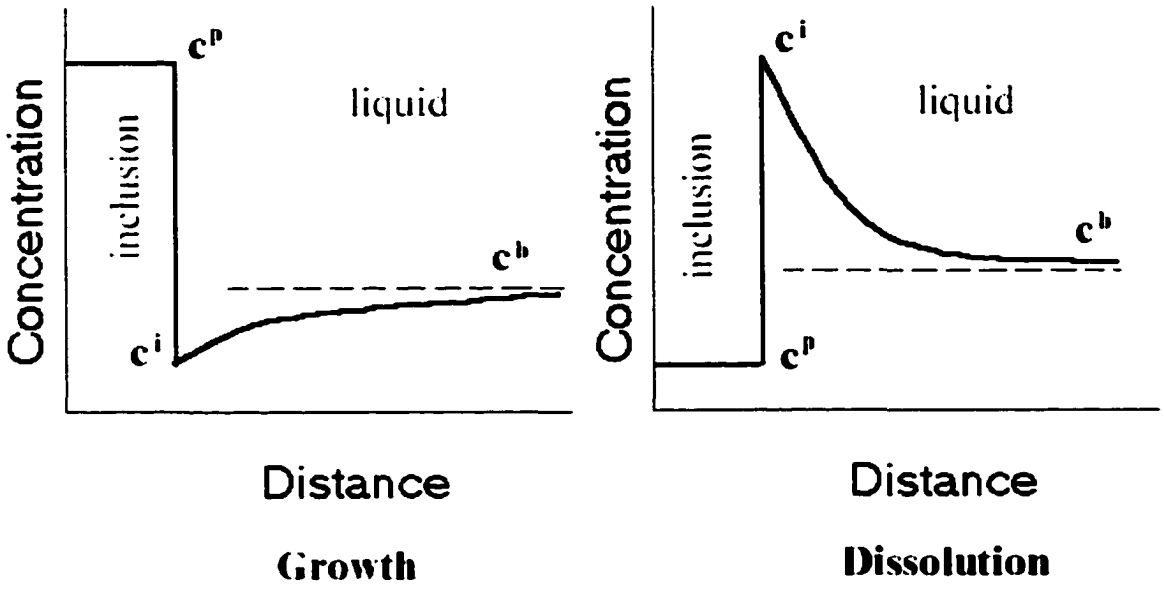

Figure 2.8 Comparison between the element concentrations near the interface of inclusion and liquid during growth and dissolution.

where c(x,t) is the concentration of constituent elements of inclusion at time t and position x, r is the radius of inclusion, D is diffusion coefficient. Considering the mass balance, the flux of solute away from the interface was assumed to be equal to the rate of the loss of solute from the precipitate, which is expressed by:

$$-4\pi r^2(c^p - c^i)\frac{dr}{dt} = -4\pi r^2 D(\frac{\partial c}{\partial x}) \tag{2.17}$$

Substitution of equation (2.16) into (2.17) gives:

$$\frac{dr}{dt} = -\frac{Dc^*}{r} - c^*\sqrt{\frac{D}{\pi t}} \tag{2.18}$$

At short time, an approximate solution of equation (2.18) is obtained as:

$$r = r_0 - \frac{c^* Dt}{r_0} - \frac{2c^*}{\sqrt{\pi}}\sqrt{Dt} \tag{2.19}$$

This equation was used to calculate the dissolution rate of θ phase precipitate in Al-Cu alloy in Whelan's paper.[18] The calculated results agreed with the experimental results very well. However, this simplified equation did not consider non-isothermal conditions. The growth and dissolution rates of inclusion in the liquid steel under non-isothermal conditions must be taken into account to develop a complete understanding of inclusion size change.

2.1.5 Simultaneous Nucleation and Growth of Inclusions

Only a few studies about simultaneous nucleation and growth of inclusions or precipitates in liquid metal have been reported in the literature.[14,18-21] Babu et al.[14,19] considered the experimental welding conditions in Kluken's work[16] and obtained the heating and cooling rates of the weld metal from a heat transfer and fluid flow model. They calculated the relative stability of several oxide inclusions and assumed that the most stable oxide was the first oxide to form. Extents of reaction in a small time interval for all oxides were calculated. After every small time step, the final number densities of various types of inclusions were considered as the integrated nucleation rate of oxides for the next time interval. This procedure was continued along the continuous cooling curve

until the temperature was lower than the solidius temperature of the weld metal. The comparisons between calculated and experimental results showed that the model was capable of predicting the reduction in the inclusion number density with increase in the heat input. However, in that model, complex oxides and other nitride and sulfide inclusion were not considered. Furthermore, the formation sequence of inclusions was preset and was not adjusted during the formation and growth of inclusions.

Bhadeshia et al[20,21] performed a serial studies on the kinetics of simultaneous phase transformations. In their model, calculation of a single transformation began with the calculation of the nucleation and growth rates using classical theory. The estimation of volume fraction was undertaken considering impingement between different particle phases. The simultaneous precipitation of hardening phases in secondary hardening steels, such as M_2X, $M_{23}C_6$, M_7C_3 and M_6C were calculated based on the equations. That model was also applied to the simultaneous phase transformation of ferrite, Widmanstaetten ferrite, and pearlite in austinite decomposition. The predicted volume fractions of various phases were in good agreement with the experimental results. However, in this model[20], the complex thermal cycles the inclusion experiences also cannot be taken into account. The liquid bulk composition cannot be updated as the inclusions grow.

2.2 Transport Phenomena in Welding Processes

The heat transfer and fluid flow in the weld pool not only determine the geometry of the fusion zone (FZ) and the heat affected zone (HAZ), but also determine the temperature and velocity fields in the weld pool. The temperature and velocity fields significantly affect the motion and thermal history of inclusions, which in turn determine the growth and dissolution rate of inclusions. Therefore, understanding the transport phenomena in the weld pool is a prerequisite for the study of inclusion behaviors.

Experimental measurement of the characteristics of fluid flow and heat transfer in the weld pool has been proven to be very difficult due to very high temperatures and sharp temperature gradients in a fairly small region. Direct measurement of temperatures inside the weld pool by using thermocouples is inherently inaccurate because of the errors caused by the existence of thermocouple in a very small weld pool.[22] Therefore, several indirect measurement techniques have been developed to measure the weld pool surface temperatures, including narrow band infrared pyrometry,[23] thermographic sensing,[24] optical spectral radiometric/laser reflectance,[25] and infrared thermographic cameras.[26] For instance, Figures 2.9 (a) and (b) show the experimentally measured surface temperatures of the weld pool using infrared thermographic cameras.[26] The experiments were performed with a continuous wave CO_2 laser at powers of 4800W and 3200W on low alloy steel St52 (0.21C-0.36Si-1.52Mn-0.006S-0.21Cr-0.05Mo-0.14Ni-0.14Cu-<0.02V-<0.05W,Co-<0.005Ti,Nb,P wt%). The welding speed was 0.2 m/min. Most of the indirect techniques have inherent uncertainty because of the difficulty nn determining some important factors, such as the emissivity as a function of temperature, the associated angle, the exact wavelength of emission, and etc.

Measurement of flow velocities in a small and intensely heated weld pool is more difficult using the techniques currently available. Very few data has been reported on the measurement of velocities in the weld pool.[27] One technique is to introduce a small particle on the weld pool surface and use a high-speed camera to record its movement and calculate its velocities on the surface of the weld pool. This information can be used to understand the fluid flow velocities in the weld pool. Apparently, this method is inaccurate and very costly because of the limitation of camera and irregular movement of the particle[28]. It cannot give useful information about the fluid velocity inside the weld pool. Figure 2.10 presents a snapshot of a high-speed camera video which shows a moving particle at the surface of the weld pool.[28]

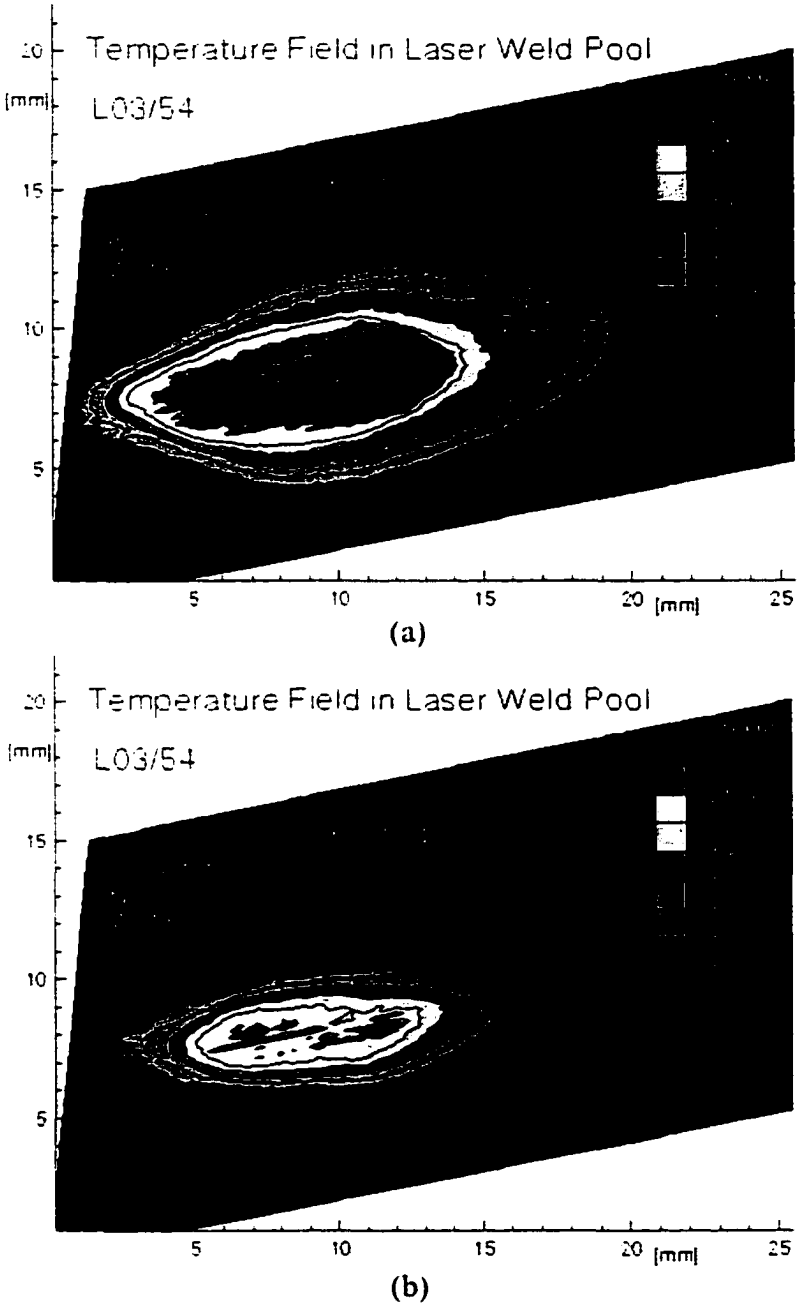

Figure 2.9 Infrared camera images of surface temperature of the weld pool. Laser welding, St 52 steel, (a) power = 4800 W, (b) power = 3200 W.[26]

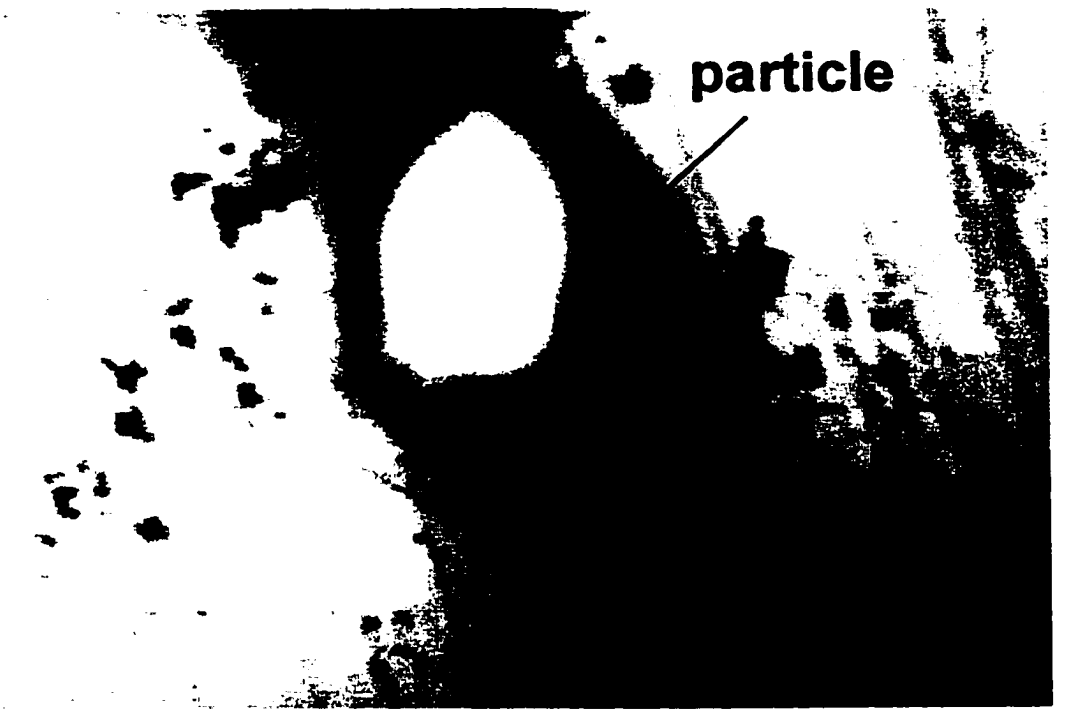

Figure 2.10 High speed image of a particle flowing in the weld pool.[28]

Due to the difficulties in the experimental measurements, mathematical modeling has become an essential way to study the fluid flow and heat transfer in the weld pool. Modeling can provide quantitative fundamental understanding which cannot be obtained by any other ways. In recent years, significant progress has been made in understanding the heat transfer and fluid flow in the weld pool by mathematical modeling. In this chapter, the fundamental principles involved in the heat transfer and fluid flow modeling and some major previous work are carefully reviewed.

There are many physical processes that take place during welding.[29-34] The surface of base material interacts with the heat source and absorbs energy from the heat source. In many cases, plasma is formed above the heating area. The presence of electrical arc and plasma plays an important role in the interaction between the base material and heat source. Some regions of the base material are heated above their melting point and form a molten weld pool. The molten liquid flows in the weld pool driven by surface tension, electromagnetic and buoyancy forces. The nature of fluid flow in turn determines the weld pool geometry. In many cases, the fluid flow in the weld pool is turbulent in nature due to the high current and voltage used in the weld processes. At the surface and inside the weld pool, alloy composition undergoes change due to the dissolution and dissociation of gases, and vaporization of alloying elements. In this section, the previous investigations on above aspects are discussed.

2.2.1 Heat Transfer between Heat Source and Base Material

Heat source of welding can be electrical arc, laser beam, electron beam, or mechanical force. Although the interaction between different heat sources with the target materials are different, there are some common issues. For example, the heat transfer between heat source and workpiece depends on several factors irrespective of the heat source which includes: (a) the power density and the total energy input, (b) the spatial distribution of the energy inputs, and (c) the presence of plasma above the workpiece except for the mechanical force weldings.

Local value of heat input at the weld surface is determined by the power density supplied by heat source and the energy absorption efficiency, which depends on factors such as type of heat source, surface condition, shielding gas, wire feed rate, arc length, and electrode diameter. The heat source power density and energy absorption efficiency vary significantly for different welding processes, as presented in Table 2.2:

Table 2.2 Power density and heat transfer efficiency for different welding processes[6]

Weld processes	Power density (W/cm^2)	Total efficiency, η (%)
Gas Tungsten Arc (GTA or TIG)	$10^3 - 10^5$	40-80
Gas Metal Arc (GMA or MIG)	$10^3 - 10^5$	65-85
Submerged Arc (SA)	$10^4 - 10^6$	90-95
Laser Beam (LB)	$10^6 - 10^8$	20-75
Electronic beam (EB)	$10^6 - 10^{10}$	70-95

The spatial distribution of input energy on the workpiece surface has a direct influence on the heat transfer and fluid flow pattern in the weld pool. The format of Gaussian distribution had been widely used in the previous researches to model heat distribution in arc welding.[29-31] In laser and electronic beam weldings, although Gaussian distribution was commonly used, some researchers used uniform distribution when the beam profiles were relatively flat.[32,33] Two types of Gaussian distribution have been reported in the literatures. One is the classical Gaussian distribution, which is extensively used in the simulation of heat flow during welding and can be expressed as[29]:

$$Q(r) = \frac{3\eta P}{\pi R^2} \exp\left(-\frac{3r^2}{R^2}\right) \qquad (2.20)$$

where Q is the heat flux at the location where the distance to the center of heat source is r, η is the absorption efficiency, P is the power input, and R is the nominal radius of the

heat source. The other commonly used energy distribution equation is modified Gaussian distribution based on experimental results. Tsai et al[31] and Smartt[32] et al modified some parameters in equation (2.20) to simulate the heat distribution in GTA welding from experimental data. The modified equation is given by[32]:

$$Q(r) = \frac{\eta P}{2\pi\sigma^2}\exp(-\frac{r^2}{\sigma^2}) \qquad (2.21)$$

where Q, P, and r have the same definition as those in equation (2.20). The symbol σ, named as distribution parameter, is determined from experimental results considering factors such as arc length, current, and electrode tip angle. Calculated from equation (2.20), Figure 2.11 shows a classical Gaussian distribution of energy where x-axis is the distance from the center point of heat source.

After the base materials absorb energy and are heated to elevated temperatures, considerable vaporization of alloying elements may take place. Plasma forms on the top of molten zone. The presence of plasma plume may change the absorption efficiency and the interaction between material and energy source significantly. It was also observed by Sahoo *et al*[33] that the presence of plasma lowers the vaporization rate of alloying elements significantly. In laser beam welding, because plasma absorbs laser energy, its presence always lowers the efficiency for the heat transfer between the laser beam and workpiece.

The formation of plasma during welding and its effect on heat transfer and fluid flow in the weld pool is not a main topic in this thesis. However, its influence is represented by the selection of energy absorption efficiency in the model.

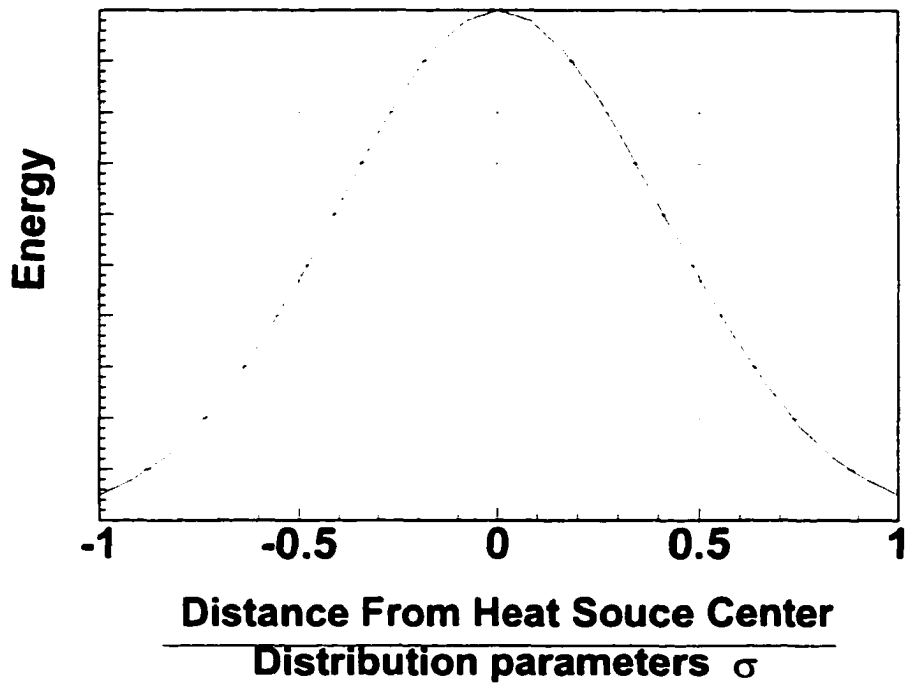

Figure 2.11 Schematic illustration of Gaussian distribution of energy during welding plotted from equation (2.21).

2.2.2 Fluid Flow and the Driving Forces in the Weld Pool

Although the significant effect of the fluid flow and heat transfer in the weld pool has been recognized for a long time, the systemically theoretical studies have been preformed only in recent decades[31,33-41] due to the development of high performance computers and software. It is already a clearly known fact that the mathematical modeling supplemented by the experimental studies results in insight not attainable by experiments alone.

During welding, the fluid flow in the weld pool is driven by a combination of several driving forces such as surface tension, buoyancy force, impinging and dragging forces of the arc plasma in arc welding, and electromagnetic force when electric current is used.[34,39,42] Because the impinging and dragging forces of the arc plasma are only important at very high welding currents, for example in excess of 500 A,[42,43], it is not a significant factor in most cases. Figure 2.12 shows the basic flow patterns and the resulting weld pool geometry driven by different forces schematically. Only half of the cross section of the weld pool is plotted because of the symmetric shape. The circular arrows point to the fluid flow direction. Buoyancy force is caused by density variation due to the temperature gradients within the weld pool. The flow pattern driven by buoyancy forces is shown in Figure 2.12(a). The direction of flow is from the hotter region (around the heat source center) outward to the cooler region. The buoyancy force can be expressed by[44]:

$$F_b = \rho g \beta (T - T_0) \tag{2.22}$$

where T_0 is any arbitrarily selected reference temperature, ρ is the density of liquid metal at T_0, g is the acceleration of gravity and β is the thermal expansion coefficient.

Electromagnetic force is generated by the interaction of the diverging current and resulting magnetic field. It is also called Lorentz force that leads the fluid to flow inwards and downwards as shown in Figure 2.12(b). The magnitude of electromagnetic force can be expressed as[45]:

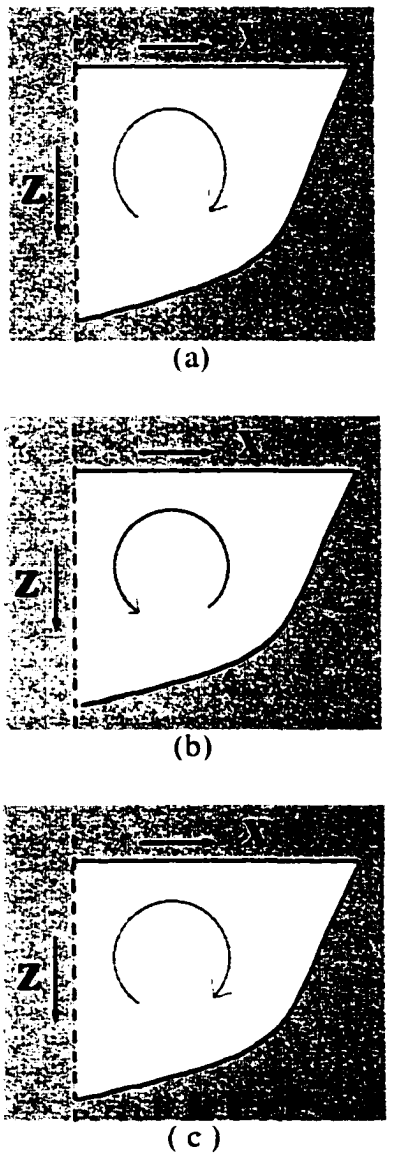

Figure 2.12 Schematic fluid flow patterns driving by different forces (a) buoyancy force; (b) electromagnetic force; (c) surface tension.

$$\bar{F}_e = \bar{J} \times \bar{B} \tag{2.23}$$

where $\bar{J}$ is the vector of current density and $\bar{B}$ is the vector of magnetic flux. The calculation procedures for the electromagnetic force during arc weldings are available in the literature.[45]

The difference of surface tensions between the regions close to the heat source and at the edges of weld pool induces a shear stress, known as Marangoni stress (or force) which can be expressed as[46]:

$$\tau = \frac{\partial \sigma}{dx} = \frac{d\sigma}{dT} \cdot \frac{dT}{dx} \tag{2.24}$$

where τ is Marangoni stress, σ the is surface tension, $d\sigma/dT$ is the temperature gradient of interfacial tension, x is the distance along the surface from the center of the heat source. The flow direction shown in Figure 2.12(c) is determined by the value of $d\sigma/dT$. dT/dx is always negative because the temperatures at the center of weld pool are always higher than those at the edge. The interfacial tension gradient can be negative or positive depending on temperature and composition. Figure 2.13 (a) shows the surface tension gradients as functions of temperature in pure iron and Fe-S alloy.[47] In the case of pure iron, the surface tension gradients are always negative, the resulting shear stress becomes positive, which means the stress will induce a flow outward from the heat source center to the weld pool edges as shown in Figure 2.13 (b). Because the heat is carried by the fluid flow from the heat source center outward to the edge of weld pool, the geometry of the weld pool is shallow and wide. In the case of Fe-S alloy, the surface tension gradients are positive at lower temperature, the resulting shear stress becomes negative, which means the stress will lead a flow inward and downward as shown in Figure 2.13 (c). Because the heat is carried by the fluid flow from the center of heat source downward to the bottom of the weld pool, the geometry of the weld pool is narrow and deep.

Sahoo et al[48] developed a model to calculate the temperature coefficient of surface tension in binary alloy systems considering surface active elements such as sulfur. Pitscheneder et al[49] developed a mathematical model to explain the major differences

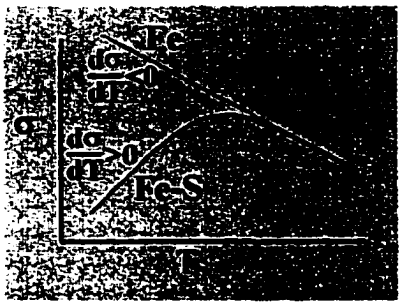

(a)

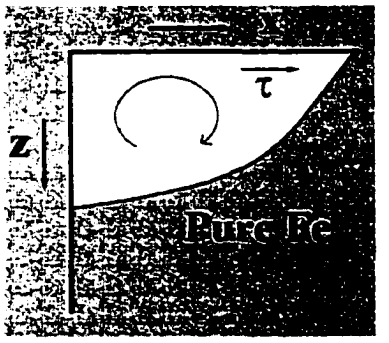

(b)

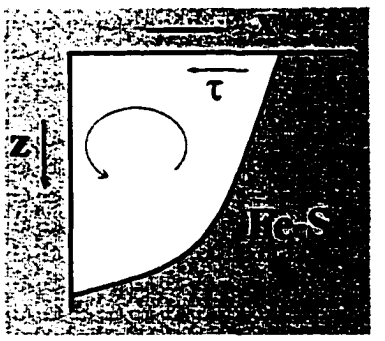

(c) The flow direction is depended on dσ/dT

Figure 2.13 (a) The temperature coefficient of surface tension (b) flow in pure iron with negative surface tension coefficient, (c) flow in Fe-S alloy with positive surface tension coefficient.[47]

between the geometry of weld pools due to changes in the concentrations of surface active elements such as sulfur. Their results agreed with the experimental results very well and explained the experimental results from fundamentals of transport phenomena in the weld pool.

Although there are several driving forces of fluid flow in the weld pool, their relative importance are quite different. To estimate the relative magnitude of these driving forces, several dimensionless numbers which have been used in the previous research to determine the relative magnitude of different driving forces are listed in Table 2.3. A set of calculated values of the dimensionless numbers for a typical welding conditions are also given in Table 2.3. The welding conditions and parameters used for the estimation are presented in Table 2.4. The definitions of all variables in Table 2.3 are also listed in Table 2.4.

The importance of various driving forces can be presented by following equations: the ratio of surface tension to buoyancy force can be expressed as[37]:

$$\frac{\text{Marangoni force}}{\text{Buoyancy force}} = \frac{\text{Ma}}{\text{Gr}} \tag{2.25}$$

The ratio of electromagnetic force to buoyancy force can be expressed as[37]:

$$\frac{\text{Electromagnetic force}}{\text{Buoyancy force}} = \frac{\text{Rm}}{\text{Gr}} \tag{2.26}$$

The ratio of electromagnetic force to Marangoni force can be expressed as[37]:

$$\frac{\text{Electromagnetic force}}{\text{Marangoni force}} = \frac{\text{Rm}}{\text{Ma}} \tag{2.27}$$

It is observed that buoyancy force represented by Grashof number is the smallest and always negligible. The electromagnetic force, represented by Magnetic Reynolds number Rm, is about one quarter of the Marangoni force, represented by surface tension Reynolds number, Ma. The ratio, Rm/Ma, can increase when the arc current increases.

This fact implies that the electromagnetic force cannot be neglected during modeling transport phenomena in the weld pool.

Table 2.3 Dimensionless numbers concerning different driving force[50]

Dimentionless numbers	**Expressions**	**Calculated values**
Reynolds number, Re	$Re = \frac{\rho u L_R}{\mu}$	2958
Grashof number, Gr	$Gr = \frac{g\beta L^3 \rho^2 \Delta T}{\mu^2}$	1610
Magnetic Reynolds number, Rm	$Rm = \frac{\rho \mu_m I^2}{4\pi^2 \mu^2}$	63000
Surface tension Reynolds number, Ma	$Ma = \frac{\rho L_R \Delta T}{\mu^2} \cdot \frac{\partial \sigma}{\partial T}$	254000

Table 2.4 Typical welding parameters[50] for the calculation of the dimensionless numbers in Table 2.3

Thermal expansion coefficient, β	1.0×10^{-4} K^{-1}
Gravitational acceleration, g	9.8 m/s^2
Materials density, ρ	7100 kg/m^3
Magnetic permeability, μ_m	1.26×10^{-6} N/A^2
Viscosity, μ	6.0×10^{-3} kg/m·sec
Surface tension temperature gradient, $\partial\sigma / \partial T$	-4.3×10^{-4} N/m·K
Characteristic length of the weld pool, L_R	5 mm
Characteristic length in Gr, L	1.25 mm
Average velocity in the weld pool, u	0.05 m/s
Temperature different between center and edge of the weld pool, ΔT	600 K
Arc current, I	100 A

2.2.3 Conduction and Convection Heat Transfer in the Weld Pool

2.2.3.1 Criterion of Conduction and Convection Mode of Heat Transfer

In the weld pool, heat is transported by a combination of conduction and convection. The relative importance of convection and conduction heat transportation can be estimated by calculating the value of a dimensionless number: Peclet number, Pe, expressed by:

$$Pe = \frac{u\rho C_p L_R}{k} \tag{2.28}$$

where u is the characteristic velocity of fluid flow, ρ is the density of the base material, C_p is the specific heat of liquid metal at constant pressure, L_R is the characteristic length of the weld pool, and k is the thermal conductivity of the melt. When Pe is much larger than unity, which in physical terms means large fluid flow velocity, large weld pool size, and poor thermal conductivity, convection is the dominant mechanism for heat transportation. The following example of a typical steel arc welding[50] gives a general idea of the value of Pe: Assuming the fluid flow velocities in the weld pool to be 0.2 m/s, the density of steel 7200 kg/m^3, the specific heat of steel 754 J/kg·K, the weld pool length 5 mm, and the thermal conductivity 25 W/m·K, Pe is calculated to be 217.2 from equation (2.28). When the value of Pe is much higher than 1, it implies that the convection is the dominant mechanism of heat transfer. Under most welding conditions, Peclet numbers are much larger than unity and heat is transported mostly by convection in the weld pool.

Another important dimensionless number, Prandtl number (Pr), is used for judging the relative importance of the viscous diffusivity and thermal diffusivity in heat dissipation. Prandtl number Pr is expressed by[51]:

$$Pr = \frac{C_p \mu}{k} \tag{2.29}$$

where μ is the viscosity of the liquid material, C_p is the specific heat, and k is the thermal conductivity. As an extension of Prandtal number, turbulent Prandtal number, Pr_t, has

been introduced to describe the heat dissipation mechanism in turbulent flow. The turbulent Prandtal number is very important for turbulent heat transfer and fluid flow calculations and will be discussed later in this section.

2.2.3.2 Modeling Conduction Mode of Heat Transfer

For several decades, extensive efforts have been made to calculate the heat transfer and fluid flow in the weld pool. However, most efforts were limited to pure conduction mode of heat transfer. It is worth looking at one of the classic and still widely used[52-55] simplified solution of the generalized equations of the conduction heat flow in welding, i.e., Rosenthal equations. Rosenthal[52] derived analytical solutions of temperature distribution for heat conduction equations with a moving point heat source under the assumption of quasi or pseudo-steady state. For heat conduction in a thick plate assuming finite thickness and infinite length and width, the analytical solution is as follows:

$$T - T_0 = \frac{Q}{2\pi k} e^{vx/2\alpha_s} \frac{e^{-vr/2\alpha_s}}{r} \tag{2.30}$$

where T is the temperature at point (x,y,z), T_0 is the initial temperature of workpiece, Q is the input heat flux with unit of cal/cm·s (because it is a point heat source), k is the thermal conductivity, v is the moving velocity of heat source, α_s is the thermal diffusivity which is given by $\lambda/\rho C_p$, where λ is the thermal conductivity, ρ is density of workpiece, C_p is the heat capability of workpeice material, and r is the distance between the monitoring point to the heat source center. For heat conduction in thin plate assuming the temperature variation along thickness or z direction is negligible, the analytical solution is given by:

$$T - T_0 = \frac{Q}{2\pi k} e^{vx/2\alpha_s} \frac{K_0(vr/2\alpha_s)}{d} \tag{2.31}$$

where $K_0(\ )$ is the zero order, second kind of Bessel function and d is the thickness of workpiece, other variables have the same definitions in equation (2.30). Figure 2.14 presented a typical temperature distribution calculated from thick plate Rosenthal

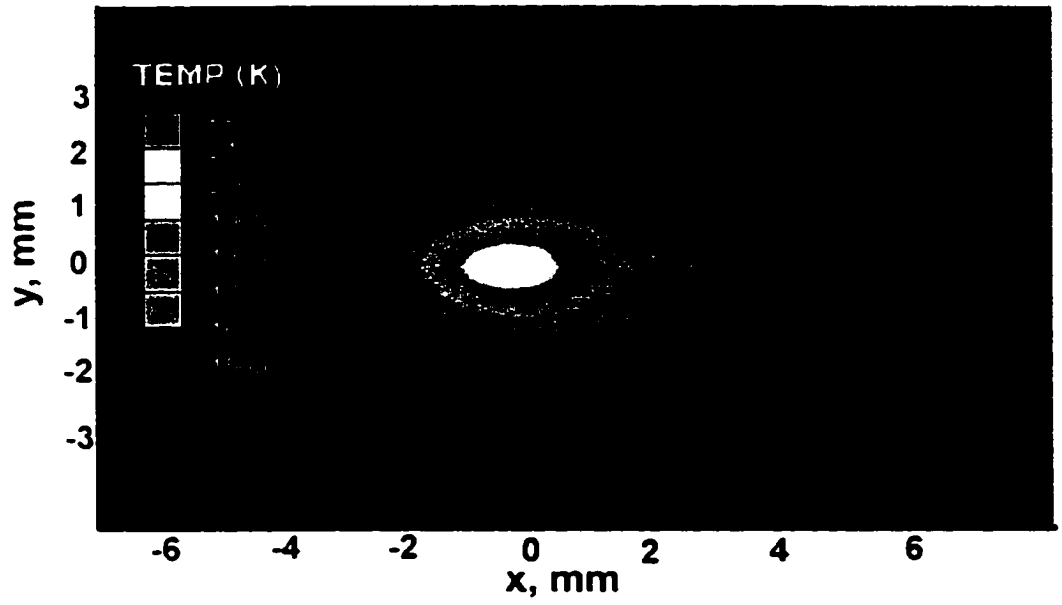

Figure 2.14 Temperature distribution calculated from thick plate Rothenthal equation. Welding speed: 5 mm/sec, ampere: 35 A, voltage: 280 V. The other data of material properties can be found in Table 2.1.

equation (2.30). It can be observed that the calculated temperature gradients in the front of the weld pool are higher than that at the trailing edges. The weld pool shows elongated geometry. These general characteristics of calculated weld pool geometry can be observed in every kind of fusion weld pool with moving heat source.

Rosenthal equations are still widely used in welding community because of the simplicity and reasonable accuracy. It is also easy to derive some important parameters during welding processes from the analytical solutions, for instance, the length and width of the molten zone, the peak temperatures in the liquid region, the width of the heat affected zone, heating and cooling rates of any location, and etc. The detailed derivations are not given in this thesis. However, there are many publications[53-55] which dealt with these issues from many aspects.

Although Rosenthal equations are well recognized and utilized, some assumptions made in the calculation will over-simplify the real situation. These assumptions include:

1) Convection heat transfer is ignored;
2) Enthalpy of solidification is not considered
3) Characteristics of heat source are not taken into account.

In the following section, numerical methods developed in recent to understand the heat transfer and fluid flow phenomena and predict temperature and velocity fields of the weld pool are discussed.

2.2.3.3 Modeling of Convection Heat Transfer and Fluid Flow

From early 80s, many numerical models[56-60] have been developed to study the convective heat transfer and fluid flow in the weld pool. Most work in the beginning started modeling heat transfer and fluid flow in the weld pool in two dimensions. In their model, the driving forces such as surface tension, electromagnetic, and buoyant forces were considered. It was found that the surface tension and electromagnetic forces

dominate the flow behavior in the weld pool. They also found that the surface tension might produce high surface velocities. For example, with welding current of 100A, the maximum velocity at the surface was calculated to be 83.8 cm/s by considering surface tension and 4.5 cm/s without considering surface tension[61].

Extensive efforts have been made at Penn State in understanding heat transfer and fluid flow in the weld pool by mathematical modeling in the last two decades.[8-11,62-81] Starting from the calculations of temperature and velocity fields in the weld pool, various aspects of weld processes were systematically investigated by a combination of modeling and experiments. These phenomena include the effects of surface active elements on weld pool geometry,[65,77] dissolution of gases such as oxygen, nitrogen, and hydrogen,[8-10] vaporization and concentration change of alloying elements,[68,69] weld metal microstructure evolution,[70-72] growth and dissolution behavior of inclusions[73-76], keyhole mode penetration,[77] grain growth in HAZ,[78,79] general correlation for the of prediction of weld pool geometry for spot welds,[80] and mechanism of porosity formation during laser welding of aluminum and magnesium alloys.[81] These theoretical studies have been applied to various materials including pure iron, stainless steels, low alloy steels, aluminum alloys, titanium and even some non-metallic materials such as $NaNO_3$, for different welding conditions, such as GTA welding, GMA welding, SA welding, laser and electronic beam welding. A careful review of the work done in Penn State on 3-D heat transfer and fluid flow model is presented below because the thesis presented here is mainly based on the previous research at Penn State.

The studies on 3D modeling of heat transfer and fluid flow at Penn State was started in the eighties. Paul and DebRoy[62] calculated the heat transfer and fluid flow in the weld pool of pure iron and pure iron doped with different concentrations of sulfur. The weld pool geometry and the secondary dendrite arm spacing in solidified structure were predicted based on the calculated temperature field and cooling rates. The effect of sulfur on the weld pool geometry was investigated. The theoretically predicted results were comparable with corresponding experimental results. Zacharia et al.[63] developed a

model to simulate the heat transfer and fluid flow in the weld pool of 304 stainless steel welded by GTA and laser welding. In their work, the coefficient of surface tension was taken as a function of both temperature and sulfur concentration. Good agreement was achieved between the calculated and experimental results in the respect of the shape and size of the weld pool.

Mundra[64] et al. examined the effects of thermophysical properties on the transport phenomena in the weld pool. They investigated the effects of thermal diffusivity of liquid metal and temperature coefficient of surface tension on weld pool geometry, peak temperature and maximum velocity of fluid flow in the weld pool. The modeling results were in good agreement with the experimental observations. Mundra et al.[40,43] further developed a comprehensive 3-D model to study the heat transfer and fluid flow in the weld pool. The velocity and temperature fields, and the shape and size of the fusion zone were calculated through the solution of the equations of conservation of mass, momentum and energy in three dimensions for different welding parameters using the in-house developed model. The governing equations were modified and formulated in a coordinate system attached to the moving heat source. The enthalpy-porosity technique was implemented for heat transfer and fluid flow modeling in the mushy zone. The model was well verified by comparing experimental measurements of weld pool geometry and transient temperatures at several selected locations in the weldment with the corresponding calculated results for gas metal arc (GMA) welding of mild steels[40]. They also calculated the vaporization rate of different elements during laser welding and obtained results which agreed well with the experimental data. Figures 2.15(a) and (b)[64] show good agreement between the experimental and the predicted values of the cross section area of the weld pool and vaporization rates in laser welding. The model was also used to predict the weld geometry and cooling rates in low alloy steels for GMA welding. The agreement between calculated and measured results was also good.

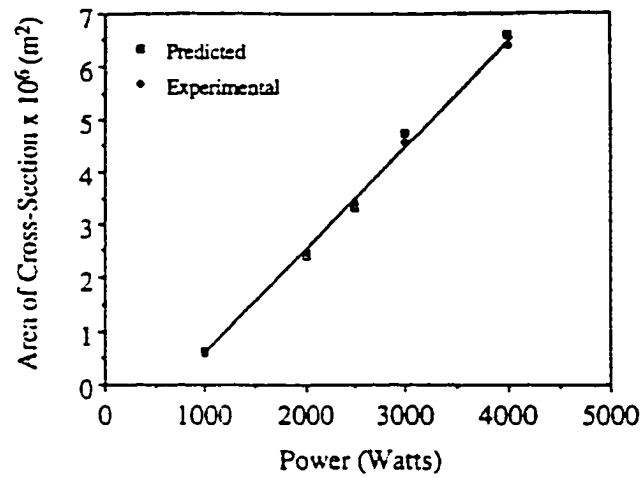

(a)

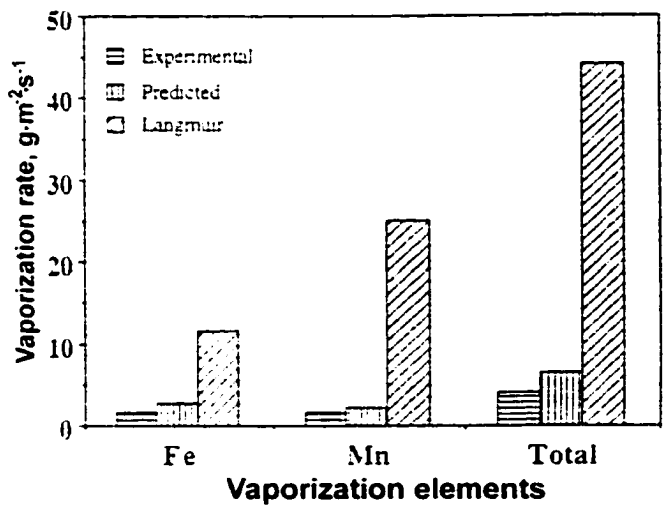

(b)

Figure 2.15 Comparison of calculated and experimental results of (a) the cross section area and (b) vaporization rates in the laser weld pool.[64] AIMS 1040 Steel, welding speed: 12mm/s, ampere: 50 A, voltage: 330V

Pitscheneder et al.[66,67] performed a serial of experiments on the laser beam welding of Bohler S 705 high speed steel (AISI M41) in the as-cast state. The optical images of the weld pool cross section showed that the minor change in sulfur concentration can induce major change in weld pool geometry at high heat input, 5200 W. However, this did not happen at lower welding power condition, 1900 W. The mathematical model was applied to explain this phenomenon. Figure 2.16 shows[67] the comparison of the predicted weld geometries with two different sulfur contents with the corresponding experimental results at both high and low heat input. The predicted results showed that this phenomenon is due to the relative importance of convective and conductive heat transfer in the weld pool. It was calculated that the flow velocities in the weld pool at lower laser power (1900W) were two orders of magnitude lower than that at high laser power (5200W). Thus, the values of the Peclet number (refer to equation (2.28)) in the lower laser power welds were less than unity for both sulfur concentrations, i.e., conduction heat transfer was dominant in both sulfur concentrations for low laser power. By contrast, much larger Peclet numbers were found at high laser power, which implied that convective heat transfer was the dominant mechanism. The modeling research explained that the effect of sulfur was only pronounced under convection condition.

Figure 2.17 shows another example of comparison of the calculated temperature fields at the weld pool surface with the temperature fields which were measured with infrared camera during laser welding.[66] It is observed that the surface temperature profiles agreed with the calculated results very well for different laser power.

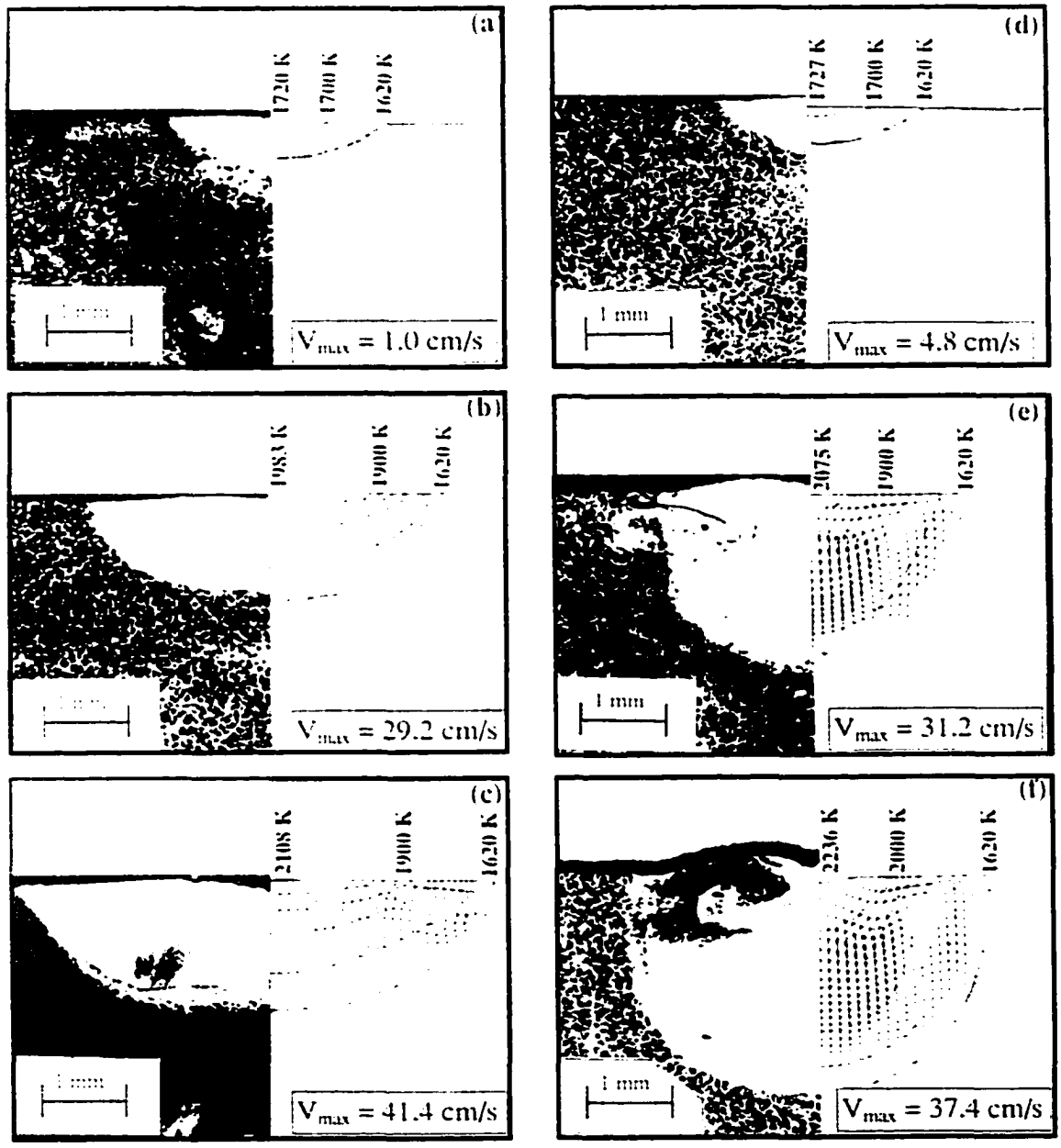

Figure 2.16 Comparison of the calculated and experimentally measured weld pool geometries for the steel containing 20 ppm sulfur for laser powers of (a) 1900 W, (b) 3850 W and (c) 5200 W, for the steel containing 150 ppm sulfur for laser powers of (d) 1900 W, (e) 3850 W and (f) 5200 W.[67]

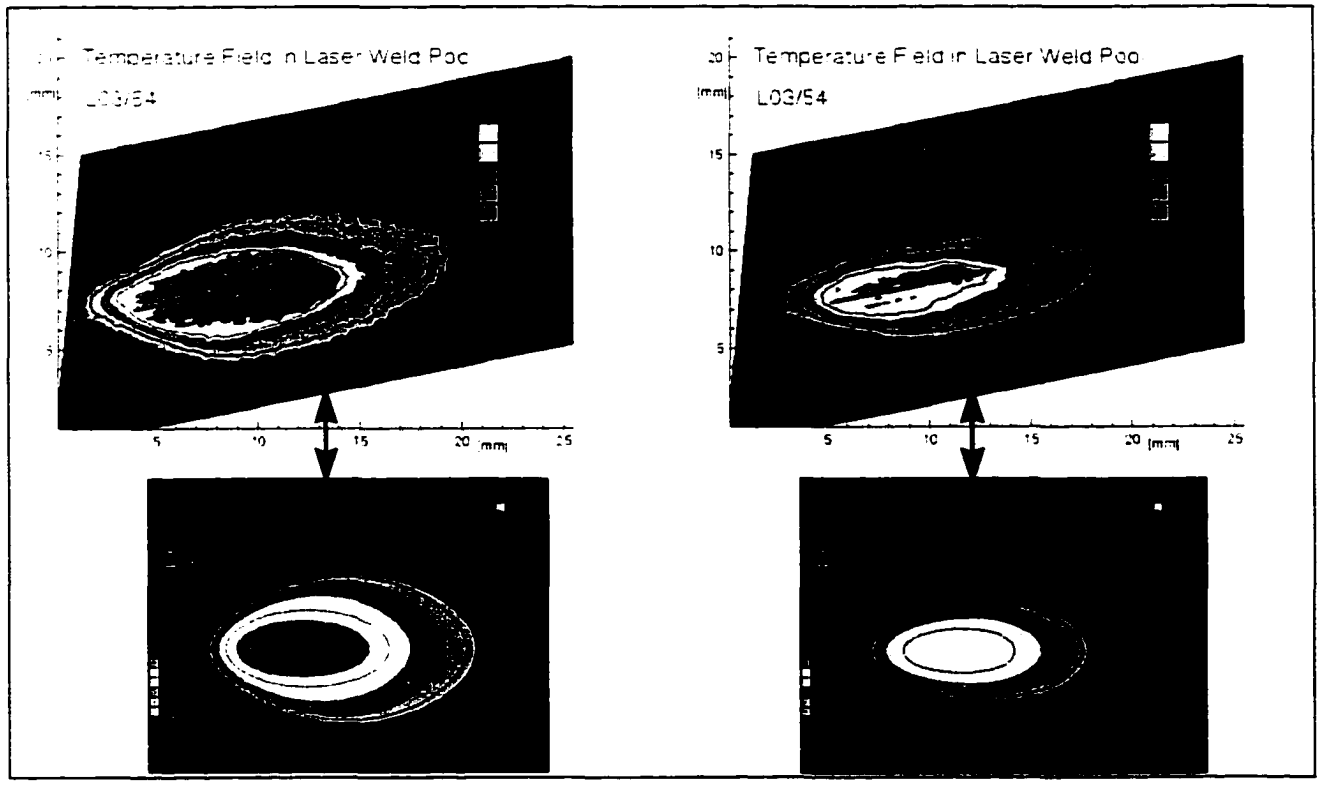

Figure 2.17 Comparison of calculated and experimental observed temperature profiles.[66] St 52 high speed steel, welding power: 4800 W and 3200 W, welding speed: 200 mm/min

2.2.4 Turbulent Heat Transfer and Fluid Flow

Most existing models of heat transfer and fluid flow in the weld pool reviewed in the previous sections implicitly assumed laminar flow in the weld pool. However, many experimental observations and theoretical studies in GTA welding and SA welding have indicated that the fluid flow in the weld pool is turbulent in nature.[82-84] Malinowski and Brodnicka et al.[85] measured the flow velocity in AISI 310 stainless steel weld pools and concluded that the Reynolds number was about 3,000. Comparing the result with classical critical Reynolds number of 2,100 for transition from laminar to turbulent flow in pipes, they concluded that the flow in the weld pools was probably turbulent. In modeling, when full laminar flows were assumed, the calculated weld pool tended to be narrower but deeper than the actual welds, and the predicted peak temperatures in the weld pool were usually much higher than the actual values because the influence of turbulence in the weld pool were ignored.[82-85]

It is well known that the existence of turbulence in the fluid flow greatly enhances the rates of transport and mixing of mass, momentum and energy. The enhanced transport and mixing in the turbulent flow are characterized in term of turbulent viscosity and turbulent thermal conductivity which are properties not only of the fluid but also of the system. The values of these quantities at different regions of the weld pool depend on the flow conditions in the weld pool. In highly turbulent systems, these quantities can be several orders of magnitude higher than the corresponding molecular values used in laminar flow. In the previous work on weld pool modeling, the enhanced viscosity and thermal conductivity due to turbulence have been well recognized and were commonly used to model turbulent flow.[83-84]

In order to simulate the enhanced rates of transport and mixing of mass, heat, and momentum due to the turbulence in the weld pool, one simple and efficient way is to use effective viscosity and effective thermal conductivity, which are much higher than the molecular quantities in the transport equations for laminar flows, taking into account the

enhanced turbulence viscosity and conductivity. The proper values of effective viscosity and thermal conductivity had to be chosen by trial-and-error in the past. Recently, the K-ε turbulence model has been adopted in the modeling of stationary GTA welding to study the role of turbulence.[84] Since it is extremely difficult to quantitatively characterize the influence of turbulence in the weld pool using experimental techniques, modeling of weld pool using a turbulence model is needs to be undertaken. The calculated effective viscosity and thermal conductivity through K-ε model make it possible to quantitatively determine the influence of turbulence on the weld pool behavior. A comparison of the calculated weld pool geometry using different models is shown[83] in Figure 2.18. It is observed that the calculated weld pool geometry agreed well with the experimental results only when the influence of turbulence was considered in the calculations.

Modeling of turbulence in the weld pool using K-ε model provides the spatial distribution of effective viscosity and thermal conductivity. As shown in Figure 2.19, the values of effective viscosity and thermal conductivity of the fluid flow vary in different regions of the weld pool[83] and can be quite different for different welding conditions. It is also observed that the enhanced factor of viscosity and conductivity is actually 10 – 35 times higher than the values used in laminar flow.

From the above discussions, it is suggested that the progress made in the recent past on the modeling of transport phenomena in the weld pool makes it possible for the study of inclusion behavior in this thesis. Incorporating with the fundamental thermodynamics and kinetics of nucleation, growth, and dissolution of inclusions, the calculated temperature and velocity fields is the starting point of study inclusion behavior in the weld pool.

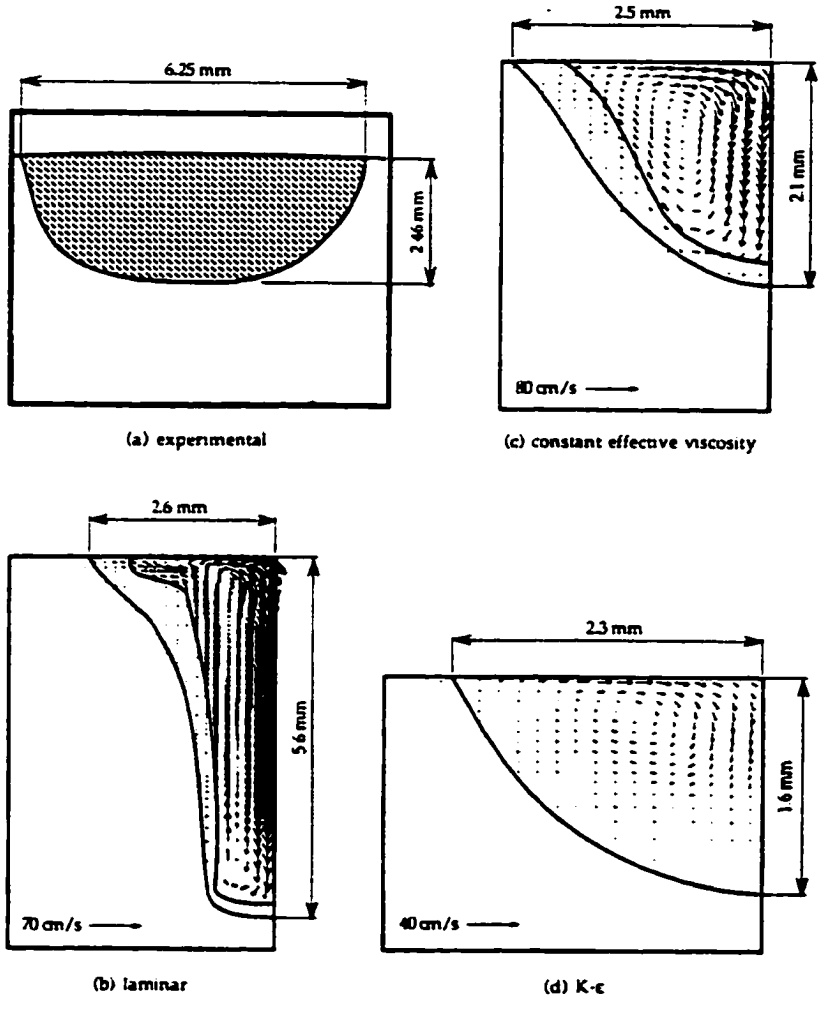

Figure 2.18 Comparison of weld pool shapes for: (a) experimental results, (b) numerical results based on laminar properties, (c) numerical results using a constant effective viscosity and thermal conductivity which are 30 times of the molecular values, (d) numerical results based on the K-ε turbulence model.[83]

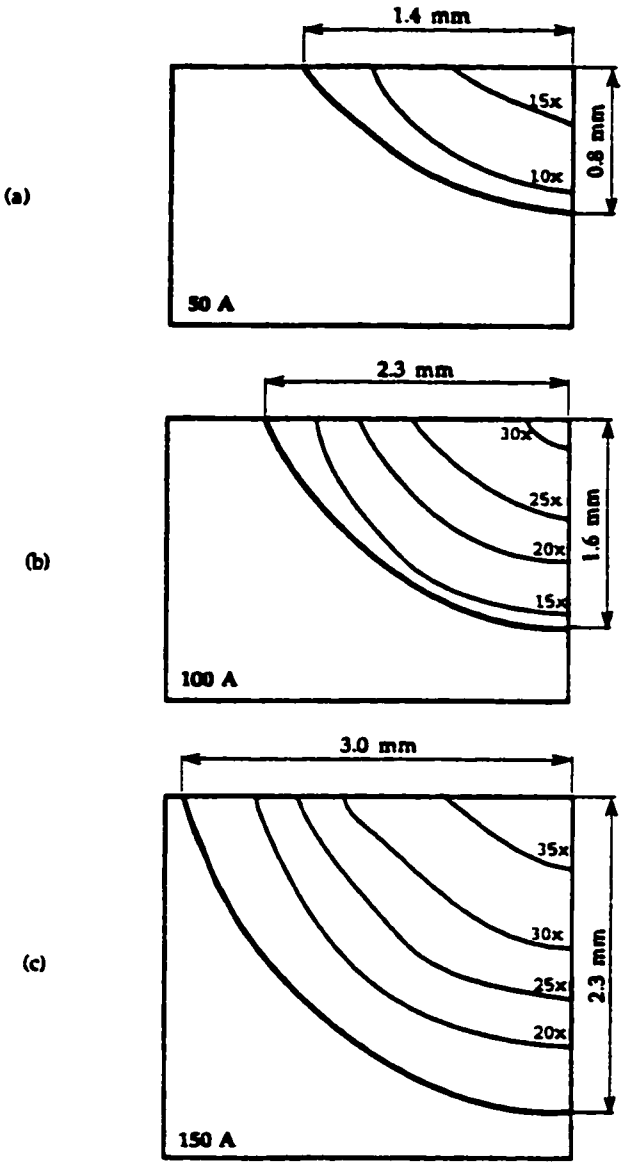

Figure 2.19 Contour plots of effective viscosity as calculated from the K-ε model for GTA stationary welding of AISI 304 stainless steel with different currents: (a) 50 A; (b) 100 A; (c) 150 A. The numbers on the contour lines represent the ratios of effective viscosity to molecular viscosity.[83]

2.3 Inclusion Behaviors in the Weld Pool

Inside the weld pool, molten liquid undergoes vigorous circulation resulting from various driving forces. Since the fluid flow in the weld pool is recirculatory in nature, an inclusion grows or dissolves while in a state of varying motion, experiencing thermal excursion within the weld pool during its entire life-cycle. At any given instant, its velocity and temperature depend on the velocity and temperature fields prevailing in the weld pool. While the nucleation of inclusions can occur at various regions of the weld pool, the welding variables and the material of the work-piece determine the size and shape of the weld pool and the temperature and velocity fields which in turn determine the thermal cycles of inclusions. Calculation of transient velocity and temperature fields in a moving weld pool with a fair degree of accuracy is computationally intensive. However, in the recent past, significant advances have been made in the calculation of fluid flow and heat transfer in the weld pool. These calculations can provide significant insight about the welding process that cannot be achieved otherwise. The progress provides a solid base for the study of inclusion in the weld pool.

Meaningful tracking of the temperature and velocities of thousand of inclusion particles as they move through regions of varying temperatures is an arduous task. Motivation for undertaking such calculations arises from the fact that the growth and dissolution of individual inclusion particles are determined by their temperature excursions and residence times at various temperatures. In order to understand the effects of welding variables and weld metal composition on the size distribution and the composition of inclusions from fundamentals, temperature histories and residence times of inclusions must be understood for each welding condition.

2.3.1 Particle Tracking of Inclusions in the Weld Pool

A calculation procedure was developed to trace trajectories of inclusion particles during their transport within the weld pool by Pitscheneder[49]. An inclusion moves under the influence of buoyancy, drag, gravity and inertia forces. The buoyancy force is small compared to the drag force for usual welding conditions and was neglected in the work. The gravity and inertia forces acting on the particle were also neglected for simplicity.[86] Pitscheneder[86] also investigated the influence of drag force and concluded that small spherical particles in the weld pool move essentially at the velocity and in the direction of the surrounding fluid. If the particles are considered to have negligible mass, their trajectories are conformed by the streamlines in the weld pool and given by:

$$r_1 = r_0 + v \cdot \Delta t \tag{2.32}$$

$$v = v(r_0) \tag{2.33}$$

where r_1 is the new location vector after time Δt, r_0 is the old location vector at the beginning of the time step, v is the velocity value at the old location and Δt is the adaptive time-step. For each time step, we can obtain the new location and corresponding temperature and velocity values.

The derivative of the inclusion path with respect to time depends on the local fluid velocity. Therefore, fluid flow velocity at the current location of the inclusion had to be determined by interpolation from adjacent points. Pitscheneder[49] used "predictor-corrector algorithm" to solve the initial value problem. The Adams-Bashforth formula[87] was used to predict the inclusion location at the next time step, and then an Adams-Moulton formula was used to correct the predicted value[87]. Because the solution had to be known at 4 preceding mesh points to calculate a solution at the next mesh point, the classical 4^{th}-order Runge-Kutta algorithm (one step algorithm) was employed for the first 3 steps of the calculations.

Although the particle tracking model provides us with useful information on the inclusion behavior in the weld pool, it had not been applied for understanding the growth

and dissolution of inclusions before. To have a meaningful statistical idea on the inclusion size distribution and number density, a large number of inclusion particles must be tracked. In this thesis, the particle tracking model is combined with thermodynamics and kinetics of inclusion growth and dissolution. The comprehensive model is applied to thousand of particles to predict the characteristics of inclusions, such as size distribution, number density and composition.

2.3.2 Size and Spatial Distribution of Inclusions

Growth and dissolution rates of inclusions are determined by the diffusion of their constituent elements in the liquid metal. The driving force of element diffusion is the concentration gradient near the interface between liquid metal and inclusions.

When the interfacial concentrations of constituent elements of inclusions are lower than the corresponding concentrations in the bulk liquid at a given temperature, the diffusion takes place from the bulk liquid toward the interface and the inclusions undergo growth. Equation (2.34) is used to calculate the change of inclusion radius iteratively: [88]

$$r_{i+1} - r_i = \frac{\alpha}{2\sqrt{t}} \Delta t_i \tag{2.34}$$

where r_i and r_{i+1} are the radii of the inclusion before and after the ith time step, Δt_i, respectively, t is the growth time, and α is a growth rate parameter expressed by[88]:

$$\alpha = \sqrt{2Dc^*} \tag{2.35}$$

where D is the diffusion coefficient of the inclusion element whose diffusion coefficient is comparably lower in liquid steel. D can be given by:

$$D = D^0 \cdot e^{-\frac{E}{RT}} \tag{2.36}$$

where D^0 is a temperature independent pre-exponential term and E is the activation energy for diffusion. c^* is defined as the dimensionless supersaturation[15] expressed by:

$$c^* = (c^b - c^i)/(c^p - c^i) \tag{2.37}$$

where c is the concentration of element with lower diffusivity in weight percent, the superscript *p*, *i*, and *b* represent the concentration in the solid inclusion particle, at the interface between inclusion and liquid, and in the bulk liquid, respectively. c^p and c^i are known for specific inclusion and alloy system, the method to calculate c^i will be discussed in Chapter 3.

When the interfacial concentrations of constituent elements of the inclusion is higher than the concentrations in the bulk liquid at a given temperature, there is a concentration gradient from the interface to liquid. Therefore, the elements diffuse from the interface into the bulk liquid and the inclusions experience dissolution. Considering diffusion-controlled precipitation with a quasi-steady state approximation, Whalan[18] derived the following expression for the kinetics of dissolution:

$$r_{i-1} - r_i = -\frac{k}{2}\left[\frac{D}{r_i} + \sqrt{\frac{D}{\pi t}}\right]\Delta t_i \qquad (2.38)$$

Many researchers studied the composition, size and spatial distribution of inclusions experimentally.[16,89-91] Kluken and Grong[16] studied mechanisms of inclusion formation in Al-Ti-Si-Mn steel weld metals and precipitate stability in weld metals. They calculated the volume fraction, size, and chemical composition of inclusions from weld metal chemistry. They determined the volume fraction of inclusions from an empirical relation involving both oxygen and sulfur concentrations. They modeled the chemical composition of inclusions in low-alloy steel welds as a function of weld-metal chemistry with stoichiometric relations and a fixed oxidation sequence based on the standard free energy of oxide formation. Kluken and Grong[16] also showed that welding parameters have a significant effect on the size distribution of oxide inclusions, and they related the same to Ostwald ripening mechanisms. However, they ignored the effects of weld-metal composition and cooling rate. Hsieh et al.[89] predicted sequential inclusion formation in low-alloy steel welds considering equilibrium thermodynamics. This method considered the weld-metal composition but ignored temperature histories of inclusions which are important for the calculation of inclusion growth and dissolution rates. Babu et al.[90,91] have shown that the number density of inclusions can be calculated from the nucleation

rate of the first forming oxide. Therefore, by relating the time spent in the temperature range of the first-forming oxide, the effect of the weld-metal cooling rate on the inclusion number density can be described. However, these methods all ignore that inclusions may experience thermal excursions because of their motion with the weld pool.

Babu[90] also considered the nucleation rates in different locations of the weld pool to estimate the number density. When the final size of an inclusion is obtained, they traced back this inclusion to its original location of nucleation and calculated the nucleation rate in this location based on the local temperatures. The product of nucleation rate and the time spent by the inclusion at that location was used to determine the final number density. The final calculation of inclusion number density was explained by the following equation:

$$\text{Number Density of inclusion for specific size} = \sum_{i=1}^{n} I_i \times t_i , \qquad (2.39)$$

where n is the number of inclusions with such a size, I_i is the homogeneous nucleation rate as a function of temperature, and t_i is the residence time of the inclusions at that instance at that location in the weld pool. This is an approximate calculation and the final value is only an estimation of the number density. However, the trends of number density change of inclusions under different welding conditions can be clearly observed.

2.3.3 Collision, Coalescence, and Coarsening of Inclusions

The initial discussions on inclusion growth during ladle steel deoxidation included the work done by Iyengar and Philbrook[92] and Lindborg and Torssell[93]. Kluken and Grong[19] divided the weld pool into two regions, 'hot' and 'cold' region. In the 'hot' region, oxidation and deoxidation as well as phase separation of oxide inclusions to the slag occur. In the 'cold' region, dispersion of fine oxide particles happens. They only considered the inclusion growth in the 'cold' region in the weld pool. They ignored the collision and coalescence because the inadequate stirring in cold part of the weld pool. They assumed the coarsening of inclusions takes place by Ostwald ripening mechanism. Their observation results of inclusion size as a function of retention time of inclusion

in the liquid region agreed with Wagner equation. The calculated mean size from Wagner equation and the sizes of several inclusions as a function of $t^{1/3}$. Their results also showed that the number density of the inclusion decreased as the retention time increased because during Ostwald ripening, the big inclusions grow at the expense of the small particles.

Babu et al[90] did series of experiments to study the inclusion coarsening in low alloy steel. Figure 2.20 shows the micrographs of the welded samples in the as welded condition and after various hold times at 1480°C. The resulting size distribution is presented in Figure 2.21. It can be observed from Figure 2.20 that the inclusions grow not only by Oswalts ripening, but also by collision and coalescence.

Lindborg and Torssell[93] quantitatively estimated precipitate growth based on diffusion from the melt and redistribution of elements from small particles to large ones. They concluded that these mechanisms could not explain the experimentally observed growth of inclusions and resulting size distribution solely. There are two types of collisions considered in their model: Stocks and gradient collisions. Inclusions tend to rise in the liquid steel because they usually have lower density. Collisions take place when larger inclusions rising through the liquid and collide with smaller particles in their way. This type of collision is referred as Stokes collision. Particles may also flow and collide each other following the flow of the liquid. The larger the local velocity gradient, the higher is the rate of collisions. This type of collision is referred as gradient collision. In the modeled size distribution of precipitates implied that collision and coalescence provide the important growth mechanism. The details of the collision and coalescence model are described as below:

$W(r_1,r_2)$ is defined as collision volume, which is the probability of collision between two particles with radii of r_1 and r_2 within a unit time. The number of collisions per unit volume per unit time between two particles of size r_1 and r_2 is given by[93]:

$$N(r_1,r_2) = W(r_1,r_2)n(r_1)n(r_2) \qquad (2.40)$$

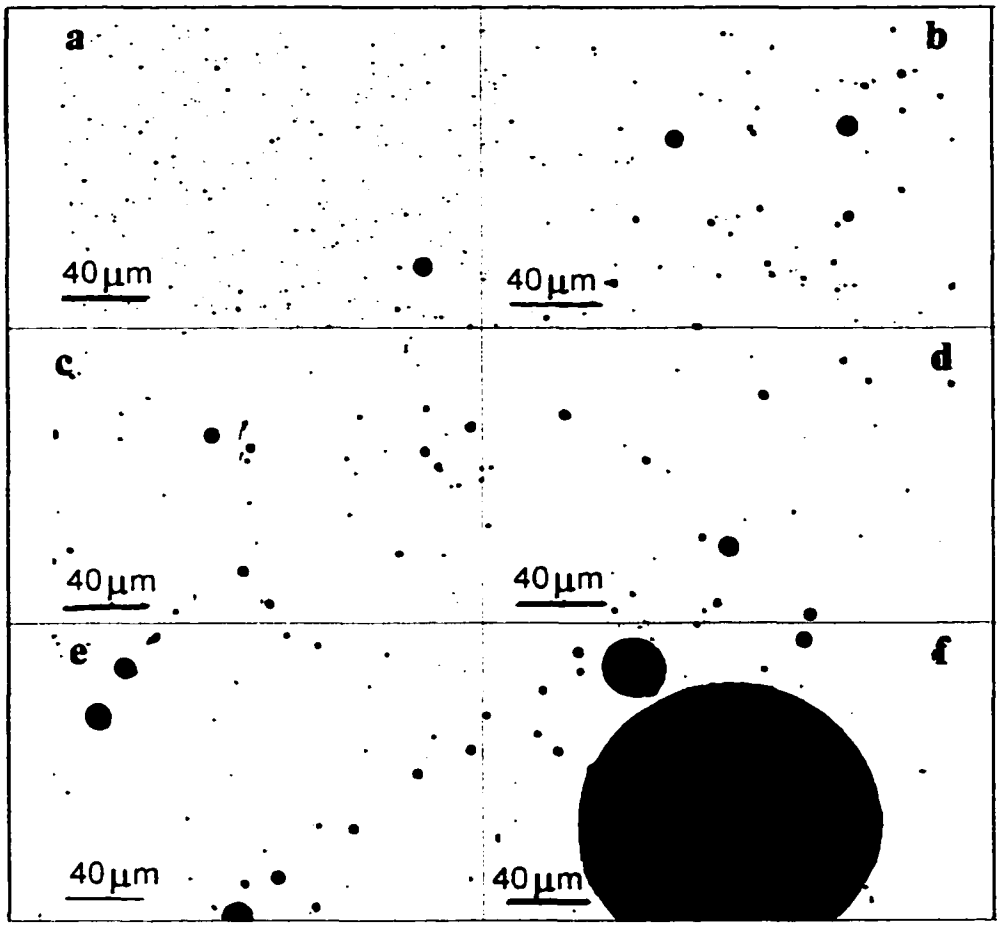

Figure 2.20 Micrographs of samples from melting experiments in the as welded condition and after various hold times at 1480°C[90]
(a) as welded; (b) 10s; (c) 20s; (d) 40s, (e) and (f) 60s.

where $n(r_1)$ and $n(r_2)$ are the number densities of r_1 and r_2 particles, i.e., the particle number per unit volume. For gradient collisions caused by flow velocity gradient in the liquid, $W(r_1,r_2)$ is given by:

$$W(r_1, r_2) = \frac{4}{3}(r_1 + r_2)^3 \text{grad } v \tag{2.41}$$

where *grad v* is the local velocity gradient of fluid flow. When two particles with radii r_1 and r_2 collide, a new particle with radius $r = \sqrt[3]{r_1^3 + r_2^3}$ forms to keep the particle volume constant. Therefore, the number densities of r_1 and r_2 particles decrease while the number density of r particles increases.

Considering the collisions between n(r) particles with radius r and $n(r_3)$ particles with radius r_3, the number of collisions between the particles which sizes range from r_3 to r_3+dr_3 and particles of size r within unit time, i.e., annihilation rate of n(r) due to size range of dr_3, is $W(r,r_3)n(r)n(r_3)dr_3$. Integrating the variables r_3, the total annihilation (decreasing) rate of r particles is given by:

$$\frac{dn(r)}{dt} = -\int_0^{r_{max}} n(r)n(r_3)W(r, r_3)dr_3 \tag{2.42}$$

Assuming a particle with radius r_1 colliding with another particle to form a new particle, in order to get a particle with radius between r and r+dr, the other particle's radius must be in the range from $\sqrt[3]{(r+dr)^3 - r_1^3}$ to $\sqrt[3]{r^3 - r_1^3}$. Substituting r with $r = \sqrt[3]{r_1^3 + r_2^3}$ and doing the series expansion, this size range can be written as from $r_2 + (\frac{r}{r_2})^2 dr$ to r_2. If $n(r_1)$ particles of size r_1 collide with particles which sizes range from r_2 to r_2+dr_2, and dr_2 is taken as $(\frac{r}{r_2})^2 dr$, the generation rate of particles of size r is given by:

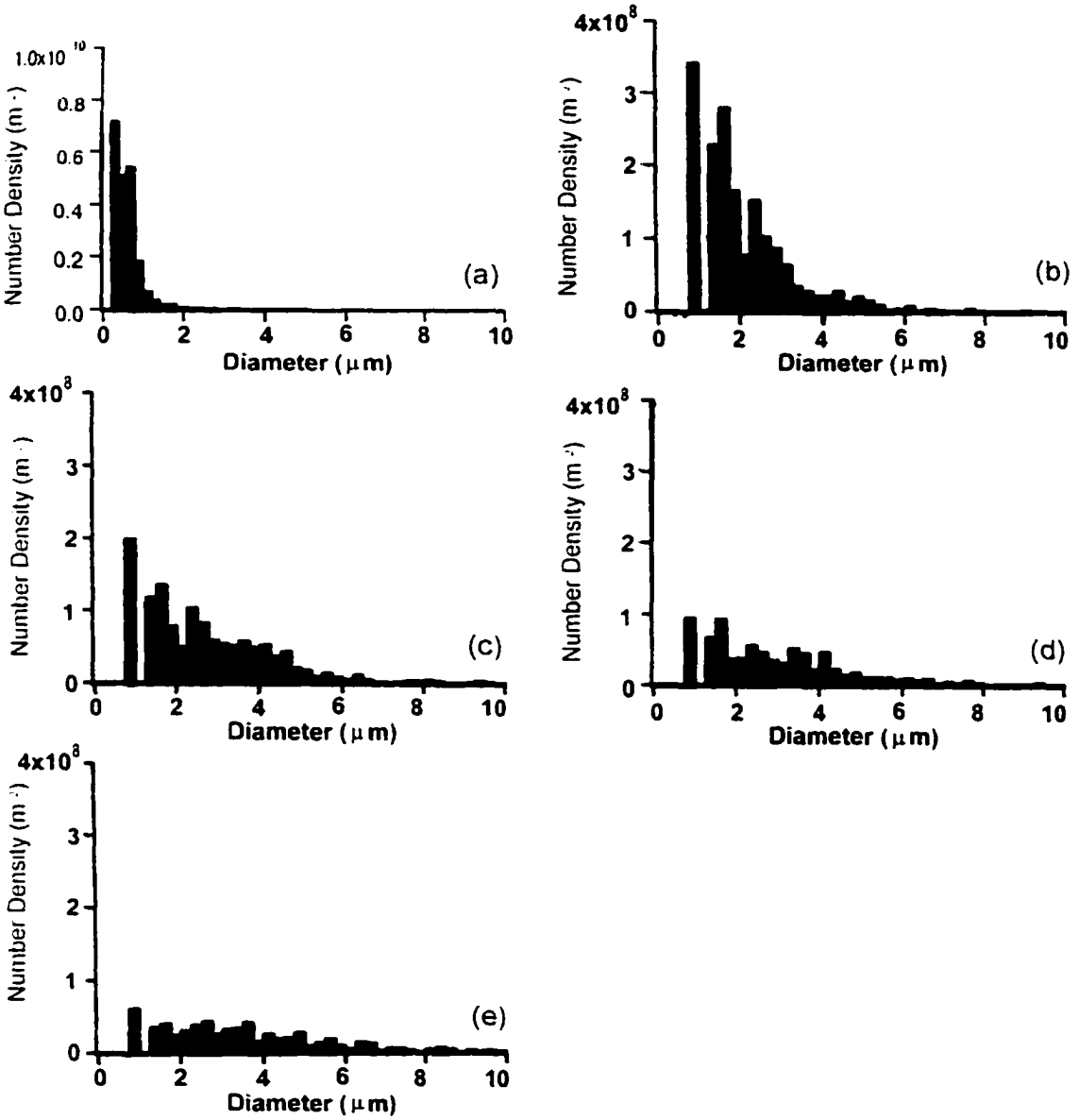

Figure 2.21 Inclusion size distribution[90] in the as welded condition and after various hold times at 1480°C.

$$dN(r_1,dr_2)= W(r_1,r_2)n(r_1)n(r_2)(\frac{r}{r_2})^2 dr \tag{2.43}$$

Particles of all sizes from r_1=0 to r_1=r may contribute to form the new particles of size r. Therefore, integration of equation (2.43) for r_1 from 0 to r gives the generating (increasing) rate of r particles. The integration includes every particle twice, once as an r_1 and once as an r_2, so the resulting rate must be divided by 2. The increasing rate of number density of size r particle is given by[93]:

$$\frac{dn(r)}{dt} = \frac{1}{2}\int_0^r n(r_1)n(r_2)W(r_1,r_2)(\frac{r}{r_2})^2 dr_1 \text{ , with } r_2^3 = r^3 - r_1^3 \tag{2.44}$$

When the increasing and decreasing rates for the number density of size r expressed in equations (2.42) and (2.44) are added up, the overall changing rate is:

$$\frac{dn(r)}{dt} = \frac{1}{2}\int_0^r n(r_1)W(r_1,r_2)f(r_2)(\frac{r}{r_2})^2 dr_1 - \int_0^{r_{max}} f(r_3)W(r,r_3)f(r)dr_3 \text{ , with } r_2^3 = r^3 - r_1^3 \tag{2.45}$$

In the calculation presented in the thesis, the initial size distribution between 0 to 1 μm is considered. The original size distribution calculated from fluid flow and particle tracking models is rearranged to a new size distribution with size intervals of 0.04 μm. Thus, a series of 25 data from 0 to 1 μm is obtained. The following functions $g(r_1)$ and $h(r_2)$ are calculated:

$$\begin{cases} g(r_1) = n(r_1)n(r_2)\frac{4}{3}(r_1+r_2)^3(\frac{r}{r_2})^2 GradV \\ h(r_2) = n(r_1)n(r_2)\frac{4}{3}(r_1+r_2)^3 GradV \end{cases} \quad \text{where } r^3 = r_1^3 + r_2^3 \tag{2.46}$$

$g(r_1)$ and $h(r_2)$ were then integrated using the rectangular method:

$$\begin{aligned} I_1 &= \int_{r_1=0}^{r_1=r} g(r_1)dr_1 = \sum_{r_1=0}^{r_1=r} g(r_1)\Delta r \\ I_2 &= \int_{r_1=0}^{r_1=r_{max}} h(r_2)dr_2 = \sum_{r_2=0}^{r_2=r_{max}} h(r_2)\Delta r \end{aligned} \tag{2.47}$$

The change rate in number density of r is then calculated by:

$$c(r) = \frac{dn(r)}{dt} = \frac{1}{2}I_1 - I_2 \tag{2.48}$$

The change of number density of inclusion which size is r in a small time interval, Δt, is calculated by $\Delta n(r)=c(r)\Delta t$. This number is used to adjust the original number densities iteratively. After every iteration, equation (2.48) is recalculated until the expected time reaches.

In the research presented in this thesis, collision and coalescence are taken into account to further adjust the resulting size distribution and number density of inclusions from calculation of growth and dissolution of thousands of particles in the liquid melts.

2.4 Summary

In fusion welds, the characteristic of different types of inclusions is one of the most important factors which affect the structure and mechanical properties of weldment. Although the importance of inclusions has been recognized for a long time, the systematic study was carried out only in the last one or two decades.

Due to the inherent difficulties of studying inclusion behavior in the weld pool experimentally, the experiments solely cannot offer significant insight unless associating with mathematical modeling which has already been widely adapted as the major tool to investigate heat transfer and fluid flow in the weld pool, to learn the nucleation, growth, and dissolution of inclusions in the liquid steels considering the thermodynamics and kinetics during the entire processes. Although many progresses of mathematical modeling welding processes have been made, none of the previous researches tried to synthesis these knowledge to gain a comprehensive understanding on inclusion behaviors and predict the inclusion characteristics in the weldment.

The research reported in this thesis combines the up-to-data progress in computational dynamic fluid calculation in the weld pool with thermodynamics and kinetics of inclusion growth and dissolution. Non-isothermal growth and dissolution,

simultaneous growth of different types of inclusions, collision and coalescence of particles are also taken into account. A comprehensive understanding of inclusion behavior in the weld pool is accomplished.

References:

1. E. T. Turkdogan: *J. Iron Steel Inst.*, **204**, 914-919 (1966)

2. M. L Turpin, and J.F. Elliot: *J. Iron Steel Inst.*, **204**, 217-225 (1966)

3. W. O. Philbrook: *Intl Metals Rev.*, **22**, 187-201 (1977)

4. E. T. Turkdogan: *Trans. Metall. Soc.* AIME, **223**, 2100-12 (1965)

5. O. Grong, T. A. Siewart, G. P. Martins, and D. L. Olson: *Metall. Trans. A.*, **17A**, 1797-1807, (1986)

6. Welding Handbook, 8th edition, Vol. 2, American Welding Society, Miami, Florida, (1991)

7. P. Sohoo, T. DebRoy and M. J. McNallan: *Metall. Trans. B*, **19B**, 483 (1988)

8. T. A. Palmer, K. Mundra, and T. DebRoy: *Trends in Welding Research - Proceedings of the Fourth International Conference*, Edited by: H. B. Smartt, J. A. Johnson, and S. A. David, ASM International, Materials Park, Ohio, 141-146 (1996).

9. T. A. Palmer and T. DebRoy, proceedings of a conference entitled *5 th International Conference on Mathematical Modeling of Weldability*, Graz-Seggau, October 4-6 (1999).

10. T. A. Palmer and T. DebRoy: *Metall. Mater. Trans. B*, **31B**, 1371-1385, (2000)

11. G. den Ouden and O. Griebling, "Nitrogen Absorption during Arc Welding", in Recent Trends in Welding Science and Technology, ed. S.A. David and J.M. Vitek, (ASM International, Materials Park, OH), 1990, 431-435

12. T. Palmer: Nitrogen in Plasmas and Steel Weld Metal, Ph.D. Thesis, The Pennsylvania State University (1999)

13. J. W. Christian: *The Theory of Transformations in Metals and Alloy - Part I: Equilibrium and General Kinetic Theory*, 2nd ed., Pergamon Press, Oxford, (1981)

14. S. S. Babu, S. A. David, J. M. Vitek, K. Mundra, and T. DebRoy: *Mater. Sci. Tech.*, **11**, 186-199 (1995).

15. C. Zener: *J. Applied Physics*, **20**, 950-953, (1949).

16. O. Kluken and O. Grong: *Metall. Trans. A*, **20A**, 1335-49 (1981).

17. H. B. Aaron, D. Fainstein, and G. R. Kotler: *J. Appl. Physics*, **41**, 4404-10 (1970)

18. M. J. Whelan: *Metal Science J.*, **3**, 95-97 (1969)

19. S. S. Babu, S. A. David, J. M. Vitek, K. Mundra, and T. DebRoy: *Sci. Tech. Weld Join*, **4**, 276-284 (1999).

20. H. K. D. H. Bhadeshia: Kinetics of Simultaneous Transformations, Proceedings of Solid-Solid Phase Transformations'99, Japan, (1999)

21. J. D. Robson and H. K. D. H. Bhadeshia: *Mater. Sci. Tech.*, **13**, 631-639 (1997)

22. D. A. Schauer, W. H. Giedt, and S. M. Shintaku: *Weld. J.*, **57**, 127s (1978)

23. J. D. Boillot, P. Cielo, G. Begin, C. Michel, and M. Lessard: *Weld. J.*, **64**, 209s (1985)

24. H. G. Kraus: *Weld. J.*, **66**, 353s (1987).

25. H. G. Kraus: *Weld. J.*, **68**, 84s (1989).

26. W. Pitscheneder, T. Hong, T. DebRoy, R. Ebner, K. Mundra, and R. Benes: "*Mathematical Modeling of Weld Phenomena 4*", edited by H. Cerjak, University Press, Cambridge, UK, 3-25 (1998).

27. C. R. Heiple and J. R. Roper: *Weld. J.*, **61**, 97s (1982).

28. W. Pitscheneder: Contributions to the Understanding and Optimization of Laser Surface Alloying, Ph.D thesis, University of Leobon, Austria (2001)

29. V. Pavelic, L. R. Tanbakuchi, O. A. Oyehara, and P. S. Myers: *Weld. J.*, **48**, 295s (1969).

30. M. C. Tsai and S. Kou: *Intl. J. for Numerical Method in Fluids*, **9**, 1503 (1989)

31. M. C. Tsai and S. Kou: *Weld. J.*, **69**, 241s (1990).

32. H. B. Smartt, J. A. Stewart, and C. J. Einerson: *ASM International Welding Congress*, paper no. 8511-011, Toronto, Canada, (1985)

33. P. Sohoo, T. DebRoy and M. J. McNallan: *Metall. Trans. B*, **19B**, 483 (1988)

34. D. R. Atthey: *J. Fluid Mech.*, **98**, 787 (1980)

35. G. M. Oreper and J. Szekely: *J. Fluid Mech.*, **147**, 53 (1984)

36. M. C. Tsai and S. Kou: *Numerical Heat Transfer*, **17**, 73(1990)

37. S. Kou and Y. H. Wang: *Metall. Trans. B*, **17B**, 2271 (1986)

38. T. Zacharia, S. A. David, J. M. Vitek, and T.DebRoy: *Weld. J.*, **68**, 499s(1989)

39. A. Paul and T. DebRoy: *Metall. Trans. B*, **19B**, 851(1988)

40. K. Mundra, J. M. Blackburn, and T.DebRoy: *Sci. Tech. Weld. Join.*, **2**, 174 (1997)

41. T. Zacharia, S. A. David, J. M. Vitek, and T. DebRoy: *Metall. Trans B.*, **21B**, 600 (1990)

42. Z. J. Zhu: *Trend Trends in Welding Research*, Ed. By H. B. Smartt, J.A. Johnson and S.A. David, 127, ASM International, (1996)

43. K. Mundra and T. DebRoy: *Metall. and Mat. Trans.*, **26B**, 149 (1995)

44. K. Mundra, T. DebRoy, and K. Kelkar: *Numerical Heat Transfer*, **29**, 115 (1996)

45. S. Kou and Y.H. Wang: *Weld. J.*, **65**, 62s (1986)

46. S. Kou: *Welding Metallurgy*, John Wiley and Sons, New York (1987)

47. Presentation of T. DebRoy in AWS Adams Lecture, Chicago, IL, (2000)

48. P. Sohoo, T. DebRoy and M. J. McNallan: *Metall. Trans. B*, **19B**, 483 (1988)

49. W. Pitscheneder, M. Grubock, K. Mundra, T. DebRoy, and R. Ebner, *Mathematical Modeling of Weld Phenomena 3*, Edited by H. Cerjak, The Institute of Materials, 41-63, (1997)

50. Z. Yang: Modeling Weldment Macro and Microstructure from Fundamentals of Transport Phenomena and Phase Transformation Theory, Ph.D. thesis, The Pennsylvania State University (1999)

51. G. M. Opeper, T. W. Eager, and J. Szekely: *Weld. J.* **62**, 307s (1983)

52. D. Rosenthal: *Weld. J.*, **12**, 220s (1947)

53. S. A. David, R. Trivedi, J. M. Vitek, S. S. Babu, T. Hong, and T. DebRoy: "Observation of Weld Pool Solidification Using Transparent Metal-analog System", (to be submitted soon).

54. R. W. Messler, Jr.: *Principles of Welding*, John Wiley and Sons, New York, (2000)

55. K. Eastering: *Introduction of the Physical Metallurgy of Welding*, 2nd Edition, Butterworth- Heinemann, Oxford, England, (1992)

56. G. M. Opeper, T. W. Eager, and J. Szekely: *Weld. J.* **62**, 307s (1983)

57. V. R. Voller and C. Prakash: *Intl. J. Heat Mass Transfer*, **30**, 1709-1719, (1987)

58. A. D. Brent, V. R. Voller, and K. J. Reid: *Numerical Heat Transfer*, **13**, 297-318 (1988)

59. S. V. Patankar: Numerical Heat Transfer and Fluid Flow, Hemisphere Publicating Corp, New York, 1980

60. D. J. Abson and R. J. Pargeter: *Intl. Metals Rev.*, **31**, 141-194(1986)

61. S. Liu and D. L. Olson, *Weld. J.*, **65**, 139s-149s (1986)

62. A. Paul and T. DebRoy, *Modeling and Control of Casting and Welding Processes*, IV, A. F. Giamei and G. J. Abbaschian, Editors, TMS Publication, 421-431, (1988)

63. T. Zacharia, J. M. Vitek, J. A. Goldak, T. DebRoy, M. Rappaz, and H. K. D. H. Bhadeshia, *Modeling and Simulation in Materials Science and Engineering*, **3**, 265 (1995)

64. K. Mundra, T. DebRoy, T. Zacharia, and S. A. David, *Weld. J.*, **71**, 313s (1992).

65. P. A. Khan and T. DebRoy, *Laser Materials Processing*, K. Mukherjee and J. Mazumder, Editors, AIME Publication, Warren-dale, PA, 71-81, (1985)

66. R. Ebner, W. Pitscheneder, R. Benes, T. DebRoy, and K. Mundra, *Proceedings of the Second International Austria-Israel Technion Symposium cum Industrial Forum*, June, 1997, Graz, Austria, published by Austrian Technion Society, Vienna, 79-93 (1997).

67. W. Pitscheneder, T. DebRoy, K. Mundra, and R. Ebner: *Weld. J.*, **75**, 71s-80s.(1996)

68. H. Zhao and T. DebRoy: *Metall. Mater. Trans. B*, **32B**, 163-172 (2001)

69. M. Pastor, H. Zhao, and T. DebRoy, *Proceedings of the National Welding Seminar '97*, Indian Institute of Welding, held in Bangalore, India, 11-13 December 1997, Indian Institute of Welding, Bangalore, India, 31-46 (1997)

70. Z. Yang and T. DebRoy: *Sci. Tech. Weld Join*, **2**, 53-58, (1997)

71. Z. Yang, J. W. Elmer, J. Wong, and T. DebRoy, *Weld. J.*, **79**, 97s-112s, (2000)

72. Z. Yang, J. W. Elmer, J. Wang and T. DebRoy, *Joining of Advanced and Specialty Materials II*, M. Singh, J.E. Indacochea, K. Ikeuchi, and J. Martinez-Fernandez (Editors), ASM International, Materials Park, Ohio (2000).

73. T. Hong, T. DebRoy, S. S. Babu, and S. A. David, *Metall. Mater. Trans. B*, **31B**, 161-169 (2000).

74. T. Hong and T. DebRoy, *Trends in Welding Research*, J. M. Vitek, S. A. David, H. Smartt, J. A. Johnson, and T. DebRoy (Editors), ASM International and American Welding Society, Materials Park, Ohio, (1999).

75. T. Hong, W. Pitscheneder, and T. DebRoy, *Sci. Tech. Weld. Join.*, **3**, 33-41 (1998).

76. T. Hong, T. DebRoy, S. S. Babu, and S. A. David, *Metall. Mater. Trans. B*, **31B**, 161-169 (2000).

77. M. Pastor, H. Zhao and T. DebRoy: *J. Laser Appl.*, **12**, 91-100 (2000).

78. S. Sista, Z. Yang and T. DebRoy: *Metall. Mater. Trans. B*, **31B**, 529-536 (2000).

79. Z. Yang, S. Sista, J. W. Elmer, and T. DebRoy: *Acta Mater.*, **48**, 4813-4825 (2000).

80. A. Robert and T. DebRoy: *Metall. Mater. Trans. B*. **32B**, 941-947 (2001).

81. M. Pastor, H. Zhao and T. DebRoy: *Revista de Metalurgia*, **36**, 108-117(2000).

82. K. Hong, D. C. Wechman, and A. B. Strong: Trends in Welding Research, Ed. By H. B. Smartt, J.A. Johnson and S.A. David, 399, ASM International, (1996)

83. R. T. C. Choo and J. Szekely: *Weld. J.*, **73**, 25s (1994)

84. B. E. Launder and B. D. Spalding: Mathematical Models of Turbulence, Academic Press, New York, (1972)

85. M. Malinowski-Brodnicka, G. DenOuden, and W. J. P. Vink: *Weld. J.*, **69**, 52s (1990)

86. W. Pitscheneder, R. Ebner, T. Hong, T. Debroy, K. Mundra, and R. Benes: Mathematical Modelling of Weld Phenomena 4, edited by H. Cerjak, University Press, Cambridge, UK, 3-25 (1998)

87. J. B. Scarborough: *Numerical Mathematical Analysis*, 6th edition, The Johns Hopkins Press, Baltimore, MD, 320-324, (1966)

88. J. W. Christian: *The Theory of Transformations in Metals and Alloy - Part I: Equilibrium and General Kinetic Theory*, 2nd ed., Pergamon Press, Oxford, (1981)

89. K. C. Hsieh, S. S. Babu, J. M. Vitek, and S. A. David: *Mater. Sci Engi.*, **A215**, 84-91, (1996)

90. S. S. Babu, S. A. David, and T. DebRoy: *Sci. Tech. Weld. Join.*, **1**, 17-27, (1996)

91. S. S. Babu, S. A. David, J. M. Vitek, K. Mundra, and T. DebRoy: Trends in Welding Research, Proceedings of the 4th International Conference, Gatlinburg, TN(1995)

92. R. K. Iyengar and W. O. Philbrook: *Metall. Trans.*, **3**, 1823-30, (1972)

93. U. Lindborg and K. Torssell: *Trans. Metallurgical Society of AIME*, **242**, 94-102 (1968)

CHAPTER 3

ISOTHERMAL NUCLEATION, GROWTH AND DISSOLUTION OF INCLUSIONS IN LIQUID STEELS

Although significant advances have been made in the study of inclusions in welded steel through experiments[1-3] and theoretical understanding[4-7], synthesis of these component processes to gain a comprehensive understanding of the nucleation, growth and dissolution of inclusions in the weld pool has been largely overlooked. Many examples in the literatures[8-10] demonstrated the importance of such synthesis.

Time-Temperature-Transformation (TTT) diagram, which is well-accepted in the current theories of phase transformation during heat treatment of steels, is a good example of such synthesis. In TTT diagrams, not only the effects of temperature and alloy composition but also the time effects are revealed. Both the kinetics and the thermodynamics of phase transformations are taken into account when constructing TTT diagrams. The growth and dissolution of inclusions in the weld pool is a special kind of phase transformation with some unique features: 1) inclusions undergo vigorous thermal cycles in the weld pool, therefore, non-isothermal condition must be considered; 2) the composition of liquid always changes with the time; and 3) The most favorable inclusion to form depends on many factors, such as temperature and bath composition.

To understand such a complex problem, a simple case must be fully addressed as the starting point: isothermal growth and dissolution of a single type inclusion in the

liquid steel with constant composition. At first, the basic concepts of TTT diagrams applications on phase transformation in low alloy steels are discussed because the concepts are similar to the basis of TTT diagram study of inclusion growth and dissolution in the liquid steel. The research reported in this thesis extends the concepts to construct a set of TTT diagrams that describes the effects of time, temperature, and steel compositions on the nucleation, growth and dissolution of inclusions in liquid steel.

3.1 Applications of TTT Diagrams on Phase Transformation in Steels Weldment

Based on thermodynamics and kinetics of phase transformation, Bhadeshia et al[10] developed a comprehensive model to simulate and study the decomposition of austenite in the low alloy steel weldment. In his model, the phase transformation mechanisms for various microconstituents, multi-component phase transformation, and non-equilibrium cooling conditions were considered in predicting the microstructural development in the weld metal. The Time-Temperature-Transformation (TTT) diagrams and Continuous-Cooling-Transformation (CCT) diagrams of austenite decomposition in low alloy steels were calculated. The volume fractions of various phases were predicted based on their corresponding phase transformation mechanisms. Following is a brief description of the phase transformation mechanisms in low alloy steel.

In the weld metal of low alloy steel, the final microstructure is determined by austenite decomposition within the temperatures range from 1073 K down to 773 K. During cooling, alltriomorphic ferrite is the first ferrite phase to nucleate and grow by a diffusional mechanism in austenite. As the temperature decreases, diffusion becomes sluggish and displacive transformation is kinetically favored. At low undercooling, plates of Widmanstatten ferrite form by displacive mechanism. At high undercooling, bainite forms and grows in the form of sheaves of small platelets. Acicular ferrite nucleates intragranularly at impurities (inclusions, liquid-solid interface, etc.) and grows by displacive mechanism. TTT diagrams calculated from Bhadeshia's model are powerful

demonstration of the assumed phase transformation mechanisms. They also reveal the effects of temperature and alloy elements on the transformation kinetics. As the modeling results[11] shown in Figure 3.1, most TTT diagrams for the decomposition of austenite can be classified into two C curves. The one at higher temperatures represents diffusive transformation from austenite to ferrite or pearlite. It refers to the time taken for the initiation of the allotriomorphic ferrite or pearlite transformation. That at lower temperatures represents displacive reactions such as the formation of Widmanstatten ferrite and bainite. The lower C curve, or shear (displacive) curves, refers to the initiation time of Widmanstatten ferrite, bainite and acicular ferrite reactions. The martensite starting temperature (M_s) is generally represented as a horizontal line parallel to the time axis. In the figure, α is allotriomorphic ferrite, α_w is Widmanstatten ferrite, B_s is bainite starting point. α^b/α^a represents bainite or acicular ferrite. The weld parameters for the calculation of Figure 3.1 are: voltage 23 V, current 180 A, welding speed 4mm/s, and a maximum interpass temperature of 523 K.

Weld metal is not chemically homogeneous because of non-equilibrium solidification due to sharp cooling rates in the weld pool. Because of the element segregation during solidification, the first solidified regions are depleted of solute alloying elements. This phenomenon is also considered in Bhadeshia's model. The computed equilibrium concentrations of various alloying elements in the solute depleted region and original bulk region are listed in Table 3.1. The corresponding TTT diagrams

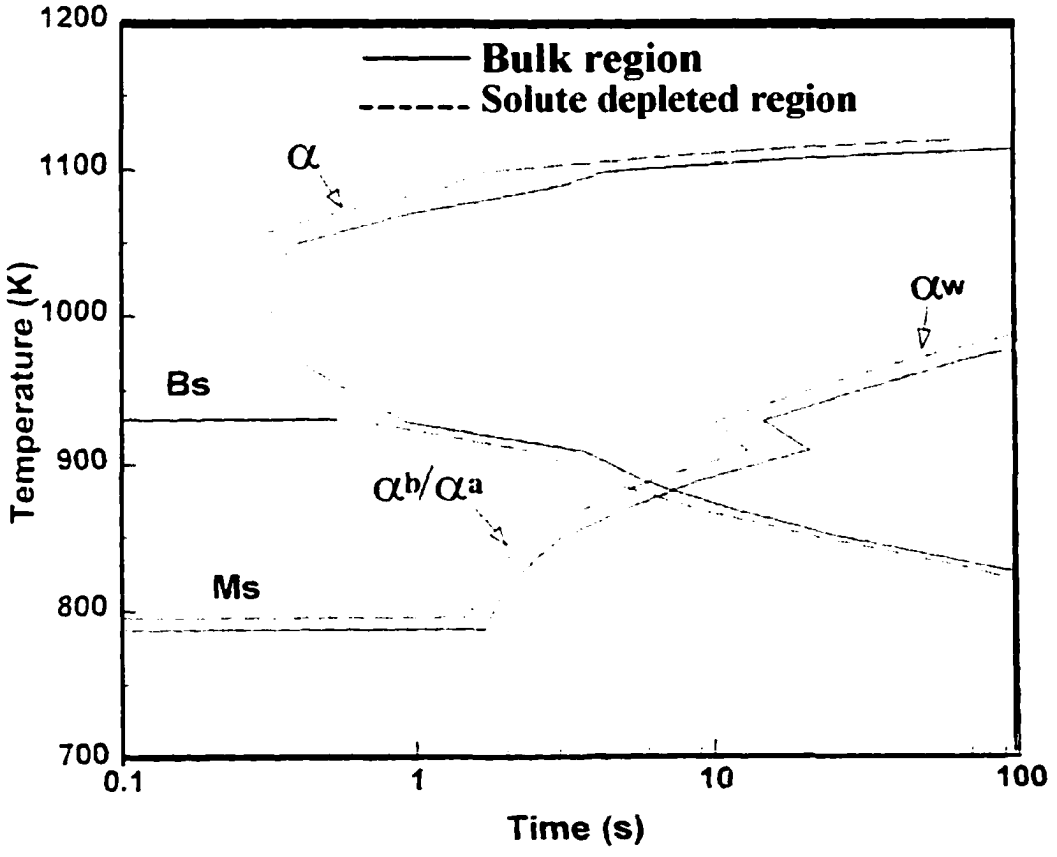

Figure 3.1 Comparison of TTT diagrams of solute depleted region and bulk region in GTA welding of C-Mn steel.[11] The compositions at solute depleted region and bulk region are shown in Table 3.1.

n the solute depleted region was calculated and shown as dashed line and that calculated from bulk alloy compositions was drawn as solid lines in Figure 3.1. It is observed that austenite decomposition is dominant by diffusion at high temperatures and displacive mechanism at low temperatures

Table 3.1 Chemical compositions of the selected C-Mn steel welds (wt% or ppm for N and O)[11]

Regions	C	Si	Mn	P	S	Al	Ti	N	O
Bulk Region	0.059	0.34	0.77	0.01	0.01	0.007	0.011	66	306
Solute Depleted Region	0.059	0.24	0.58	0.01	0.01	0.007	0.011	66	306

The driving force (supersaturation during nucleation and growth of phases) is small in the close vicinity of the transformation start temperature and increases with temperature decreasing; meanwhile, diffusion becomes sluggish as the temperature decreases. Therefore, the classic characteristics of C shape in TTT diagrams are attributed to the balancing contributions from the driving force (supersaturation) and the diffusion. In Bhadeshia's model, modified Johnson-Mehl-Avrami equation is used to calculate the overall phase transformation kinetics.[10]

It is observed that the critical temperature to form martensite is about 785 K, and that for bainite is 930 K. At around 1000 K, allotriomorphic ferrite has the optimized forming rate. Above 880 K, allotriomorphic ferrite is the dominant austenite decomposition phase, however, when the temperature is below 880K, the formation of Widmanstatten ferrite, bainite and acicular ferrite become predominant. From the above example, it is clearly seen that many useful information can be extracted from TTT diagrams in the study of phase transformation in steel weld metals. The same ideas can be applied to diffusion controlled nucleation and growth in inclusion formation. The formlism to construct the TTT diagrams for nucleation, growth and dissolution of inclusions are described in the next section.

3.2 Construction of TTT Diagrams for Nucleation, Growth and Dissolution of Inclusions in Liquid Steels

Inclusion nucleation and growth is a special kind of phase transformation. Above discussion implies that TTT diagram can be a powerful tool to present and illustrate the thermodynamics and kinetics of nucleation, growth and dissolution of inclusions in the liquid steels. In this section, the details on how to construct the TTT diagrams for nucleation, growth and dissolution of inclusion in liquid steel are presented. In the research reported here, 6 oxide inclusions, 3 nitride inclusions, 2 sulfide inclusion and 3 complex oxide inclusions are considered. Some of their physical properties are listed in Table 3.2.

Table 3.2 Inclusions considered and their properties[12,13]

	Molecular weight (g/mol)	Density (g/cm^3)	Melting Point (K)	Mole volume (cm^3/mol)
Al_2O_3	102	3.7	2327	27.56
TiO_2	79.87	4.2	2130	19.04
Ti_3O_5	223.60	7.2	205	31.1
SiO_2	60	5.6	1996	10.71
ZrO_2	79.87	4.2	2130	19.04
MnO	71	6.5	--	11.45
AlN	41	3.4	3000	12.06
TiN	62	4.6	3220	13.49
Si_3N_4	137	6.7	3000	20.14
MnS	87	6.2	1789	14.03
$Al_2O_3 \cdot SiO_2$	162.05	8.3	2532	19.52
$SiO_2 \cdot MnO$	131	6.4	2324	20.47
$Al_2O_3 \cdot MnO$	157	6.7	2756	23.4

3.2.1 Assumptions in the Model

The construction of TTT diagrams requires consideration of growth and dissolution rates of inclusions at different temperatures. As discussed in Chapter 2, many previous researches indicated that the nucleation, growth and dissolution of inclusions in weld liquid are controlled by diffusion. The diffusion-controlled growth and dissolution rates depend on the element diffusion rates near the inclusion/alloy interface. These diffusion rates depend on the difference between the concentrations of various species in the bulk alloy and inclusion/liquid interface. Therefore, the calculation of the interfacial concentrations of the constituent elements of the inclusions is a prerequisite for the calculations of TTT diagrams of growth and dissolution of inclusions. In order to simplify calculations, the following assumptions are made:

1. The activities of liquid iron and all solid compounds in liquid steel are assumed to be unity.
2. Chemical compositions of inclusion particles are assumed to be isotropic, which means a single inclusion is only consisted of one composition. The inclusions have spherical shape and do not have core-shell structure.
3. The concentration field near each inclusion is assumed to be constant during the nucleation, growth or dissolution of inclusions because the consumed elements near inclusion can be supplied by new come-in molten metal.
4. At the interface between inclusion and liquid steel, only the concentrations of those elements that constitute the inclusion are calculated. The concentrations of all other elements are assumed the same as those in the bulk metal.
5. The growth and dissolution of inclusions are assumed to be solely controlled by the diffusion of constituent elements in liquid steels. This assumption is based on enormous previous studies on precipitation and deoxidization reactions in liquid metals presented in Chapter 2.
6. The nucleation rates of inclusions are very high as shown in the following discussions. Therefore, the incubation time of growth is very short compared with the

total growth time. In this research, the nucleation phenomenon is ignored in the calculations of growth rate and is considered separately with inclusion growth. The justification of this assumption will be discussed later in this chapter.

7. The constituent elements of inclusion in the liquid steel exist dominantly in monatomic or ionic state. This assumption is credited by the research by Palmer et al. at Penn State[14].

3.2.2 Equilibrium Concentrations at the Interface

For a known alloy composition and temperature, the interfacial concentrations can be calculated assuming equilibrium of inclusion formation reaction at the interface between the inclusion and the liquid steel. The inclusion formation reaction is expressed by:

$$xM + yQ \quad \leftrightarrow \quad M_xQ_y\,(\text{solid}) \tag{3.1}$$

where M is a metallic element such as Al, Ni, Mn, Si or Ti, and Q stands for a deoxidant element, such as O, N, or S. The equilibrium constant for the reaction is given by:

$$k_{eq} = \frac{1}{a_M^x a_Q^y} = \frac{1}{[f_M c_M']^x [f_Q c_Q']^y} = e^{-\frac{\Delta G^0}{RT}} \tag{3.2}$$

where $a_{M_xQ_y}$, a_M, and a_Q are the activities of M_xQ_y, M and Q, c_M' and c_Q' are the interfacial concentrations of M and Q in weight percent, ΔG^0 is the standard free energy change for the reaction (3.1), and f_M and f_Q are the activity coefficients of M and Q given by:

$$f_i = 10^{\sum_{j=1}^{n} e_{ij} c_j'} \tag{3.3}$$

where e_{ij} is the first order interaction parameter between element i and j, c_j' is the concentration of element j at the interface, n is the number of elements considered in the alloy. The values of ΔG^0 for all considered inclusion formation reactions are presented in Table 3.3. The interaction parameters between different elements are presented in Table 3.4.

Considering the diffusion fluxes of M and Q toward and away from interface, the following equation can be derived: [19]

$$c_M^i = c_M^b - \frac{xm_M}{ym_Q}\sqrt{\frac{D_Q}{D_M}}(c_Q^b - c_Q^i) \tag{3.4}$$

where c_M^b and c_Q^b are the concentrations of M and Q in weight percent in the bulk metal, m_M and m_Q are the atomic weights of M and Q, and D_M and D_Q are the diffusion coefficients of M and Q in liquid steel given by:

$$D = D^0 \cdot e^{-\frac{E}{RT}} \tag{3.5}$$

where D^0 is a temperature independent pre-exponential term and E is the activation energy for diffusion. The values of D^0 and E in equation (3.5) of all elements considered in the liquid steel are presented in Table 3.5. Because of the lack of availability of the diffusion coefficient data at high temperatures, some of the data presented in Table 3.5 are extrapolated from lower temperature values.

Table 3.3. Standard free energy for various reactions [15-18]

$\Delta G^o = a + bT$, cal/mole

Formation Reaction	**a**	**b**
$2\underline{Al}+3\underline{O}=Al_2O_3$	-289060	93.52
$3\underline{Ti}+5\underline{O}=Ti_3O_5$	-419680	136.5
$\underline{Ti}+2\underline{O}=TiO_2$	-161460	55.95
$\underline{Si}+2\underline{O}=SiO_2$	-140950	54.62
$\underline{Mn}+\underline{O}=MnO$	-68816	29.95
$\underline{Al}+\underline{N}=AlN(s)$	-134000	46.5
$3\underline{Si}+4\underline{N}=Si_3N_4$	-203000	75.3
$\underline{Ti}+\underline{N}=TiN$	-80380	24.29
$\underline{Fe}+\underline{S}=FeS$	-111370	57.0
$\underline{Mn}+2\underline{Al}+4\underline{O}=MnO.Al_2O_3$	-369376	125.22
$\underline{Si}+2\underline{Al}+5\underline{O}=SiO_2.Al_2O_3$	-319875	97.32
$\underline{Mn}+\underline{Si}+4\underline{O}=MnO.SiO_2$	-200466	75.0

Table 3.4. First order interaction parameters[16], e_{ij}

i \ j	C	Si	Mn	Zr	Cr	Ti	Al	N	O	S
Si	0.19	0.11	0.002	0.005	-0.0003	0	0.058	0.09	-0.24	0.056
Mn	-0.07	0	0	0	0	0	0	-0.091	-0.083	-0.048
Zr	0	0	0	0	0	0	0	-4.1	0	-0.16
Ti	0	0	0	0	0.055	0.013	0	-1.8	-1.8	-0.11
Al	0.091	0.0056	0	0	0	0	0.045	-0.058	-6.6	0.03
N	0.13	0.047	-0.02	0.01	-0.047	-0.53	-0.028	0	0.05	0.007
O	-0.45	-0.131	-0.021	0.006	-0.04	-0.6	-3.9	0.057	-0.23	-0.133
S	0.11	0.063	-0.026	0	-0.011	-0.072	0.035	0.01	-0.27	-0.028

Table 3.5. Diffusion Coefficients of Elements in Alloy Considered[15-16]

Element	C	Si	Mn	Ni	Cr	Ti	Al	N	O	S
D_0 (10^{-8} m^2/s)	0.72	2.4	1.93	-	-	0.74	0.83	0.37	0.92	0.48
E (cal/mol)	-	8200	5800	-	-	42000	56000	-	-	8600

The interfacial concentrations of M and Q, c^i_M and c^i_Q, considered as two unknowns in equations (3.2) and (3.4), can be solved for a given temperature taking the following steps:

1. The value of k_{eq} is calculated from equation (3.2) for a given temperature. The initial values of c^i_M and c^i_Q are assumed to be half of the corresponding bulk concentrations.
2. Substitute current values of c^i_M and c^i_Q in equation (3.3) to obtain the corresponding values of f_M and f_Q.
3. Using the calculated values of f_M and current value of c^i_M, the value of a_M is calculated from the following relation: $a_M = f_M c^i_M$
4. The value of a_Q is calculated from equation (3.2) for known values of a_M and k_{eq}. A new value of c^i_Q is calculated by $c^i_Q = a_Q / f_Q$.
5. A new value of c^i_M is calculated by substituting the new c^i_Q in equation (3.4).

6. With the new values of c_M^i and c_Q^i, calculations are repeated starting from step 2 until the new values of c_M^i and c_Q^i are close enough to their values in the previous loop.

Figure 3.2 shows the interfacial concentrations of Al and O between Al_2O_3 inclusion and liquid steel as a function of temperature in an alloy which composition is shown in Table 3.6. Y-axis is plotted as the ratio of interfacial concentration of Al and O to the bulk concentration of Al and O, respectively. It is observed that below certain temperature T_e, named as equilibrium temperature between inclusion and liquid, the concentration ratio, c^i/c^b, of both elements are lower than unity, e.g., the interfacial concentration is smaller than that in the bulk. Hence, concentration flux is from liquid bulk towards inclusion/liquid interface. As a result, Al_2O_3 inclusion grows. On the contrary, when the temperature is higher than T_e, the interfacial concentrations of elements are higher than bulk concentration. Therefore, there is mass flux from inclusion/liquid interface to the liquid. Al_2O_3 inclusion dissolves. The phenomenon was also explained in Chapter 2 from fundamental thermodynamics.

Table 3.6. Concentrations of Elements in Alloy Considered[15]

Element	C	Si	Mn	Ni	Cr	Ti	Al	N	O	S
wt%	0.09	0.53	1.9	0.001	0.01	0.005	0.01	0.008	0.032	0.020

When a complex inclusion such as $MnO{\cdot}Al_2O_3$ is considered, the equations to be solved are somewhat different. For the following general complex inclusion formation reaction:

$$x_1M' + x_2M'' + yQ = M'_{x_1}Q_{y_1} \cdot M''_{x_2}Q_{y_2} \tag{3.6}$$

where M' and M'' stand for the two metallic elements, Q stands for a nonmetallic element, and y is equal to y_1+y_2, the equilibrium constant of this reaction is given by:

$$k_{eq} = \frac{1}{a_{M'}^{x_1} a_{M''}^{x_2} a_Q^y} = \frac{1}{[f_{M'}c_{M'}^i]^{x_1}[f_{M''}c_{M''}^i]^{x_2}[f_Q c_Q^i]^y} = e^{-\Delta G_n^\circ / RT} \tag{3.7}$$

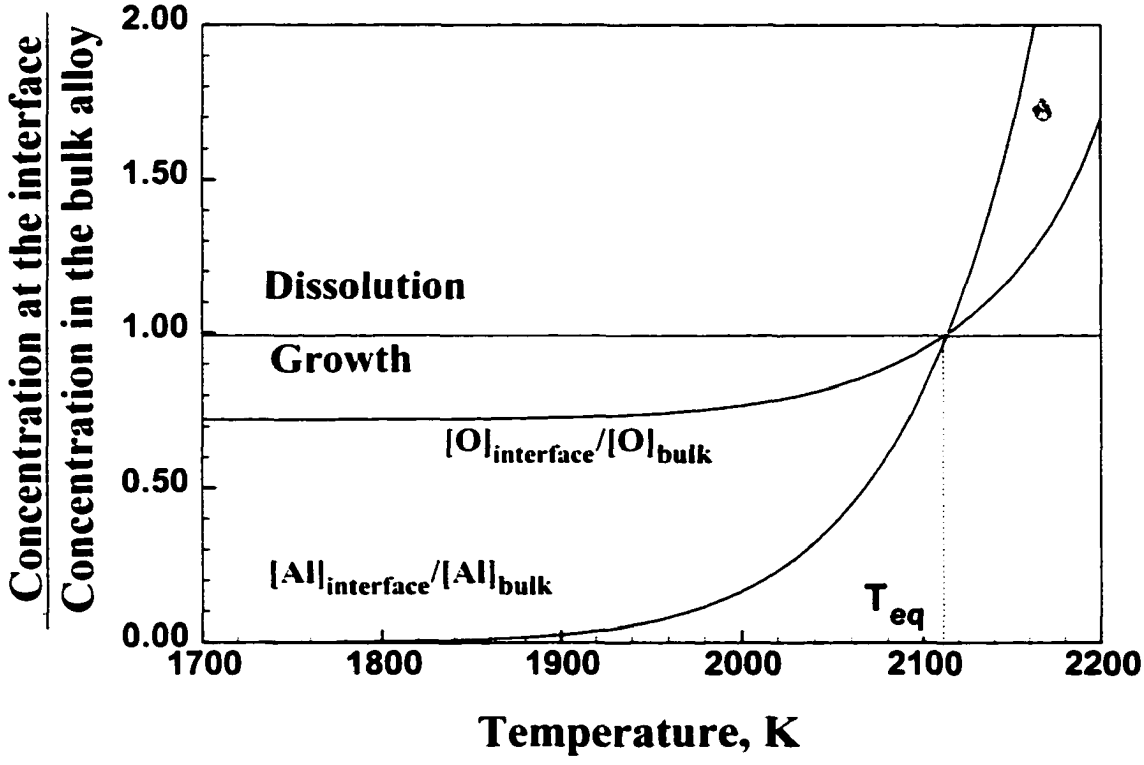

Figure 3.2 Interfacial concentrations as a function of temperature for Al_2O_3 in the alloy composition shown in Table 3.6.

The interfacial concentrations of M', M" and Q are related to their corresponding bulk values by the following relations considering stoichiometric relation,. Mass balance and diffusion flux[19]:

$$c^i_{M'} = c^b_{M'} - \frac{x_2 m_{M''}}{x_1 m_{M'}} \sqrt{\frac{D_{M'}}{D_{M''}}} (c^b_{M'} - c^i_{M'}) \tag{3.8}$$

$$c^i_Q = c^b_Q - \frac{y m_Q}{x_2 m_{M''}} \sqrt{\frac{D_M}{D_Q}} (c^b_{M'} - c^i_{M'}) \tag{3.9}$$

where $c^i_{M'}$, $c^i_{M''}$ and c^i_Q are the equilibrium concentrations of M', M" and Q at the interface expressed in weight percent, $c^b_{M'}$, $c^b_{M''}$ and c^b_Q are the concentrations of M', M" and Q in bulk and $m_{M'}$, $m_{M''}$, and m_Q are the atomic weights of M', M" and Q, respectively. Three interfacial concentrations, $c^i_{M'}$, $c^i_{M''}$ and c^i_Q, can be solved as 3 unknowns in equations (3.7) – (3.9).

After calculating the interfacial concentrations, a variable c^* is defined[20] as the dimensionless supersaturation of the element, M or Q, whichever diffusion coefficient is lower in the liquid steel:

$$c^* = (c^b - c^i)/(c^p - c^i) \tag{3.10}$$

where c stands for the concentrations of the element that has lower diffusivity in weight percent and superscript p, i, b stand for the element concentrations in the particle, at interface, and in the bulk liquid, respectively. Figure 3.3 shows c* of oxygen as a function of temperature for 5 oxide inclusions in a liquid alloy which composition is shown in Table 3.3. It is observed that the supersaturations of oxygen for different inclusions vary a lot. At lower temperatures, the supersaturations of oxygen for Al_2O_3, TiO_2, and Ti_3O_5 can be considered as constant, however, that for MnO and SiO_2 at low temperatures change significantly with the temperature. Above the equilibrium temperatures, T_e, between inclusions and liquid alloy, the supersaturations of elements become zero, which means there is no driving force for inclusion growth.

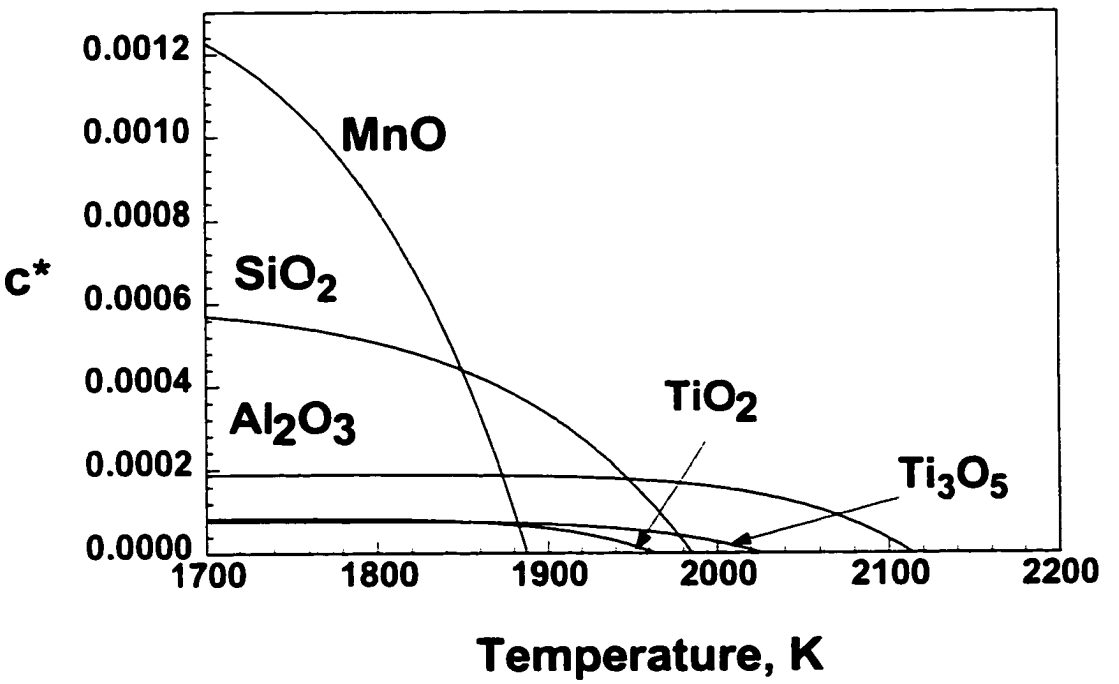

Figure 3.3 Dimensionless supersaturation c^* as a function of temperature for 5 oxide inclusions. The alloy composition is shown in Table 3.6.

3.2.3 TTT Diagrams for Inclusion Nucleation

Considering both nucleation and growth rates of inclusions, an overall kinetic approach is applied to construct the TTT diagrams for the nucleation of inclusion. This approach was discussed in details by Christian[20] for precipitation from a supersaturated solution involving long-range diffusion and precipitation. Christian[20] expressed the results in the term of extent of nucleation, ζ, as a function of time:

$$\zeta = 1 - \exp(8I_v \pi \alpha^3 t^{\frac{5}{2}} / 15c^*), \tag{3.11}$$

where I_v is the nucleation rate, t is the time, c* is defined in equation (3.10), α is a parabolic growth rate parameter expressed by:

$$\alpha = \sqrt{2Dc^*} \tag{3.12}$$

where D is the diffusion coefficient of the element with lower diffucivity between M and Q in liquid steel. The expression of D is given in equation (3.5). The transformation extent, ζ, in phase transformation means the fraction of the whole assembly which has transformed. For diffusion controlled reaction, such as continuous nucleation of precipitation, the meaning of ζ is different[20]. Let V^i defined as the equilibrium volume of inclusion in the whole assembly of volume V and, $V^i(t)$ as the total volume of inclusion at time t during reaction, then ζ is defined as:

$$\zeta = V^i(t)/V^i \tag{3.13}$$

Therefore, ζ=0.01 implies inclusion volume fraction is only 1% of equilibrium volume fraction, ζ=0.99 implies most (99%) inclusion volume fraction reaches its equilibrium volume fraction.

If homogeneous nucleation is considered, the nucleation rate, $I_v=I_{hom}$, can be calculated[21] using the following equation:

$$I_{hom} = Ae^{-\frac{\Delta G^*_{hom}}{k_0 T}} = Ae^{-\frac{16\pi\sigma^3 V_m^2}{3k_0 T \Delta G^2}} \tag{3.14}$$

where ΔG^*_{hom} is the molecular activation energy for homogeneous nucleation of the inclusion considered, A is a constant, k_0 is the Boltzmann constant, σ is the interfacial energy, V_m is the molar volume of the inclusion, and ΔG can be calculated by:

$$\Delta G = \Delta G^0 + RT \ln(\frac{a_{M_xN_y}}{a_M^x a_Q^y}) = \Delta G^0 + RT \ln[\frac{1}{(f_M c_M^b)^x (f_Q c_Q^b)^y}] \quad (3.15)$$

The nucleation rate will be further enhanced if the heterogeneous nucleation is taken into account. Heterogeneous nucleation I_{het} is calculated by[22]:

$$I_{het} = Bf(\theta)^{1.6} e^{-\frac{\Delta G^*_{het}}{k_0 T}} \quad (3.16)$$

where B is a constant, ΔG^*_{het} is the molecular activation energy for heterogeneous nucleation, and θ is the contact angle between inclusion free surface and substrate phase. Because of the lack of data on θ in liquid steel, default value of 50^0 is assumed in this calculation. The value of ΔG^*_{het} and $f(\theta)$ are given by as discussed in Chapter 2:

$$\Delta G^*_{het} = f(\theta)\Delta G^*_{hom} \quad (3.17)$$

$$f(\theta) = \frac{1}{4}(2 + \cos\theta)(1 - \cos\theta)^2 \quad (3.18)$$

The enhancement influence of heterogeneous nucleation and effect of contact angel θ are presented in Figure 3.4. It is observed that heterogeneous nucleation mechanism enhances the nucleation rate significantly. The bigger the contact angel, the bigger the heterogeneous nucleation rate.

To calculate the TTT diagrams for nucleation of various inclusions, equation (3.11) is rewritten as:

$$t = \left[-\frac{15c^* \ln(1-\zeta)}{8I_{het}\pi\alpha^3}\right]^{2.5} \quad (3.19)$$

Since the values of c_Q^i, I_{het} and α have been calculated, the corresponding time t at temperature T for any given value of ζ is able to be calculated to construct the TTT diagrams for the nucleation of inclusions.

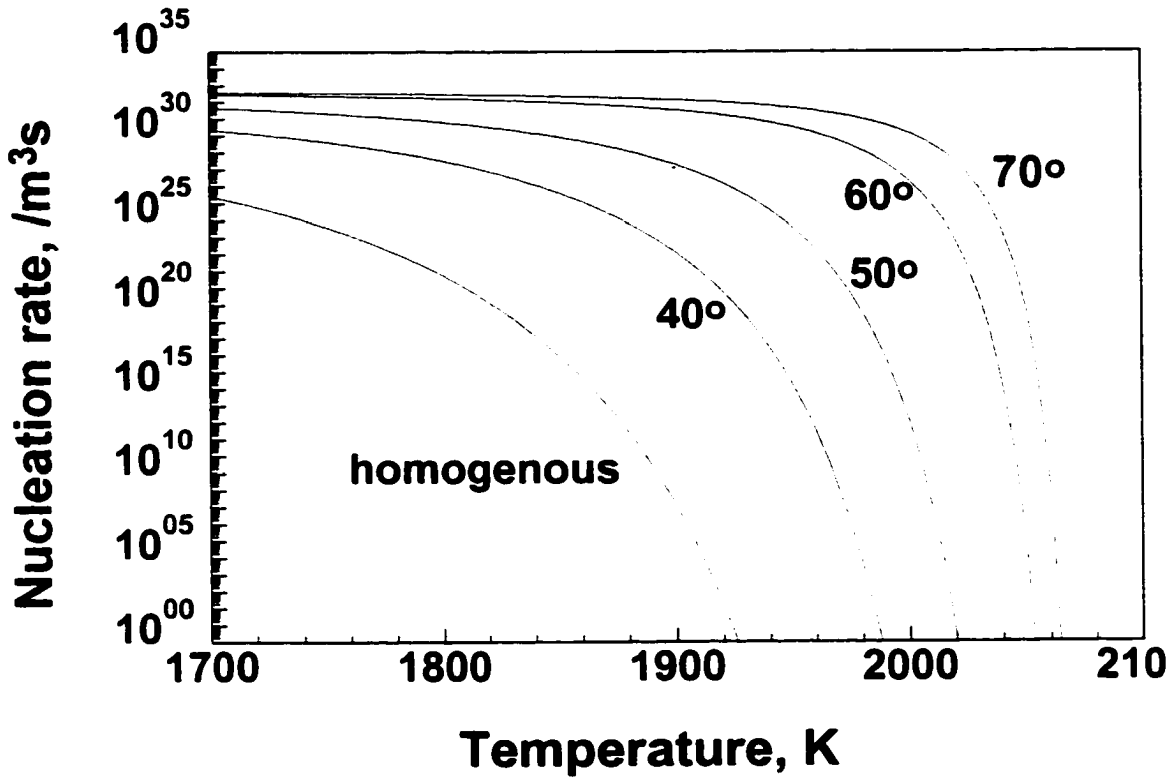

Figure 3.4 The effect of contact angel on heterogeneous nucleation rates of Al_2O_3 inclusion in the liquid steel which composition is shown in Table 3.6.

3.2.4 TTT diagrams for growth

Because the nucleation rates are very high and nucleation time is very short compared with growth time as the following discussion, the nucleation is not considered in the calculation of growth TTT diagram. The growth of inclusion is assumed to be controlled by diffusion of elements. The approach, described by Zener,[23] for diffusion controlled growth of precipitates in solid solutions can be applied to inclusion growth in liquid steel. The change of inclusion radius as a function of growth time is give by:

$$r = \sqrt{-2c^{\cdot}Dt} = \alpha\sqrt{t}\,, \tag{3.20}$$

where r is the radius of the inclusion, t is the growth time after nucleation. If the composition and temperarture are variables, equation (3.20) can be discrized by calculation of very small time step iteratively:

$$r_{i+1} - r_i = \frac{\alpha}{2\sqrt{t}}\Delta t_i \tag{3.21}$$

where r_i and r_{i+1} are the radii of the inclusion before and after the ith time step, respectively, Δt_i, is the time step, t is growth time, and α is defined in equation (3.12). The time necessary to increase the inclusion radius to a certain value at different temperatures is calculated from equation (3.21) to construct the TTT diagrams for the growth of inclusions.

3.2.4 TTT diagrams for dissolution

When the interfacial concentrations of constituent elements of the inclusion exceed the concentrations in the bulk liquid at a given temperature, the elements diffuse from the interface into the bulk liquid and the inclusion dissolves. Considering diffusion-controlled precipitation with a quasi-steady state approximation in alloy matrix, Whelan[24] derived the following expression from kinetics of dissolution:

$$r_{i+1} - r_i = -\frac{k}{2}\left[\frac{D}{r_i} + \sqrt{\frac{D}{\pi t}}\right]\Delta t_i \tag{3.22}$$

where r_i and r_{i+1} are the radii of the inclusion before and after the *i*th time step Δt_i, respectively, t is the dissolution time of the inclusion, $k = -2c^*$, and c^* is defined in equation (3.10). The time needed to decrease the particle size to a certain value can be calculated from equation (3.22) to construct the TTT diagrams for the dissolution of inclusions.

3.3 Results and Discussion

3.3.1 Nucleation Rates

Fig. 3.5 shows the calculated nucleation rates of Al_2O_3 inclusions using equation (3.18). The alloy composition is shown in Table 3.3. It is observed that the nucleation rates change significantly with temperature. Nucleation rates of Al_2O_3 in the liquid steel are very high, especially at lower temperatures. When the temperature is above certain value, the nucleation rates are so small that they are neglected. Figure 3.6 shows the TTT diagrams of ζ = 0.01 and 0.99 for the nucleation of Al_2O_3 inclusions in the steel of composition indicated in Table 3.3. ζ = 0.01 stands for almost the starting point of inclusion nucleation, and ζ = 0.99 means nearing the ending point of inclusion nucleation. The TTT diagram in Figure 3.6 presents the time necessary for Al_2O inclusion to start and end equilibrium nucleation. It is observed that the starting and ending time are very short, in the magnitude of 10^{-9} – 10^{-7} s at lower temperatures. Therefore, it is reasonable to assume that the nucleation rates are much faster compared with the inclusion growth rates. Therefore, the nucleation phenomenon is not considered in the calculations of growth rates and TTT diagrams for growth of inclusion. Growth is treated as an independent procedure of nucleation.

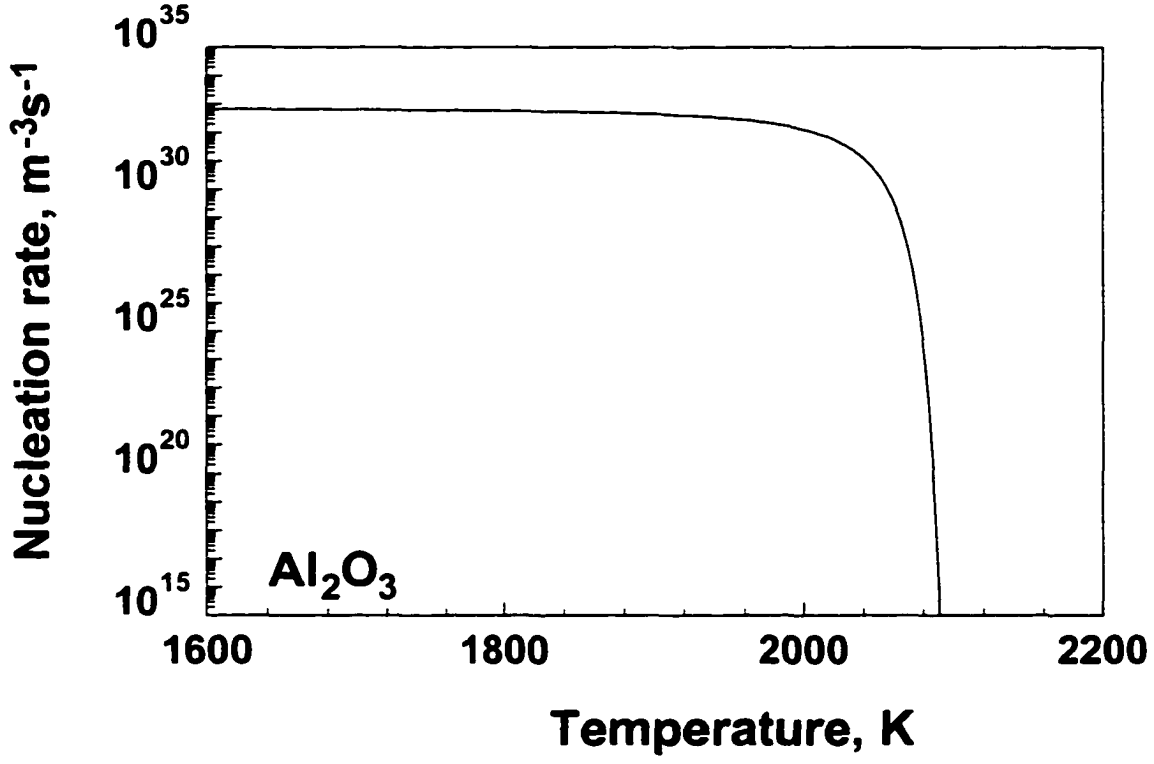

Figure 3.5 Homogeneous nucleation rate of Al_2O_3 inclusoins as a function of temperature. The alloy composition is shown in Table 3.6.

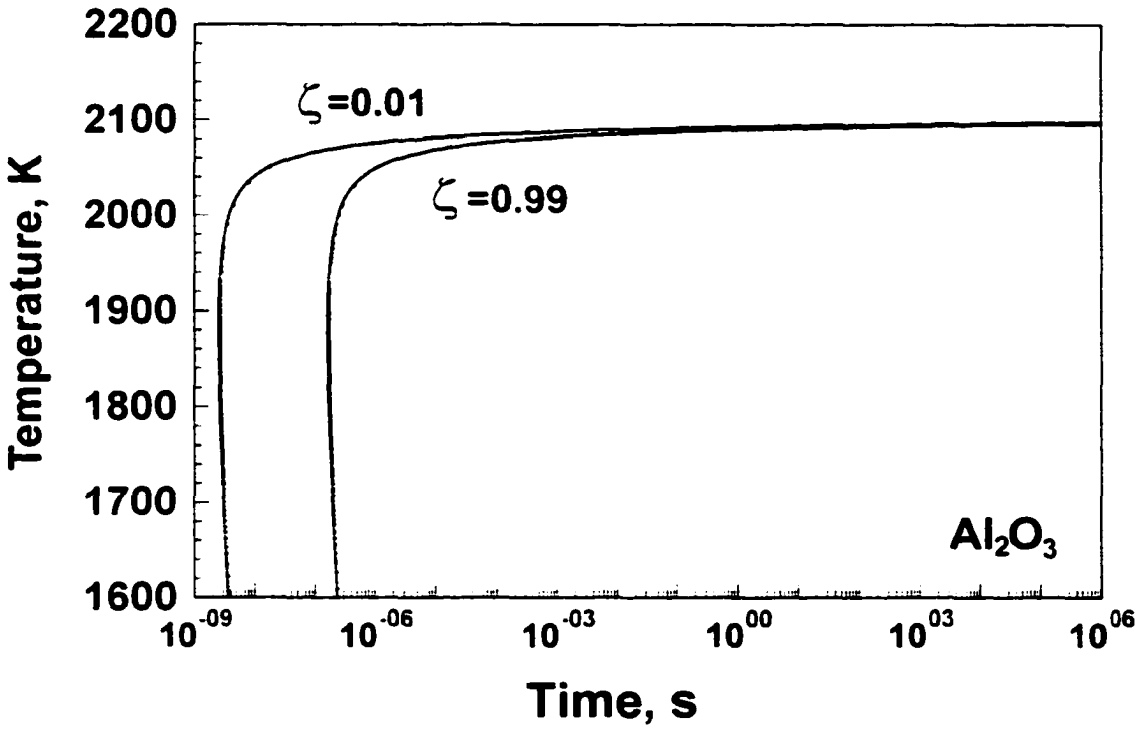

Figure 3.6 TTT diagrams for the homogenerous nucleation of Al_2O_3 inclusions in the liquid steel which composition is shown in Table 3.6.

3.3.2 TTT Diagrams for Growth and Dissolution of Inclusions

Fig. 3.7 shows the TTT diagram for the growth and dissolution of Al_2O_3 inclusions in the steel of composition listed in Table 3.3. For growth, the diagrams indicate the time necessary for inclusions to reach particular target radii (r_t = 1, 2, and 3 μm in this figure) at various temperatures during isothermal growth. The diagrams for dissolution indicate the time necessary for inclusions to dissolve to the final radius r_f (1% of initial radius in this figure) from various initial radii (r_0 = 1, 2, and 3 μm).

The growth rates of inclusions depend on diffusion coefficient, D, and the concentration gradient represented by the dimensionless supersaturation, c^*. The diffusion coefficient in the liquid metal calculated from equation (3.5), decreases with the reduction of temperature. However, the dimensionless supersaturation c^* increases with the decrease of temperature as observed in Figure. 3.5 calculated from equation (3.10). Thus, there is an optimal value of temperature where the fastest growth rate is achieved. The resulting TTT diagram for the inclusion growth shows typical 'C' shape curve.

Both oxygen and aluminum diffuse from the bulk melt to the inclusion/melt interface during growth of Al_2O_3. The direction of transport is reversed during dissolution. The concentrations of oxygen and aluminum at the interface and in the bulk liquid determine the growth and dissolution rates of the inclusions. These interfacial concentrations vary with temperature for a given steel composition. The dimensionless interfacial concentrations of oxygen and aluminum at different temperatures are shown in Figure 3.2 for Al_2O_3 inclusion to illustrate this behavior. Growth of alumina stops at a temperature when the interfacial concentrations of oxygen and aluminum become equal to those in the bulk alloy. For the steel composition used in this calculation, the concentrations of both oxygen and aluminum at the interface and in the bulk steel become equal at 2114 K. This temperature is defined as the equilibrium temperature for the alumina inclusion/steel system. The alumina inclusions will grow in the liquid steel and below this temperature and dissolve above this temperature.

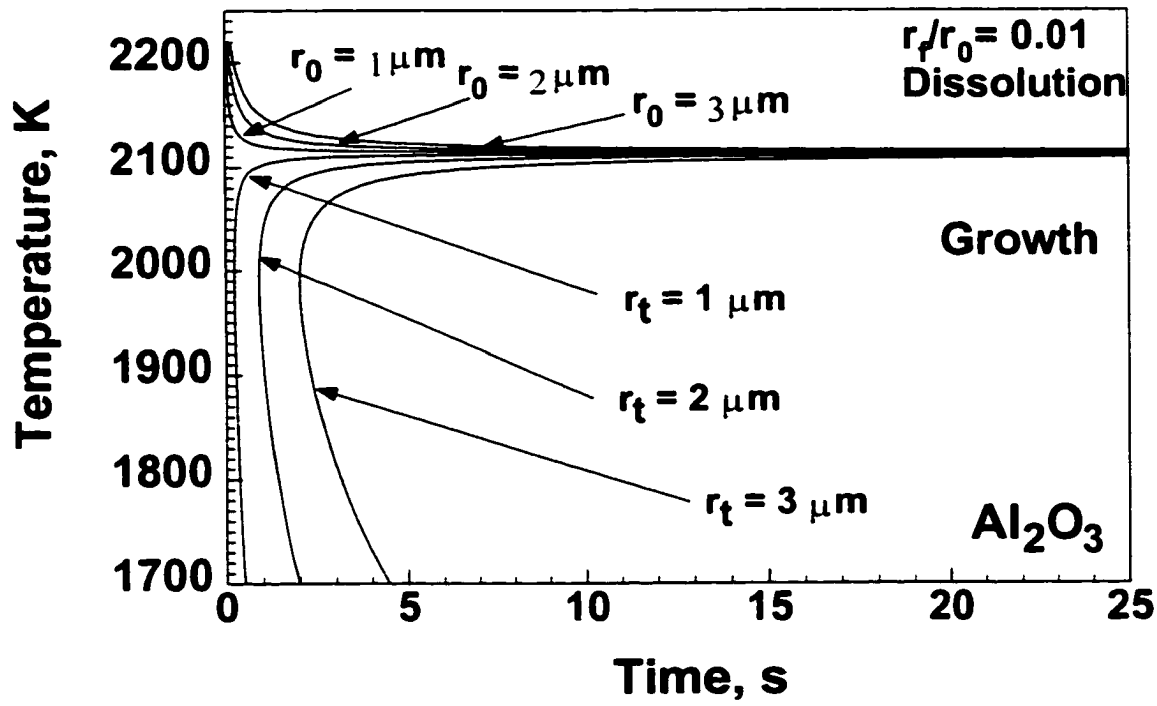

Figure 3.7 TTT diagrams for the growth and dissolution of Al_2O_3 inclusions with different radius in the liquid steel of composition indicated in Table 3.6.

Figure 3.8 shows the TTT diagrams for the growth of various oxide inclusions to 1 μm radius in a liquid steel of composition indicated in Table 3.3. Among all the oxide inclusions considered, Al_2O_3, $MnO{\cdot}Al_2O_3$, and Ti_3O_5 grow fastest at temperatures above 2000 K. It is observed from Figure 3.3 that the change of c* at lower temperatures is not very pronounced for Al_2O_3, Ti_3O_5 and TiO_2. As a result, diffusion dominates the kinetics of inclusion growth for these inclusions at low temperatures. For MnO and SiO_2, the change of c* at all temperature range dominates the kinetics of inclusion growth. Therefore, the 'C' shapes of TTT diagrams for growth of MnO and SiO_2 are not as profound as the other inclusions. It is observed from Figure 3.8 that the equilibrium temperatures of the complex oxides are intermediate between the equilibrium temperatures of the constituent simple oxides. For example, the equilibrium temperature of $MnO{\cdot}Al_2O_3$ lies between those of Al_2O_3 and MnO. A similar behavior is observed for both $SiO_2{\cdot}Al_2O_3$ and $MnO{\cdot}SiO_2$ inclusions.

Figure 3.9 shows the computed TTT diagrams for the dissolution of oxide inclusions of different initial radii in the steel which composition is shown in Table 3.1. The dissolution kinetics depends strongly on time and temperature as observed. It is observed from Figures 3.8 and 3.9 that there is an equilibrium temperature between inclusion and liquid steel. Above the equilibrium temperature, inclusions experience dissolution. We assume: the higher is the equilibrium temperature of an inclusion, the higher is its stability. Several researchers presented theoretical and experimental results on the relative stability of inclusions in low alloy steels. For example, Hsieh[4] *et al* calculated the sequence of oxidation. Their result showed that the sequence depended on the composition and temperature. Among the oxides they considered, Al_2O_3, Ti_3O_5 and $MnO{\cdot}Al_2O_3$ were calculated to be most stable at high temperatures in the low alloy steels. These relative stability results agreed well with computed results in Figures 3.8 and 3.9. However, their calculations did not consider some complex oxides. Dowling et al[25] studied the inclusions in submerged arc welds in low alloy steels using TEM and EDS. They found that $MnO{\cdot}Al_2O_3$, a titanium-rich compound, and an aluminum-rich phase (probably Al_2O_3) were the main constituents. Kluken and Grong[6] studied inclusion

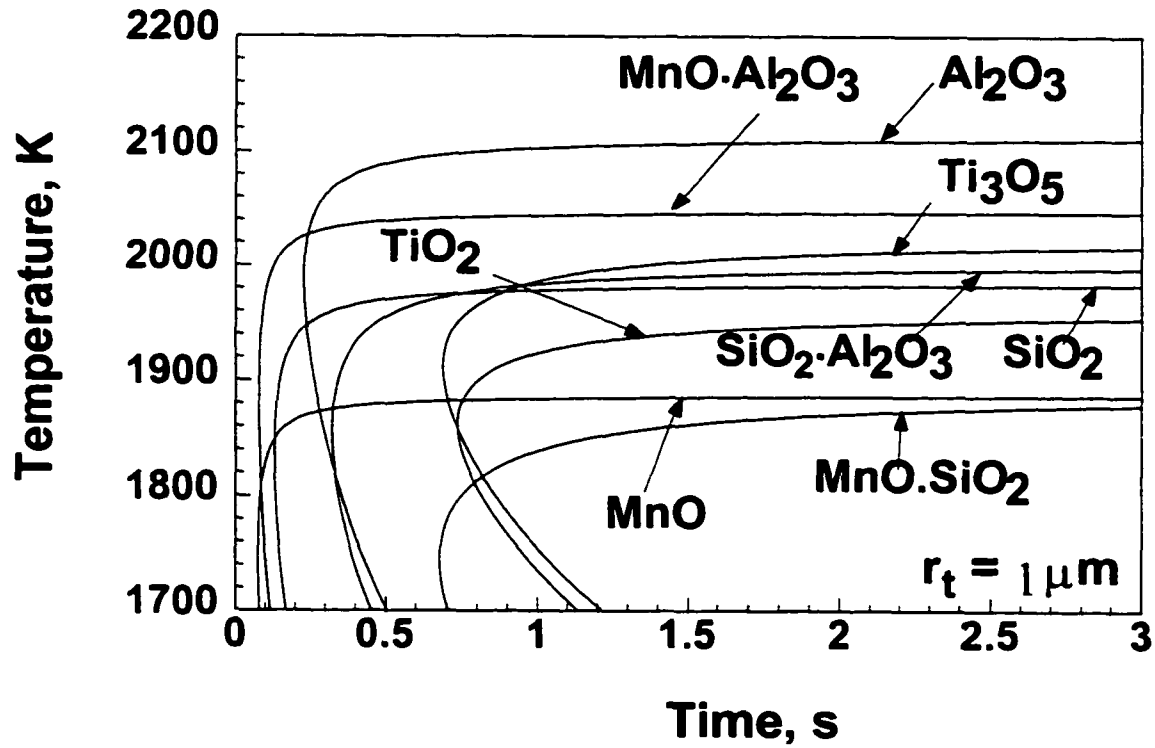

Figure 3.8: TTT diagrams for the growth of various oxide inclusions in liquid steel of composition indicated in Table 3.6.

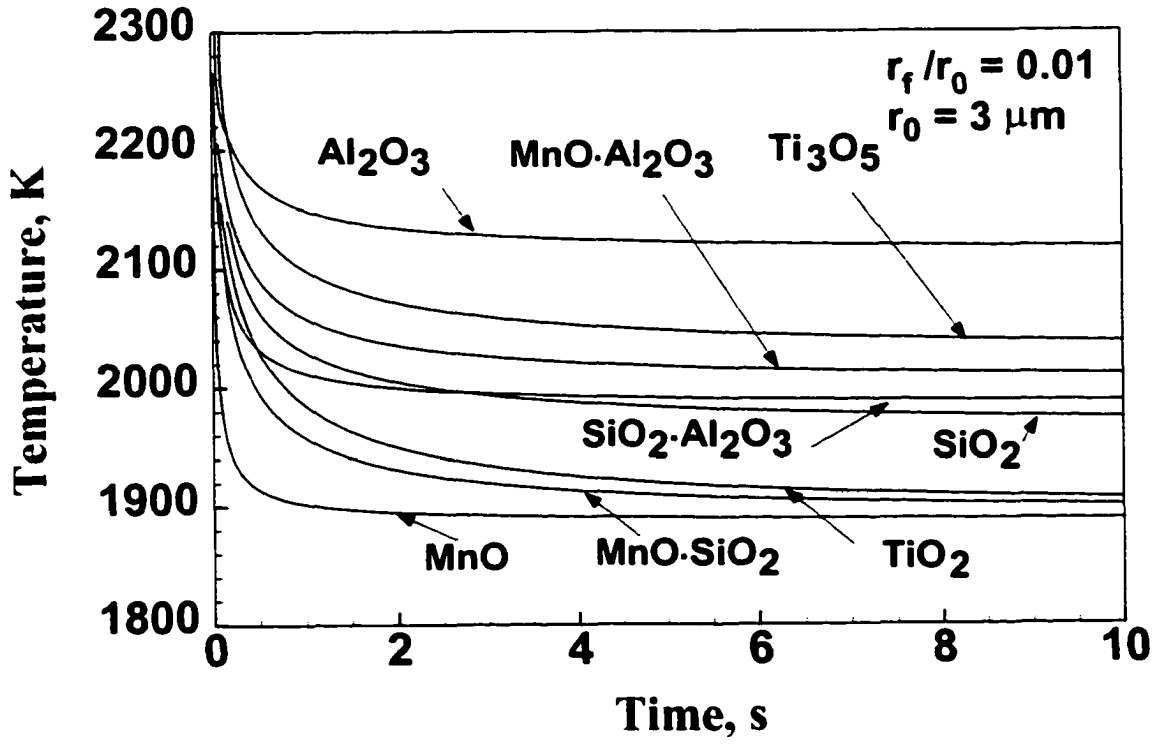

Figure 3.9 TTT diagrams for the dissolution of all oxide inclusions considered in the liquid alloy of composition shown in Table 3.6.

formation in Al-Ti-Si-Mn dexoidized steel welds. The calculated stability of various oxides decreases in the following order: Al_2O_3, Ti_2O_3, SiO_2 and MnO. The high stability of Al_2O_3, $MnO{\cdot}Al_2O_3$, and Ti_3O_5 observed by these investigators is consistent with the computed time-temperature-transformation diagrams presented in Figures 3.8 and 3.9.

Figures 3.10 and 3.11 show the TTT diagrams for the growth and dissolution of several nitride and sulfide inclusions, respectively. The equilibrium temperatures for TiN, Si_3N_4, MnS and FeS inclusions are much lower than the corresponding metal oxides. Other features of these plots are similar to those for the oxide inclusions. Because of their low equilibrium temperatures, sulfide inclusions cannot form in the low alloy steel weld pool where the temperatures are higher than the equilibrium temperatures of the inclusion/steel. However, they can form during solidification of the weld metal. From Figure 3.10, it is observed that although the equilibrium temperature of MnS is lower than FeS, its growth rate at low temperatures is higher, which implies that MnS may become the dominant sulfide inclusion during solidification and cooling. This conclusion from theoretical calculations matches experimental observations well in the sense that MnS is known to be the dominant sulfide inclusion in many steels.[26,27]

3.3.3 Influence of Alloy Compositions

To investigate the influence of alloy composition on growth kinetics, the TTT diagrams for growth of Al_2O_3 inclusion in liquid steels of compositions 1 and 2 presented in Table 3.7 are shown in Figure 3.12. The growth rate of Al_2O_3 inclusion in the steel of composition 2 is much faster than that in composition 1. This phenomenon can be explained from the calculated values of dimensionless supersaturation c* in these two cases which is presented in Figure 3.13. It is observed that c* for steel composition 2 is much higher than that for steel 1. It can be derived from equations (3.11) and (3.21) that the growth rate increases with the increase of c*. Therefore, the growth kinetics for steel 2 is faster than that for steel 1.

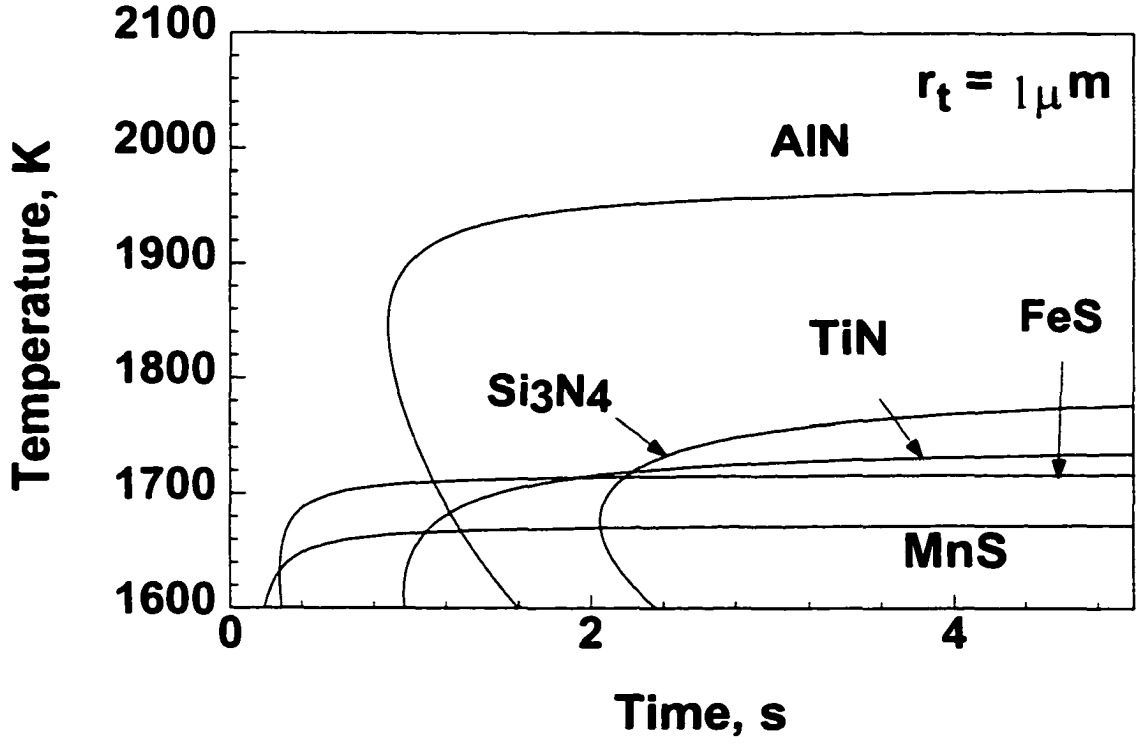

Figure 3.10 TTT diagrams for the growth of several nitride and sulfide inclusions in the liquid alloy of composition in Table 3.6.

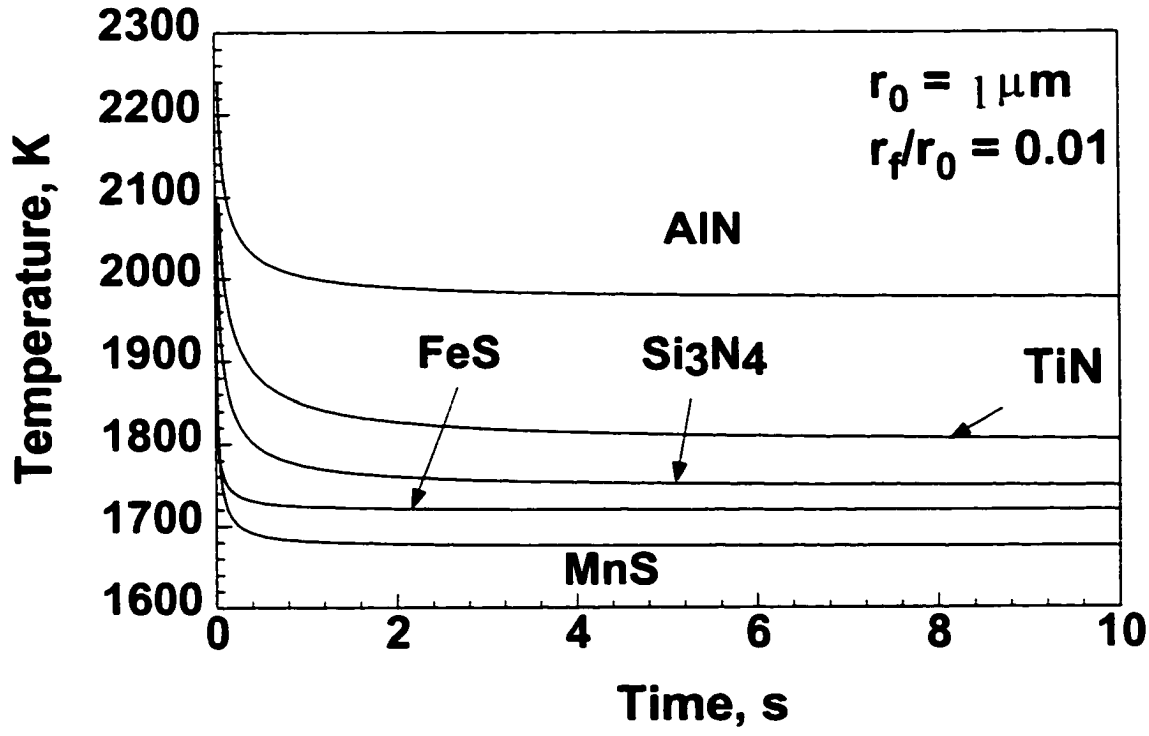

Figure 3.11 TTT diagrams for the dissolution of several nitride and sulfide inclusions in the liquid alloy of composition shown in Table 3.6.

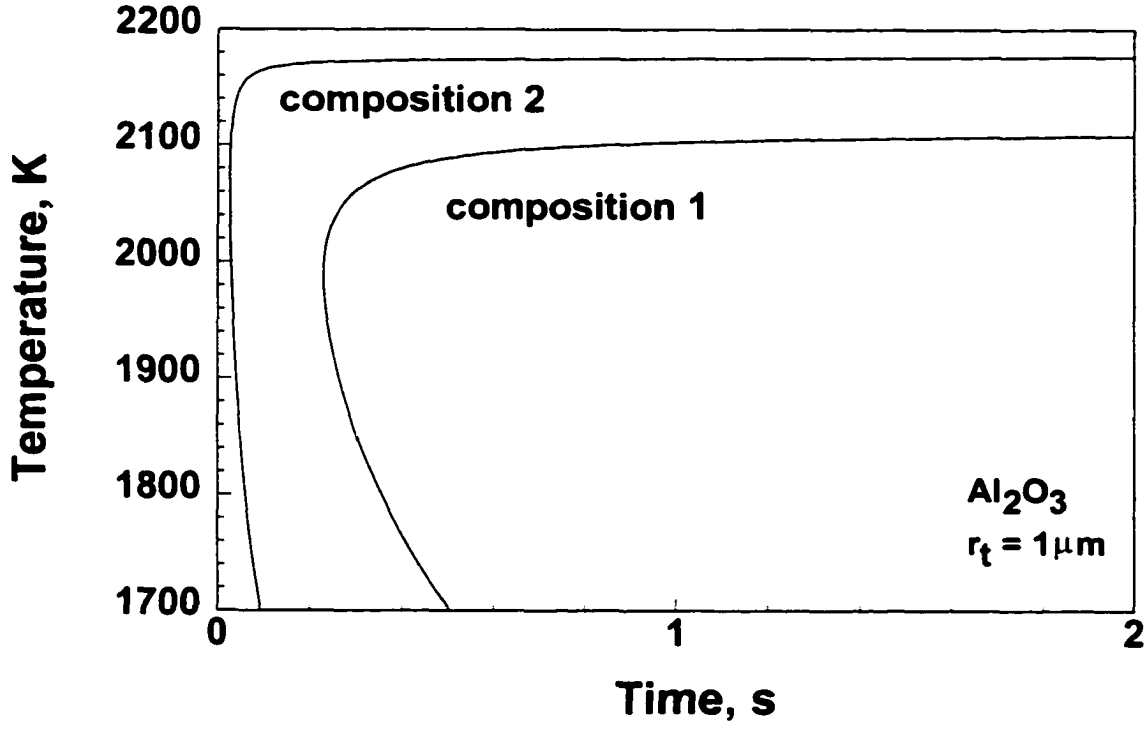

Figure 3.12 Comparison of growth rates of Al_2O_3 inclusions between composition 1 and composition 2 in Table 3.7.

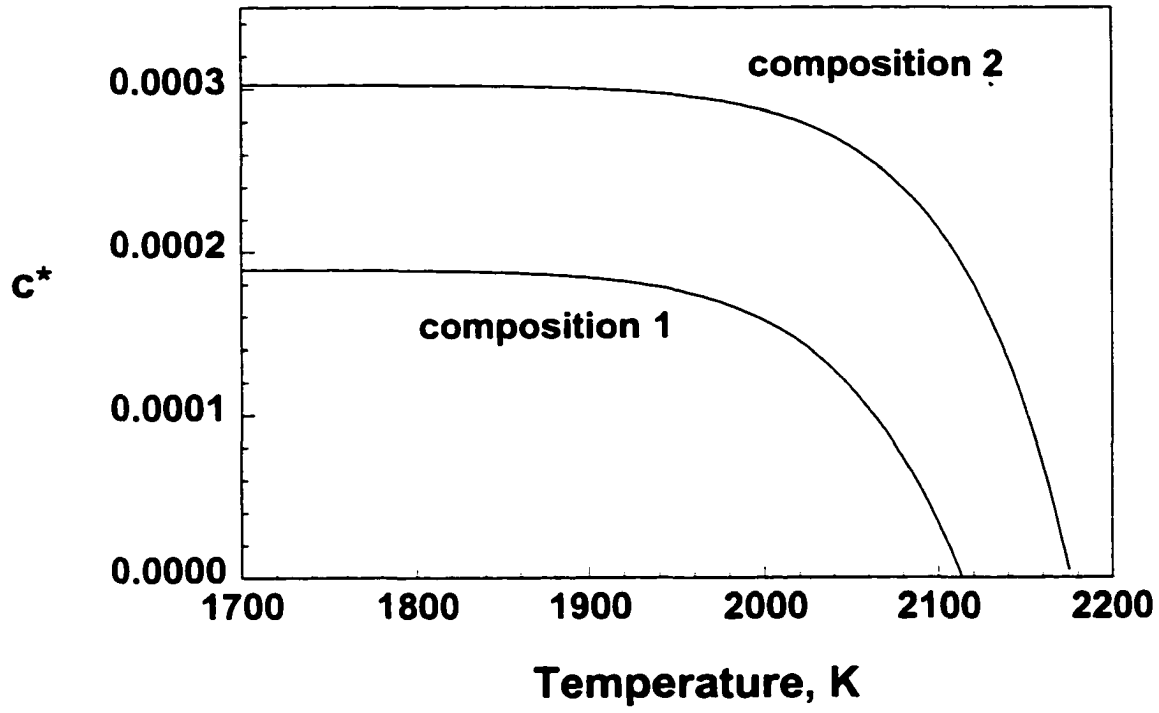

Figure 3.13 Comparison of dimensionless supersaturation of oxygen, c*, at the interface of Al_2O_3 inclusions and liquid steels of composition 1 and composition 2 in Table 3.5.

Table 3.7. Alloy composition and diffusion coefficient of oxygen in calculations[6]

Element	C	Si	Mn	Ni	Cr	Ti	Al	N	O	S
Composition 1 (wt%)	0.09	0.53	1.9	0.09	0.01	0.005	0.010	0.008	0.032	0.020
Composition 2 (wt%)	0.06	0.39	1.55	0.2	0.01	0.003	0.016	0.004	0.054	0.009

Figure 3.14 shows another example about how the alloy composition affects the inclusion growth and dissolution, in turn the relative stability of inclusions in the liquid steel. Assuming three alloy systems with same composition except for aluminum concentrations which are 0.006%, 0.016% and 0.026%, respectively, the equilibrium temperatures of three oxide inclusions, Al_2O_3, TiO_2, and SiO_2, at the three alloy systems are plotted in Figure 3.14. It is observed that at higher aluminum concentration, the equilibrium temperature between Al_2O_3 inclusion and liquid is the highest, which implies that alumina would be the most stable inclusion in higher Al steels. However, when the aluminum concentration reduces, equilibrium temperature of alumina decreases while those of TiO_2 and SiO_2 increase. Below certain aluminum concentration, TiO_2 becomes the most stable in the given steel among the three inclusions.

3.4 Conclusions

The diffusion controlled growth and dissolution behavior of oxide, nitride, and sulfide inclusions can be represented by a series of TTT diagrams that indicate the strong effects of time and temperature on the kinetics of inclusion growth and dissolution. In the low alloy steel investigated, Al_2O_3, $MnO{\cdot}Al_2O_3$, and Ti_3O_5 are the most stable inclusions that form during welding. Some complex oxide inclusions such as $SiO_2{\cdot}Al_2O_3$ are also stable at temperatures higher than 2000K. The composition of steel has a strong effect on kinetics of inclusion growth and dissolution. Apart from the stability of various inclusions in a given composition of steel, TTT diagrams provide important kinetic information of diffusion controlled growth and dissolution.

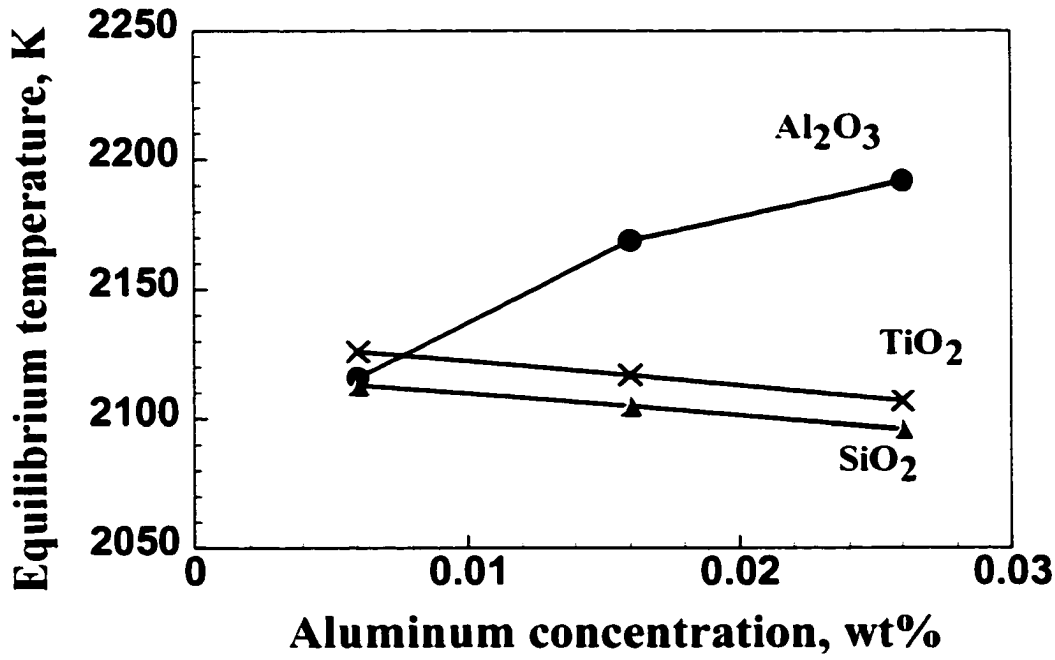

Figure 3.14 Equilibrium temperatures for the co-existence of inclusions and liquid steel as a function of aluminum concentration for 3 oxide inclusions. All element concentrations keep constant as shown in Table 3.6 except aluminum.

In this chapter, the nucleation, growth and dissolution of inclusions in the liquid steels are study by constructing time-temperature-transformation diagrams considering both thermodynamics and kinetics basis of inclusion formation and growth under isothermal condition. In the next chapter, the non-isothermal inclusion growth and dissolution are studied by constructing continuous-cooling-transformation (CCT) diagrams and continuous-heating-transformation (CHT) diagrams.

References

1. S. A. Court and G. Pollard: *Metallography*, **22**, 219 (1989).
2. J. .M. Dowling, J. M. Corbett and H. W. Kerr: *Metall. Trans. A*, **17A**, 1611 (1986).
3. E. T. Turkdogan: *J. Iron and Steel Inst.*, **203**, 914 (1966).
4. K. C. Hsieh, S. S. Babu, J. M. Vitek, and S. A. David: *Mater. Sci. Engi.*, **A215**, 84 (1996).
5. D. J. Abson: *Welding in the World*, **27**, 76 (1989).
6. O. Kluken and O. Grong: *Metall. Trans. A*, **20A**, 1335 (1989).
7. T. Koseki, S. Ohkita, and N. Yurioka: *Sci. Tech. Welding and Joining*, **2**, 65-69 (1997)
8. M. J. Houle: Introduction to the Metallurgy of Ferrous Materials, Practical Guide to ASME Section IX - Welding Qualifications, Practical Guide Book Series - Volume 2, Ed: J.E.Bringas, Casti Publishing Inc, Edmonton, Canada, 1996.
9. H. K. D. H. Bhadeshia: *Progress in Materials Science*, **29**, 321 (1985).
10. H. K. D. H. Bhadeshai: *Metal Science*, **16**, 159 (1982).
11. Z. Yang: Modeling Weldment Macro and Microstructure from Fundamentals of Transport Phenomena and Phase Transformation Theory, Ph.D. thesis, The Pennsylvania State University (1999)
12. TAPP^{TM}, Thermochemical and Physical Properties, Version 2.0, ES Microware Inc.
13. Materials Properties Handbook: Ed. R. Boyer, G. Welsch, E. W. Collings, Materials Park, OH : ASM International (1994).
14. T. Palmer: Nitrogen in Plasmas and Steel Weld Metal, Ph.D. Thesis, The Pennsylvania State University (1999).
15. G. H. Geiger and D. R. Poirier: Transport Phenomena in Metallurgy, 458, Addison-Wesley Publishing Company, Reading, Massachusetts (1986).
16. J. F. Elliott, M. Gleiser, and V. Ramakrishna: Thermochemistry for steelmaking, Addison-Wesley Publishing, Reading Massachusetts, 687-702, (1963).
17. E. T. Turkdogan: Physical Chemistry of High Temperature Technology, New York, Academic Press, (1980).
18. G. K. Sigworth and J. F. Elliott: *Met. Sci. J.*, **8**, 298 (1974)
19. F. D. Richardson: Physical Chemistry of Melts in Metallurgy, vol. 2, , London, Academic Press, 413, (1974).
20. J. W. Christian: The Theory of Transformations in Metals and Alloy - Part I: Equilibrium and General Kinetic Theory, 2nd ed., Oxford, Pergamon Press (1981).
21. S. S. Babu, S. A. David, J. M. Vitek, K. Mundra, and T. DebRoy: *Mater. Sci. Tech.*, **11**, 186 (1995).

22. M. L. Turpin and J. F. Elliot: *J. Iron Steel Inst.*, **204**, 217 (1966).

23. C. Zener: *J. Applied Physics*, **20**, 950 (1949).

24. M. J. Whelan: *Metal Science J.*, **3**, 95 (1969).

25. J. M. Dowling, J. M. Corbett and H. W. Kerr: *Metal. Trans. A*, **17A**, 1611 (1986).

26. B. R. Keville: *Weld. J.*, **62**, 253s (1983).

27. M. Wintz, M. Bobadilla, J. Lehmann and H. Gaye: *ISIJ International*, **35**, 715 (1995).

CHAPTER 4

NON-ISOTHERMAL GROWTH AND DISSOLUTION OF INCLUSIONS IN LIQUID STEELS

Synthesis of our current knowledge of thermodynamics and kinetics of inclusion growth and dissolution can provide important insight about the behavior of inclusions in liquid steels. In Chapter 3, we showed that the effects of alloy composition and temperature on the nucleation, growth, and dissolution of inclusions in liquid steels can be represented by a set of time-temperature-transformation (TTT) diagrams. Apart from the information about stability of various inclusions in a given composition of steel, the TTT diagrams provide important kinetic information about diffusion-controlled growth and dissolution. However, TTT diagrams are constructed assuming equilibrium between inclusions and liquid steel under isothermal condition. In the weld pool, inclusions undergo vigorous thermal excursions. Non-isothermal condition must be taken into account. In this chapter, the method to extend the concepts of TTT diagrams construction to create continuous cooling transformation (CCT) diagrams of inclusion growth and dissolution under non-isothermal conditions is presented.

Previous research[1-3] indicated that continuous cooling transformation (CCT) diagrams are useful tools to study non-isothermal phase transformation in steels. In this chapter, a new type of diagram, continuous heating transformation (CHT)

diagrams for the dissolution of inclusion in liquid steels, is introduced. CCT diagrams for the growth and CHT diagrams for the dissolution of inclusions are calculated from the corresponding TTT diagrams. This method was similar to that discussed in some literatures to construct the CCT diagrams of phase transformation in steels. The approach is presented in the following sections.

4.1 CCT Diagrams in Phase Transformation of Low Alloy Steels

In Chapter 3.1, we discussed the application of TTT diagram on phase transformation of low alloy steels. Among the solid curves representing TTT diagrams shown in Figures 4.1, the upper C curves represent the time necessary for the initiation of allotriomorphic ferrite formation in the specific steel composition. The lower C curves represent the time necessary for the initiation of formation of Widmanstatten ferrite, acicular ferrite and bainite which formation is controlled by displacive mechanism. The horizontal lines represent the start temperatures of martensite and bainite, which are labeled as M_s and B_s, respectively. The TTT diagrams drawn in thin solid line in Figure 4.1 are calculated using bulk alloy composition and that drawn in thick solid line is calculated using composition in solution depleted region as explained in Chapter 3.1. It is observed that the characteristics temperatures for bulk alloy composition and depleted composition do not have significant difference except the phase transformation in solute depleted region is faster. Therefore, if only isothermal conditions represented by TTT diagrams are considered, it is not possible to explain the very different microstructure formed in bulk liquid region and solution depleted region during cooling.

Although the basic kinetics theory of phase transformation is confined to isothermal reactions, some efforts have been made to predict the non-isothermal phase transformation from the corresponding isothermal transformation curves. Yang et al[2,3] applied Badheshia's model[1] to calculate CCT diagram from the corresponding TTT

diagram using Scheil additive rule[4,5]. The dashed lines in Figure 4.1 show the calculated CCT diagrams from the corresponding TTT diagrams.

In Yang's work, the cooling curve calculated from 3D welding model developed in Penn State was imposed on TTT-CCT diagrams (as shown in Figure 4.1) to predict the microstructural evolution in heat affected zone. It is observed that the cooling curve intercepted with both upper C curve (diffusional curve) and lower C curve (displacive curve) of TTT diagrams for both bulk region (thin solid lines) and solution depleted region. If only TTT diagrams are considered to predict the phase evolution, the predicted results cannot explain the microstructure difference between bulk region and depleted region. However, if CCT diagrams are considered, it is observed that the cooling curve intercepts both the upper and the lower C curves of CCT curves of solute depleted region (thick lines) but neither of CCT diagrams of bulk region (thin lines). Thus, various phases such as allotriomorphic ferrite, Widmanstatten ferrite and acicular ferrite/bainite are expected in this solution-depleted region of the weld but not in bulk region. The experimental results are well explained by CCT diagrams.

This example indicates that the combination of CCT diagram calculation with heat transfer and fluid flow modeling in the weld pool is a powerful tool to understand the microstructure evolution in the weldment during cooling. The same concept can be applied to the study of inclusion growth and dissolution in liquid melts as well.

4.2 Prediction of CCT and CHT Diagrams from TTT Diagrams for Growth and Dissolution of Inclusions

In this section, the concepts of applying TTT and CCT diagrams to study phase evolution in steels are extended to understand the inclusion growth and dissolution in liquid steels. From the discussion in Chapter 3, the TTT diagram is a powerful tool to understand not only the stability of inclusion formation, but also

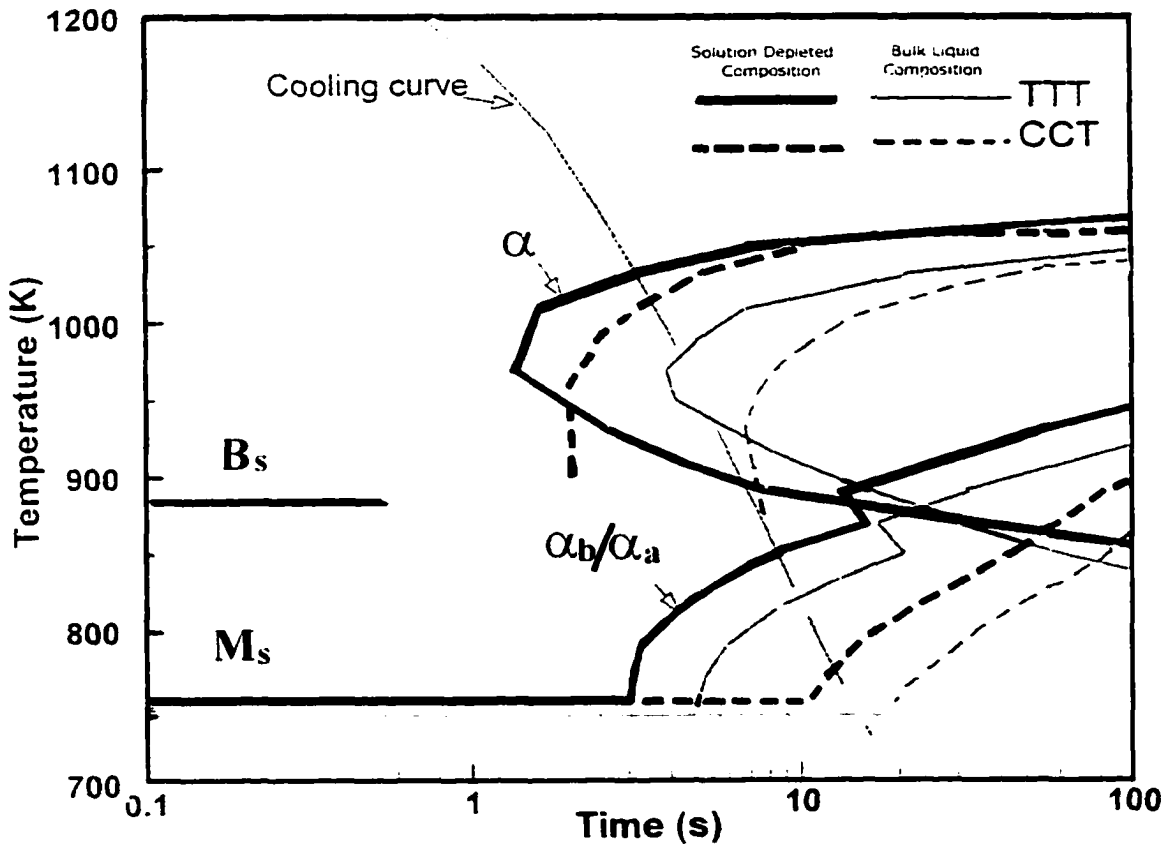

Figure 4.1 Comparison of CCT and TTT diagrams in the bulk region and solution depleted region. The alloy composition shown in Table 3.1.

temperature and alloying composition on the growth and dissolution of inclusions in the liquid steels under isothermal conditions. Because inclusions experience complicated thermal histories in the weld pool due to the presence of vigorous circulation of melted metal in the weld pool, the non-isothermal growth and dissolution of inclusions must be taken into account. Therefore, TTT diagrams alone cannot provide the accurate information to predict the growth and dissolution of inclusions.

In the calculations of TTT diagrams presented in Chapter 3, the growth and dissolution rates of inclusion are assumed to be controlled by the diffusion of constituent elements in liquid steel. The equilibrium concentrations of the elements at the interface between inclusion and liquid steel are required to calculate the element diffusion rates at various temperatures. The method of calculating interfacial equilibrium concentrations is discussed in Chapter 3. After the interfacial concentrations of constituent elements of the inclusion are known, a dimensionless concentration of the constituent element of the inclusion, c^*, is defined as[5]:

$$c^* = (c^b - c^i)/(c^p - c^i) \qquad (4.1)$$

where c is the concentration of the constituent element which diffusion coefficient is lower. The subscripts p, b, and i refer to element concentrations in the inclusion particle, in bulk liquid metal, and at inclusion/steel interface, respectively. Because the concentration of element in the inclusion particle, c^p, is always higher than that at the interface, c^i, i.e., (c^p-c^i) is always positive, the sign of c* depends on the relative values of c^b and c^i. As shown in Figure 3.2, when the temperature is lower than the equilibrium temperature for the co-existence of inclusion and liquid steel, c^b is higher than c^i, and as a result, c^* is positive. In this case, the elements are diffused from the bulk liquid toward the interface resulting in inclusion growth. On the contrary, when the temperature is lower than the equilibrium temperature for the co-existence of inclusion and liquid steel, c^b is lower than c^i and, as a result, c^* is negative. The inclusion experiences dissolution.

4.2.1 Scheil's Additive Rule

The TTT diagrams for the growth and dissolution of inclusion in the liquid steel are largely restricted to isothermal situations. However, they can be readily extended to predict the non-isothermal behavior from the isothermal transformation curves. The goal of this section is to present the methods to calculate the continuous cooling transformation (CCT) or continuous heating transformation (CHT) curves from the isothermal TTT diagrams using Scheil additive rule[5]. The procedure of calculating CCT diagram from TTT diagram is sketched in Figure 4.2. In this procedure, the total time to reach a specified stage of transformation (expressed as final size in the case of inclusion growth and dissolution) is obtained by adding the fractions of time to reach this stage isothermally until the sum reaches unity along the cooling curve. Assuming the cooling curve starts from temperature T_0 at step 0 and the time step equals to Δt. At step 0, the time needed to reach certain stage (in this case, inclusion grows to 1μm) isothermally is t_a^0. Similarly, at step m, the time needed for inclusion to grow to 1μm is t_a^m. If at step n, the formula expressed below reach unity, that point is recorded as one point in the predicted CCT diagram:

$$\sum_{t=0}^{n} \frac{1}{t_a^t} = 1 \qquad (4.2)$$

Above equation shows the discrete expression of Sheil additive rule. It also[4,5] can be expressed by following integration equation:

$$\int_0^t \frac{dt}{t_i(T)} = 1 \qquad (4.3)$$

where $t_i(T)$ is the time needed for isothermal growth or dissolution to a specified extent at a temperature T, t is the time to that extent for the non-isothermal growth or dissolution and dt is the time interval used in the calculation during heating or cooling.

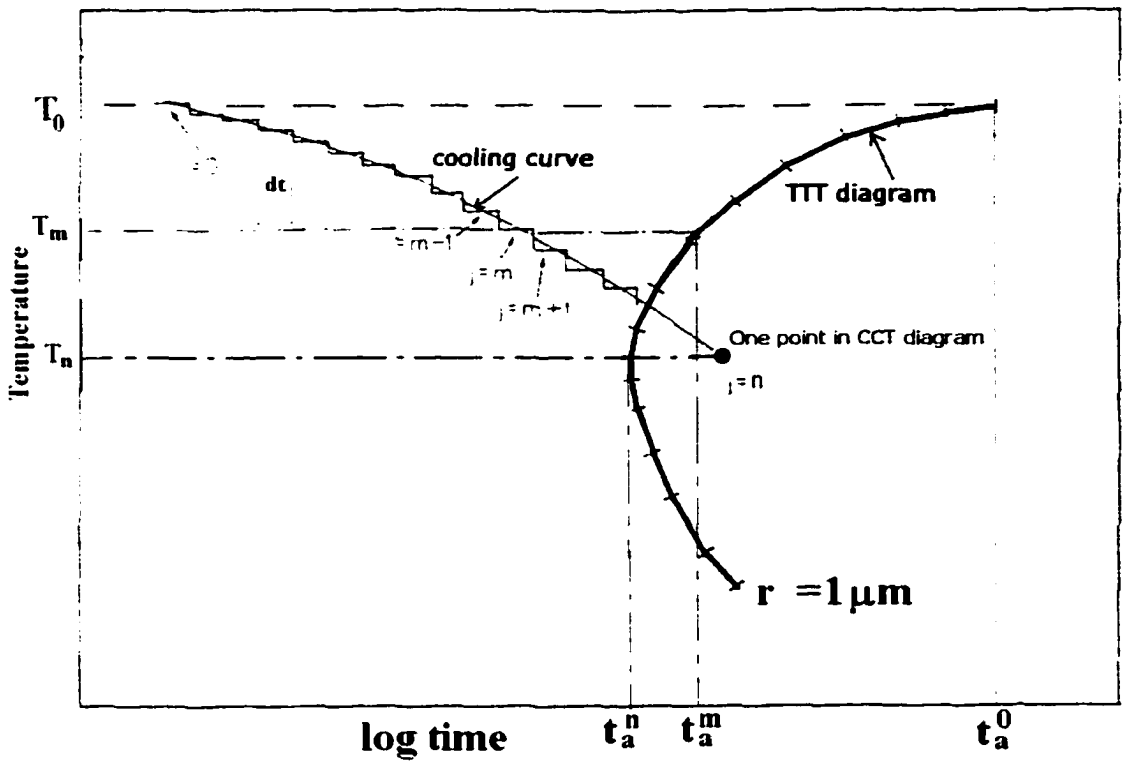

Figure 4.2 Schematic diagram for the calculation of CCT diagrams from Sheil additive rule.

4.2.2 Results and Discussions

The TTT curve in Figure 4.3 shows the time necessary for an Al_2O_3 inclusion to reach the target final radius (r_t = 3 μm) at various temperatures during isothermal growth. It is observed that the TTT diagrams show the characteristics 'C' shape. The growth rates of inclusions depend on diffusion coefficient, D, and dimensionless supersaturation, c^*, as explained in equations (3.2) and (3.4). When the temperature decreases from the equilibrium temperature of inclusion/alloy system, the element supersaturation increases and the diffusion coefficient decreases. Therefore, there is an optimal temperature where the growth rate is the fastest. When the temperature is above the equilibrium temperature for the inclusion/alloy system, the inclusions will dissolve.

The CCT curve in Figure 4.3 shows the time necessary to reach the same target radius (r_t = 3 μm) for an inclusion which forms at temperature of 2200K and non-isothermally grows during cooling. The computed CCT diagram shows some characteristics that are similar to the corresponding TTT diagram. For example, both TTT and CCT diagrams for the growth of Al_2O_3 inclusions have similar shape as the upper C curves (diffusional curves) of austenite decomposition shown in Figure 4.1. The cooling curves plotted in Figure 4.3 have the same initial temperature of 2200 K and different cooling rates of 250 K/sec and 125 K/sec. The cooling curve with cooling rate of 250 K/s does not intersect with the CCT diagram, which implies that it is impossible for an Al_2O_3 inclusion to grow to 3 μm radius at a constant cooling rate of 250 K/s starting from the initial temperature of 2200K. However, at cooling rate of 125 K/sec, an Al_2O_3 inclusion can grow to 3 μm radius in slightly over 3 seconds as indicated by the intersection of the cooling curve with the CCT diagram.

Figure 4.4 shows the TTT and CCT curves for the growth of Al_2O_3 inclusion to various target radii: 1 μm, 3 μm, and 5 μm. The effect of cooling rate on the growth of Al_2O_3 inclusion can be easily evaluated from this figure. For example, in the case of cooling from 2200 K at a cooling rate of 200 K/s, the radius of an Al_2O_3 inclusion can

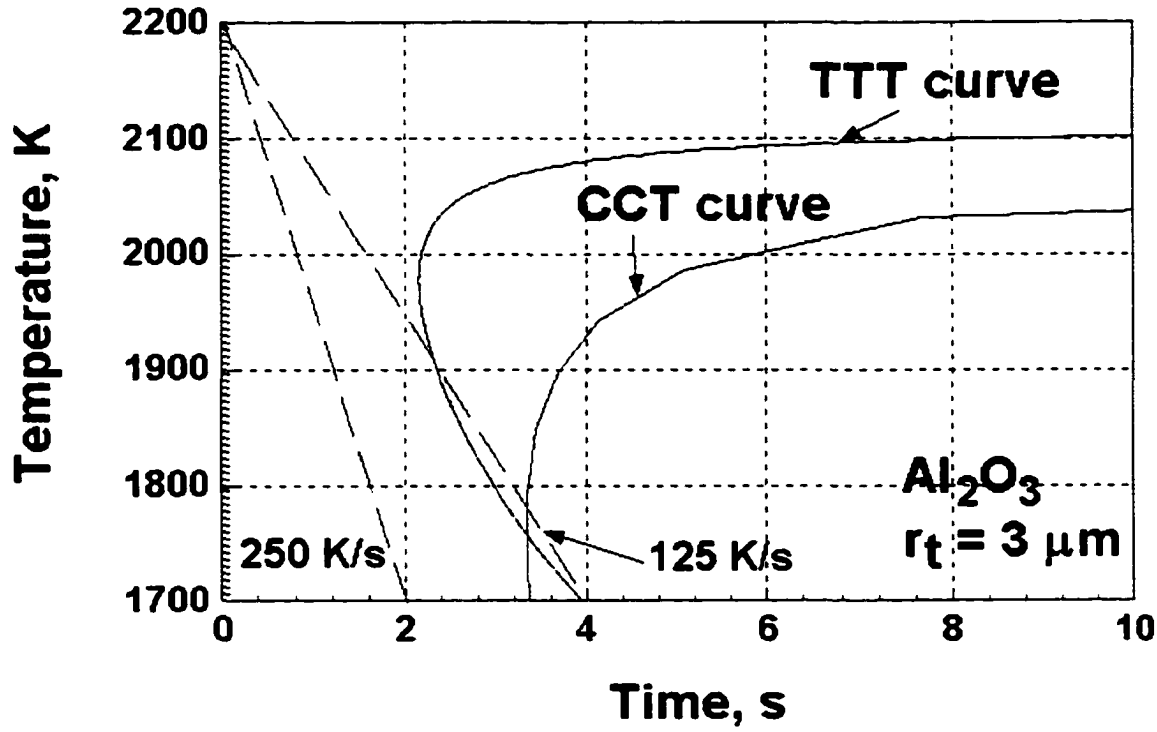

Figure 4.3 CCT and TTT diagrams for the growth of Al_2O_3 inclusions to the target radius of 3 μm in the liquid alloy which composition is shown in Table 3.6.

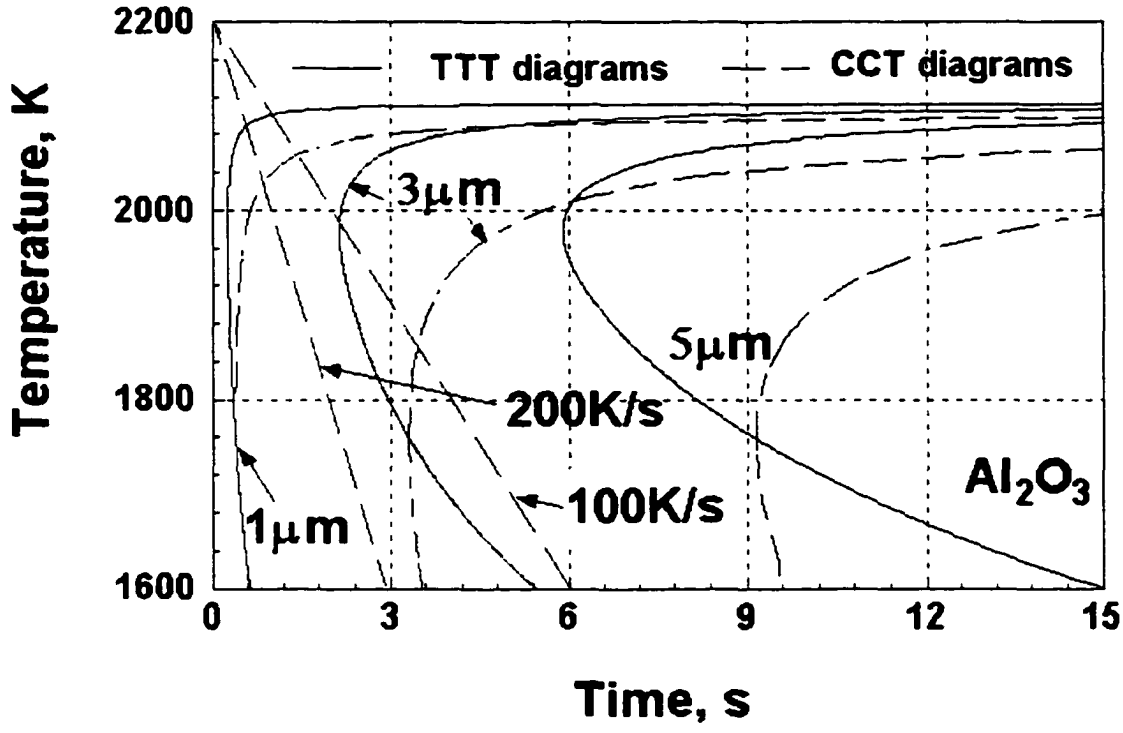

Figure 4.4. CCT and TTT diagrams for the growth of Al_2O_3 inclusions to various target radii in the liquid alloy which composition is shown in Table 3.6.

reach 1 μm but never grow to 3 μm. However, when the cooling rate becomes 100 K/s, the inclusion can grow to 3 μm in about three seconds.

The TTT and CCT curves for the growth of three types of oxide inclusions to the same target radius, 1 μm, are presented in Figure 4.5. Using this diagram, whether a curtain type of inclusion will grow to a target size at a fixed cooling rate can be calculated. For example, cooling from 2200 K at the fixed cooling rate of 400 K/s, the Al_2O_3 and Ti_3O_5 inclusions can form and grow to 1 μm radius but TiO_2 cannot. At the cooling rate of 100 K/s, three types of inclusions can form and grow to 1 μm radius in 1.5, 2.8, and 3.4 seconds, respectively.

To study the non-isothermal dissolution behavior of inclusions, a new type of diagrams, continuous heating transformation (CHT) diagrams, is constructed from the corresponding TTT diagrams using the same method as that of CCT diagrams. The TTT curve in Figure 4.6 shows the time necessary for an Al_2O_3 inclusion to dissolve from the original size of 1 μm radius to 1% of the original radius at various temperatures under isothermal condition. The continuous heating transformation (CHT) curve in Figure 4.6 shows the time necessary to dissolve the inclusion after the inclusion is heated from 1800 K at a fixed heating rate. The diagram shows that the heating curve does not intersect with the CHT diagram below the temperature 2250K at a constant heating rate of 400 K/s, which indicates that an inclusion of 1 μm radius will not dissolve to 0.01 μm.

In Figure 4.7, CCT and TTT diagrams for the growth of several nitride and sulfide inclusions are displayed. In Figure 4.8, CHT diagrams and TTT diagrams for the dissolution of AlN inclusion are displayed. It is observed that the CCT and CHT diagrams for nitride and sulfide inclusions have the same characteristics with oxide inclusions.

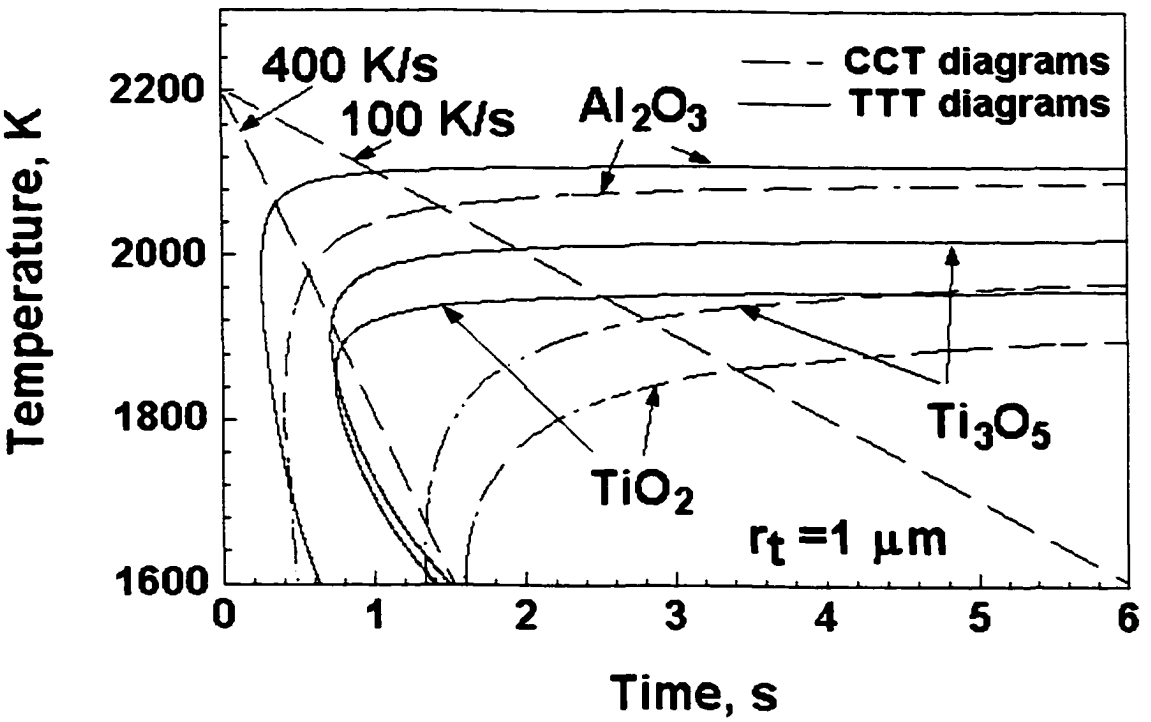

Figure 4.5. CCT and TTT diagrams for the growth of several oxide inclusions to the target radius of 1 μm in the liquid alloy which composition is shown in Table 3.6.

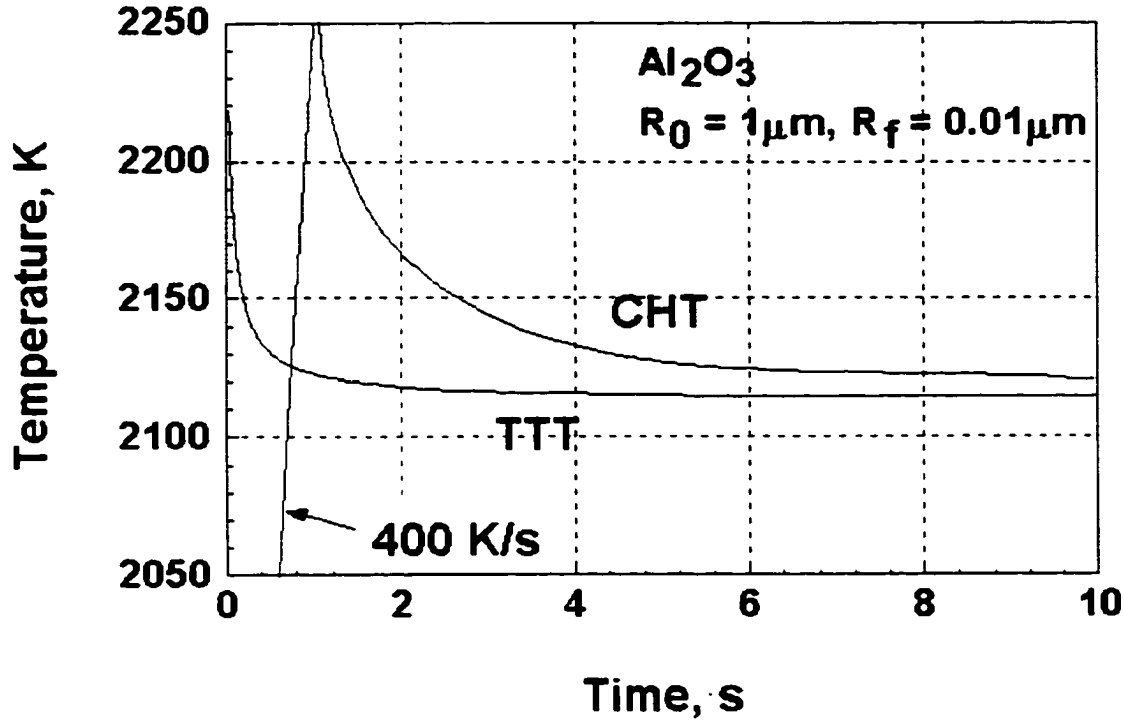

Figure 4.6. CHT and TTT diagrams for the dissolution of Al_2O_3 inclusions from the initial radius 1 μm to 0.01 μm in the liquid alloy which composition is shown in Table 3.6.

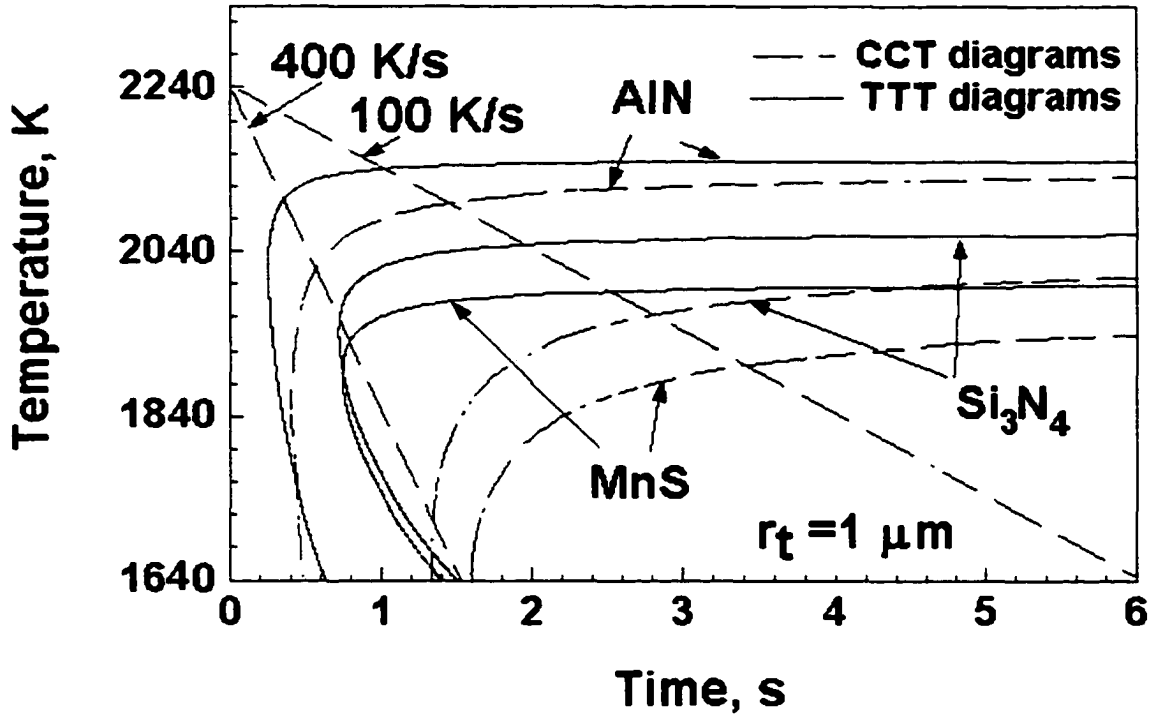

Figure 4.7. CCT and TTT diagrams for the growth of several nitride and sulfide to the target radius of 1 μm in the liquid alloy which composition is shown in Table 3.6.

4.4 Conclusions

The non-isothermal behavior of growth and dissolution of inclusion can be predicted from their isothermal growth behavior by constructing CCT diagrams for growth and CHT diagrams for dissolution from the corresponding TTT diagrams for the growth and dissolution of inclusions. This approach offers tool to better understand the effects of temperature and time on the growth and dissolution of inclusions in liquid steels under non-isothermal conditions.

Considering the element concentration change and competition among inclusions on element consumption rate, simultaneous nucleation and growth of different types of inclusions are modeled. The predicted number density and size distribution of inclusions show some common characteristics as experimentally observed results. Although this approach is very straightforward and need further development, it reflects more realistic situation of different types of inclusions in the weld pool.

References

1. M. Takahashi and H. K. D. H. Bhadeshia: *Mater. Trans., JIM*, **32**, 689 (1991)

2. Z. Yang: Modeling Weldment Macro and Microstructure from Fundamentals of Transport Phenomena and Phase Transformation Theory, Ph.D. thesis, The Pennsylvania State University (1999)

3. Z. Yang and T. DebRoy: *Metall. Trans. B*, **30B**, 483 (1999).

4. J. W. Christian: '*The Theory of Transformations in Metals and Alloys - Part I: Equilibrium and General Kinetic Theory*', 2nd ed., Pergamon Press, Oxford, 544-545, (1981).

5. E. Scheil: *Arch. Eisenhuttenwesen*, **12**, 565 (1935).

6. S. S. Babu, S. A. David, J. M. Vitek, K. Mundra, and T. DebRoy: *Mater. Sci. Tech.*, **11**, 186-199 (1995).

7. S. S. Babu, S. A. David, J. M. Vitek, K. Mundra, and T. DebRoy: *Sci. Tech. Weld. Join.*, **4**, 276-284 (1999).

CHAPTER 5

HEAT TRANSFER, FLUID FLOW AND PARTICLE TRACKING IN THE WELD POOL

Heat transfer and fluid flow in the weld pool contribute significantly not only to the development of weld metal properties,[1,2] but also to the geometry and internal fluid movement of the molten zone, which determine the thermal histories of inclusions in the weld pool.[3,4] To understand the heat transfer and fluid flow in the weld pool, mathematical modeling has been intensively used.[5-10] In the first section of this chapter, the details of a model developed at Penn State to study transport phenomena during welding are discussed. The comparison between calculated and experimentally measured weld pool geometry for different welding parameters is presented to verify the theoretical model. In the second section, particle tracking technique, which is used to calculate the motions and thermal gyrations of large number of inclusions based on the calculated temperature and velocity fields in the weld pool, is presented. The particle tracking results of thousands of inclusions are discussed.

5.1 Modeling Transport Phenomena in the Weld Pool

During fusion welding, the interaction between heat source and material leads to heating, melting, vigorous motion, cooling and solidification of the molten metal. The motion of molten metal in the weld pool is driven by forces such as buoyancy, surface tension (or Marangoni) force, electromagnetic (or Lorentz) force, and aerodynamic drag

force from the arc plasma[1]. It is well known that convection mode is the dominant mechanism of heat transfer and fluid flow, which determine the size and shape of the weld pool, the heating and cooling rate of material, and the kinetics of various solid state transformation reactions in the fusion zone and heat-affected zone[1,2] for most welding processes. Recent modeling efforts in understanding high temperature physical processes, such as growth and dissolution of inclusions in the molten pool[3,4] and compositional change due to vaporization at the weld pool surface[11-12], have to rely on the accurately calculated velocity and temperature fields in the weld pool. Therefore, a comprehensive understanding of the fluid flow and heat transfer in the weld pool is the starting point of studying other physical processes during welding.

Due to the small size of the weld pool and the extremely sharp temperature gradient, experimental study of the nature of fluid flow and measurement of temperatures in the weld pool are difficult, as discussed in Chapter 2. However, computational modeling of the fluid flow and heat transfer can help address some of these difficulties. Systematic and parametric analyses of the various driving forces over a wide range of operating conditions using mathematical modeling can achieve fundamental understanding of the interactive nature of the welding parameters. These calculations can provide detailed insight about welding processes that could not be achieved otherwise.

The concept of modeling fluid motion in weld pools was first proposed by Shercliff[6]. Since then, numerous papers had been published[7-14] dealing with various aspects of the problem. Normally, calculations of fluid flow and heat transfer in the weld pool are now performed through numerical solution of the equations of conservation of mass, heat, and momentum with a stationary heat source. In practice, the heat source moves with a certain constant velocity. The solution of the equations of conservation of mass, momentum, and energy in moving heat source system requires a large number of very fine grids for accurate representation of the heat source position and spatial variation of heat flux. During calculation, small time step is needed to ensure accuracy and stability of the solution. The computation becomes very CPU intensive. In the following section,

some advanced techniques are employed in the heat transfer and fluid flow model developed in Penn State to overcome the computational difficulties.

5.1.1 Governing Equations and Boundary Conditions of Laminar Model

5.1.1.1 Governing Equations and Driving Forces

In the heat transfer and fluid flow model developed at Penn State, the governing equations are formulated in a coordinate system attached to the heat source. Therefore, the system becomes a stationary heat source interacting with moving materials. The net velocity in the computational domain is divided into two parts: the convective velocity and the welding velocity. Convective velocity of the fluid is treated as the primary unknown velocity. The enthalpy-porosity technique is implemented for heat transfer modeling in the mushy zone. A control volume method described by Patankar[17] has been implemented for the discretization of governing equations. The SIMPLE algorithm is employed for the solution of the discretization equations[17]. The details are presented as follows.

The governing equations, which are the conservation equations of momentum, mass, and energy, are formulated in a coordinate system (ξ,y,z,t) attached to the moving heat source where:

$$\xi = x + vt \tag{5.1}$$

where v is the welding velocity, t is the time and x is the x-coordinate of initial heat source position. The schematic diagram of this model is shown in Figure 5.1. The conservation equations are formulated as below[17]:

Conservation of mass:

$$\nabla \cdot (\rho \bar{V}) = 0 \tag{5.2}$$

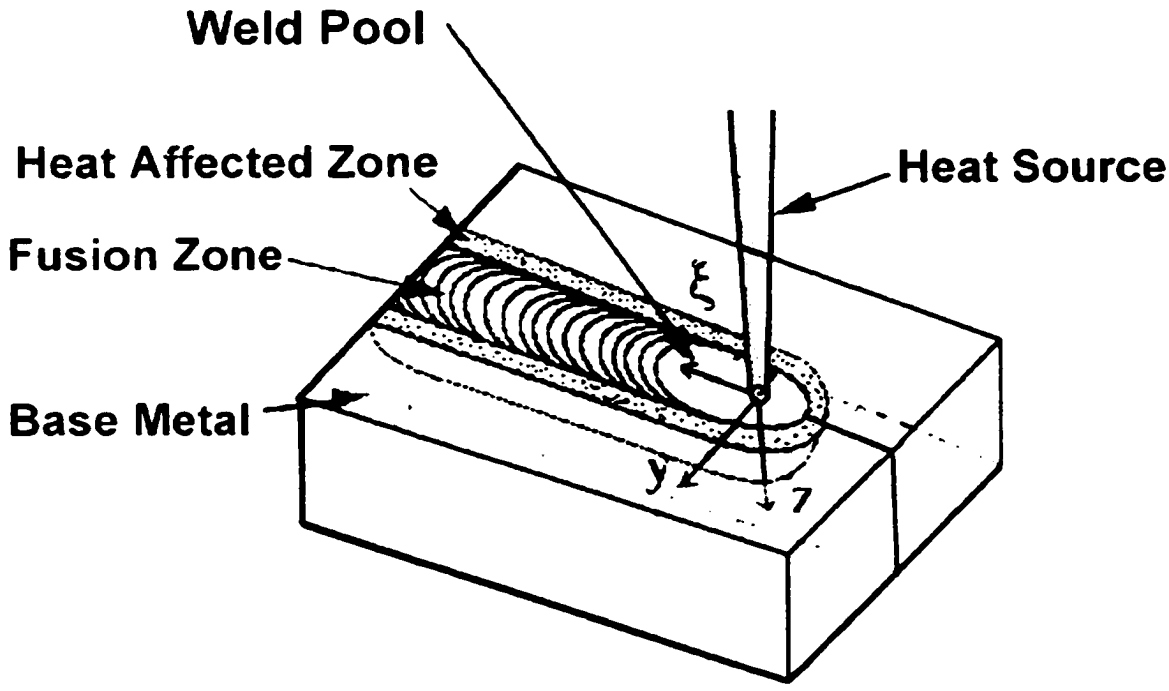

Figure 5.1 Schematic diagram of the 3D heat transfer and fluid flow model

Conservation of momentum:

$$\nabla \cdot (\rho \bar{V} \bar{V}) = -\nabla P + \nabla \cdot (\mu \nabla \bar{V}) + S_{e-p} + S_b - \nabla \cdot (\rho \bar{U} \bar{V}) \quad (5.3)$$

Conservation of energy:

$$\nabla \cdot (\rho \bar{V} h) = \nabla \cdot (\frac{k}{C_p} \nabla h) + S_l - \nabla \cdot (\rho \bar{U} h) \quad (5.4)$$

where V is the convective component of the velocity, U is the welding velocity, ρ is the density of weld metal, P is pressure, μ is the viscosity of liquid metal, S_{e-p}, S_b, S_l are different source terms, k is thermal conductivity, C_p is specific heat, and h is sensible enthalpy. The net velocity of fluid flow in the weld pool is subdivided into two parts, convective and welding velocities, as following:

$$\bar{V}' = \bar{V} + \bar{U} \quad (5.5)$$

In the solution of conservation equations, convective velocity V is treated as the primary unknown.

The temperature in the weldment is represented by the enthalpy. The total enthalpy of the material, H, is represented as a sum of sensible heat h and latent heat content ΔH:

$$H = h + \Delta H \quad (5.6)$$

where $h = \int C_p dT$ and ΔH is defined as 0 when the temperature is lower than the solidus temperature of weld metal, as L when the temperature is higher than the liquidus temperature, and as $f_l \times L$ in between where f_l is the liquid fraction at a given location. The schematic figure of this relation is shown in Figure 5.2. In solid zone, total enthalpy is equal to sensible enthalpy. Normally, the heat capacities of material in solid and liquid, $C_{p\text{-solid}}$ and $C_{p\text{-liquid}}$, are not significantly temperature dependent, i.e., the curves representing sensible enthalpy h are considered as straight lines. This approach makes the distinction between solid region, liquid region, and mushy zone.

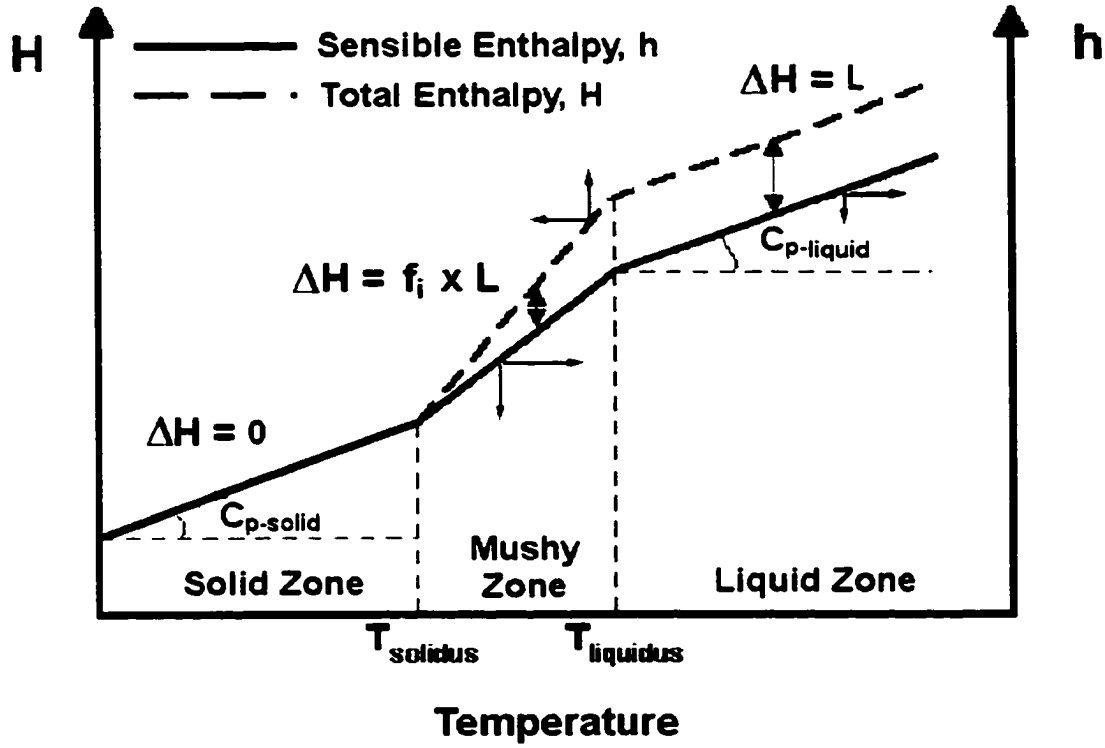

Figure 5.2 Schematic figure of the transformation method from enthalpy to temperature in conservation equation of energy, $H=h+\Delta H$, f_i is the volume fraction of liquid, $C_{p\text{-solid}}$ and $C_{p\text{-liquid}}$ are specific heat of base material in solid and liquid state.

The source terms in equation (5.3) represent different components of the driving forces of fluid flow. The buoyancy force, $\mathbf{F_b}$, is a convection effect caused by material density difference at various temperatures and is defined as[13]:

$$F_b = \rho g \beta (T - T_{ref}) \tag{5.7}$$

where ρ is the fluid density, g is the acceleration of gravity, β is the thermal expansion coefficient, and T_{ref} is an arbitrarily defined reference temperature.

The force due to Marangoni or surface tension convection is introduced in the momentum equations [equation (5.3)] of convective velocity **V** as boundary condition and will be discussed later.

When an electric arc is used as the power source, the interaction between the divergent current in the weld pool and the magnetic field it creates gives rise to electromagnetically driven fluid flow in the pool.[2,18] The vector of electromagnetic force, $\mathbf{F_e}$, is given by:

$$\mathbf{F_e} = \mathbf{J} \times \mathbf{B} \tag{5.8}$$

where **J** is the current density vector and **B** is the magnetic flux vector. The electromagnetic field in the workpiece is defined by the steady-state version of Maxwell's equations using MHD approximation.[2,18,19] The electromagnetic force is incorporated as part of the source term, S, defined in the governing equation (5.3) for the conservation of momentum.

5.1.1.2 Boundary Conditions

Boundary conditions contain two parts, velocity component and heat (temperature) component. Due to the symmetry of the weld pool geometry, only half the weld pool is considered in the following discussion. The symmetrical plane is the vertical plane of y = 0. Along the vertical symmetry plane, the boundary conditions of velocity components are defined as[17]:

$$\begin{cases} \dfrac{dV_x}{dy} = 0 \\ V_y = 0 \\ \dfrac{dV_z}{dy} = 0 \end{cases} \tag{5.11}$$

where V_x, V_y, and V_z are the components of the convective velocity **V** in the x, y, and z directions, respectively.

Along the top surface (z=0), the boundary conditions for the velocity components are determined by the Marangoni stress and are given by[17]:

$$\begin{cases} -\mu \dfrac{dV_x}{dz} = f_l \dfrac{d\gamma}{dT}\dfrac{dT}{dx} \\ -\mu \dfrac{dV_y}{dz} = f_l \dfrac{d\gamma}{dT}\dfrac{dT}{dy} \\ V_z = 0 \end{cases} \tag{5.12}$$

where μ is the viscosity, γ is surface tension, $d\gamma/dT$ is the temperature coefficient of surface tension and f_l is the liquid fraction at particular location. The symbol f_l represents the liquid fraction and it has a value of 0 in solid region, 1 in liquid region and in between in mushy zone. The velocity components at the surface of solid region are set to be zero. At other surfaces of the weldment, there is no velocity component of the boundary condition.

The heat component of boundary conditions on the top surface is defined as the heat exchange between the heat source and metal surface, and heat fluxes on the top surface[17]:

$$J(\xi,y,z)_{z=0} = \frac{Q\eta}{2\pi r_b^2} e^{-\frac{\xi^2+y^2}{2r_b^2}} - \varepsilon_l \sigma (T(\xi,y,z)^4 - T_a^4) - h_c (T(\xi,y,z) - T_a) \tag{5.13}$$

where J is the heat flux at position (ξ,y,z) on the top surface (z=0), Q is the power density of heat source, η is energy absorption efficiency, r_b is the radius of heat source, T is the

temperature at (ξ,y,z), ε_l is the emissivity, σ is the Stefan-Boltzmann constant, h_c is the convective heat transfer coefficient, and T_a is ambient temperature. The first term in the right side of equation (5.13) is heat source with Gaussian energy distribution, the second term represents radioactive heat loss, and the third term is convective heat transfer loss.

At the symmetry plane (y=0), the gradients of the temperature or enthalpy are defined as zero. At other surfaces of the weldment, the temperatures are assumed as the ambient temperature. The schematic diagram for boundary conditions of velocity and temperature components at all surfaces is shown in Figure 5.3.

Solving the conservation equations of mass, energy and momentum with the boundary conditions discussed above generates the temperature and velocity fields in the weld pool. The information provides us profound insight of transport phenomena during welding and is the base of every further study in this thesis. The equations are solved using COMPACT-3D, a finite difference based commercial software package. The details of the solution procedure are discussed later.

5.1.2 K-ε Turbulent Model

The governing equations and boundary conditions described above assume laminar flow in the weld pool. However, presence of turbulence in the fluid flow within the weld pool can provide a significant enhancement to the mass transport properties, and in turn affects the heat transfer mechanism. The role of turbulence on enhancing the heat transfer and fluid flow in the weld pool has been examined by previous researchers using mathematical simulation approaches.[20-23] Among all the mathematical tools of modeling turbulent flow, K-ε model is a simple, effective, and common used model. The effects of turbulence are considered using the concepts of effective viscosity and effective thermal conductivity, which are expressed by:

$$\mu_{eff} = \mu_t + \mu \tag{5.14}$$

$$k_{eff} = k_t + k \tag{5.15}$$

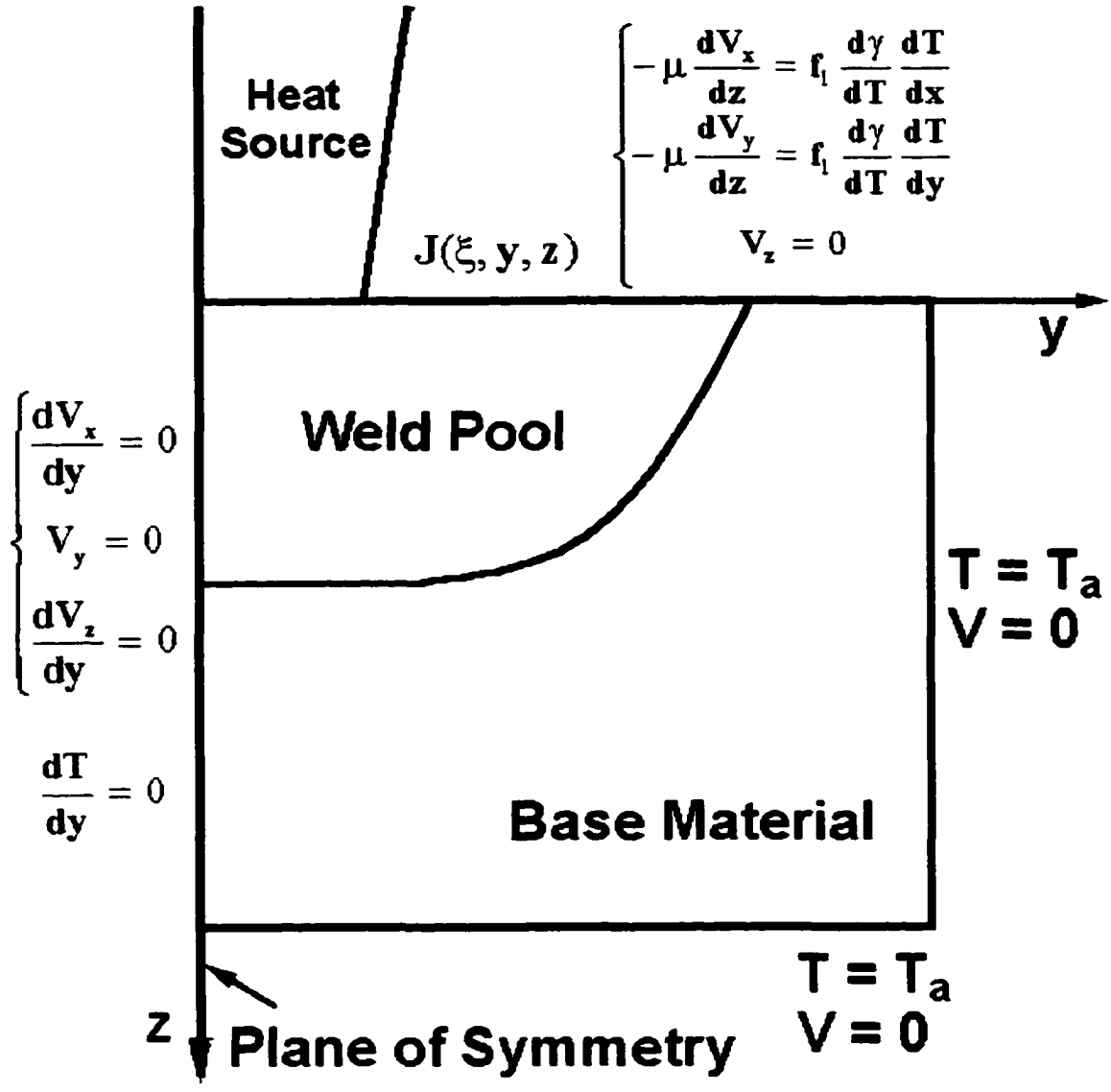

Figure 5.3 Schematic diagram of the boundary conditions used in the heat transfer and fluid flow calculation in the weld pool.

where μ_{eff} and k_{eff} are the effective viscosity and thermal conductivity, respectively, μ and k are the molecular values, and μ_t and k_t are the turbulent values. Turbulent viscosity μ_t can be calculated by[20]:

$$\mu_t = \frac{C_\eta \rho K^2}{\varepsilon} \tag{5.16}$$

where C_η is an empirical constant, K is the turbulent kinetic energy, ρ is the material density, and ε is the dissipation rate of turbulent kinetic energy. The values of K and ε are obtained through the solution to their respective conservation equations:

Conservation of K

$$\rho\frac{dK}{dt} = \frac{1}{\sigma_k}\left[\frac{\partial}{\partial x}\left(\mu_t\frac{\partial K}{\partial x}\right)+\frac{\partial}{\partial y}\left(\mu_t\frac{\partial K}{\partial y}\right)+\frac{\partial}{\partial z}\left(\mu_t\frac{\partial K}{\partial z}\right)\right]+\mu_t G_k-\rho\varepsilon \tag{5.17}$$

Conservation of ε

$$\rho\frac{d\varepsilon}{dt} = \frac{1}{\sigma_\varepsilon}\left[\frac{\partial}{\partial x}\left(\mu_t\frac{\partial \varepsilon}{\partial x}\right)+\frac{\partial}{\partial y}\left(\mu_t\frac{\partial \varepsilon}{\partial y}\right)+\frac{\partial}{\partial z}\left(\mu_t\frac{\partial \varepsilon}{\partial z}\right)\right]+\frac{\varepsilon}{K}(c_1 G_k - c_2\rho\varepsilon) \tag{5.18}$$

where σ_k, σ_ε, c_1, and c_2 are constants, and G_k is defined as:

$$G_k = 2\left[\left(\frac{\partial \overline{v_x}}{\partial x}\right)^2+\left(\frac{\partial \overline{v_y}}{\partial y}\right)^2+\left(\frac{\partial \overline{v_z}}{\partial z}\right)^2\right]+\left[\left(\frac{\partial \overline{v_x}}{\partial y}+\frac{\partial \overline{v_y}}{\partial x}\right)^2+\left(\frac{\partial \overline{v_x}}{\partial z}+\frac{\partial \overline{v_z}}{\partial x}\right)^2+\left(\frac{\partial \overline{v_z}}{\partial y}+\frac{\partial \overline{v_y}}{\partial z}\right)^2\right] \tag{5.19}$$

The standard boundary conditions for conservation of mass, momentum, and energy have been discussed in the previous section. Only the boundary conditions for conservation of K and ε will be defined here. The first type of boundary condition is at the plane of symmetry. This type of boundary condition for K and ε can be shown as[21]:

$$\frac{\partial K}{\partial y} = 0 \quad \text{and} \quad \frac{\partial \varepsilon}{\partial y} = 0 \tag{5.20}$$

The second type of boundary condition is for the free shear flow on the surface of the weld pool. Using the approach of Pun and Spalding[22], the turbulent kinetic energy K on the free surface is assigned to be 5 percent of the mean kinetic energy in the present formulation. The value of ε on the free surface is determined by:

$$\varepsilon = \frac{K^{3/2}}{fL} \tag{5.21}$$

where f is constant (= 0.3) and L is the characteristic length of the weld pool.The third type of boundary is the no-slip solid-liquid interface. At the interface, the values of K and ε are forced to be zero by assigning a very large viscosity.

Turbulent thermal conductivity, k_t, is related to the turbulent viscosity, μ_t, by turbulent Prandtl number, Pr_t:

$$Pr_t = \frac{C_p \mu_t}{k_t} \tag{5.22}$$

where C_p is the specific heat of the base metal in liquid state. Previous researches estimated the value of turbulent Prandtl number to be 0.9 for liquid steel in the weld pool. Table 5.1 presents some turbulent values with the other thermophysical properties used in the calculations.

Table 5.1 Thermophysical properties used in the calculations (Low alloy steel)

Specific heat in solid	0.168 Cal/g.K
Specific heat in liquid	0.193 Cal/g.K
Molecular viscosity	0.06 g/cm.s
Molecular thermal conductivity of solid	0.05 Cal/cm.s.K
Molecular thermal conductivity of liquid	0.2 Cal/cm.s.K

Palmer[21] considered the effect of turbulence on the transport of nitrogen in the weld pool. The existence of turbulence further enhances the mixing and transport of nitrogen in the weld pool. An enhancement factor is applied to the diffusion coefficient of nitrogen in liquid iron to consider the enhanced mass transport of nitrogen in the weld pool by turbulent flow.

5.1.3. Solution Procedure of Governing Equations

A control-volume-based computational method[23] has been used in this research to solve the governing equations. The governing equations are represented in a finite difference form and solved iteratively. The Semi-Implicit Method for Pressure-Linked Equations (SIMPLE) algorithm[17] has been employed for the discretization of the equations. Commercial software package of finite difference solution, COMPACT-3D™ from Innovative Research Inc., has been used to solve the discretized governing equations[24]. COMPACT-3D is a general-purpose program for the calculation of fluid flow, heat and mass transfer, chemical reaction, turbulence, and related processes in three-dimensional situations. In order to solve each of these different conditions, the program utilizes the solution of a generalized equation which is shown below:[24]

$$\frac{\partial}{\partial t}(\rho\phi) + \frac{\partial}{\partial x_i}(\rho u_i \phi) = \frac{\partial}{\partial x_i}\left(\Gamma \frac{\partial}{\partial x_i}\right) + S \qquad (5.23)$$

where ρ is the density, ϕ is the dependent variable to be solved, Γ is considered as the diffusion coefficient, u_i is the velocity term, x_i is the i^{th} coordinator in the calculation domain (x,y,z in three dimension situation), and S is the source term. The general equation contains basically four terms: the unsteady term, the convection term, the diffusion term, and the source term. The dependent variable ϕ can stand for a variety of physical quantities, and the choice of ϕ gives appropriate meaning to both Γ and S. In order to solve specific situations, such as heat transfer and fluid flow in the weld pool, a separate adaptation scheme has been developed.

In the development of the governing equations tailored for this adaptation, the value of Γ can be defined individually for the conservation equations of momentum, energy, and mass, respectively, using the following equations:

$\Gamma = \nu$ for conservation of momentum (5.24)

$\Gamma = \frac{K}{C_p}$ for conservation of energy (5.25)

$\Gamma = \rho D$ for conservation of mass (5.26)

where υ is the viscosity of the liquid metal, K is the thermal conductivity, C_p is the specific heat, ρ is the density, and D is the diffusivity. Table 5.2 lists the thermophysical properties used in these calculations.[23-25]

Table 5.2. Summary of the thermophysical properties used in the calculations described here.[22-25]

Material Property	**Value**
Density of Liquid Metal (gm/cm^3)	7.20
Liquidus Temperature (K)	1811
Solidus Temperature (K)	1811
Viscosity of Liquid (gm/cm-sec)	0.06
Thermal Conductivity of Solid Iron (cal/cm-sec-K)	0.05
Thermal Conductivity of Liquid Iron (cal/cm-sec-K)	0.2
Specific Heat of Solid Iron (cal/gm-K)	0.168
Specific Heat of Liquid Iron (cal/gm-K)	0.193
Enthalpy of Solid Iron at Melting Point (cal/gm)	250.76
Enthalpy of Liquid Iron at Melting Point (cal/gm)	314.76
Temperature Coefficient of Surface Tension (dynes/cm K)	-0.43
Coefficient of Thermal Expansion (1/K)	1×10^{-5}

Figure 5.4 shows a schematic diagram of the components of the grid system used in the solution scheme. Locations for the solution of scalar quantities and the velocity components are specifically defined in the figure. The velocity components are solved at the center of each control volume, defined by the locations of the solution of the scalar quantities at each corner. In order to solve for these specific conditions, the thermophysical properties for desired alloy are placed in the adaptation routine of COMPACT 3-D.

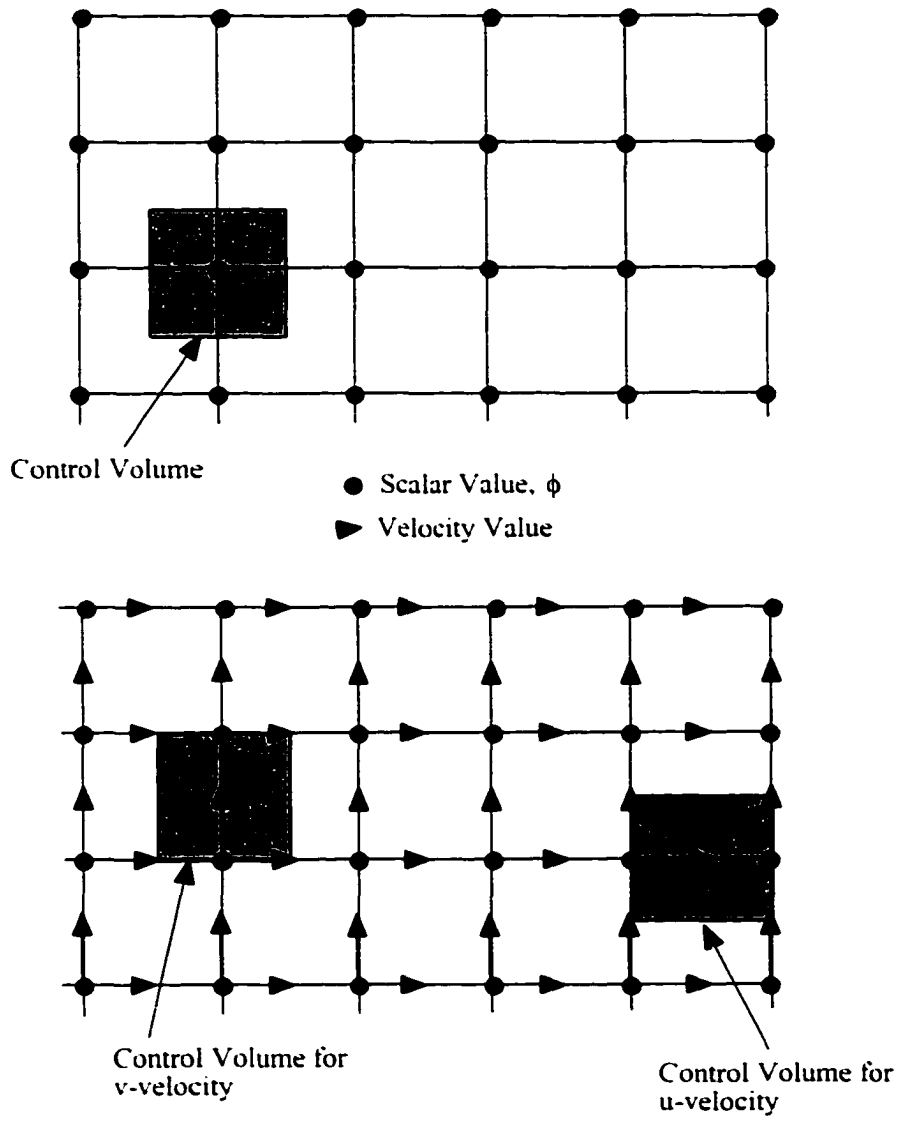

Figure 5.4. Schematic diagram of grid scheme used in the calculations.

A non-uniform grid system has been used in this calculation scheme to account for the large temperature gradients commonly present in welding operations. Most calculations in the thesis are in a non-uniform grid system which has 56 grids in the x direction, 28 grids in the y direction, and 28 grids in the z direction (please see the Appendix II for calculation details). This grid system allows for finer grids to be used in the region under the heat source and to become coarser in other regions. Using this grid system, the enthalpies and velocities at all grid points (refer to Figure 5.4) are solved to get the temperature and velocity fields in the weld pool.

In arc welding, the weld pool geometry reaches steady-state conditions in a very short time after the start of welding. This condition allows the transient terms of the governing equations to be removed and only the steady state versions of the governing equations to be solved.

5.1.4 Calculated Results of Temperature and Velocity Fields

Figure 5.5 shows one typical example of the calculated temperature and velocity fields in the weld pool of GTA welding. To clearly show the features of calculated temperature and velocity fields, the results are interpolated in a uniform grid system. The welding voltage is 527 V and current is 27 A. The welding speed is 12.7 mm/s. The calculated maximum cross-sectional area is shown in Figure 5.6(a) and the calculated temperatures and velocities along the symmetric plane (y=0 plane) are shown in Figure 5.6(b). It is observed that the velocities in the weld pool are radically outward, i.e., the fluid flows away from the heat source towards the periphery of the weld pool. The

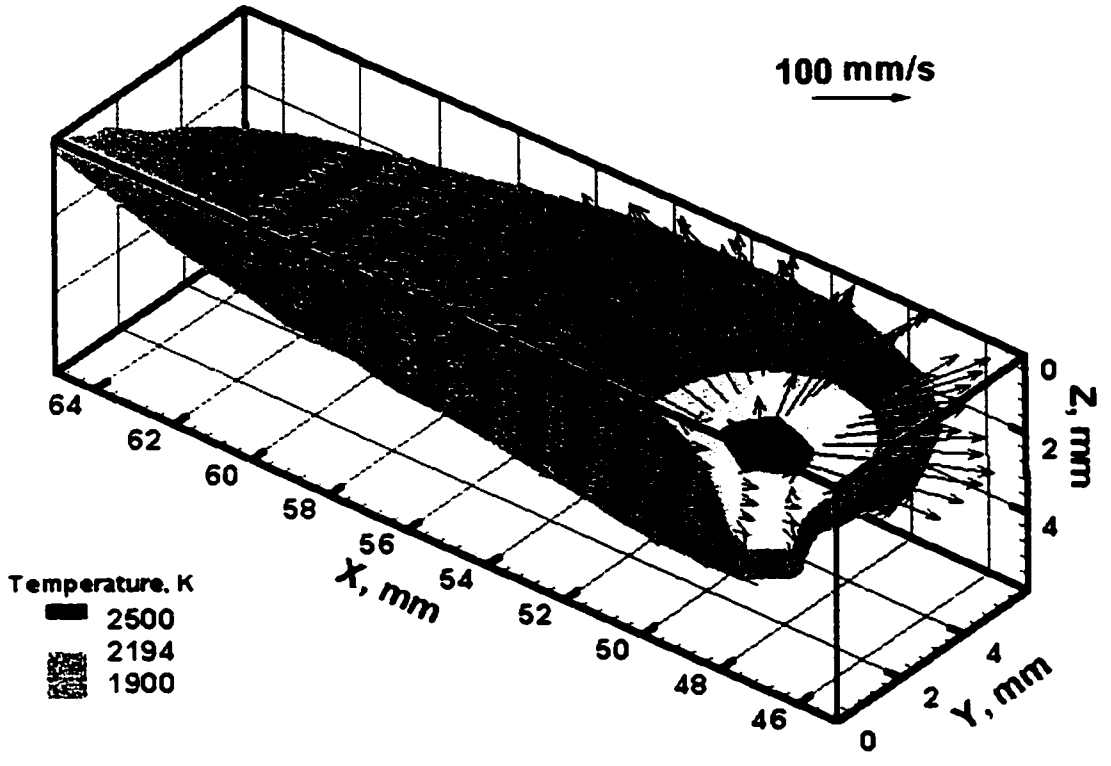

Figure 5.5 Calculated temperature and velocity fields in the weld pool. GTA welding parameters: curent = 590 A, ampere = 27 V, welding speed = 12.7 mm/s. Low alloy steel which composition is shown in Table 3.6.

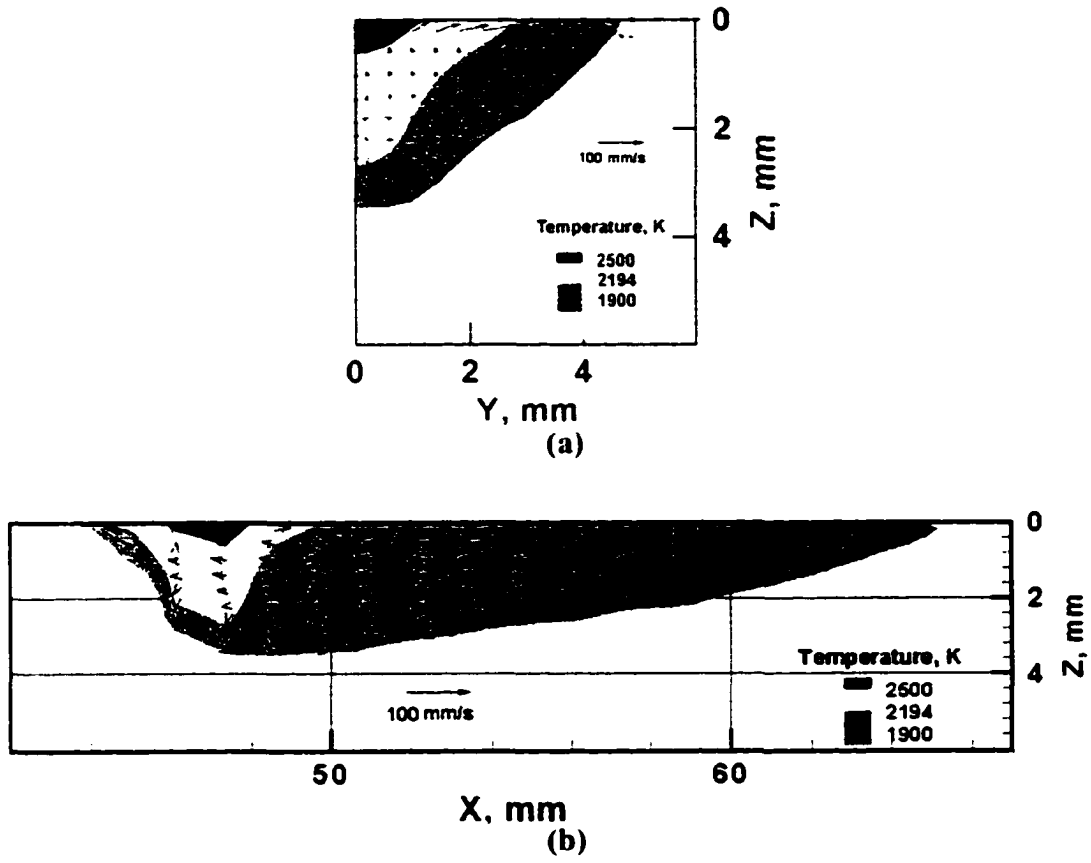

Figure 5.6 (a) Calculated temperature and velocity fields, cross-sectional area at x-axis (b) Temperature and velocity fields of the symmetric plane. GTA welding parameters: current = 590 A, voltage = 27 V, welding speed = 12.7 mm/s. Low alloy steel which composition is shown in Table 3.6.

temperatures are higher near the heat source and decrease rapidly away from this region. Figure 5.5 also indicates higher temperature gradients ahead of the heat source than the temperature gradients behind it. Since the spatial temperature gradient determines the Marangoni stress, which is the major driving force for the circulation of liquid metal in the weld pool, the velocities ahead of the heat source are higher than the velocities behind it. The weld pool shape obtained from the temperature field shows a typical elongated profile. Mundra did a comparison between the calculated and experimentally measured cross-section areas of the laser weld pools of AISI 201 steel. It is observed that they were in good agreement[27] with the corresponding experimental data as shown in Figure 5.7. The agreement indicates appropriateness of the calculation procedure. The calculated temperature and velocity fields in the weld pool provide the basic information to study inclusion growth and dissolution in the weld pool considering the recirculatory motion and temperature excursion experiences of inclusions.

Turbulent effects are considered in the calculations using the K-ε model discussed in the previous section. Figure 5.8 shows the ratio of the effective viscosity to the molecular viscosity, μ_{eff}/μ, at different locations of the cross-section of the weld pool. Table 5.3 gives a comparison of the calculated peak temperatures, cross section areas, and weld pool lengths between using laminar and K-ε turbulent model. The material properties and welding parameters are the same as those used in the calculation of Figure 5.5. It is very clear that turbulent model enhances fluid flow and heat transfer in the weld pool, as the consequence, the cross section area and weld pool depth increase, and the peak temperature decrease while turbulent model is employed.

Table 5.3 Comparison of calculated results of weld pool characteristics by laminar and turbulent model

Model	Peak Temperature	Cross Section Area	Weld Pool Length	Weld Pool Depth
Laminar	3215 K	2.12 mm^2	4.12mm	0.74mm
Turbulent	2109 K	2.43 mm^2	5.23mm	0.89mm

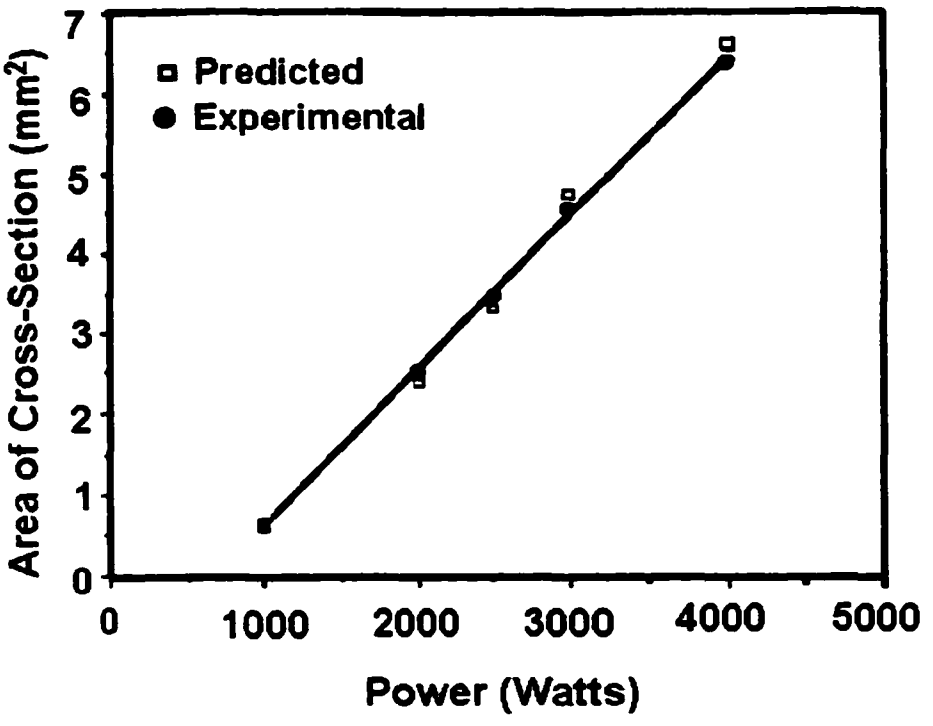

Figure 5.7 Comparison of calculated and experimentally determined cross section area of weld pool.[27] AINI 201 steel. Laser welding with welding speed of 15.24 mm/s. The laser beam radius and absorption coefficient are adjusted for different laser power.

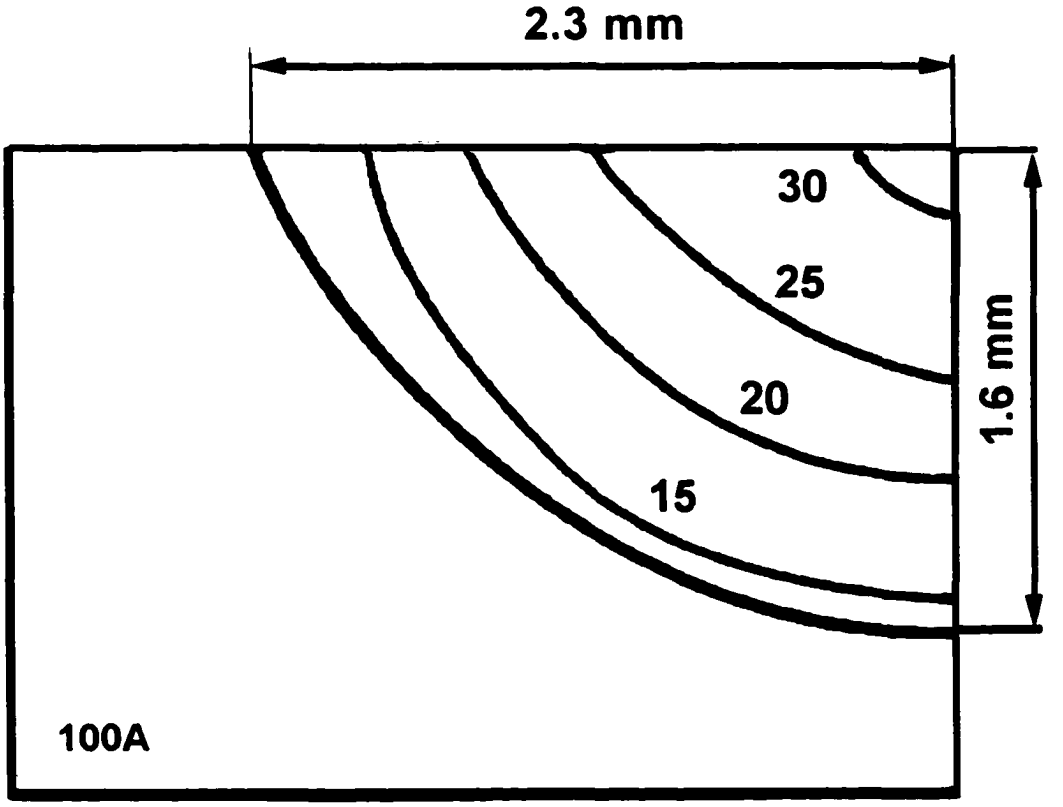

Figure 5.8 Enhanced effective viscosities in K-ε turbulent model. The values of the contour lines are the ratios of the effective viscosity to the molecular viscosity, μ_{eff}/μ. Low alloy steel which composition is shown in Table 3.6. Welding parameters used in the calculation: GTA welding, current = 590 A, voltage = 27 V, welding speed = 12.7 mm/s.

5.2 Motions, Gyrations and Thermal Cycles of Inclusions in the Weld Pool

5.2.1 Particle Tracking in the Weld Pool

Inside the weld pool, molten liquid undergoes vigorous circulation resulting from buoyancy, surface tension, and electromagnetic forces. Since the fluid flow in the weld pool is recirculatory in nature, an inclusion grows or dissolves while in a state of varying motion, experiencing thermal excursions within the weld pool during its entire life-cycle after the nucleus is formed. At any given instant, its velocity and temperature depend on the velocity and temperature fields prevailing in the weld pool. While the nucleation of inclusions can occur at various regions of the weld pool, the welding variables and the material chemistry of the work-piece determine the size and shape of the weld pool and the temperature and velocity fields. In the recent past, significant advances have been made in the calculation of fluid flow and heat transfer in the weld pool and these calculations can provide significant insight about the welding process that cannot be achieved otherwise. However, very little effort has been made to combine these new powerful capabilities to understand inclusion behavior in the weld pool.

Meaningful tracking of the temperatures and velocities of thousands of inclusion particles as they move through regions in the weld pool is an arduous task even with the help of powerful computers. Motivation for undertaking such calculations arises from the fact that the growth and dissolution rates of individual inclusion particle are determined by its temperature excursion and residence time at various temperatures. In order to understand the effects of welding variables and weld metal composition on growth and dissolution behaviors of inclusions from fundamentals, thermal histories and gyrations of a large number of inclusions must be understood for each welding condition. In this thesis, inclusion growth and dissolution in a low alloy steel weld pool are studied considering their path, temperature history, velocities, and element diffusion kinetics.

A calculation procedure, named "particle tracking", was developed to trace trajectories of inclusion particles during their transport within the weld pool iteratively. The time step of each iteration was calculated in an adaptive way. A submerged inclusion moves forced by buoyancy, drag and inertia forces. A massless particle which is solely driven by the drag force would theoretically follow a streamline in the velocity field of the weld pool. In contrast to that, a particle with nonzero mass will not exactly follow a streamline, but will be accelerated by a net force, which consists of the particle's inertia and drag force. Pitschneder et al[23,28] investigated the relative importance of different driving forces on particle motion. They concluded that the buoyancy force and inertia force have smaller effect on particle motion compared to the drag force for normal weld pool conditions.[23] Only when the particle's radius is bigger than 1 mm, the inertia and buoyancy forces are detectable. The regular size of inclusions in the weld metal is in the range of tenth of micron to tens of micron, therefore, the buoyancy and inertia force acting on the particle are neglected for simplicity in this thesis[23]. The particles considered are assumed massless. The position and velocity at every time step can be calculated by following equations:

$$\mathbf{r}_{i-1} = \mathbf{r}_i + \mathbf{v}_i \cdot \Delta \mathbf{t}_i \tag{5.27}$$

$$\mathbf{v}_i = \mathbf{v}(\mathbf{r}_i) \tag{5.28}$$

where $\mathbf{r}_{i-1}$ is the vector of new location, $\mathbf{r}_i$ is the vector of old location, $\mathbf{v}_i$ is the velocity at the old location and Δt_i is the adaptive time-step. For each time step, we can obtain the new location from the location at previous time step and the corresponding temperature history.

The derivation of inclusion path with respect to time depends on the local fluid velocity. A "predictor-corrector algorithm"[28] is used to solve the initial value problem. The Adams-Bashforth formula[28] is used to predict the inclusion location at the next time step, and then an Adams-Moulton formula is used to correct the predicted value[28]. The four-step Adams-Bashforth formula is used to predict the approximate solution in the inclusion tracking calculation:

$$\bar{r}(t_{i-1}) = \bar{r}(t_i) + \frac{h_i}{24}(55\bar{v}(t_i, \bar{r}_i) - 59\bar{v}(t_{i-1}, \bar{r}_{i-1}) + 37\bar{v}(t_{i-2}, \bar{r}_{i-2}) - 9\bar{v}(t_{i-3}, \bar{r}_{i-3}))(5.29)$$

where t_i is the time at the i-th time step, r_i is the location of inclusion at the i-th time step, $\bar{v}(t_i, \bar{r}_i)$ is the velocity of inclusion in i-th time step and at $\bar{r}_i$ location, and h_i is the time gap in the i-th time step. Then use the three-step Adams-Moulton algorithm to correct the predicted value with the $r(t_{i-1})$ we get from equation. (5.30):

$$\bar{r}(t_{i-1}) = \bar{r}(t_i) + \frac{h_i}{24}(9\bar{v}(t_{i-1}, \bar{r}_{i-1}) + 19\bar{v}(t_i, \bar{r}_i) - 5\bar{v}(t_{i-1}, \bar{r}_{i-1}) + \bar{v}(t_{i-2}, \bar{r}_{i-2})) \qquad (5.30)$$

The time gap of each time step is determined in a adaptive way when the global error is found to be too big or too small. Because the solution has to be known at 4 preceding mesh points to calculate a solution at the next mesh point, the classical 4^{th}-order Runge-Kutta algorithm (one step algorithm) has been employed for the first 3 steps calculation.

Figures 5.9 and 5.10 show 2 typical inclusion gyrations in the weld pool. Their thermal cycles are presented in Figure 5.11(a) and (b), respectively. The first inclusion whose thermal history are shown in Figure 5.11(a) experiences many temperature peaks in the weld pool and undergoes vigorous circulation. The other inclusion only experiences a continuous cooling behavior within the liquid alloy. It is also observed that although the one with continuous cooling history undergoes much shorter gyration than the one with many temperature peaks, their residence times in the weld pool do not vary significantly, which implies that the inclusion with many temperature peaks move very fast in the weld pool.

5.2.2 Evaluation of Particle Tracking Calculation

The thermal history of a movable particle in the weld pool is controlled by its trajectory through the temperature field of the pool. In order to obtain a basic understanding of the thermal history of solid particles - such as inclusions in the weld

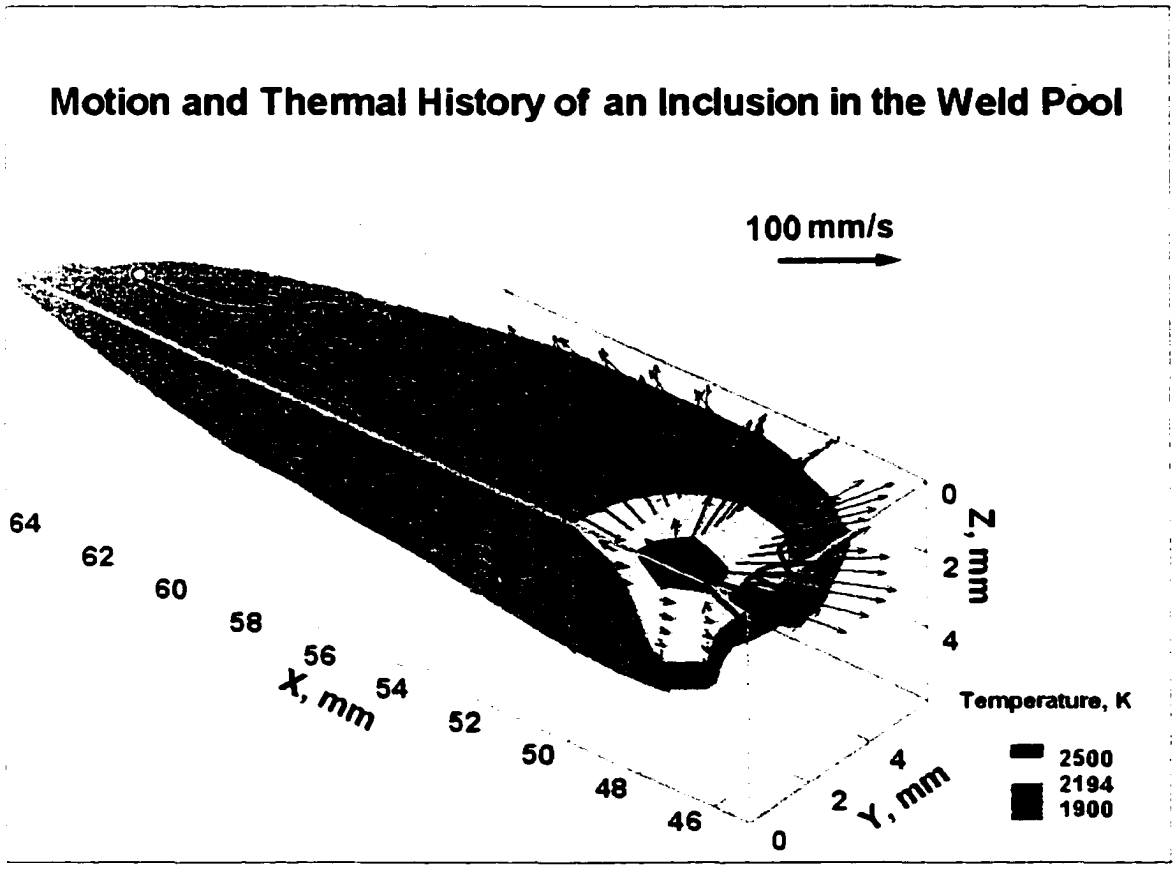

Figure 5.9 Temperature and velocity fields in the weld pool and a typical inclusion locus. Welding parameters: GTA welding, current = 590 A, voltage = 27 V, welding speed = 12.7 mm/s. Low alloy steel which composition is shown in Table 3.6.

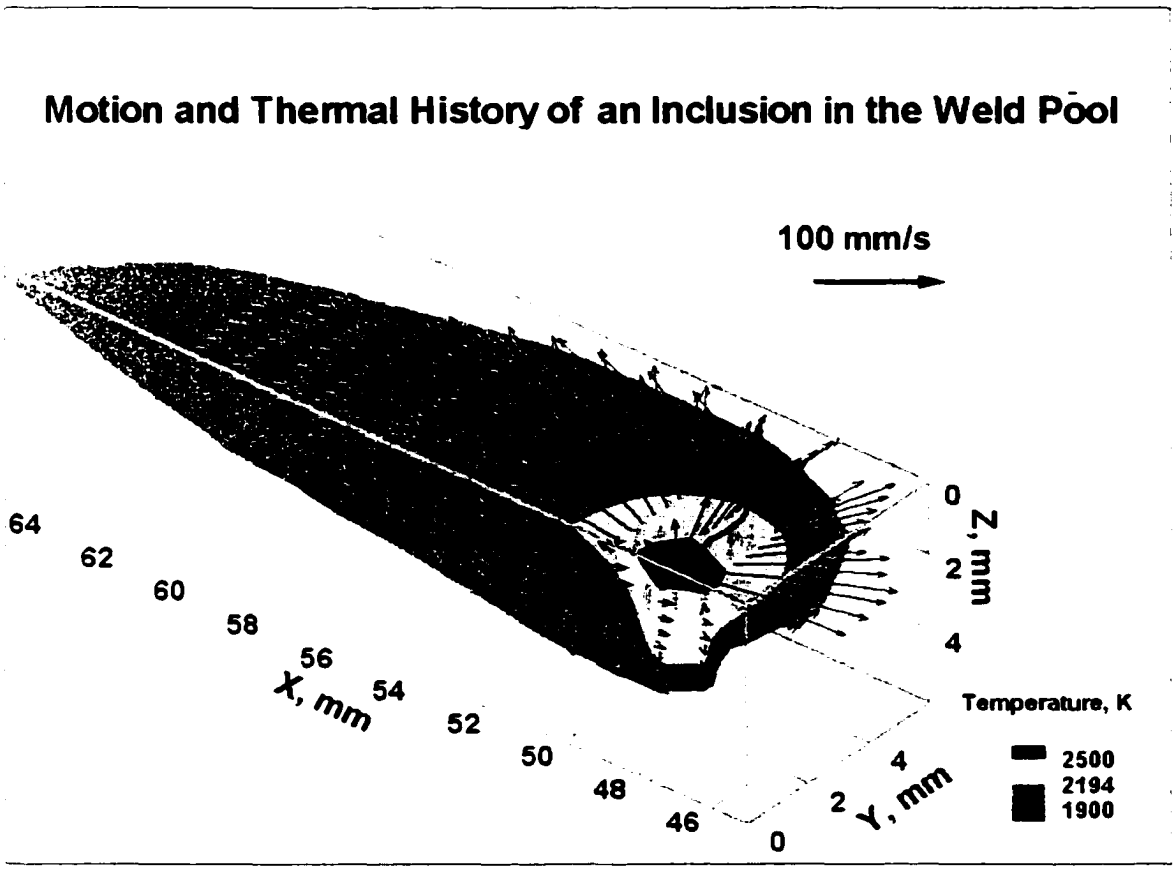

Figure 5.10 Temperature and velocity fields in the weld pool and an inclusion loci with continuous cooling behavior. Welding parameters: GTA welding, current = 590 A, voltage = 27 V, welding speed = 12.7 mm/s. Low alloy steel which composition is shown in Table 3.6

pool, particle trajectories through the weld pool are numerically calculated. The trajectories are calculated from velocity fields, which are obtained from numerical calculations of weld pool heat and fluid flow.

In order to investigate the structure of streamtraces and thermal histories in a systematic way, a well-defined evaluation of the streamtrace data is required. The thermal histories of particles in the weld pool are often oscillatory in nature, and feature a sequence of several local maxima and minima. Therefore, we attempt to characterize the thermal history of a particle by statistical evaluation of data, which characterize the subsequent heating and cooling cycles. For example, we can determine the average cooling rate for each cooling cycle in a thermal history. From the cooling rates of all cycles we can then calculate the mean value and standard deviation. The same procedure may be applied to a number of variables, which characterize a heating or cooling cycle. Examples of such variables are maximum and minimum temperature, the duration of a cycle, and temperature peak number so on. These evaluation can be applied to thousands of inclusions and obtain some meaningful statistic nature of inclusions in the weld pool

5.2.3 Calculated Thermal Cycles of Inclusions in the Weld Pool

In this subsection, the details of how to calculate the thermal history of thousand of inclusion in the weld pool are described. After the temperature and velocity fields are calculated and the results are stored in a non-uniform grid system, which is finer near the heat source and coarser along the edge of workpiece, the calculated results are interpolated into a uniform grid. The detailed procedures are presented in the documentation of the source code in Appendix. Thousands of particles are assumed to nucleate evenly distributed in the uniform grid system at every grid point of the calculation domain. Particle tracking calculations are applied to the assumed particles and their trajectories and corresponding thermal cycles are calculated. Figure 5.12 (a) –(c) shows some statistical properties of the calculated trajectories and thermal cycles of more than 7600 particles through the melted region. It is observed that the residence time for

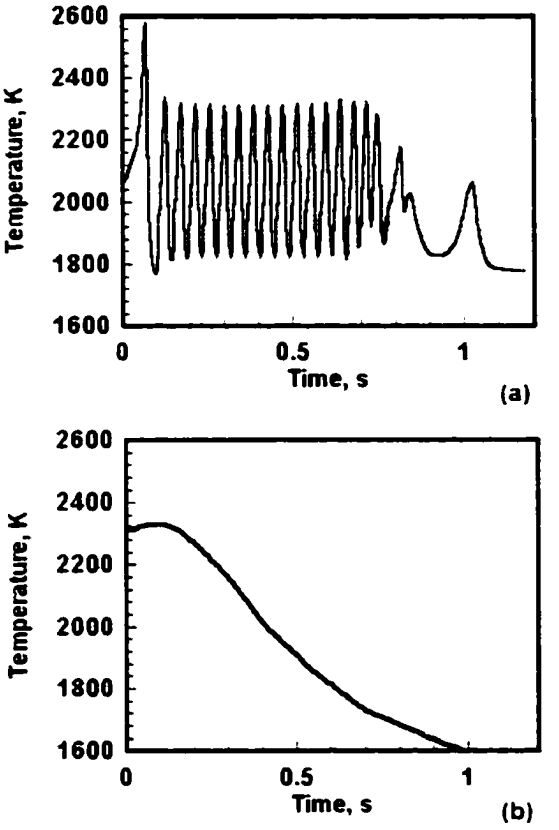

Figure 5.11 Two thermal cycles of inclusions experienced in the weld pool shown in (a) Figure 5.9 and (b) Figure 5.10. Welding parameters: GTA welding, current = 590 A, voltage = 27 V, welding speed = 12.7 mm/s. Low alloy steel which composition is shown in Table 3.6.

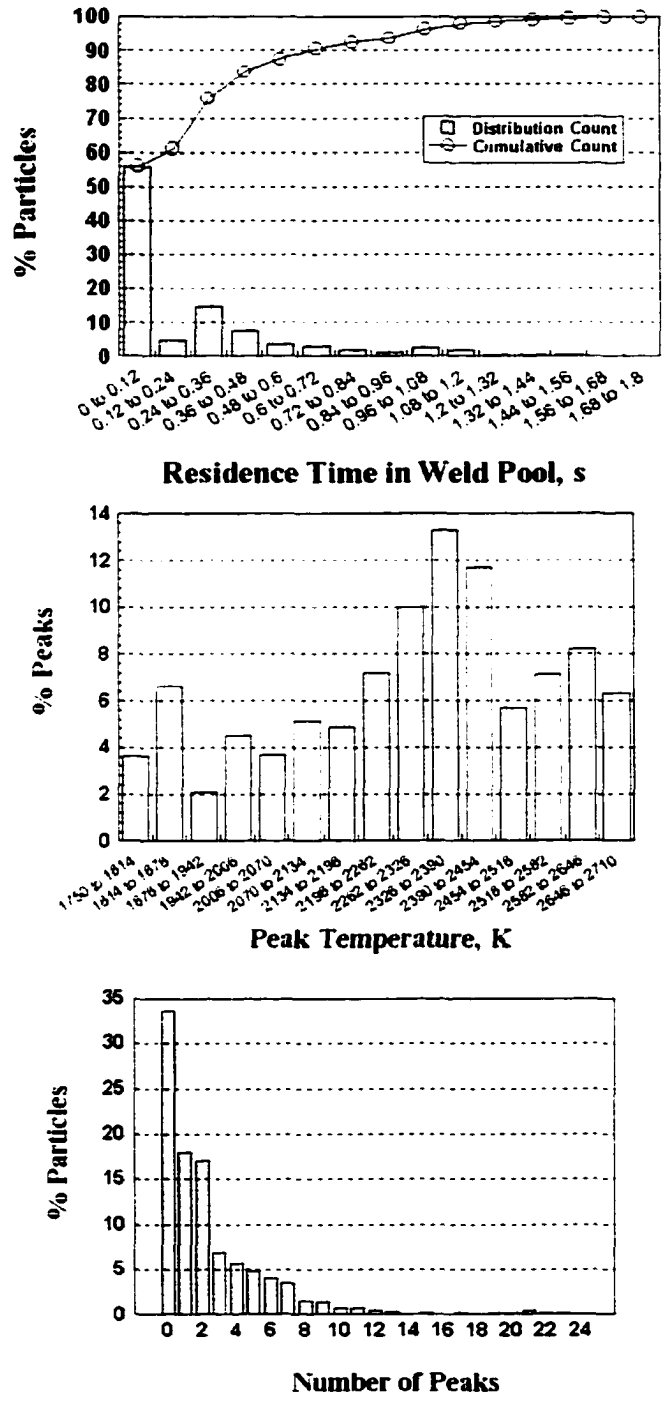

Figure 5.12 (a) Distribution of residence time, (b) distribution of peak temperature, and (c) distribution of peak number of thermal cycles of thousands of inclusions in the weld pool. Welding parameter used in the calculation: Parameter 1 in Table 5.4. The material composition is shown in Table 3.6.

most inclusions are shorter than 0.5s. Most inclusions experience temperature higher than its melting point (for Al_2O_3, 2043 K, for TiO_2, 2340K) in the weld pool. Therefore, the effect of dissolution cannot be ignored. It is also observed from Figure 5.12 (c) that about 1/3 of the inclusions experience continuous cooling behavior without any temperature peaks while the rest experience at least one temperature peak. Some even have tens of thermal cycles in their lifetime.

To investigate the effect of different welding parameters on the inclusion behavior in the weld pool, another set of statistic properties of particle trajectories calculated from the same scheme shown above are presented in Figure 5.13. The welding parameters are listed in Table 5.4. The material properties are assumed to be the same. Comparing Figures 5.12 and 5.13, it is observed that welding parameters have great effects on the inclusion behavior. Generally speaking, the more heat input, the bigger weld pool and vigorous circulation of liquid in the weld pool. Therefore, the inclusions in the weld pool experience longer floating time and more complex thermal history. The difference of final inclusion size between the two sets of welding parameters will be shown in the following discussion.

Table 5.4 Two sets of welding parameters in the calculation of Figures 5.12 and 5.13

	Parameter 1	Parameter 2
Voltage (V)	27	27
Current (A)	590	590
Welding Speed (mm/s)	6.35	12.7

Along the temperature cycles of the residence time in the weld pool, inclusions experience both growth and dissolution. The growth and dissolution rates can be calculated from the basic thermodynamics and kinetics considerations. The corresponding inclusion size change along the temperature cycles can be monitored numerically. The details of the calculation of growth and dissolution rates are described in the next section.

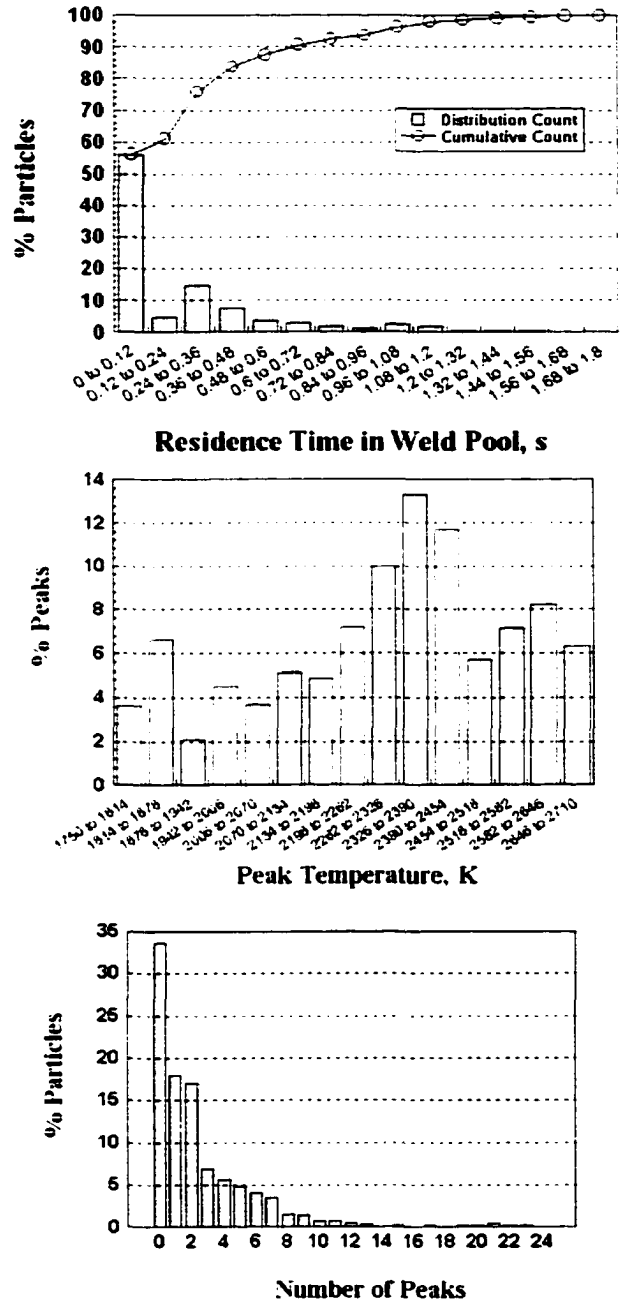

Figure 5.13 (a) Distribution of residence time, (b) distribution of peak temperature, and (c) distribution of peak number of thermal cycles of thousands of inclusions in the weld pool. Welding parameter used in the calculation: Parameter 2 in Table 5.4. The material composition is shown in Table 3.6.

5.3 Conclusions

Understanding transport phenomena in the weld pool is the prerequisite of studying formation, growth, and dissolution of inclusions in the weld metals. The mathematical model developed in Penn State is used to study heat transfer and fluid flow in the weld pool by solving conservative equations of mass, energy, and momentum in a finite difference form. A control-volume-based computational method was used. K-ε model was applied to consider turbulent fluid flow in the weld pool. The model is verified by comparing calculated weld pool profiles and experimental measured weld pool geometries for many welding cases.

Inclusions undergo vigorous motion along the velocity field of fluid flow in the weld pool. The motions and thermal cycles of thousands of inclusions are calculated using particle tracking technique. The statistical properties of the thermally gyrations of these particles, such as number of temperature peaks, residence time in the weld pool, and average temperature, are investigated. The thermal histories of inclusions will be useful for the calculation of inclusion growth and dissolution which will be discussed in Chapter 6.

References

1. S. A. David and T. DebRoy, *Science*, **257**, 487 (1992)

2. D. A. Schauer, W. H. Giedt, and S. M. Shintaku: *Weld. J.*, **57**, 127s (1978)

3. T. Hong, T. DebRoy, S. S. Babu, and S. A. David: *Metall. Mater. Trans. B*, **31B**, 161-9 (2000).

4. T. Hong and T. DebRoy, *Trends in Welding Research*, J. M. Vitek, S. A. David, H. Smartt, J. A. Johnson, and T. DebRoy (Editors), ASM International and American Welding Society, Materials Park, Ohio, May 1999.

5. M. C. Tsai and S. Kou: *Weld. J.*, **69**, 241s (1990).

6. J. A. Shercliff: *Met. Technol.*, **11**, 71-76, (1984).

7. P. Sohoo, T. DebRoy and M. J. McNallan: *Metall. Trans. B*, **19B**, 483 (1988).

8. D. R. Atthey: *J. Fluid Mech.*, **98**, 787 (1980).

9. G. M. Oreper and J. Szekely: *J. Fluid Mech.*, **147**, 53 (1984).

10. M. C. Tsai and S. Kou: *Numerical Heat Transfer*, **17**, 73(1990).

11. S. Kou and Y. H. Wang: *Metall. Trans. B*, **17B**, 2271 (1986).

12. T. Zacharia, S. A. David, J. M. Vitek, and T. DebRoy: *Weld. J.* **68**, 499s(1989).

13. A. Paul and T. DebRoy: *Metall. Trans. B*, **19B**, 851(1988).

14. H. G. Kraus: *Weld. J.*, **66**, 353s (1987).

15. H. Zhao and T. DebRoy: *Metall. Mater. Trans. B*, **32B**, 163-172 (2001).

16. M. Pastor, H. Zhao, and T. DebRoy, *Proceedings of the National Welding Seminar '97*, Indian Institute of Welding, Bangalore, India, December 1997, Indian Institute of Welding, Bangalore, India, 31-46 (1997).

17. S. V. Patankar: Numerical Heat Transfer and Fluid Flow, Hemisphere Publicating Corp. New York, 1980.

18. C. R. Heiple and J. R. Roper: *Weld. J.*, **61**, 97s (1982).

19. V. Pavelic, L. R. Tanbakuchi, O. A. Oyehara, and P. S. Myers: *Weld. J.*, **48**, 295s (1969).

20. K. Hong, D. C. Wechman, and A. B. Strong: Trends in Welding Research, Ed. By H. B. Smartt, J. A. Johnson and S. A. David, 399, ASM International, (1996)

21. R. T. C. Choo and J. Szekely: *Weld. J.*, **73**, 25s (1994)

22. B. E. Launder and B. D. Spalding: Mathematical Models of Turbulence, Academic Press, New York, (1972)

23. W. Pitscheneder, T. Hong, T. DebRoy, R. Ebner, K. Mundra, and R. Benes: "Mathematical Modeling of Weld Phenomena 4", edited by H. Cerjak, University Press, Cambridge, UK, 3-25 (1998).

24. Menu of Compact-3D, Innovative Co., 1990

25. Welding Handbook, 8th edition, Vol. 2, American Welding Society, Miami, Florida, (1991)

26. Materials Properties Handbook: Ed. R. Boyer, G. Welsch, E. W. Collings, Materials Park, OH : ASM International (1994).

27. K. Mundra, J.M. Blackburn, and T.DebRoy: *Sci. Tech. Weld. Join.*, **2**, 174 (1997)

28. W. Pitscheneder: Contributions to the Understanding and Optimization of Laser Surface Alloying, Ph.D thesis, University of Leobon, Austria (2001)

CHAPTER 6

PREDICTION OF INCLUSION CHARACTERISTICS

Growth and dissolution of different types of inclusions are simulated considering their thermal cycles which are calculated from particle tracking. The final size distribution, number density, and composition of inclusions are predicted based on a large number of such calculations. The collision and coalescence model is applied to modify the calculated size distribution and number density of inclusions. The predicted results are compared with experimentally measured results to verify the model.

6.1. Inclusion Characterization

The basic information of particle shape, composition, number density, and size distribution can be retrieved from inclusion characterization with the help of modern equipments, such as SEM, EDS, and image processing software. The basic procedure of characterization of inclusions in the steel weldment is briefly described as below:

After welding, samples are cut from the weldment. The cross section area of the samples should contain the fusion zone, HAZ, and base metal so that the complete information of inclusion characteristics at all locations can be revealed. The cross section of the sample is ground and polished. The as-polished surface is etched with 2% Nital to reveal the inclusions but not the martensitic microstructure in steels. SEM equipped with energy-dispersive x-ray detector and interfaced with an image analysis system is the most

common tool to measure the size distribution and composition of inclusions in the sample. The inclusion composition can be measured from the energy-dispersive x-ray spectrum EDS. Using image analysis software, the size distribution and volume fraction of inclusions can be measured and calculated from SEM images.

Although there are extensive experimentally measured results about inclusion characteristics available in the literature, inclusion characterization has some inherent limitations. First, it is not a real time technique. The measured data are the integrating results of various events taking place during the entire welding process. It can not reveal the fundamental insight of inclusion behavior in the weld pool. Because most measurement techniques are only for sample's cutting surface, the measured results are only 2-D rather than 3-D. Some approximation must be employed to transfer 2-D results to 3-D results. Therefore, without the help of theoretical simulation and modeling, experiment itself cannot provide us the fundamental insights about inclusion growth and dissolution behavior in the weld pool.

Considering the thermodynamics and kinetics of inclusion growth and dissolution, fluid flow and particle gyration in the weld pool, collision and coalescence of inclusions, it is possible to predict the inclusion characteristics such as composition, size distribution, number density from the alloy composition and welding parameters. In this chapter, the simulation results are summarized and presented in details. To validate the model, many data from literatures are collected and compared with simulated results.

6.2 Prediction of Inclusion Composition

Figure 6.1 shows the calculated nucleation rate of Al_2O_3 inclusions using the procedure described in Chapter 3. It is observed from the computed results that the nucleation rate is very high. Therefore, it is reasonable to assume that the nucleation rate is much faster compared with the growth and dissolution rates. The nucleation time and incubation time were not considered in the calculations of growth and dissolution of inclusions in this thesis.

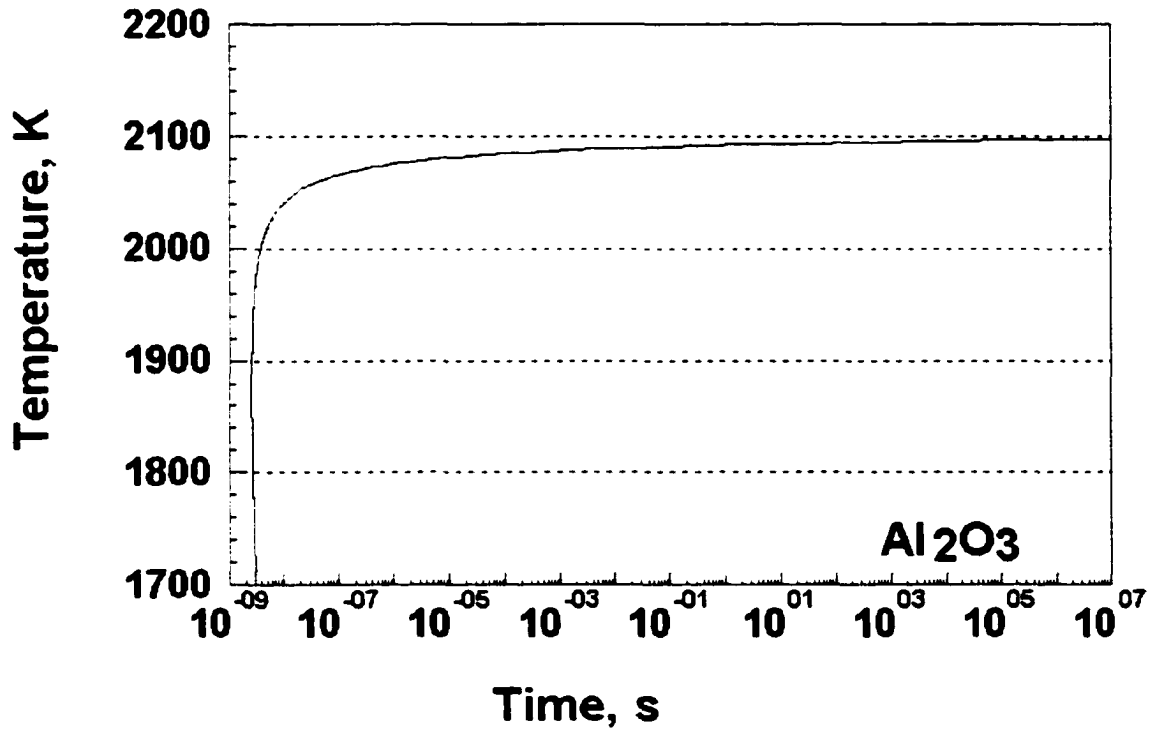

Figure 6.1 Homogeneous Nucleation rate of Al_2O_3 inclusion as a function of temperature. Alloy composition is shown in Table 3.6. The material properties and other data used in the calculation are shown in Table 3.2-3.5.

Figure 6.2 shows the TTT diagrams for the growth of various oxide inclusions to 1 μm radius in the liquid steel of composition 1 indicated in Table 3.6. Among all considered oxide inclusions, Al_2O_3, $MnO{\cdot}Al_2O_3$, and Ti_3O_5 grow fastest at temperatures above 2000 K. It is observed from Figure 3.4 that the change of c* at lower temperatures is not very pronounced for Al_2O_3, Ti_3O_5 and TiO_2. As a result, the change of diffusion coefficient dominates the kinetics of inclusion growth. For MnO and SiO_2, the change of c* with reduction in temperature exceeds the corresponding change of diffusion coefficient and the change in concentration, c*, dominate the kinetics of inclusion growth. Therefore, the 'C' curve shapes of TTT diagrams for growth of MnO and SiO_2 are not as pronounced as the other inclusions. From Figure 6.2, the equilibrium temperatures of the complex oxides considered in this paper are intermediate between the equilibrium temperatures of the constituent simple oxides. For example, the equilibrium temperature of $MnO.Al_2O_3$ lies between those of Al_2O_3 and MnO. A similar behavior is observed for both $SiO_2.Al_2O_3$ and $MnO.SiO_2$.inclusions

There is an equilibrium temperature between the inclusions and steel. Above the equilibrium temperature, the inclusions experience dissolution rather than growth. The higher is the equilibrium temperature of an inclusion, the higher is its stability. Several researchers presented theoretical and experimental results of the relative stability of inclusions in low alloy steels. For example, Hsieh[1] *et al* calculated the sequence of oxidation. Their result showed that the sequence depended on the composition and temperature. Among the oxides they considered, Al_2O_3, Ti_3O_5 and $MnO{\cdot}Al_2O_3$ were calculated to be most stable at high temperatures in the low alloy steels. These relative stability values agree well with computed results in Fig. 6.2. However, their calculations did not consider some complex oxides. Dowling et al[2] studied the inclusions in submerged arc welds in low alloy steels using TEM and EDS. They found that $MnO{\cdot}Al_2O_3$, a titanium-rich compound, and an aluminum-rich phase (probably Al_2O_3) is the main constituents. Kluken and Grong[3] studied inclusion formation in Al-Ti-Si-Mn dexoidized steel welds. The calculated stability of various oxides decreases in the following order: Al_2O_3, Ti_2O_3, SiO_2 and MnO. The high stability of Al_2O_3, $MnO{\cdot}Al_2O_3$,

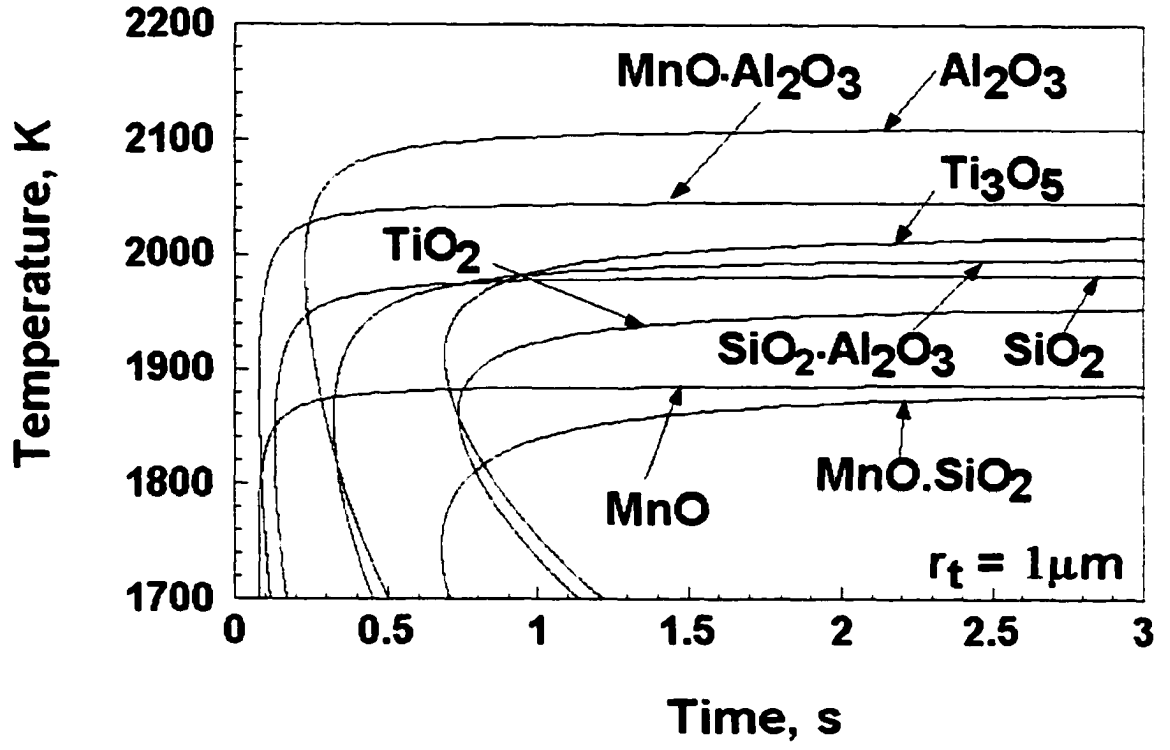

Figure 6.2 TTT diagrams for the growth of all oxide inclusions considered. Alloy composition is shown in Table 3.6. The material properties and other data used in the calculation are shown in Table 3.2-3.5.

and Ti_3O_5 observed by these investigators is consistent with the computed time-temperature-transformation diagrams presented in Figure 6.2.

Figures 6.3 and 6.4 show the TTT diagrams for the growth and dissolution of several nitride and sulfide inclusions, respectively. It is observed that the equilibrium temperatures for the stability of FeS, Si_3N_4, MnS and TiN inclusions are much lower than the corresponding metal oxides. Other features of these plots are similar to those for the oxide inclusions. Because of their low equilibrium temperatures, the sulfide inclusions cannot form in the weld pool of low alloy steel where the temperatures are higher than the equilibrium temperature for these inclusions. However, they can form during solidification of the weld metal. From Figure 6.3, it is observed that although the equilibrium temperature of MnS is lower than FeS, its growth rate at low temperatures is higher, which implies that MnS may become the dominant inclusion during solidification and cooling. This conclusion from theoretical calculations matches experimental observations[4,5] well in the sense that MnS is known to be the dominant sulfide inclusion in many steels.

6.3 Size Distribution of Inclusions

6.3.1. Growth and Dissolution of Inclusions considering Thermal Cycles in the Weld Pool

As discussed in the previous chapters, growth and dissolution rates of inclusions are determined by the diffusion of their constituent elements in the liquid metal. The driving force of element diffusion is the concentration gradient near the interface between liquid metal and inclusions.

When the interfacial concentrations of constituent elements of inclusions are lower than the corresponding concentrations in the bulk liquid at a given temperature, the diffusion takes place from the bulk liquid toward the interface and the inclusions undergo growth. In Chapter 2, the method of calculating the size change of inclusion during

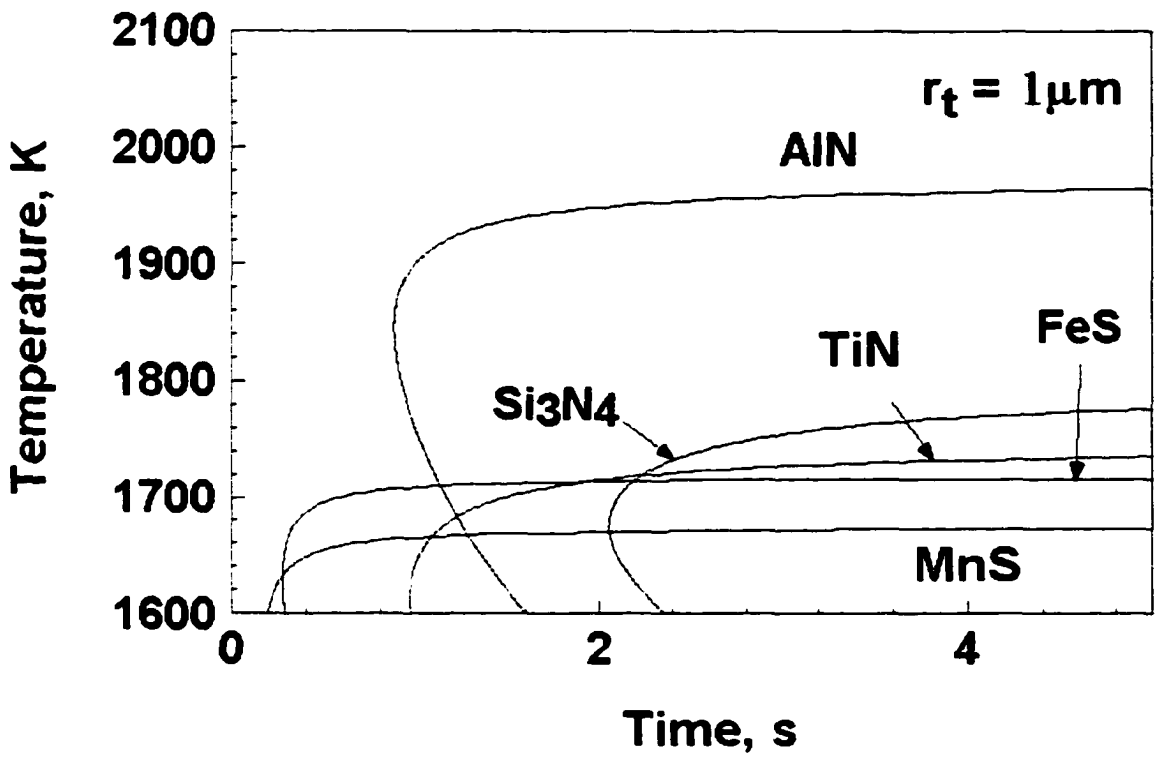

Figure 6.3 TTT diagrams for the growth of several nitride and sulfide inclusions. Alloy composition is shown in Table 3.6. The material properties and other data used in the calculation are shown in Table 3.2-3.5.

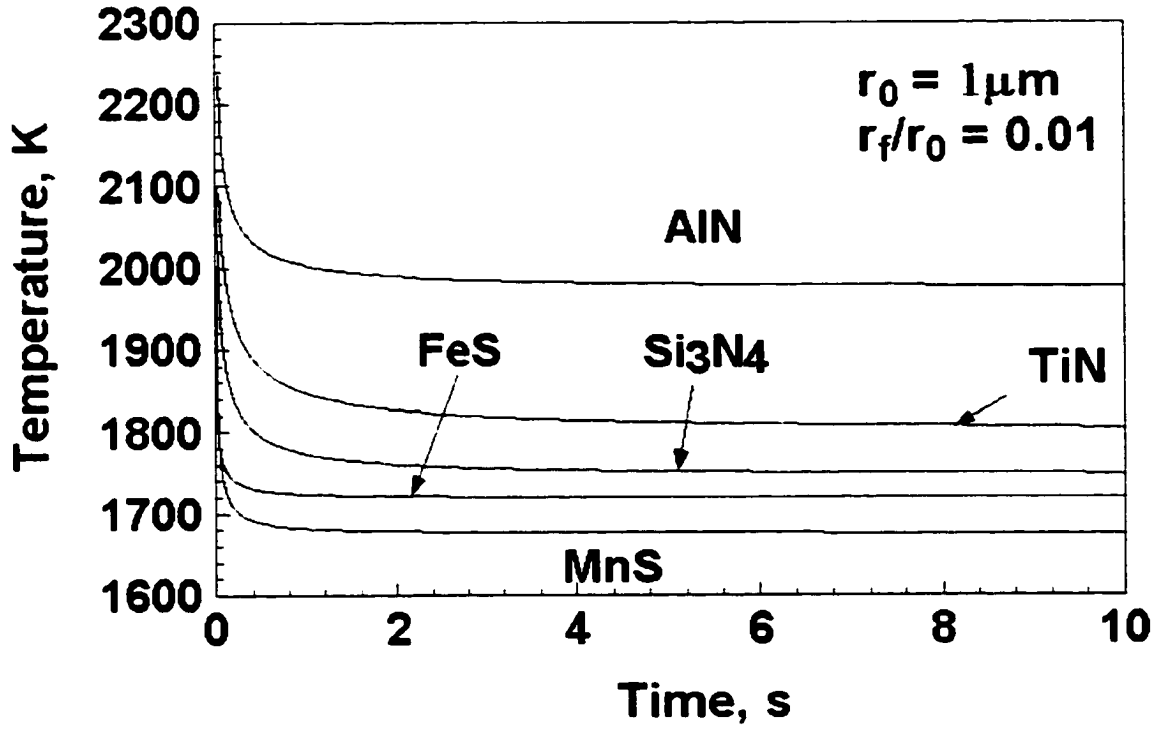

Figure 6.4 TTT diagrams for the dissolution of several nitride and sulfide inclusions. Alloy composition is shown in Table 3.6. The material properties and other data used in the calculation are shown in Table 3.2-3.5.

growth was discussed. Equation (6.1) is used to calculate the change of inclusion radius iteratively:[6]

$$r_{i-1} - r_i = \frac{\alpha}{2\sqrt{t}}\Delta t_i \tag{6.1}$$

where r_i and r_{i-1} are the radii of the inclusion before and after the ith time step, Δt_i, respectively, t is the growth time, and α is a growth rate parameter expressed by[6]:

$$\alpha = \sqrt{2Dc^*} \tag{6.2}$$

where D is the diffusion coefficient of the inclusion element whose diffusion coefficient is comparably lower in liquid steel. D can be given by:

$$D = D^0 \cdot e^{-\frac{E}{RT}} \tag{6.3}$$

where D^0 is a temperature independent pre-exponential term and E is the activation energy for diffusion. c^* is defined as the dimensionless supersaturation[7] expressed by:

$$c^* = (c^b - c^i)/(c^p - c^i) \tag{6.4}$$

where c is the concentration of element with lower diffusivity in weight percent, the superscript p, i, and b represent the concentration in the solid inclusion particle, at the interface between inclusion and liquid, and in the bulk liquid, respectively. c^p and c^i are known for specific inclusion and alloy system, the method to calculate c^i was discussed in the Chapter 3.

When the interfacial concentrations of constituent elements of the inclusion is higher than the concentrations in the bulk liquid at a given temperature, there is a concentration gradient from the interface to liquid. Therefore, the elements diffuse from the interface into the bulk liquid and the inclusions experience dissolution. Considering diffusion-controlled precipitation with a quasi-steady state approximation, Whalan[8] derived the following expression for the kinetics of dissolution:

$$r_{i-1} - r_i = -\frac{k}{2}\left[\frac{D}{r_i} + \sqrt{\frac{D}{\pi t}}\right]\Delta t_i \tag{6.5}$$

where r_i and r_{i+1} are the radii of the inclusion before and after the ith time step Δt_i, respectively, t is the dissolution time, and k is defined as $k = -2c^*$ as c* is defined in equation (6.4).

Figure 6.5 shows thermal history of an Al_2O_3 inclusion with many temperature peaks before it reaches solid region and the corresponding size change calculated from equations (6.1) and (6.5). The steel composition is shown in Table 3.6. Figure 6.6 shows size change and thermal history of an Al_2O_3 inclusion that completely dissolves within its life cycle in the same liquid composition as Figure 6.5. In Figure 6.5, Al_2O_3 inclusion grows at the temperature lower than 2214K. When the temperature exceeds 2214 K, Al_2O_3 inclusion starts to dissolve. The inclusion experiences several dissolution and growth loops and reaches the final size of 1.1 μm before it is embedded in the solid region of the weldment. If the thermal history of inclusion is not taken into account and only isothermal growth at 2000 K is considered, the final size of the Al_2O_3 inclusion is calculated as 2.3 μm in the same period (1.5 second). The Al_2O_3 inclusion that undergoes thermal cycle shown in Figure 6.6 will completely dissolve. This phenomenon cannot be explained by isothermal growth or dissolution. It is concluded that the loci and thermal history of inclusions are important factors to study the growth and dissolution behavior of inclusions in the weld pool.

6.3.2 Size Distribution of Inclusions in the Weld Pool

To predict the size distribution and number density of the inclusions in the weld pool, thermal gyrations and loci of thousands of inclusions are calculated. The original positions of the thousands of inclusions are located in uniformly in the weld pool. The final sizes of these inclusions are calculated using the same approach discussed above. The histogram figures of the size distribution of all calculated inclusions are presented in Figure 6.7. To evaluate the effect of welding parameters on inclusion characteristics, the final size distributions of Al_2O_3 inclusions under two sets of welding parameters presented in Table 6.1 are calculated. It is observed the average inclusion size increases

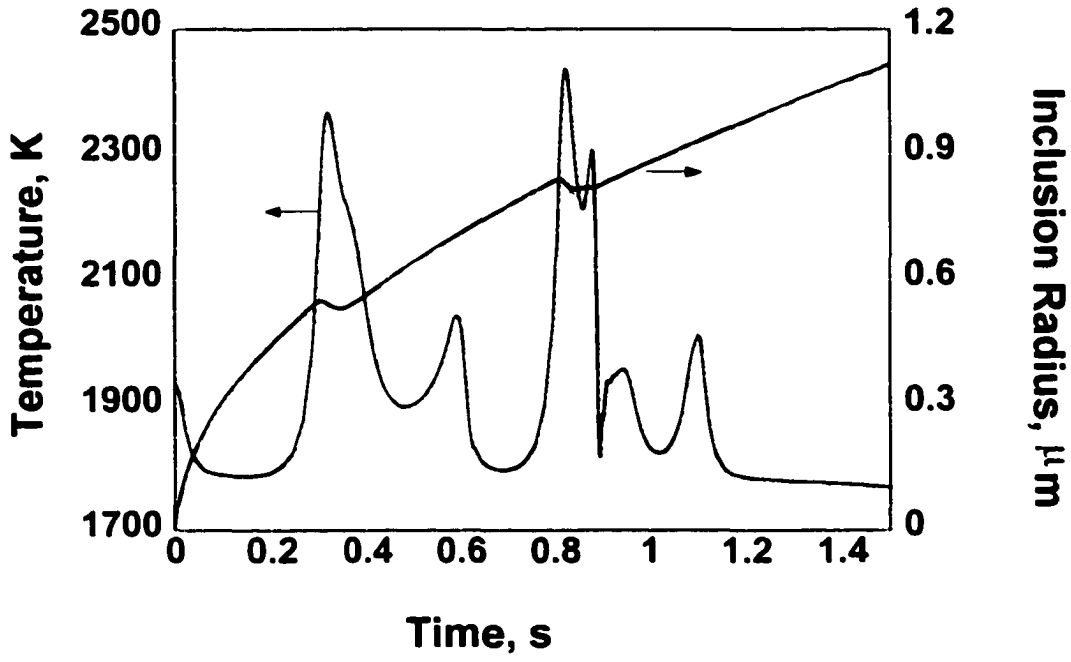

Figure 6.5 Size change and thermal history of an inclusion with many temperature peaks in the life cycle. Alloy composition is shown in Table 3.6. The material properties and other data used in the calculation are shown in Tables 3.2-3.5. The welding parameters are: voltage = 27 V, current = 590 A, welding speed = 12.7 mm/s.

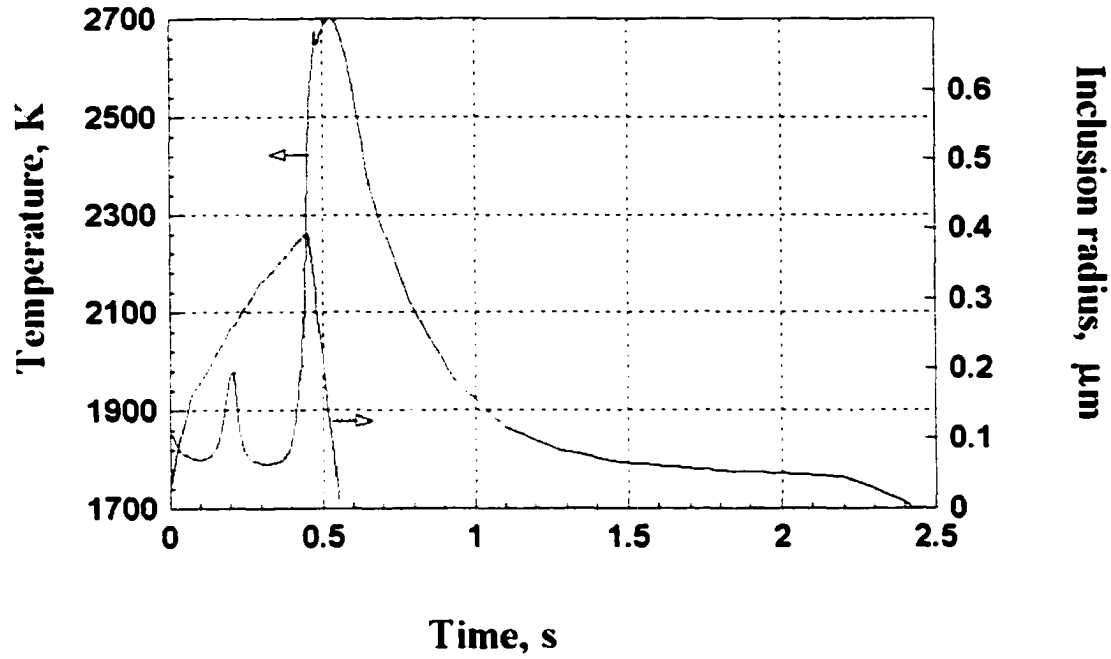

Figure 6.6 Size change of an inclusion which totally dissolves in the life cycle. Alloy composition is shown in Table 3.6. The material properties and other data used in the calculation are shown in Tables 3.2-3.5. The welding parameters are: voltage = 27 V, current = 590 A, welding speed = 12.7 mm/s.

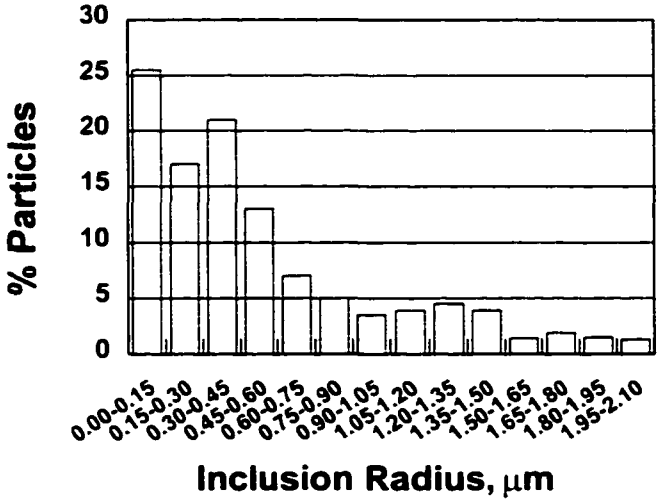

(a) Computed size distribution for the welding parameters indicated under 'case 1' in Table 6.1.

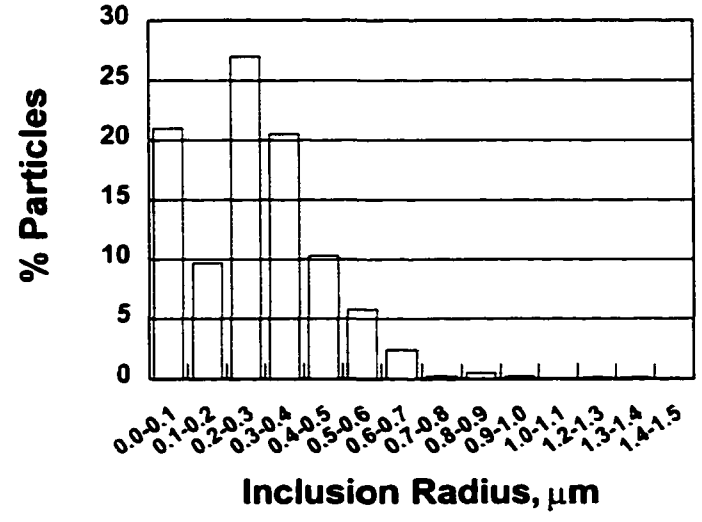

(b) Computed size distribution for the welding parameters indicated under 'case 2' in Table 6.1.

Figure 6.7 Size distribution of Al_2O_3 inclusions at two welding conditions presented in Table 6.1. The alloy composition is shown in Table 3.6. Other data used in the calculation are shown in Tables 3.2-3.5. The welding process used was gas-tungsten-arc (GTA) welding.

with the heat input during welding. The calculated results of weld pool geometry presented in Table 6.1 show that the length and width of the weld pool calculated from the second set of welding parameter are about 1.5 times greater than those from the first set. The average inclusion size calculated from the second case is also higher than that from the first case. Higher heat input generates bigger weld pool and, consequently, provides longer time for inclusion to grow.

Table 6.1 Two Sets of GTA Welding Parameters used to compare the calculated size distribution of inclusions in the weld pool.

Welding Parameters	**Case 1**	**Case 2**
Voltage	27 V	27 V
Ampere	590 A	590 A
Travel Speed	6.35 mm/s	12.7 mm/s

Figure 6.8 shows the comparison between the calculated and experimentally measured size distribution[9] of Al_2O_3 inclusions in the liquid steel which composition is listed in Table 3.6. The welding parameters are as the case 2 in Table 6.1. Before comparison, the experimental two-dimensional measurements are converted to three-dimensional diameters by the following equation, assuming Fullman theory[10] for a poly-dispersed system of spheres:

$$\bar{r}_{3D} = \bar{r}_{2D} \cdot \frac{\pi}{2} \tag{6.6}$$

where $\bar{r}_{3D}$ is mean 3-D particle radius, $\bar{r}_{2D}$ is the corresponding 2-D mean particle radius.

It is observed that most inclusions are smaller than 1 μm. The computed size distribution is in good agreement with the measured values. The main difference between the experimental and computed results is that the measured values show fewer small inclusions in the size range of 0.0 to 0.16 μm. One possible explanation for this discrepancy is the inability to detect small inclusions by optical microscopy. Another reason could be related to the inherent assumption in the model that inclusions smaller than the critical nucleation size still exist and continue to grow without disappearing.

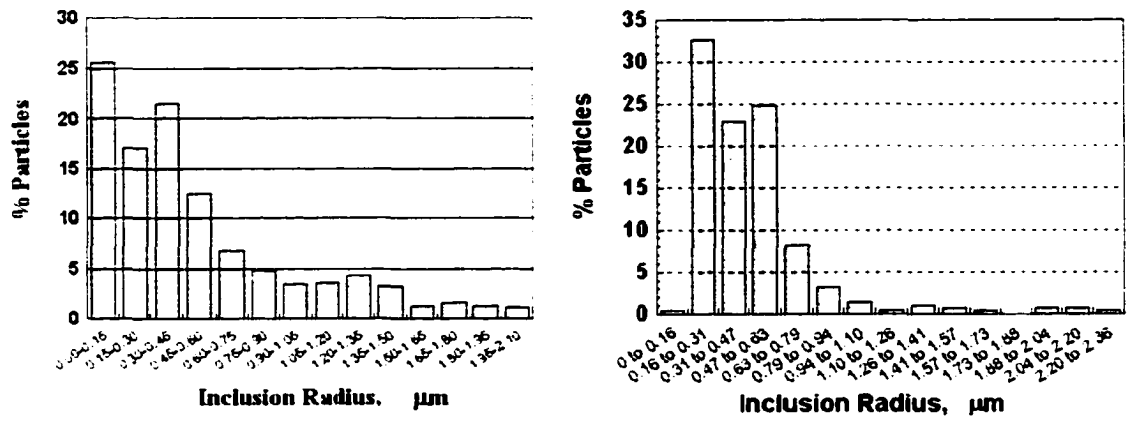

Calculated Result

Experimental Result[9]

Figure 6.8 Comparison between calculated size distribution of Al_2O_3 inclusions and experimentally measured size distribution[9] of inclusions in the weld pool. The alloy composition is shown in Table 3.6. The welding parameters: GTA welding, voltage: 27 V, current: 590 A, welding speed: 12.7 mm/s.

In the past, the mechanism of inclusion growth has been investigated by examining how the inclusion radius changes with time. For example, if the inclusions grow by Ostwald ripening[6] at the liquidus temperature, and the diffusion of oxygen is considered, the expression of final mean inclusion diameter $\bar{d}$ as a function of t is given by the Wagner equation:

$$\bar{d}^3 = \bar{d}_{in}^3 + \frac{64\sigma D_0 C_0 V_m}{9RT} t \approx Ct \qquad (6.7)$$

where D_0 is the diffusivity of oxygen, C_0 is the bulk oxygen concentration, $\bar{d}_{in}$ is the initial mean diameter of inclusions, V_m is the molar volume of the oxide, σ is the oxide-steel interfacial energy, R is the gas constant, T is the temperature, and C is a proportionality constant. The calculated mean size from Wagner equation and the sizes of several inclusions as a function of $t^{1/3}$ are shown in Fig 6.9. It is interesting to observe that the calculated results show good agreement with the Wagner equation although the growth and dissolution of the inclusions were calculated assuming diffusion control and non-isothermal temperature gyrations experienced by the inclusions. These results do not rule out the possibility of Ostwald ripening. What it shows is that examining the mechanism of inclusion growth based on how the inclusion size varies with time can lead to completely misleading conclusions.

6.3.3 Number Density of Inclusions

When the final size of an inclusion is obtained, its original location of nucleation is traced back and the local nucleation rate in this location based on the local temperatures is calculated. The product of nucleation rate and the time spent by the inclusion at that location was used to determine the final number density. The final calculation of inclusion number density was explained by the following equation:

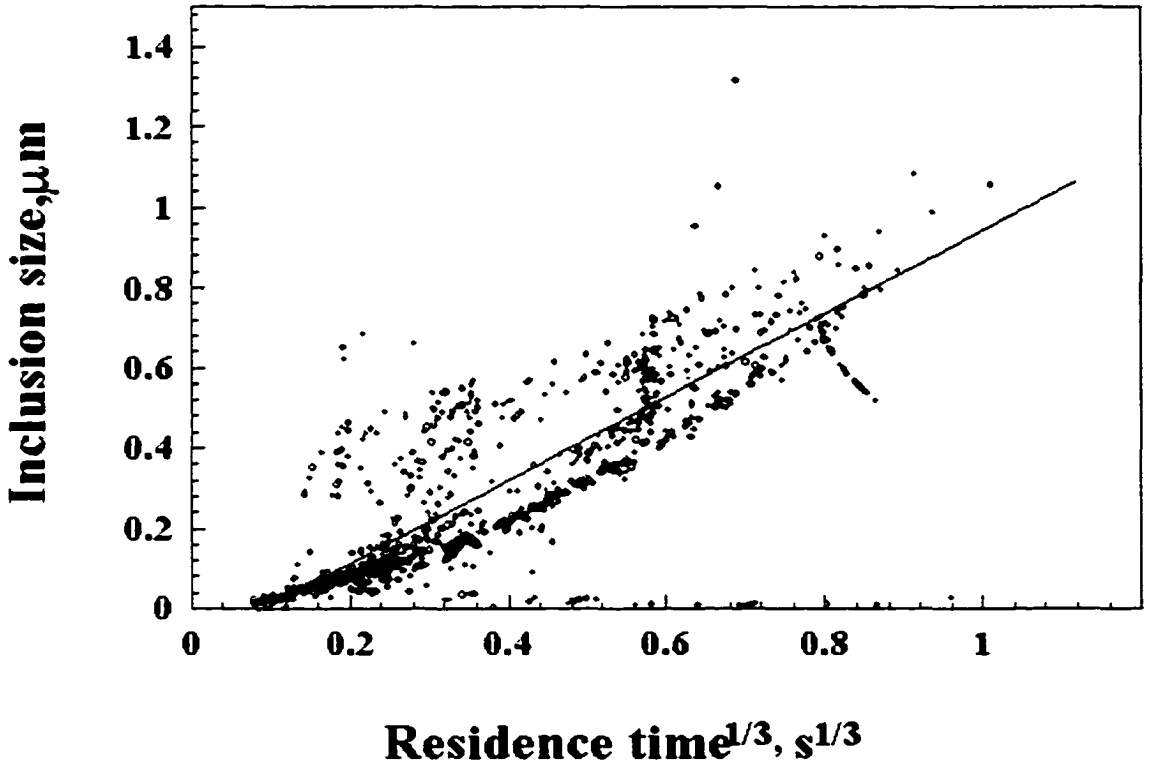

Figure 6.9 Agreement between calculated inclusion size and Wagner Equation

$$\text{Number density of inclusion for specific size} = \sum_{i=1}^{n} I_v \times t, \qquad (6.8)$$

where n is the number of inclusions with such a size, I_v is the nucleation rate as a function of temperature, and t is the residence time of the inclusions at that instance at that location in the weld pool. This is an approximate calculation and the final value is only an estimation of the number density. However, the trends for a given condition are consistence with the experimental results. The calculated results are adjusted by the collision and coalescence model discussed in the next section. It is observed that theoretical values agree with experimental data in the general trend.

When the welding heat source moves out, inclusions will be embedded in the solid region and the weld pool will solidify. Many previous researches showed that inclusions still undergo significant growth during the solidification of the weld pool. The size distribution plot shifts to the bigger size and becomes broader. The number density of inclusions becomes smaller. This phenomenon is called 'inclusion coarsens coarsening', which mechanism and modeling approaches are discussed in the following section.

6.4 Collision and Coalescence of Inclusions

Babu et al.,[11] Iyngar and Philbrook,[12] and Lindborg and Torssell,[13] etc. concluded that collision and coalescence are the major mechanism of inclusion coarsening in the liquid metal during cooling. In this section, collision and coalescence mechanism are taken into account to adjust the number density and size distribution of inclusions calculated from the combination of heat transfer and fluid flow model and fundamental thermodynamics and kinetics of inclusion growth and dissolution in the liquid steels. The details of the collision and coalescence model are described in Section 2.3 of Chapter 2.

In the calculation presented in the thesis, the initial size distribution between 0 to 1 μm is considered. The original size distribution calculated from fluid flow and particle tracking models is rearranged to a new size distribution with size intervals of 0.04 μm. Thus, a series of 25 data from 0 to 1 μm is obtained. The following functions $g(r_1)$ and $h(r_2)$ are calculated:

$$\begin{cases} g(r_1) = n(r_1)n(r_2)\frac{4}{3}(r_1 + r_2)^3(\frac{r}{r_2})^2 GradV \\ h(r_2) = n(r_1)n(r_2)\frac{4}{3}(r_1 + r_2)^3 GradV \end{cases} \quad \text{where } r^3 = r_1^3 + r_2^3 \tag{6.9}$$

$g(r_1)$ and $h(r_2)$ were then integrated using the rectangular method:

$$\begin{aligned} I_1 &= \int_{r_1=0}^{r_1=r} g(r_1)dr_1 = \sum_{r_1=0}^{r_1=r} g(r_1)\Delta r \\ I_2 &= \int_{r_1=0}^{r_1=r_{max}} h(r_2)dr_2 = \sum_{r_2=0}^{r_2=r_{max}} h(r_2)\Delta r \end{aligned} \tag{6.10}$$

The change rate in number density of r is then calculated by:

$$c(r) = \frac{dn(r)}{dt} = \frac{1}{2} I_1 - I_2 \tag{6.11}$$

The change of number density of inclusion which size is r in a small time interval, Δt, is calculated by $\Delta n(r)=c(r)\Delta t$. This number is used to adjust the original number densities iteratively. After each iteration, Equation (6.11) is recalculated until the expected time reaches.

This approach is just an estimation of the change of inclusion number density considering the effect of collision and coalescence. There are some shortcomings in this calculation. When we consider the collision and coalescence in specific time range, the whole volume of inclusion changed because some new inclusions form and growth. However, in this model, the volume of inclusion is assumed constant. The final time when the calculation will stop has not a very clear physical meaning in our calculations. Figure 6.10 shows the calculated results of inclusion coarsening based on the mechanism of collision and coalescence. Figure 6.10(a) shows the number density of Al_2O_3

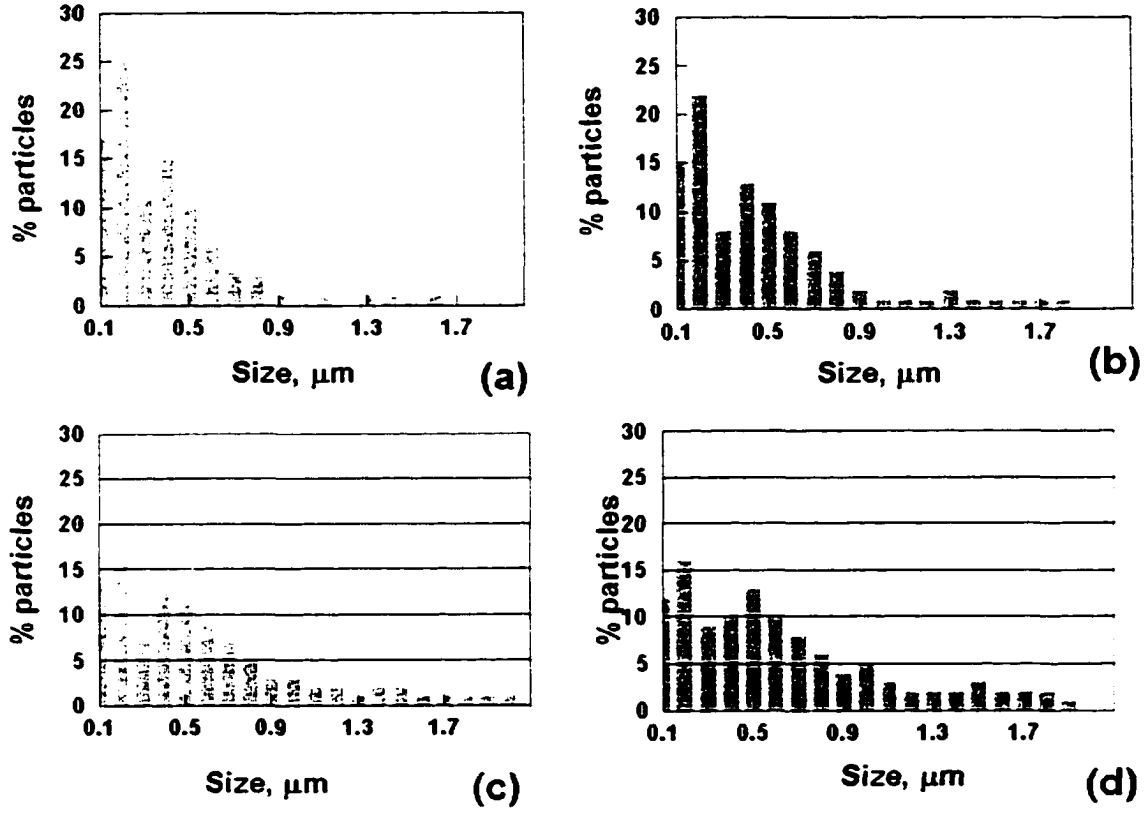

Figure 6.10 Change of calculated number densities of Al_2O_3 inclusions considering collision and coalescence mechanism (a) as welded (b) 1s, (c) 5 s, and (d) 60s. Alloy composition is shown Table 3.6. The welding parameters are shown as the set 1 in Table 6.1.

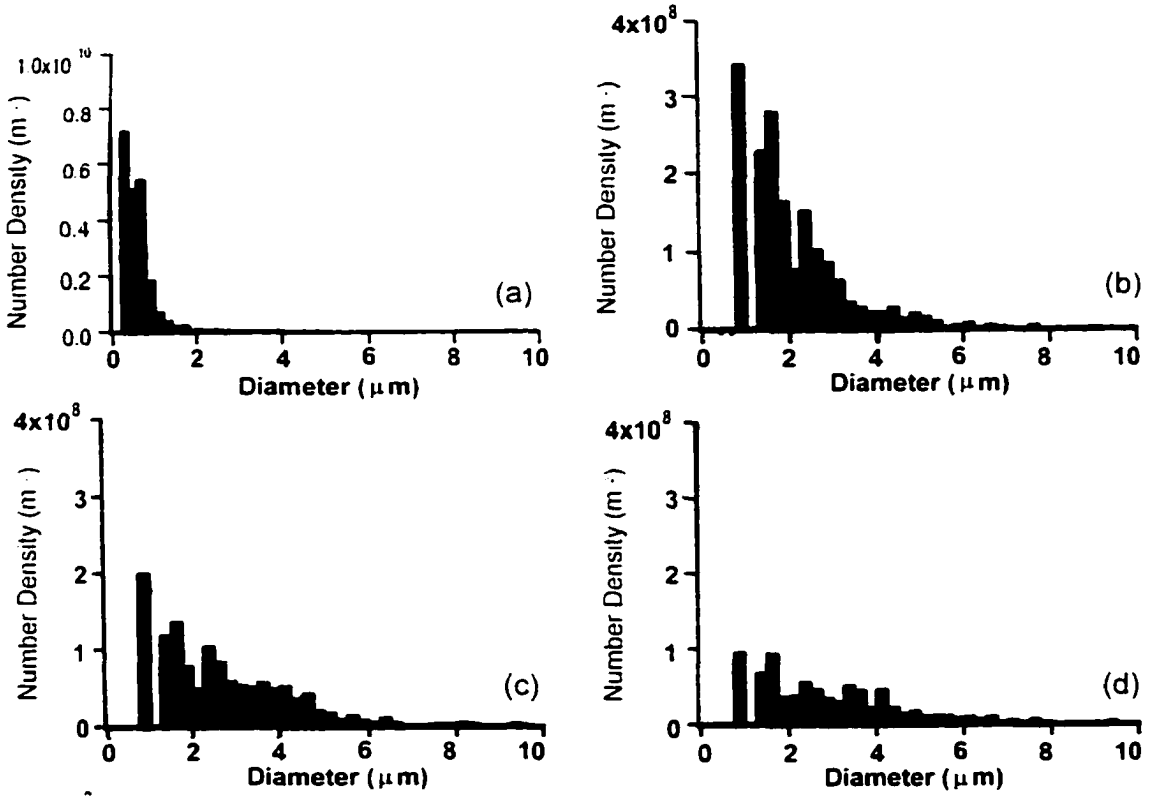

Figure 6.11 Inclusion size distribution in the as welded condition and after various hold times at 1480C. (a) as welded (b) 10s, (c) 20 s, and (d) 30s. Alloy composition: C0.095-Si0.31-Mn1.59-Ti0.003-Al0.017-O0.024wt%. Welding parameters: GTA welding, 27 V, 590 A, 12.7 mm/s.

inclusions as welded. Figures 6.10(b)-(d) shows the adjusted number density of Al_2O_3 inclusions after 1 second, 5 seconds and 10 seconds. It is observed that the size distribution becomes wider and flatter. Many bigger inclusions form and the number densities of small inclusions decrease rapidly. Babu et al[9] did an experiment to understand the particle coarsening by collision and coalescence. They melted the welded samples and hold them in a constant temperature of 1750 K for 10s, 20s, and 30s. The measured number densities of inclusions at different holding time are presented in Figure 6.11. Although the alloy composition and welding parameters used in the calculations are not exactly the same as experiments, the general trends can be compared. It is concluded that inclusion size distribution will switch to the bigger size and the number density of smaller inclusion will decrease rapidly.

6.6 Conclusions

The final size of individual inclusion is calculated by considering the growth and dissolution of inclusion considering its thermal cycle. Calculations of thousands of inclusions are carried out to predict the final size distribution, number density, and composition of inclusions. The effects of welding parameters on the final inclusion characteristics are examined. The collision and coalescence model is applied to modify the calculated size distribution and number density of inclusions. The comparison between calculated and observed size distribution of inclusion implied that the model combining thermodynamics, kinetics of inclusion growth and dissolution with transport phenomena in the weld pool can offer an insightful approach to study inclusion behavior in the weld pool. The mechanism of inclusion growth and dissolution along the fluid flow in the weld pool are revealed in the model.

The characteristics of inclusion in the weld pool are critical factors to determine the weldment microstructure and resulting mechanical properties. Computational modeling offers a powerful tool to understand and predict the inclusion characteristics from the physical fundamentals. However, what worth to mention is that the study on

inclusion characteristics alone is not the ultimate goal of the research, much more effort must be carried out to understand the effect of inclusion characteristics on weldment microstructure and properties, and in turn their influence on the quality of the final products.

References:

1. K. C. Hsieh, S. S. Babu, J. M. Vitek, and S. A. David: *Mater. Sci. Engi.*, **A215**, 84 (1996).

2. J. M. Dowling, J. M. Corbett and H. W. Kerr: *Metall. Trans. A*, **17A**, 1611 (1986).

3. O. Kluken and O. Grong: *Metall. Trans. A*, **20A**, 1335 (1989).

4. M. Wintz, M. Bobadilla, J. Lehmann and H. Gaye: *ISIJ International*, **35**, 715 (1995).

5. B. R. Keville: *Weld. J.*, **62**, 253s (1983).

6. J. W. Christian: The Theory of Transformations in Metals and Alloy - Part I: Equilibrium and General Kinetic Theory, 2nd ed., Oxford, Pergamon Press (1981).

7. C. Zener: *J. Applied Physics*, **20**, 950 (1949).

8. M. J. Whelan: *Metal Science J.*, **3**, 95 (1969).

9. S. S. Babu, S. A. David, J. M. Vitek, K. Mundra, and T. DebRoy: *Mater. Sci. Tech.*, **11**, 186 (1995).

10. R. L. Fullman: *Trans. AIME*, **197**, 447-452, (1953).

11. S. S. Babu, S. A. David, and T. DebRoy: *Sci. Tech. Weld. Join.*, **1**, 17-27, (1996)

12. R. K. Iyengar and W. O. Philbrook: *Metall. Trans.*, **3**, 1823-30, (1972)

13. U. Lindborg and K. Torssell: *Trans. Metallurgical Society of AIME*, **242**, 94-102 (1968)

CHAPTER 7

SUMMARY AND FUTURE WORK

Summary

The objectives of welding are to achieve structural continuity and sound mechanical properties. Many previous studies concluded that the characteristics of individual inclusions in the weld metal are critical factors to determine the structure and properties of weldments. The ultimate goal of this research is to guide the welding techniques to achieve the objectives practically from the fundamental understanding of the inclusion behavior and the influence of inclusions on structure evolution and mechanical properties of weldment.

The effects of time and temperature on the growth and dissolution behavior of individual inclusions in liquid steel can be represented by a set of time-temperature-transformation (TTT) diagrams. Apart from the stability of various inclusions in a given composition of steel, the diagrams provide important kinetic information of diffusion controlled growth and dissolution. The time-temperature-transformation diagrams of growth and dissolution of various types of inclusions show that Al_2O_3, $MnO{\cdot}Al_2O_3$, Ti_3O_5 are always the most stable oxide inclusions in the weld pool for the given steel composition. However, alloy composition affects the relative stabilities of inclusions dramatically.

The non-isothermal behavior of growth and dissolution of individual inclusions can be predicted from their isothermal growth behavior by constructing continuous

cooling transformation (CCT) diagrams for growth and continuous heating transformation (CHT) diagrams for dissolution using Scheil additive rule. This approach offers tool to better understand the effects of temperature and time on the growth and dissolution of inclusions in liquid steels under non-isothermal conditions.

Understanding of fluid flow and heat transfer in the weld pool as well as the thermodynamics and kinetics of inclusion growth and dissolution is a prerequisite for understanding the inclusions behavior during welding. A well verified fluid flow and heat transfer model developed in Penn State is used to calculate the temperature and velocity fields in the weld pool for different welding process, such as GTA welding, SA welding, and laser welding. Because the usage of high currents in welding, the nature of fluid flow and heat transfer in the liquid is turbulent. A turbulence model considered enhanced viscosity and thermal conductivity (k-ε model) is applied to calculate the temperature and velocity fields. The calculations show that there is vigorous circulated motion in the weld pool. The geometry of the weld pool always shows an elongated profile with high temperature gradient in the front part and low temperature gradient in the rear part. The comparison between calculated and experimentally observed weld pool geometry verified the model very well. The heat transfer and fluid flow model offers us not only the fundamentals on the physical procedures taking place during welding, but also the basis to further study on nucleation, growth and dissolution of inclusions.

Due to the fluid flow in the weld pool, the nuclei of inclusions undergo vigorous motion along the fluid. During the residence time of inclusions in the liquid bulk alloy, they experience both growth and dissolution along their thermal cycles in the weld pool. Particle tracking technique is applied to calculate a large amount of thermal cycles of inclusions in the weld pool. Particle tracking results show that most inclusions experience complex gyrations and thermal cycles before they are trapped on the solid region in the weldment. The temperature versus time plots of the inclusions in many cases displayed several characteristic temperature peaks. However, about one-third of the particles experienced continuous cooling behavior (no temperature peak).

Thermal cycles of thousand of inclusions nucleated in the weld region are tracked and their growth and dissolution are calculated to obtain the final size distribution and number density of inclusions statistically. The computed results show that inclusion size distributions are affected by the welding parameters and alloy composition. The inclusions are coarser at low welding speeds and high welding powers because inclusions will have more time to grow in a large weld pool. Good agreement between the computed and the experimentally observed inclusion size distribution indicates that the inclusion growth and dissolution can be understood from the fundamentals of transport phenomena and kinetics.

Combining the calculated temperature and velocity fields in the weld pool and thermodynamics and kinetics of inclusion growth and dissolution, the composition, size distribution, and number density of different types of inclusions are calculated and compared with the experimental results. It is concluded that trends of computed results agree with experimentally observed inclusion size distribution and indicate that inclusion growth can be understood from the fundamentals of transport phenomena and kinetics. Considering diffusion control growth and dissolution of inclusions, the increase in inclusion size with residence time exhibited a pattern characteristic of Wagner equation derived considering Ostwald ripening.

The collision and coalescence model are applied to modify the calculated number density of single kind of inclusions. With the increase of time, the number densities of smaller size inclusions become lower. The entire distribution profile becomes more uniform in size and the average size become higher.

To summarize, the model developed in this thesis combine the understanding of transport phenomena in the weld pool and thermodynamics and kinetics for the diffusion-controlled growth and dissolution of inclusions in the liquid steel to study the inclusion behavior during welding and predict the characteristics of inclusions, such as

composition, size distribution and number density. Particle coarsening by collision and coalescence are also considered in the model.

Future Work

1) The calculated number density of inclusions is modified by the collision and coalescence model after all considered inclusions reach solid region. A dynamic model which fully incorporates collision and coalescence model with the heat transfer and fluid flow model and particle tracking should be developed.

2) During the calculation of equilibrium concentrations at the interface between inclusion and liquid, when one element concentration is extremely high, calculations of equilibrium concentrations were difficult to get convergent results. A more robust and stable algorithm should be developed to solve the equilibrium concentrations.

3) One of the major troubles the author encountered during the research is the difficulty in obtaining reliable thermodynamics and kinetics data for inclusions formation reaction and the lack of physical property data of some inclusions in the literature. A complete database containing inclusion properties and thermodynamics data should be developed for all common inclusions.

4) Most study reported in this thesis assumes Al_2O_3 is the principle inclusion in the weld pool of low alloy steels. However, several types of inclusions may also nucleate and grow together in the welding process. During the nucleation and growth of inclusions, the composition of liquid will change and affect the stabilities and formation sequence of inclusions. The experimental observation and characterization only reveal the final results of many component processes of simultaneous nucleation and growth of inclusions. A model considering simultaneous nucleation and growth of different types of inclusions in the weld pool should be developed. The author proposes following calculation scheme to simulate the simultaneous nucleation and growth:

The heat transfer and fluid flow and the particle motion in the weld pool will be considered. The whole procedure of simultaneous nucleation and growth will be modeled iteratively by many small time steps along inclusion thermal cycles. The calculation scheme is shown in Table 7.1 and described as below:

1) At step zero (t = 0) where the temperature is the initial temperature T_0, the initial number densities of considered inclusions formed in a small time step Δt is expressed as $I_0\Delta t$. These inclusion particles are considered as group 0.
2) In time step 0, group 0 grows to radius r which is calculated by equation (6.4).
3) After step 0, the new temperature is calculated from the inclusion thermal cycles. The liquid composition will be adjusted from the growth rate of all previously formed groups. The nucleation rate and number density of the inclusion of group 1 are calculated based on the new composition.
4) The above procedures are repeated until the concentrations of metallic elements and oxygen reach the equilibrium concentrations of inclusions and liquid. The final number density and size distribution of various inclusions are calculated.

Table 7.1 Calculation Scheme of Nucleation and Growth of a Single Type of Inclusions in the Modeling of Simultaneous Nucleation and Growth

Step	Total time	Liquid Concentration	group0 (size, nuclei number density)	group1 (size, nuclei number density)	group2 (size, nuclei number density)	group3 (size, nuclei number density)	.....
0	Δt	c0	$(r_{0,0}, I_0\Delta t)$				
1	$2\Delta t$	c1	$(r_{0,1}, I_0\Delta t)$	$(r_{1,0}, I_1\Delta t)$			
2	$3\Delta t$	c2	$(r_{0,2}, I_0\Delta t)$	$(r_{1,1}, I_1\Delta t)$	$(r_{2,0}, I_2\Delta t)$		
3	$4\Delta t$	c3	$(r_{0,3}, I_0\Delta t)$	$(r_{1,2}, I_1\Delta t)$	$(r_{2,1}, I_2\Delta t)$	$(r_{3,0}, I_3\Delta t)$	
...	...	...	.....	.....	.....	.....	...

The calculated number density and size distribution will be compared with experimental results to verify the model.

Appendix A

MANUAL OF THE COMPUTER PROGRAM FOR THE CALCULATION OF INCLUSIONS CHARACTERISTICS

A1. INTRODUCTION

The purpose of developing this FORTRAN program is to calculate the relative stability, growth and dissolution rates of inclusions considering heat transfer and fluid flow in the weld pool, thermodynamics and kinetics of formation, growth and dissolution of inclusions. The temperature and velocity fields in the weld pool are calculated using a grid system fixed to the moving heat source. In some welding processes, turbulent model must be applied to obtain correct temperature and velocity fields. The detailed information about calculation of temperature and velocity fields is available in Chapter 5.

After interpolating the temperature and velocity fields in a uniform grid system around the melting region, inclusions are assumed to nucleate at each grid point of the uniform grid system in the weld pool. Particle tracking calculation is applied to each particle from the initial position. The trajectories and thermal histories of all particles are recorded.

Time-temperature-transformation (TTT) diagrams for the growth and dissolution of various types of inclusions are calculated. Incorporating the calculated TTT diagrams and thermal history of inclusion, size change of the inclusion along the trajectory in the liquid metal is calculated. Thousands of particles are tracked and their final sizes are calculated to obtain the statistic size distribution of inclusions.

Following is the summary of the tasks involved in the calculation procedure:

1. Calculate the temperature and velocity fields in the weld pool.
2. Interpolate temperature and velocity values in a uniformly spaced grid system.
3. Track inclusions originating at every grid point within the liquid pool and obtain their thermal histories.
4. Calculate the TTT diagrams of oxide, nitride, and sulfide inclusions based on thermodynamics and kinetics. Calculate the CCT and CHT diagrams of all inclusions considered.
5. Calculate the size change of each inclusion based on its time-temperature history.

There are many subroutines and input/output data files in this program. The relation among the subroutines and data files are shown in Figure A1. Operation of each subroutine requires input data files. Most subroutines also generate data files as output. These files are either final results of calculations or intermediate results which will be input to other subroutines. The names and functions of subroutines are presented inside the rectangles with double sidelines in Figure A1. The names and contents of data files are presented in the rectangles with round corners.

A2. FORMAT OF DATA FILES

The description of each subroutine will be presented in 'Functions and Subroutines' section. The formats and explanations of all data files in the above flow chart are presented below:

foldtec (default value: ***orig.tec***)

```
TITLE = "FLUID FLOW AND HEAT TRANSFER IN WELD POOL"
VARIABLES = "X", "Y", "Z", "TEM", "U", "V", "W","h","fracl","qin","conc"
ZONE I= 50, J= 29, K= 26, F=POINT
     .0000E+00     .0000E+00     .0000E+00     .2980E+03     .0000E+00
.0000E+00     .0000E+00     .7664E+01     .0000E+00     .0000E+00     .9098E-10
     .7705E+00     .0000E+00     .0000E+00     .2980E+03     .0000E+00
.0000E+00     .0000E+00     .7665E+01     .0000E+00     .0000E+00     .9095E-10
     .2235E+01     .0000E+00     .0000E+00     .2980E+03     .0000E+00
.0000E+00     .0000E+00     .7669E-01     .0000E+00     .0000E+00     .9097E-10
```

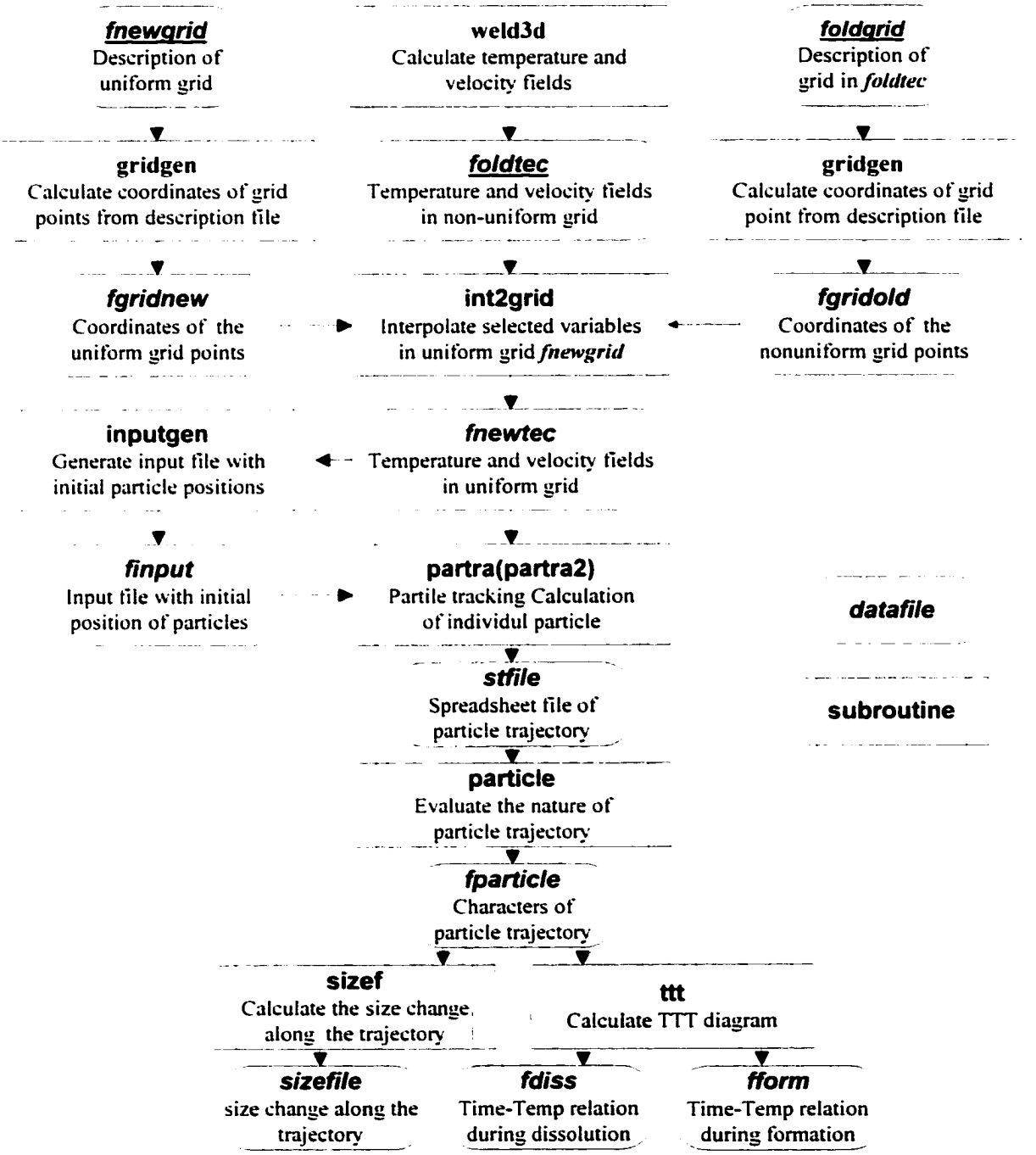

Figure A1. Flow chart of the calculation procedure

```
     .3465E+01      .0000E+00      .0000E+00      .2996E+03      .0000E+00
.0000E+00      .0000E+00      .7924E+01      .0000E+00      .0000E+00      .9432E-10
     .4051E+01      .0000E+00      .0000E+00      .4140E+03      .0000E+00
.0000E+00      .0000E+00      .2714E+02      .0000E+00      .0000E+00      .8565E-09
.      .      .      .      .      .      .      .      .      .      .      .
.      .      .      .      .      .      .      .      .      .      .      .
```

This TECPLOT files is an input data file obtained from the temperature and velocity calculations. Its size is determined by the grid defined in ***foldgrid***. For a 50x28x26 grid system, ***foldtec*** is about 5.4M bytes. The first line in the file is the title of the data. The second line defines the variable names of various columns. The third line defines the domain size and the format in which the data are stored. There are 50x28x26x11 = 400400 data in the presented ***foldtec***.

fnewgrid: (default value: ***newgrid***)

Two examples are given as below. The first file with name ***newgrid1*** defines a coarser uniform domain with grid size of 42x22x22, the second file with name ***newgrid2*** defines a finer uniform 82x42x42 domain.

newgrid1

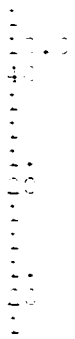

newgrid2

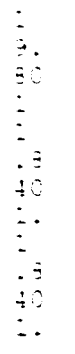

The value in the first line of the files is the number of section in x-axis. The second line indicates the length of each section in x-axis expressed in centimeter. The third line indicates the grid number in each section. The fourth line indicates the exponent value in the grid generation equations. Similarly, lines 4-7 and lines 8-12 define the nature of grid points in y- and z-axis, respectively.

***foldgrid*: (default value: *oldgrid*)**

```
9
4.0  0.6 0.1 0.1 3.5  10 50 100 0.1
3    7   4   4  15   5   6   3   1
-1.2 -1.2 1.0 1.0 1.2 1.2 1.2 1.4 1.0
5
1.1  0.6  0.55 2.e-4  4.1
4   12     4      1     3
1.0  1.2   1.2    1.0   1.5
8
0.01 0.59 0.6 2.e-4 3.9
3 12 4 1 4
1.0 1.0 1.2 1.0 1.5
```

This file defines a non-uniform grid system with a domain size of 50x28x26 in ***foldtec***. The explanation of each line is the same as that in ***fnewgrid.***

***fgridnew* (default value: *grid.new*):**

Two examples with name ***grid.new1*** and ***grid.new2*** are given here, corresponding to the two examples in ***fnewgrid***.

grid.new1

```
   42    22    22
  0.0000E+00    0.1250E+00    0.3750E+00    0.6250E+00    0.8750E+00
  0.1125E+01    0.1375E+01    0.1625E+01    0.1875E+01    0.2125E+01
  0.2375E+01    0.2625E+01    0.2875E+01    0.3125E+01    0.3375E+01
  0.3625E+01    0.3875E+01    0.4125E+01    0.4375E+01    0.4625E+01
  0.4875E+01    0.5125E+01    0.5375E+01    0.5625E+01    0.5875E+01
  0.6125E+01    0.6375E+01    0.6625E+01    0.6875E+01    0.7125E+01
  0.7375E+01    0.7625E+01    0.7875E+01    0.8125E+01    0.8375E+01
  0.8625E+01    0.8875E+01    0.9125E+01    0.9375E+01    0.9625E+01
  0.9875E+01    0.1000E+02    0.3000E+00    0.2500E-01    0.7500E-01
     .     .       .     .       .     .       .     .       .     .
```

grid.new2

```
   82    42    42
  0.0000E+00    0.6667E+00    0.2000E+01    0.3333E+01    0.4031E+01
  0.4094E+01    0.4156E+01    0.4219E+01    0.4281E+01    0.4344E+01
  0.4406E+01    0.4469E+01    0.4531E+01    0.4594E+01    0.4656E+01
  0.4719E+01    0.4781E+01    0.4844E+01    0.4906E+01    0.4969E+01
  0.5031E+01    0.5094E+01    0.5156E+01    0.5219E+01    0.5281E+01
  0.5344E+01    0.5406E+01    0.5469E+01    0.5531E+01    0.5594E+01
  0.5656E+01    0.5719E+01    0.5781E+01    0.5844E+01    0.5906E+01
  0.5969E+01    0.6031E+01    0.6094E+01    0.6156E+01    0.6219E+01
     .     .       .     .       .     .       .     .       .     .
```

grid.new1 and ***grid.new2*** are generated by subroutine **gridgen** from grid description file ***fnewgrid***. The three values in the first line are the numbers of grid points in x, y, z directions, named as *maxx, maxy, and maxz*, respectively. The values of x coordinators of all grid points are listed sequentially from the second line, then those of y and z coordinators of all grid points. In the other word, from the second line, the first *maxx* values are the x coordinators of all grid points along x-axis, the next *maxy* values are y coordinators of all grid points along y-axis, then *maxz* values of z coordinator along z-axis. After these data, the x, y, and z coordinators of the staggered points in the grid system are presented. Therefore, the total number of data in this file is maxx+maxy+maxz+(maxx-1)+(maxy-1)+(maxz-1)=2(maxx+maxy+maxz)-3. ***grid.new1*** has 42+22+22+41+21+21=169 data and ***grid.new2*** has 329 data.

fgridold (defauld value: ***grid.old***)

```
51    26    26
 1.0000E+00     1.7716E+00     1.2235E+01     3.3465E+01     3.4051E+01
 3.4160E+01     3.4246E+01     3.4339E+01     3.4425E+01     3.4504E+01
 3.4571E+01     3.4613E+01     3.4637E+01     3.4662E+01     3.4688E+01
 3.4712E+01     3.4734E+01     3.4762E+01     3.4797E+01     3.4866E+01
 3.5124E+01     3.5210E+01     3.5412E+01     3.5627E+01     3.5851E+01
 3.6084E+01     3.6324E+01     3.6571E+01     3.6824E+01     3.7082E+01
 3.7346E+01     3.7613E+01     3.7886E+01     3.8161E+01     3.8425E+01
 3.8669E+01     3.8867E+01     3.9483E+01     3.9713E+01     3.9921E+01
    .              .              .              .              .
```

This file is generated by subroutine **gridgen** from grid description file ***foldgrid***. The explanation is the same as ***fnewgrid***.

fnewtec**:** (default value: ***new.tec***)

The example shown here corresponds to the finer grid system. This file is generated by subroutine **int2grid**. It is the result of interpolated data in the new grid system defined by ***fnewgrid***. For the coarser gird defined in ***newgrid1***, the new TECPLOT file is about 1.9 M bytes. For the finer grid defined in ***newgrid2***, the new TECPLOT file is about 14 M bytes.

```
TITLE = "intropolated data    "
VARIABLES = "x" "y" "z" "u" "v" "w" "temp"
```

```
ZONE  T= "interpolated data"
I=          82,  J=          42, K=          42,  F = POINT
    0.0000E+00    0.0000E+00    0.0000E+00    0.0000E+00    0.0000E+00
0.0000E+00    0.2990E+03
    0.6667E+00    0.0000E+00    0.0000E+00    0.0000E+00    0.0000E+00
0.0000E+00    0.2990E+03
    0.2000E+01    0.0000E+00    0.0000E+00    0.0000E+00    0.0000E+00
0.0000E+00    0.2990E+03
    0.3333E+01    0.0000E+00    0.0000E+00    0.0000E+00    0.0000E+00
0.0000E+00    0.2994E+03
    0.4131E+01    0.0000E+00    0.0000E+00    0.0000E+00    0.0000E+00
0.0000E+00    0.4101E+03
    0.4194E+01    0.0000E+00    0.0000E+00    0.0000E+00    0.0000E+00
0.0000E+00    0.5029E+03
    0.4156E+01    0.0000E+00    0.0000E+00    0.0000E+00    0.0000E+00
0.0000E+00    0.6437E+03
    0.4219E+01    0.0000E+00    0.0000E+00    0.0000E+00    0.0000E+00
0.0000E+00    0.9085E+03
    0.4281E+01    0.0000E+00    0.0000E+00    0.0000E+00    0.0000E+00
0.0000E+00    0.1241E+04
```

The first line is the title of the datafile. The second line defines the variable names of various columns. The third line defines the grid size and the format of data storage. It has 82x42x42x7= 1012536 data following the first three definition lines for the finer grid.

***finput*: (default value: *input.dat*)**

Two example ***input1.dat*** and ***input2.dat*** are presented here corresponding to the two grid systems shown before.

input1.dat

```
          419
spread.dat
    4.37600
    0.00000
    0.00000
1
spread.dat
    4.42500
    0.00000
    0.00000
0
.       .
.       .
```

input2.dat

```
         3490
spread.dat
    4.40600
    0.00000
    0.00000
0
spread.dat
    4.46900
    0.00000
    0.00000
0
.       .
.       .
```

The first line is the number of particles considered in this input file. From the second line, every five lines define one particle. The second line is the spreadsheet file

name that stores the thermal history and trajectory of the particle. Line 3-5 is x, y, z coordinates of the initial position of the particle considered. The last line is a flag to indicate if the particle trajectory will be appended to the new TECPLOT files. For the coarser grid system, the input file has 419 particles and for the finer grid, 8490 particles.

***fparticle*:** (default value: ***particle.dat*)**

```
i,x0,y0,z0,T0,I0,residence,maxT,peak-No.,size
   1     0.4375E+01     0.0000E+00     0.0000E+00     0.1871E+04     0.0000E+00
0.0000E+00     0.2068E+04     0.2000E+01     0.3780E-03
   2     0.4625E+01     0.0000E+00     0.0000E+00     0.2607E+04     0.0000E+00
0.1740E+01     0.2704E+04     0.7000E+01     0.5217E-04
   3     0.4875E+01     0.0000E+00     0.0000E+00     0.2324E+04     0.0000E+00
0.1104E+01     0.2262E+04     0.4000E+01     0.6133E-04
   4     0.5125E+01     0.0000E+00     0.0000E+00     0.2034E+04     0.0000E+00
0.1381E+01     0.2300E+04     0.4000E+01     0.6946E-04
   5     0.5375E+01     0.0000E+00     0.0000E+00     0.1886E+04     0.0000E+00
0.1142E+01     0.1967E+04     0.3000E+01     0.6428E-04
   6     0.5625E+01     0.0000E+00     0.0000E+00     0.1821E+04     0.0000E+00
0.9841E+00     0.1816E+04     0.4000E+01     0.5714E-04
```

The first line defines the variable names in the file. The symbol *i* is the number of the particle considered, *x0, y0, z0* are the coordinates of the initial position of ith particle, *T0* is the temperature in the initial position, *I0* is the nucleation rate in the initial position, *residence* is the residence time of the particle in liquid metal, *maxT* is the maximum temperature the particle ever experienced in the trajectory, *peak-No* is the number of temperature peak of the trajectory, *size* is the final size of the particle when it reaches the solid region. The file has 419 rows of data for the coarser grid and 8490 rows of data for the finer grid.

***stfile*:** (default value: ***spread.dat*)**

```
   time  temp  x  y  z  u  v  w  step  trwy
    0.0000E+00     0.1839E+04     0.4875E+01     0.1250E+00     0.3250E+00
0.1698E+01     0.1400E+00    -0.1872E+00     0.0000E+00     0.0000E+00
    0.8274E-02     0.1832E+04     0.4890E+01     0.1263E+00     0.3234E+00
0.1839E+01     0.1679E+00    -0.1910E+00     0.1000E+03     0.1560E-01
    0.1682E-01     0.1825E+04     0.4906E+01     0.1279E+00     0.3218E+00
0.1771E+01     0.1979E+00    -0.1917E+00     0.2000E+03     0.3120E-01
    0.2570E-01     0.1817E+04     0.4921E+01     0.1297E+00     0.3201E+00
0.1694E+01     0.2296E+00    -0.1881E+00     0.3000E+03     0.4680E-01
    0.3503E-01     0.1809E+04     0.4937E+01     0.1320E+00     0.3184E+00
0.1608E+01     0.2660E+00    -0.1786E+00     0.4000E+03     0.6248E-01
```

The first line defines the variable names in the file. The symbol *time* is the time the particle experiences in the weld pool after it nucleates, *temp* is the temperature at this

time, *x*, *y*, *z* are the coordinates of the particle at specific time, *u*, *v*, *w* are the components of local velocity at position (x, y, z), *step* is the number of time step.

sizefile: (default value: ***sizespread.dat***)

```
   time  temp  x  y  z  u  v  w  step  trwy
    0.0000E+00     0.1839E+04     0.4975E+01     0.1250E+00     0.3250E+00
0.1499E+01     0.1400E+00    -0.1872E+00     0.0000E+00     0.0000E+00
    0.4274E-02     0.1832E+04     0.4890E+01     0.1263E+00     0.3234E+00
0.1839E+01     0.1679E+00    -0.1910E+00     0.1000E-03     0.1560E-01
    0.1662E-01     0.1826E+04     0.4906E+01     0.1278E+00     0.3218E+00
0.1771E+01     0.1978E+00    -0.1917E+00     0.2000E-03     0.3120E-01
    0.2573E-01     0.1817E+04     0.4921E+01     0.1297E+00     0.3201E+00
0.1694E+01     0.2296E+00    -0.1881E+00     0.3000E-03     0.4680E-01
    0.3503E-01     0.1809E+04     0.4937E+01     0.1320E+00     0.3184E+00
0.1608E+01     0.2660E+00    -0.1786E+00     0.4000E-03     0.6248E-01
```

The data format and explanation is the same as ***stfile***.

fform: (default value: ***form.dat***)

```
Al203
Temp,time,Ivhet,Ivhom,cqi,cmi,wt %,c*,dg(kj/mol)
1900.0    0.2673816E-007   0.6317669E+033   0.8726538E+033   0.0000000
0.0000001   0.4917446E-03    -326.046   0.1188850E-09
```

The first line indicates the name of inclusion considered. The second line defines the variable names of every column. *Temp* is the temperature, *time* is the time needed to finish the reaction extend, *Ivhet* is the heterogeneous nucleation rate, *Ivhom* is the homogeneous nucleation rate, *cqi* is the equilibrium concentration of Q at interface at the temperature, *cmi* is the equilibrium concentration of M at interface at the temperature, *c** is the variables *cstar* defined in equation 14 in page 20, and *dg* is the free energy change of the reaction at the temperature.

fdiss: (defauld value: ***diss.dat***)

```
Al2O3
 Temp,time,cqi,cmi(wt%),c*,dg(kj/mol)
2192.0   0.100000E+002   0.0843491   0.0263928   0.0000E+000        0.00
```

The explanation of this file is the same as ***fform*** except that there is no nucleation consideration during the dissolution of inclusion.

A3. USER'S GUIDE

Before particle tracking, a TECPLOT file ***foldtec***, which contents the detailed information of the temperature and velocity fields, is generated by another program **weld3d**[1]. The particle tracking calculations start with interpolation of the temperature and velocity fields and other variables, if required, into a new uniform grid. Therefore, the original and new grid systems must be stated. Two data files that describe the setup of the original and new grids, ***foldgrid*** and ***fnewgrid***, must exist before running the program. Examples of grid files are presented in Appendix A. There is an option in the program that you can select if the original positions of particles are generated from the grid system automatically or are given by other input. If the original positions of particles are given from an input file, ***finput***, it must be presented before the program running. The data format of this input file is presented before. These three (or four) files are the only required files to run the program.

A graphic interface is developed to make the calculation friendlier to users. The program is compiled and developed using Compaq Visual FORTRAN 6.0. The compiled executive file can be run in any Windows environments without the development platform. The user just needs to select options presented in the various dialog boxes.

1. Welcome!

The executable file, **inclusion.exe**, is running under Windows environment. To run this program, just double click its icon and a 'Welcome' window shown below will pop up. Just click the 'Continue' button to start the calculations.

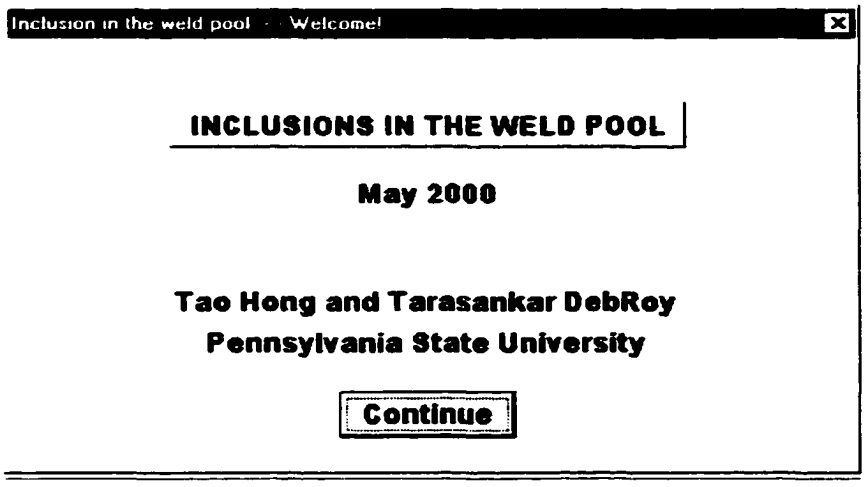

2. Select an inclusion

The user is asked to select only one inclusion at a time. Fourteen inclusions are available in this program as shown below.

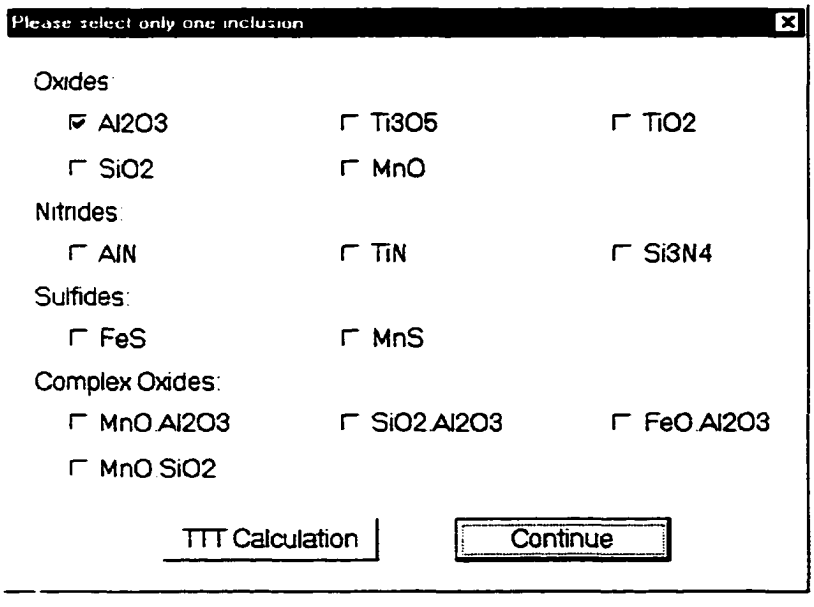

3. Data file names and directory

In the frame, the working directory in which all the following data files will be saved is asked to be clearified at first. Then the file name of original and interpolated

TECPLOT file names, the original and new grid description file names, the original and new grid file names are selected.

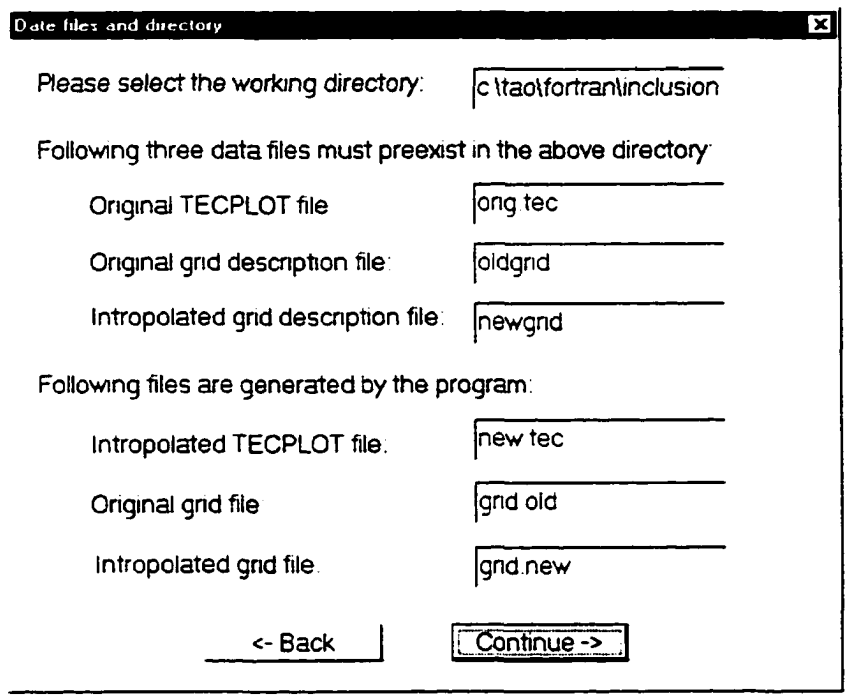

4. Data format in the original TECPLOT file

In this frame, the saving format of all variables will be verified in the original TECPLOT file which includes the temperature and velocity fields in the weld pool.

The number of total columns of data in ***foldtec***, the column numbers of three components of velocity (u, v, and w), the column number of temperature are in the first five boxes. If other variables in the TECPLOT file is selected to be interpolated in the new grid system, their column number in ***foldtec*** and variable names must be filled in. If there is no other variable to select, just leave the box as the default value '0' or blank.

The last box is the line in ***foldtec*** from where the real data is presented from. As the format of ***foldtec*** presented in preverious section, this number will be '4'.

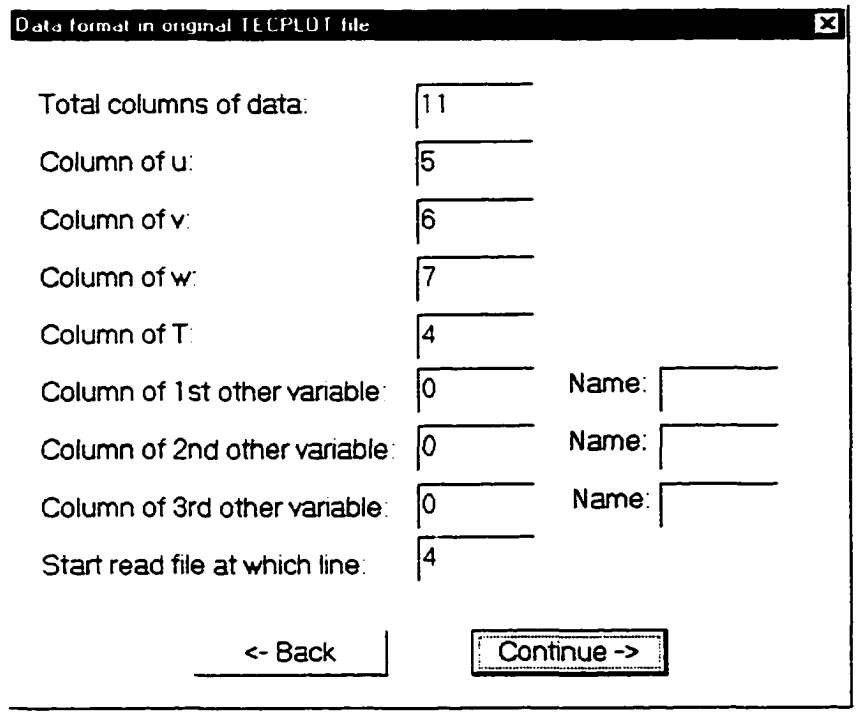

5. Particle tracking parameters

The parameters used in particle tracking calculation are stated in this frame. The initial positions of tracked particles can be generated from the interpolating grid system automatically by the program. They also can be read from an input file. The format of input file, ***finput***, is presented in the previous section.

The solidius temperature is used to filter the variables out of the liquid region. It is also a critirion to judge if the particle reach the solid/liquid interface. You can also select the particle tracking method in this frame.

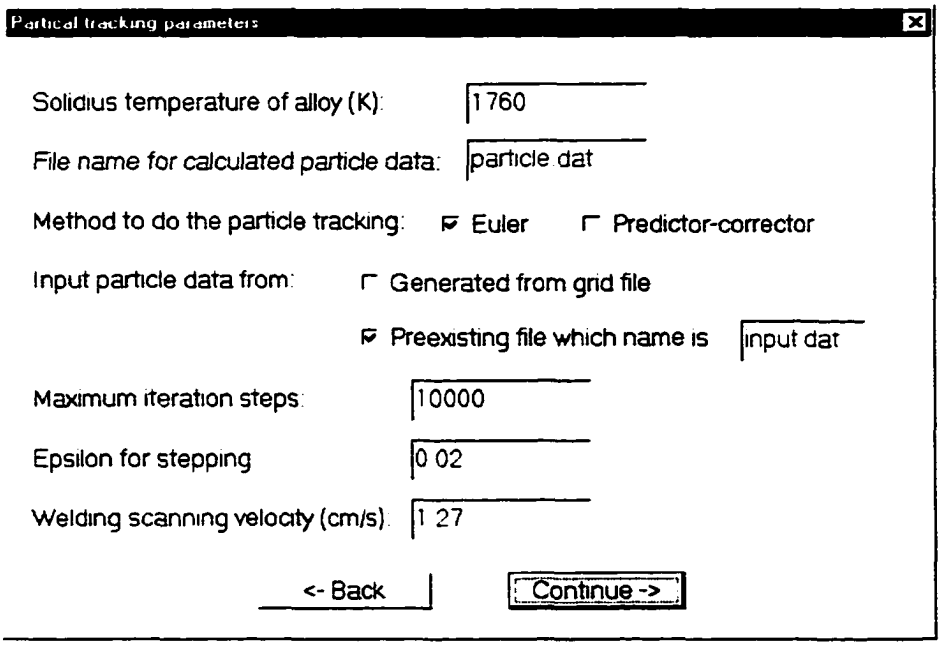

6. TTT calculation default values

In the frame shown below, user can revise four groups of default values.

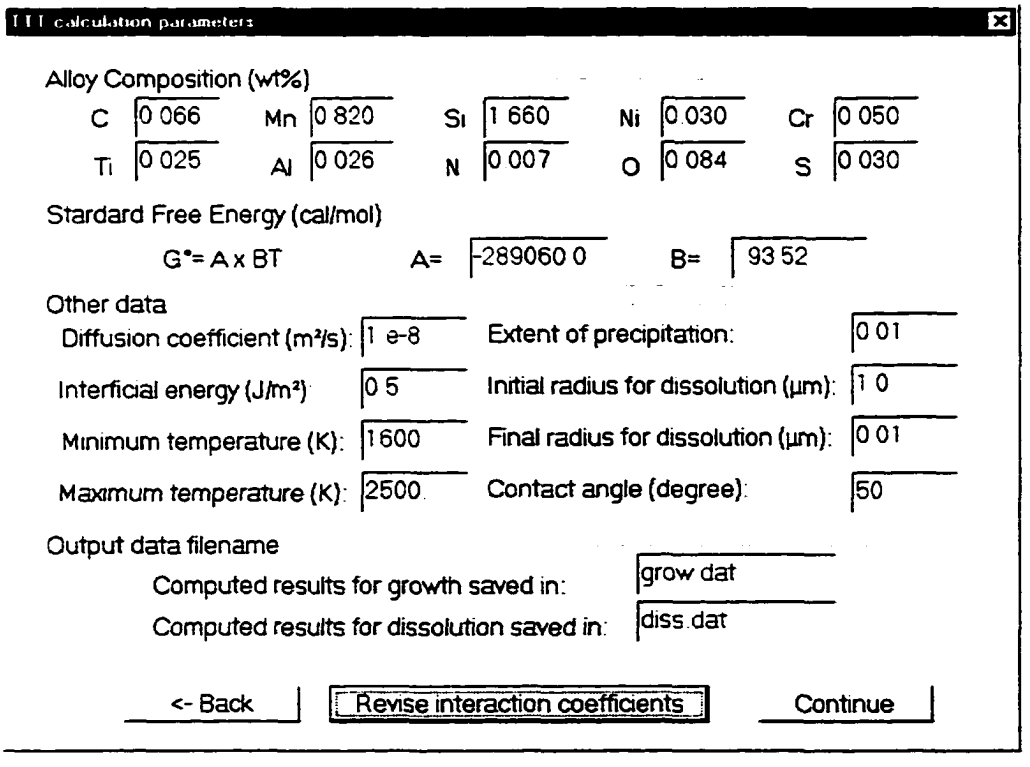

6.1. Selection of alloy composition:

Steels containing ten elements shown in the above frame are considered here. Their concentrations may be selected by the user. The default values are presented in Table 1 of Appendix C.

6.2. The standard free energy data:

The standard free energy for the formation is expressed as $\Delta G^0 = a + b \cdot T$. The values of a and b for the inclusion selected can be changed if necessary. The default values[9] of a and b are presented in Table 2 of Appendix C

6.3. Kinetic data and other:

The following parameters used in the calculations can be changed: a) diffusion coefficient, D_0, of the nonmetallic elements in equations (14), (22), (23) and (26), b) interfacial energy, σ, in equation (15), c) and d) minimum and maximum temperatures for plotting TTT diagram; e) the extent of precipitation, ζ, in equations (20) and (21), which equals to 0.01 when the precipitation starts and equals to 0.99 when the precipitation is over, f) the initial inclusion radius for dissolution, r_0, g) the assumed final inclusion radius for dissolution calculation, r_f and h) the contact angle, θ, between the free surface of inclusion nuclei and substrate phase in equation (17)-(19). The units of these parameters are presented in the dialog boxes.

6.4. Output data file names

The output data filenames for both growth and dissolution are selected. The default names are ***fform*** and ***fdiss***. The data files contain computed temperature versus time data and equilibrium concentrations versus temperature data for the inclusion selected. The formats of these two files are presented in Appendix A.

7. The first order interaction parameters

The first order interaction parameters e_i^j for all the elements are taken from reference 6. These values have been assumed to be independent of temperature. However, these values can be changed if more accurate values become available. The default values[6] are presented in Table 3 of Appendix C.

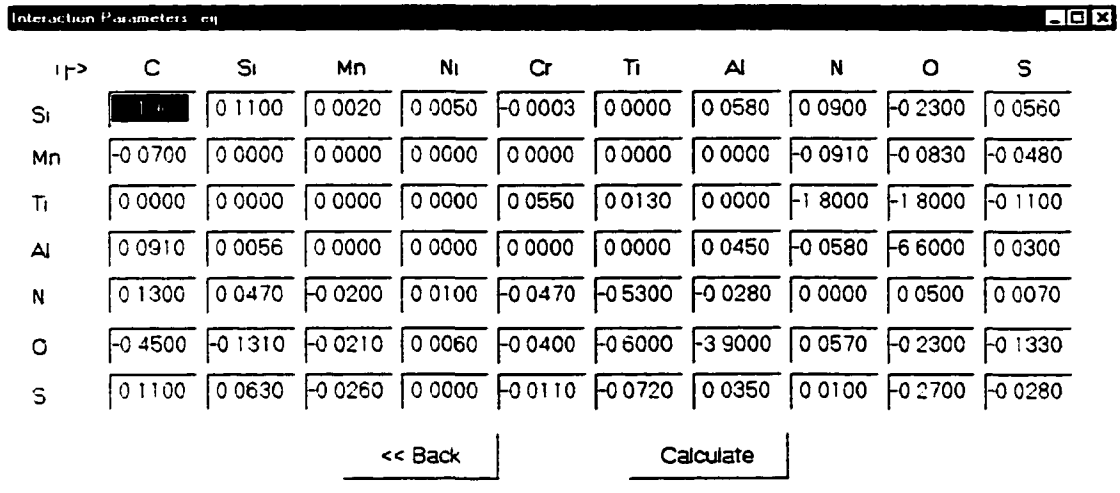

After all the dialog frames, the calculation will begin and the following data files will be generated:

fnewtec

We can plot temperature and velocity fields using TECPLOT from ***fnewtec***. If the spreadsheet files of particle tracking are selected to append to the ***fnewtec*** file, the trajactories of selected particles can also be plotted from ***fnewtec***.

fparticle and sizefile

We can plot the size distribution figures (histogram plot), check which particle with which initial position has continueous cooling behavior(no thermal peak), complicated

thermal history (tens of peaks). We can also plot the residence time distribution and final radii vs. residence time figuress. Lots of other plots can be done from this data file.

fform and fdiss

From these files, the TTT diagrams for the formation and dissolution of selected inclusion can be plotted. They also contain information about equilibrium concentrations, formation free energy and etc at different temperatures.

stfile

The size change and temperature gyration of selected particle can be plotted from this file.

A4. FUNCTIONS AND SUBROUTINES

1. Main program

To run the calculation program, three data files, ***foldtec***, ***foldgrid***, and ***fnewgrid***, must preexist in the working directory. If the original positions of particles are required to input by user from input file, an input file ***finput***, must exist.

At first, all variables and arrays are defined and assigned. A graphic interface is developed in main program, too. The user is asked to input the working directory, data file names, thermodynamics and kinetics data, input and output data format, and etc. The user is also asked to select the type of inclusion, method of particle tracking and way to generate the original input files. The details of the graphic interface programming will not be discussed in this section because the commands and syntaxes are quite different to different development environment. For the detailed reference, please read the Programming Guide of Compaq Visual FORTRAN 6.0.

The subroutine **ttt** is called after all the initialization procedure finishes. This subroutine will calculate the TTT diagrams for both formation and dissolution of selected inclusion in liquid state.

```
call ttt(con,eij,mm(nincl),qq(nincl),xx(nincl),yy(nincl),
1       am(mm(nincl)),am(qq(nincl)),gaa,gbb,tmin,tmax,nincl,
1       inclusion(nincl),sigma,fform,fdiss,vm(nincl),d00,r0,
1       rf,theta,zeta)
```

Subroutine **gridgen** is called to generate grid files from the grid description files. The two generated grid files are names ***fgridnew*** and ***fgridold*** by default setting.

```
call gridgen(foldgrid,fgridold)
call gridgen(fnewgrid,fgridnew)
```

Subroutine **int2grid** is called to interpolate the selected variables (temperature and three units of velocity, u, v, and w are default selection) into the new grid system. A new TECPLOT file, ***fnewtec***, is generated based on the new grid file.

```
call int2grid(vari,nxm,nym,nzm,maxvar,cor,nvm,maxnod,
1       varna,ttsol,fgridold,fgridnew,nfirstl,foldtec,
1       fnewtec,ncol,filoc,nodmax)
```

In order to run the particle tracking program for thousands of particles which original positions are generated automatically from the every point in the liquid domain in the new grid system, a small subroutine, **inputgen,** must be called.

```
if (iinput1) call inputgen(finput,fnewtec,fgridnew,ttsol)
```

The input file generated by **inputgen** is named as ***finput***. It includes the information of initial position of every particle, the index to show whether the calculated spreadsheet data will be appended to the TECPLOT file. This input file can also be written manually to select some particles in specific locations. The interpolated velocities are then modified to take the scanning velocity of heat source into account by the following commands:

```
      do 85 k=1,nodmax(3)
            do 85 j=1,nodmax(2)
                  do 85 i=1,nodmax(1)
                        vari(i,j,k,l)=vari(i,j,k,l)+scanvel
85 continue
```

Original position of every particle in the input file is read as (poi(1), poi(2), poi(3)), and the subroutine **partra** (for Euler method) or **partra2** (for predictor-corrector method) is called to calculate the trajectory of the particle. The particle trajectory is saved in the file ***stfile***. Subroutine **particle** is then called to calculate the nature of the particle temperature gyration, such as residence time in the liquid pool, number of thermal peaks, nucleation rate at the original position, and final size after the particle embedded in solid region, etc. The tasks shown above are done by following commands:

```
      do 90 i=1,numst
********** spreadsheet-file & append streamzone? *************
            read (37,*) stfile
            do 95 j=1,3
95          read(37,*) poi(j)
            read (37,*) aptec
            write(*,*) i, 'th particle is being tracked'
            call partra(vari,poi,cor,nodmax,varpoint,nxm,nym,nzm,
     1            maxnod,maxvar,nvm,ttsol,maxstep,epsi,stfile,aptec,i)
            call particle(stfile,ttsol,con,eij,nincl,mm(nincl),qq(nincl),
     1            xx(nincl),yy(nincl),am(mm(nincl)),am(qq(nincl)),gaa,gbb,i,
     1            d00)
90    continue
```

2. subroutine **inputgen**

This subroutine generates an input file which can be used when the program is running automatically from the new interpolated TECPLOT file. The filenames of the new grid file and new TECPLOT file are transferred from the main program. The generated file ***finput*** includes all particles locating in the every grid point of the new grid system and in the liquid region:

```
      write(*,*) 'nx,ny,nz ',nodx,nody,nodz
      do 805 i=1,nodx
            do 805 j=1,nody
                  do 805 k=1,nodz
                        read (33,*) xx,yy,zz,u,v,w,temp
                        if (temp.gt.ttsol) then
                              n=n+1
                              x(n)=xx
                              y(n)=yy
                              z(n)=zz
```

```
                        endif
805       continue
```

3. subroutine **gridgen**

This subroutine generates grid files in which the three coordinators of all grid points are clarified in (x,y,z) format. A grid description is required. For the following examples, ***fgridnew*** and ***fgridold*** are generated by **gridgen** from grid description files ***fnewgrid*** and ***foldgrid***, respectively.

```
  xu(1)=0.0
  11=2
  ilas=0.0
  do 940 j=1,nzx
          11 = 11+ncvx(j)
          in(j)=0
          ik(j)=1
          if (j.eq.1) in(j)=1
          if (j.eq.1) ik(j)=0
          ist=ilas+1+in(j)
          ilas=ist+ncvx(j)-ik(j)
          ndif = -1+ik(j)
          do 950 i=ist,ilas
                  ndif = ndif+1
                  if (powrx(j).ge.0.0) then
                          term=(float(ndif)/float(ncvx(j)))**powrx(j)
                  else
                          term=1.-(1.0-float(ndif)/float(ncvx(j)))**(-powrx(j))
                  endif
                  xu(i) = xu(ist-1)+xzone(j)*term
950               continue
940       continue
  do 960 i=2,11-1
960       x(i) = xu(i)+(xu(i+1)-xu(i))/2.0
  x(11)=xu(11)
```

From fifth to eighth lines indicates the description of y direction grid system, and from ninth to twelfth lines is that of z direction grid. The formats of these grid files are presented in Appendix A.

4. Subroutine **int2grid**

This subroutine interpolates the variables (temperature, velocity and others) into a new uniform grid system. Before calling this subroutine, two grid files, ***fgridold*** and

fgridnew, must be generated by subroutine **gridgen** as input files as well as the original TECPLOT file, ***foldtec***. It generates the new interpolated TECPLOT format file, ***fnewtec***, for further calculation. In ***fnewtec***, the value of velocities must be presented in the first column, then temperature and other selected variables. This sequence must not be changed for the subsequent routines to work. More information about this subroutine is available in Reference 2.

5. subroutine **partra and partra2**

partra2 does the particle tracking calculation in the predictor-corrector technique. **partra** does the particle tracking calculation using conventional Eular method. The original position of tracked particle is transferred from the main program. The generated file by this subroutine is the spreadsheet file ***stfile*** which contains information of the temperature-time thermal cycle of this particle. One example of the spreadsheet file is shown in Appendix B

6. subroutine **intropol**

This subroutine calculates the new value of selected variables in the new grid system. What **intropol** does is 1) for a give point, poi, determine i, j, k, i', j', and k', where the primes denote staggered locations if request start the search at a node which has been supplied as parameters; 2) interpolate the variable value from the edges of the cell to poi by using the lever rule, the distribution of the variables in the program is shown in Figure A2.

7. subroutine **particle**

This subroutine calculates the characteristic of the particle trajectory, such as residence time of particle in liquid region, number of temperature peak, peak temperature, and call the subroutine **sizef** to calculate the size change and final size. The spreadsheet

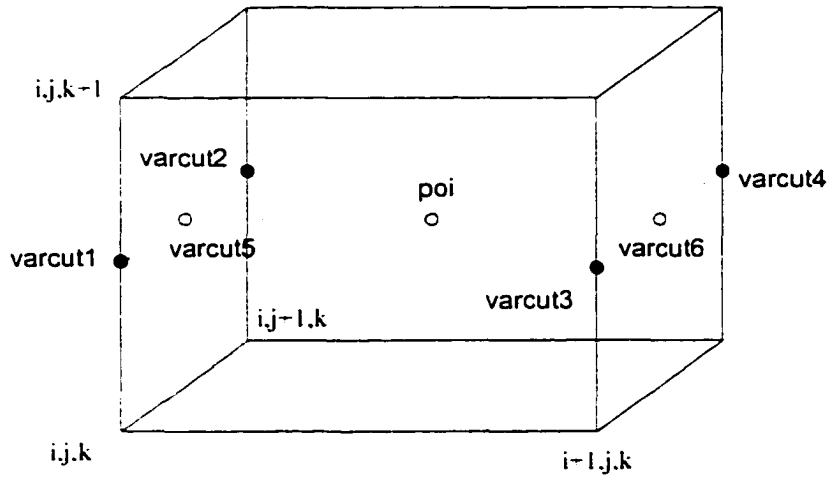

Figure A2. Definition of variables in variable interpolation

data files generated by **partra2** (or **partra**) are input file of subroutine **particle**.

This subroutine counts peak numbers, peak positions, peak temperatures, residence times and etc. of the temperature-time curves indicated in spreadsheet data file ***stfile***

The method used to find a temperature peak is illustrated in the figure above. The slopes of lines connecting sequential points were calculated one by one, for instance, slope s1 =(T2-T1)/(t2-t1), slope s2=(T3-T2)/(t3-t2). If a slope has positive value and the following slope has negative value, we can conclude that there is a temperature peak between these two points. In above figure, s1 is positive and s2 is negative, therefore, there will be a peak between t2 and t3. This evaluation is acceptable if the time step is small enough and there is no infinite slope in the whole temperature-time curve. Following sentences in the program finish this calculation. The calculation is done by following commands:

```
  do 1020 i=2,step
          if ((p(2,i).gt.ttsol).and.(pool.eq.0)) then
                  timein=p(1,i)
                  timeout=timein
                  pool=1
                  do 1030 j=1,3
1030                      poolin(j)=p(j+2,i)
          endif
          s1=p(2,i)-p(2,i-1)+1.e-30
          s2=p(2,i+1)-p(2,i)+1.e-30
          if (s1*s2.lt.0 .and. pool .eq. 1 .and. s1.gt.0)  then
                  peak=peak+1
                  peaktime(peak)=p(1,i)
                  peaktemp(peak)=p(2,i)
          endif
          if ((p(2,i).lt.ttsol).and.(pool.eq.1))then
               timeout=p(1,i)
               pool=0
                  do 1040 j=1,3
1040                      poolout(j)=p(j+2,i)
          endif
          if(maxtemp.lt.p(2,i)) maxtemp=p(2,i)
1020      continue
  du=timeout-timein
  sizefinal=sizef(stfile,ttsol,nincl,m,q,amm,amq,x,y,eij,
  1       con,gaa,gbb,d00,sigma)
  aiv0=0.0
  write(36,1006)numpar,(p(i+2,1),i=1,3),tori,aiv0,du,maxtemp,
  1       float(peak),sizefinal
1006      format(i4,9e14.4)
```

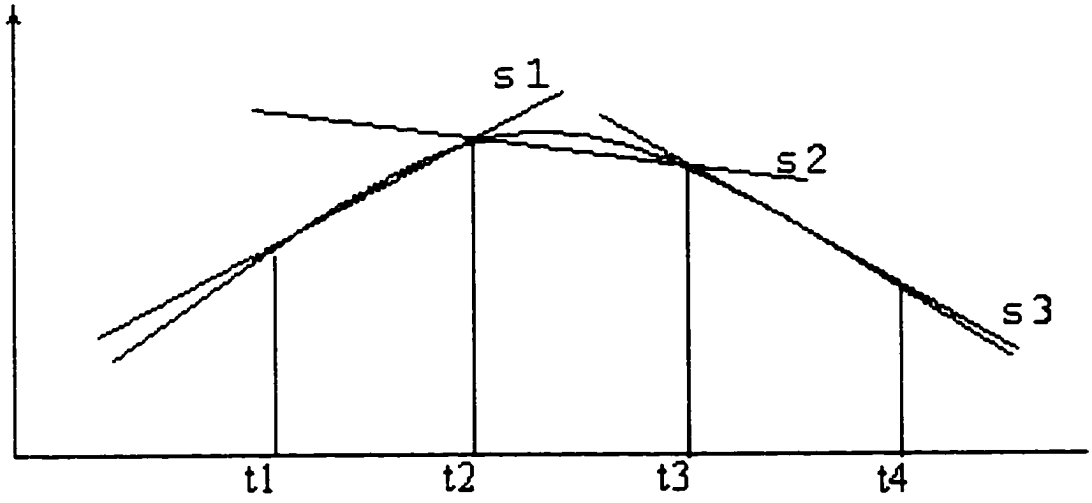

Figure A3. How to identify a temperature peak in the temperature-time curve

Subroutine **sizef** is called to calculated the size change of this particle which temperature-time history is stored in the spreadsheet data file ***stfile***.

The evaluation results of all the particles are stored in files ***fparticle***, i.e. original position, original temperature and nucleation rate, residence time, maximum temperature, temperature peak number and final size of particles before it engulf in the sold region of weldment. The typical data formats of the file are presented in Appendix A.

8. function **sizef**

In this subroutine, the size change of the particle is calculated from the equations 25 and 26. The equilibrium concentration of Q at the interface between the inclusion and liquid bulk must be calculated first by calling the subroutine **equcon**. The final size when the particle reaches the solid region is transferred to subroutine **particle**.

```
      do 710 l=2,lmax
            read(40,*,end=720) time1(l),temp(l),corx,cory,corz,u,v,w,
     1      step,trwy
            deltat=time1(l)-time1(l-1)
            if (temp(l).lt.ttsol) goto 720
            akeq=exp(-dgz(temp(l),gaa,gbb)/(1.98*temp(l)))
            cqb=con(q)
            cmb=con(m)
            cqi=cqb*.5
            cmi=cmb*.5
            cqp=(amq*y)/(amm*x+amq*y)
            call equcon(m,q,eij,akeq,x,y,con,cmi,cqi,amm,amq)
            cstar=(cqb-cqi)/(cqp-cqi)
            if (cqi.lt.cqb) then
                  alpha=sqrt(2.*d00*cstar)
                  rr=rr+alpha/sqrt(time1(l))*deltat
            else
                  ak=-2.*cstar
                  if (rr.gt.0.0) then
c                       ak=temp(l)/1800.
                        rr=rr-ak*d00*deltat/2./rr-ak*sqrt(d00*deltat/3.1416)
                  endif
                  if (rr.lt.0.0) rr=0.0
            endif
730         write(41,702) time1(l),temp(l),corx,cory,corz,u,v,w,step,
     1      trwy,rr
702         format(11e14.4)
710   continue
```

9. subroutine **ttt**

In the program an inclusion is defined by an index, nincl. When its value is less than 10, the inclusion is a simple compound whereas a higher value designates a complex inclusion.

```
if (nincl.le.10) then
.
endif
if(nincl.gt.10) then
.
endif
```

The chemical formula of the compound and the atomic weights of its constituents are then defined.

```
x=xx(nincl)
y=yy(nincl)
q=qq(nincl)
m=mm(nincl)
amm=am(m)
amq=am(q)
```

At any given temperature, a function **aiv** (**aiv2** for complex oxide) is called to calculate the heterogeneous and homogeneous nucleation rates.

```
vhetiv=aiv(temp,theta,con,x,y,eij,nincl,m,q,gaa,gbb,dg,homiv)
```

Furthermore, a subroutine named **equcon** (**equcon2** for complex oxide) is called to calculate the equilibrium concentration of M and Q at the interface, *cmi* and *cqi*, respectively at a given temperature:

```
call equcon(m,q,eij,akeq,x,y,con,cmi,cqi,amm,amq)
```

At the equilibrium temperature, the concentration of Q at the interface is equal to that in the bulk alloy. The inclusion begins to dissolve above this temperature and calculations are performed for inclusion dissolution. Below this temperature, calculations are performed for inclusion growth.

```
      if (cni.lt.cnb) then
      .
      else
      .
      endif
```

The program calculates the TTT diagram for formation from equation (21) and dissolution from equation (22) and writes the results in two data files by following commands:

```
      cstar=(cqb-cqi)/(cqp-cqi)
      if (cqi.lt.cqb) then
            alpha=sqrt(2.*d00*cstar)
            t=((-15.*cstar*log(1.-zeta))/(8.*(hetiv+small)*pi*
     1      alpha**3))**0.4
            if(t.lt.told) goto 30
            write(20,1)temp,t,hetiv,homiv,cqi,cmi,cstar,dg/1000.
     1      format(f6.1,3(e15.6e3),f11.7,f11.7,e14.6e2,f11.3)
            told=t
      else
            if(ic.eq.0) then
                  write(21,6)temp,10.,cqi,cmi,0.,0.
                  equtemp=temp
                  ic=1
            endif
            ak=-2.*cstar
            rr=r0
            do 60 time=dt,10.,dt
                  rr=rr-ak*d00*dt/(2*rr)-ak*sqrt(d00*dt/pi)/2.
                  if (rr.lt.rf) goto 70
     60           continue
     70           write(21,6) temp,time,cqi,cmi,cstar,dg/1000.
     6      format(f6.1,e15.6e3,f11.7,f11.7,e13.4e3,f11.2)
            endif
```

The computed results for the formation and the dissolution of the oxides are stored in two output files, ***fformt*** and ***fdiss***. Their formats are presented in Appendix A.

10. functions **aiv** and **aiv2**

These two functions calculate the nucleation rates at different temperatures in liquid metal for simple compounds and complex oxides. The formation free energy change is calculated from equation (5) or (11) by the command:

```
dg=dgz(temp,gaa,gbb)-1.98*temp*log((abs(actm)**x)*(abs(actq)**y))
```

The nucleation rates are calculated from equations (17) to (19) by following commands

```
      fm=0.
      fq=0.
      ftheta=0.25*(2+cos(theta))*(1-cos(theta))**2
      do 100 i=1,10
            if (m.ne.0) emj=eij(m,i)
            if (m.eq.0) emj=0.0
            fm=fm+con(i)*emj
            fq=fq+con(i)*eij(q,i)
100   continue
      actm=10.**fm*con(m)
      actq=10.**fq*con(q)
      dg=dgf(temp,gaa,gbb)-1.38*temp*log(actm**x*actq**y)
      dg=dg*4.18
      dghom=16.*pi*sigma**3.*vm*ninel**2./(3.*dq*dg)
      dghet=dghom*ftheta
      aiv=a*ftheta**(1./6.)*exp(-dghet/bk*temp)
      homiv=a*exp(-dghom/bk*temp)
```

11. subroutine **equcon** and **equcon2**

These two subroutines calculate the equilibrium concentrations of the constituent elements at the interface. When m = 0, the metallic elements in the inclusion is iron. This situation is dealt with by following commands separately:

```
      if (m.eq.0) then
            do 450 ii=1,10
                  fq=0.
                  do 460 i=1,me
                        if (i.eq.q) goto 460
                        fq=fq+con(i)*eij(q,i)
460                     continue
                  fq=fq+cqi*eij(q,q)
                  fq=10.**fq
                  cqi=((1/akeq)**(1./float(y)))/fq
450               continue
      endif
```

To achieve rapid convergence, when the concentration of the metallic element in the bulk is higher than that of the nonmetallic element, the value of cqi, is calculated first, and vice verse. This calculation is achieved by following commands:

```
            do 430 ii=1,10
                  fm=0.
                  fq=0.
                  do 420 i=1,me
                        if (i.eq.q.or.i.eq.m) goto 420
                        fm=fm+con(i)*eij(m,i)
                        fq=fq+con(i)*eij(q,i)
420                     continue
                  fm=fm+cqi*eij(m,q)+cmi*eij(m,m)
                  fq=fq+cqi*eij(q,q)+cmi*eij(q,m)
                  fm=10.**fm
                  fq=10.**fq
                  if(con(m).gt.con(q)) then
                        actm=fm*cmi
                        actq=(1./(akeq*(actm**float(x))))**(1./float(y))
                        cqi=actq/fq
```

```
                cmi=con(m)-float(x)*amm*(con(q)-cqi)/(float(y)*amq)
            endif
            if(con(m).lt.con(q)) then
                actq=fq*cqi
                actm=(1./(akeq*(actq**float(y))))**(1./float(x))
                cmi=actm/fm
                cqi=con(q)-y*amq*(con(m)-cmi)/(x*amm)
            endif
430         continue
```

A5. Examples of Calculation Results

Figure A4 shows the temperature and velocity in the original non-uniform grid system. Figures A5 and A6 show the interpolated results of temperature and velocity fields in two uniform grid systems. The grid in Figure A5 is coarser than that in Figure A6.

The number of grid points located in the liquid region in the coarse grid is 419, and that in the fine grid is 8491. Those grid points are taken as the initial position of inclusion nuclei and particle tracking calculation is applied to calculate the particle trajectories and their size change. Figure A7 shows 3 particle trajectories in the temperature and velocity fields. Figure 8 shows the thermal cycles of these 3 particle.

Figure A9 shows the comparison of the size distribution of the calculated results from both coarse and fine grid. It is observed that the trend of distribution has not big difference. Figure A10 shows the relation between particle size and residence time of particle during the growth and dissolution.

There are some other adjustable parameters in the calculation such as the contact angel θ in the calculation of heterogeneous nucleation rate. Because the lack of data, we take 50° as the contact angel.

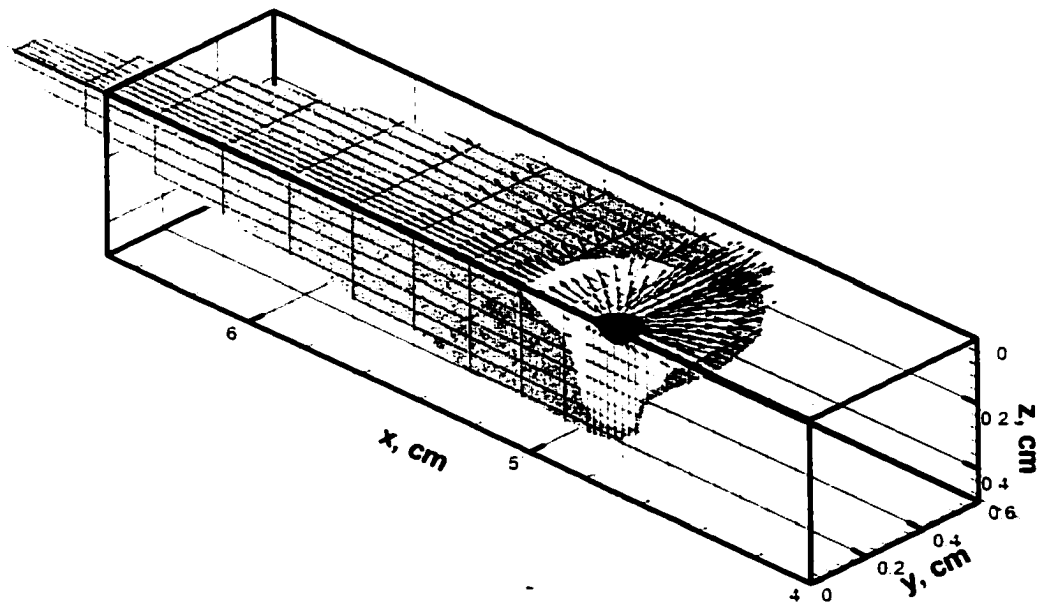

Fig.ure A4. Temperature and velocity fields in the non-uniform grid system

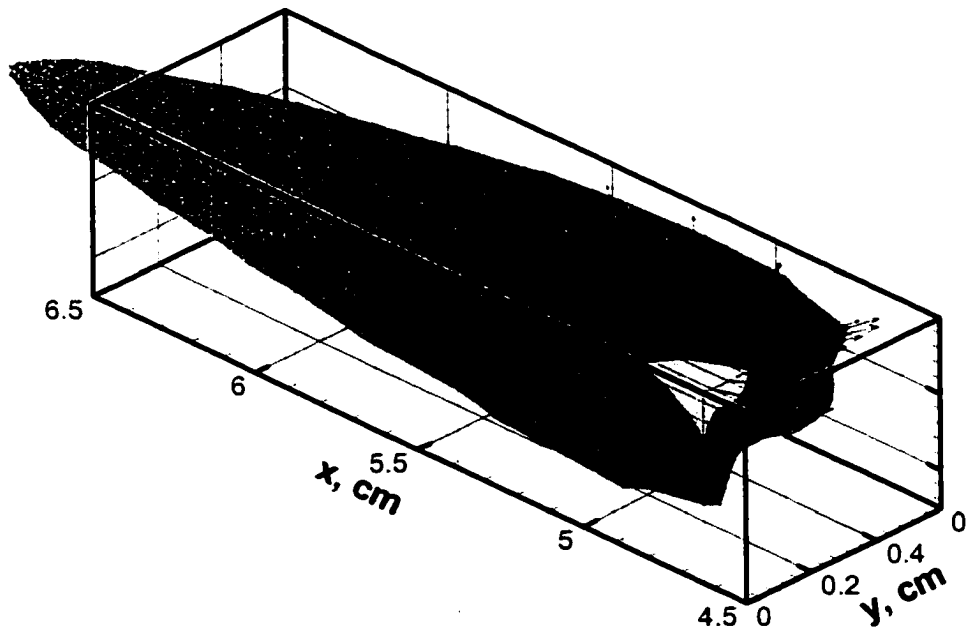

Figure A5. Temperature and velocity fields in a coarser grid system

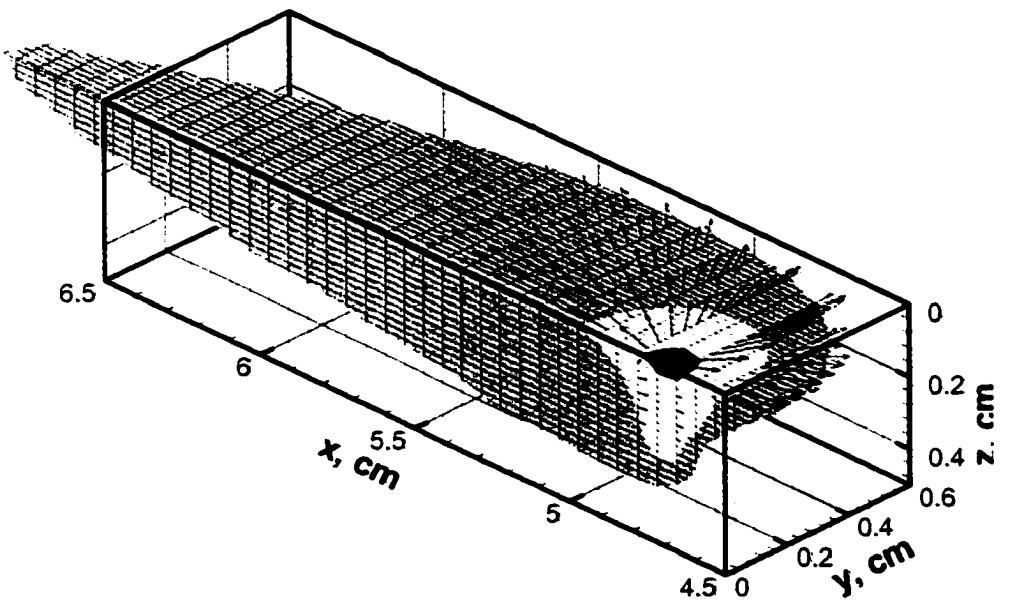

Figure A6. Temperature and velocity in a finer grid system

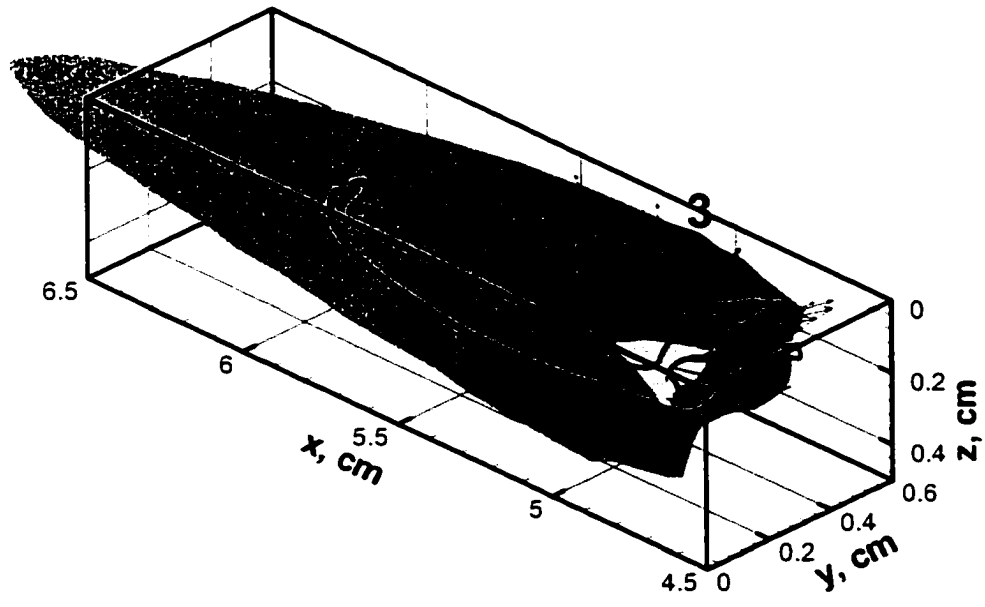

Figure A7. Temperature and velocity fields in the weld pool as well as 3 trajectories of particles numbering as 1, 2, 3.

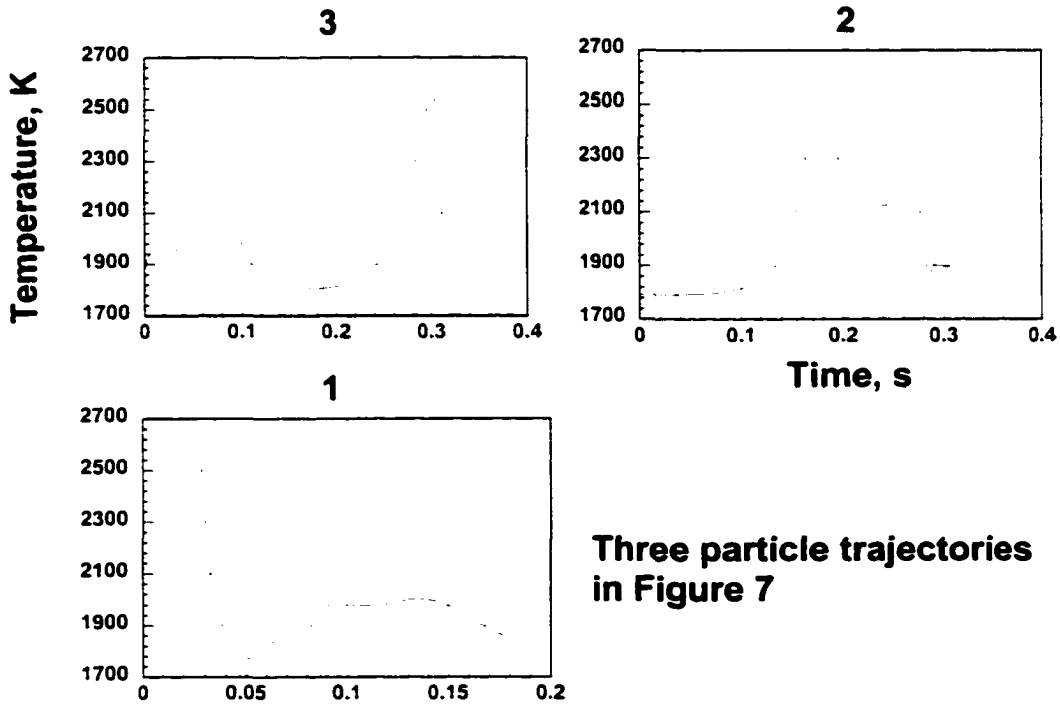

Figure A8 The thermal histories of the three particles in Figure 7

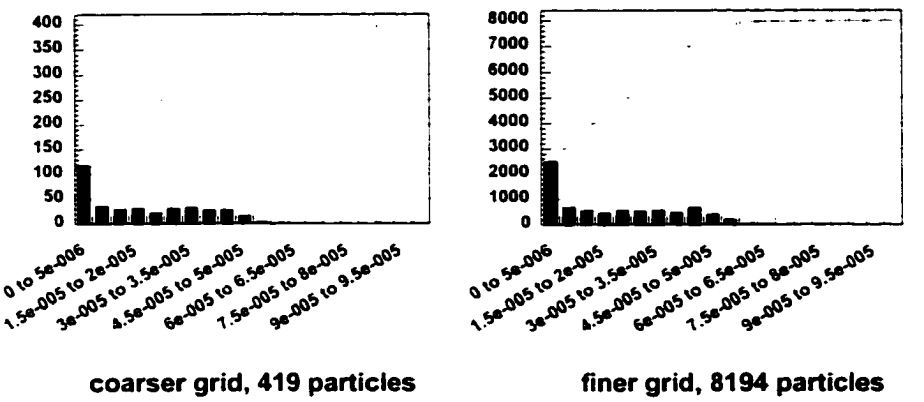

Figure A9 Comparison of calculated size distribution results from coarse and fine grid

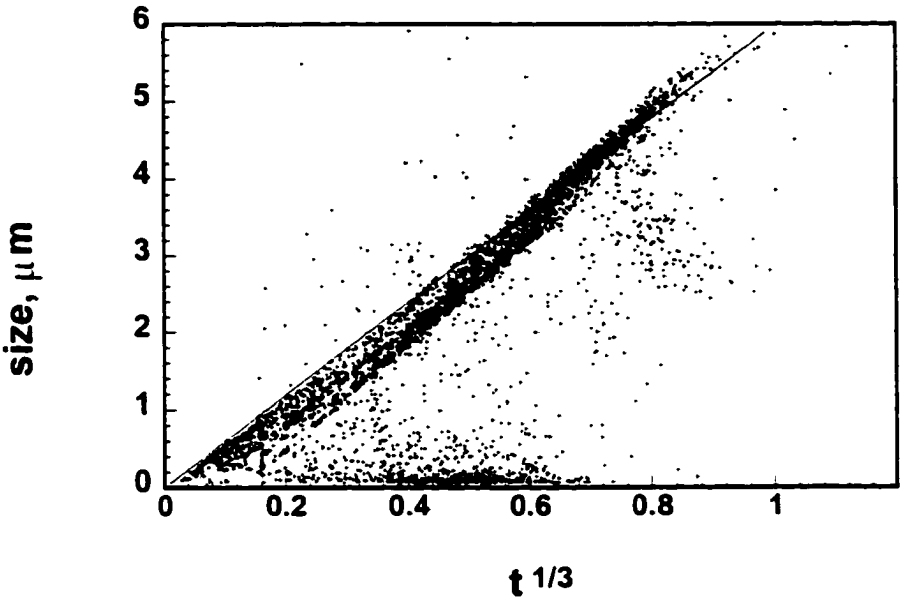

Figure A10. The relation between particle size and $t^{1/3}$

Appendix B

Nomenclature in the FORTRAN Program

Main program:

a:	A in overall kinetics equation
am(me):	atomic masses of elements
aptec:	index of append spreadsheet to TEC file?
bk:	Boltzman constant
col(maxvar):	columns of variables in old TEC file(string)
cor(maxnod,3,2):	coordinate at a-location of grid c (c=1 for scalars, 2 for velocities)
con(me):	concentrations of elements
d00:	diffusivity of selected elements
d0(me):	diffusivity of elements
eij(me,me):	interaction coefficients
epsi:	σ for stepping in particle tracking
fdir:	working directory
filoc(maxvar):	columns of variables in old TEC file
foldtec, fnewtec:	names of old and new TEC files
foldgrid, fnewgrid:	names of old and new grid description files
fgridold, fgridnew:	names of old and new grid files
fparticle:	file names storing info of every particles
finput:	input file names(x,y,z) of particles
fform, fdiss:	TTT diagram data file for formation and dissolution
ga(mi), gb(mi):	a and b in ΔG^0=a+bT for every inclusion
gaa, gbb:	a and b in ΔG^0=a+bT for selected inclusion
idialog:	return variable of dialog functions
iindex(mi):	indexes of inclusions
iinput1, iinput2:	index of input method, 1: file 2: generate
ieuler, ipc:	index of tracking method and
inclusion(mi):	name of inclusions
nodmax(3):	number of grids in three-direction
nodsm(3,2):	last node of grid b in a-direction before poi(a)
ncol:	total column number in old TEC files
nincl:	index of selected inclusion
nfirstl:	first line of data in old TEC file
nvm:	number of variables need intropolated
nxm, nym, nzm:	the maximum nod of grid

numst: number of particle in inputfile
maxnod: max(nxm,nym,nzm)
maxvar: maximum number of variables in TEC files
maxstep: maximum step in particle tracking
mi: number of inclusion
me: number of elements
mm(mi),mm2(mi): index of M and M" of every inclusions
m, m1, m2: index of M and M" of selected inclusions
poi(3): coordinate of particle (poi(1),poi(2),poi(3))
qq(mi): index of Q of every inclusions
q: index of Q of selected inclusion
retlog, retint: returning value of dialog functions
r0,rf: initial and final radii for dissolved particle
scanvel: scanning velocity of power source
stfile: file name of spread sheet (particle tracking)
string: a character variable in dialog box
sigma: interfacial energy
tmin, tmax: min and max temperature in TTT diagram.
theta: contact angle for heterogeneous nucleation
ttsol: solidous temperature of alloy
vari(nxm,nym,nzm,maxvar): value of variable maxvar at grid-location (a,b,c)
varna(maxvar): name of variables
varpoint(maxvar): value of variable a at point poi
vm(mi): molar volume of inclusions
xx(mi), xx2(mi): x, x1, x2 in inclusions formation formula
x, x1, x2: x,x1,x2 of selected inclusion
yy(mi): y in inclusions formation formula
y: y of selected inclusion

inter2grid:

corna(3): name of three coordinators, 'x', 'y', 'z'
found: number of nodsm have been found by `interpol`
head(n): the first several text lines in old TECPLOT file
l1, m1, n1: local convenient variables of nodmax(1-3)
maxdi: max distance in current cell
newcor(maxnod,3): coordinators of every nod in 3 directions in new grid
newnodmax(3): the number of nod in 3 directions
nvari(nxm,nym,nzm,maxvar): interpolated value of selected variables in new grid
startat: index of if search for poi in interpolation routine should be started at nodsm
vari(nxm,nym,nzm,maxvar): value of every selected variables in new grid

other variables: same as those in Main Program

partra (partra2):

accu1,accu2,accu3:	accuracy criterion to stop the tracking
cha:	fraction of change between old (oldpoi) and new (poi) fluid velocity vectors
cosan:	fluid velocity at oldpoi
coord(3):	coordinator of particle
deltim1:	current timestep
difvel:	difference in particle- and fluid-velocity
epsi:	max. allowed fraction of change
found:	number of nodsm have been found by interpol
inst:	counter for inner (adaption of stepwidth-) loop
maxdi:	max distance in current cell
maxstep:	max. step if the calculation will not end
maxtrace:	maximum number of trace way.
maxv:	maximum number of variables
minfac:	minimum fraction of cell to be covered by a time step
minst:	max. iterations of inner loop
mintim:	minimum time step
pminst:	preset value for minst
parvel:	particle velocity
parvelv(3):	particle velocity vector
oldpoi(3):	old point (from where current timestep starts)
oldvel:	|fluid velocity| at oldpoi
oldvelv(3):	fluid velocity at oldpoi
oldstep:	step number at last logging
oldtrwy:	total way of trace at last logging
startat:	index of if search for poi in interpolation routine should be started at nodsm
step:	number of time step
stepfac:	initial fraction of cell covered by a timestep
trdis:	maximum fraction of actual cell distance, after which trace-information is logged
trstep:	maximum number of steps after which trace is logged
trwy:	total way of trace
trflag:	1 if logging has to be done in this iteration
tracies:	number of loggings
tracy(maxtrace,maxv+3):	coordinates and variable values along trace format as in new (interpolated) tecplot file
time:	current time of tracking
vrat:	ratio of velocities at presumptive new point (poi) and point from which current time step starts (oldpoi)
vel:	|fluid velocity| at poi

velv(3): fluid velocity at poi

Other variables: same as those in Main Program

ttt

a	A in equation (15)
ak	k in equation (22)
akeq	K_{eq} in equation (6)
alpha	α in equation (14)
am(me)	atomic masses of the 10 elements
bk	Boltzman constant, k_0, in equations (15) and (17)
con(me)	concentrations of the 10 elements and iron
cmp, cm1p, cm2p, cqp	weight percentage of M, M', M" and Q in inclusion particle
cmb, cm1b, cm2b, cqb	weight percentage of M, M', M" and Q in bulk liquid metal
cmi, cm1i, cm2i, cqi	weight percentage of M, M', M" and Q at interface
d00	diffusion coefficient of the selected nonmetallic element (Q)
d0(me)	diffusion coefficients of all nonmetallic elements
dissf	data file name of TTT diagram for inclusion dissolution
dt	small time step in the calculation of the dissolution TTT diagram
eij(me,me)	interaction parameters e_i^j
equtemp	equilibrium temperature
formf	output data file name for inclusion formation
ga(mi), gb(mi)	a and b in the equation of $\Delta G^0 = a + bT$ for all inclusions
gaa,gbb	user selected values of a and b in the equation of $\Delta G^0 = a + bT$
homiv, hetiv	homogeneous and heterogeneous nucleation rates in equations (15), (17) and (18)
ic	the index to decide if inclusion growth calculations are over
inclusion(mi)	name strings of the 14 inclusions considered
index required	index to decide if the calculations for another inclusion are
mi	number of inclusions, equal to 14 in this program
me	number of elements, equal to 10 in the program
mm(mi), mm2(mi)	index of metallic elements for mi number of inclusions
m, m1, m2	index of constituent elements M, M', M" for the inclusion selected
pi	$\pi = 3.1416$
qq(mi)	index of element Q for every inclusion
q	index of element Q for the selected inclusion
retlog	a logical variable to indicate success of an internal subroutine call
rr	instantaneous radius in every time step
r0, rf	initial and final radii
sigma	interfacial energy, σ, in equation (15)
t	time t in equation (21)
theta	contact angle, θ, in equation (19)

vm(mi)	molar volumes of the inclusions
xx(mi), xx2(mi)	x (or x1) and x2 in equations (3) and (10) for all inclusions
x, x1, x2	x (or x1) and x2 for the inclusion selected in equations (3) and (10)
yy(mi)	y in equation (3) and (10) for all inclusions
y	y in equation (3) and (10) for the selected inclusion

equcon and **equcon2**

akeq	equilibrium constant k_{eq} in equation (6)
amm, amm1, amm2	atomic mass of M, M' and M"
amq	atomic mass of Q
actm, actm1, actm2	activities of M, M' and M"
actq	activity of Q
cmi, cm1i, cm2i, cqi	equilibrium concentrations of M, M', M" and Q at interface
con(0:10)	concentrations of elements in alloy
eij(10,10)	interaction coefficients, eij
fm, fq, fm1, fm2	activity coefficients of M, M', M" and Q
m, m1, m2, q	indices of M, M', M" and Q in the selected inclusion
me	number of elements considered
x, x1, x2, y	stoichiometric parameters of M, M', M" and Q

aiv and **aiv2**

a	constant A in equation (15)
aiv, aiv2	heterogeneous nucleation rates of simple and complex inclusions
actm, actm1, actm2, actq	activities of M, M', M" and Q
akeq	equilibrium constant k_{eq} in equation 3
amm,amm1, amm2	atomic mass of M, M' and M"
amq	atomic mass of Q
bk	Boltzman constant
cmi, cm1i, cm2i, cni	equilibrium concentrations of M, M', M" and Q at the interface
con(0:10)	concentrations of elements in alloy
eij(10,10)	interaction coefficients, eij
d0(10)	diffusion coefficients of all elements
dg	free energy of formation
dghet, dghom	activation energy for heterogeneous and homogeneous nucleations
dgz	standard free energy of formation
fm, fm1, fm2, fq	activity coefficients of M, M', M" and Q
ftheta	f(θ) in equation (19)
gaa, gbb	a and b in standard free energy equation
homiv	homogeneous nucleation rate
m, m1, m2	indices of M, M' and M" in the selected inclusion
me	number of elements considered
nincl	index of the inclusion selected
pi	$\pi = 3.11416$

q	index of element Q in the selected inclusion
sigma	interfacial energy in equation (15)
theta	contact angle θ in equations (17) and (19)
vm(14)	molar volume of inclusions
x, x1, x2, y	stoichiometric coefficients of M, M', M" and Q

Appendix C

Default Thermodynamics Data and Alloy Composition

Table C1. Original composition and diffusion coefficient of the elements in liquid steel

Element	C	Si	Mn	Ni	Cr	Ti	Al	N	O	S
wt%	0.066	0.82	1.66	0.03	0.05	0.025	0.026	0.007	0.084	0.030
D_o (m^2 s)	8×10^{-9}	3.8×10^{-9}	2×10^{-8}	-	5×10^{-9}	1×10^{-9}	2×10^{-9}	1.2×10^{-8}	1×10^{-8}	2.8×10^{-8}

Table C2. Standard free energy expressions for various reactions in the form of

$$\Delta G_0 = a + bT, Cal / mole$$

Precipitation Reaction	a	B
$2\underline{Al}+3\underline{O}=Al_2O_3$	-289060	93.52
$3\underline{Ti}+5\underline{O}=Ti_3O_5$	-419680	136.5
$\underline{Ti}+2\underline{O}=TiO_2$	-161460	55.95
$\underline{Si}+2\underline{O}=SiO_2$	-140950	54.62
$\underline{Mn}+\underline{O}=MnO$	-68816	29.95
$\underline{Al}+\underline{N}=AlN(s)$	-154000	44.5
$3\underline{Si}+4\underline{N}=Si_3N_4$	-203000	75.3
$\underline{Ti}+\underline{N}=TiN$	-80380	24.29
$\underline{Fe}+\underline{S}=FeS$	-111370	57.0
$\underline{Mn}+\underline{S}=MnS$	-39500	17.00
$\underline{Mn}+2\underline{Al}+4\underline{O}=MnO\times Al_2O_3$	-369376	125.22
$\underline{Si}+2\underline{Al}+5\underline{O}=SiO_2\times Al_2O_3$	-319875	97.32
$\underline{Fe}+2\underline{Al}+4\underline{O}=FeO\times Al_2O_3$	-330180	108.4
$\underline{Mn}+\underline{Si}+4\underline{O}=MnO\times SiO_2$	-200466	75.0

Table C3. The first order interaction parameters e_i^j, in liquid iron (1873K)

i↓ j →	C	Si	Mn	Ni	Cr	Ti	Al	N	O	S
C	0.14	0.08	-0.012	0.012	-0.024	-	0.043	0.11	-0.34	0.67
Si	0.188	0.11	0.002	0.005	-0.0003	-	0.058	0.09	-0.23	0.64
Mn	-0.07	0	0	-	-	-	-	-0.091	-0.083	-0.31
Ni	0.042	0.0057	-	0.0009	-0.0003	-	-	0.028	0.01	-0.25
Cr	-0.12	-0.0043	-	0.0002	-0.0003	0.059	-	-0.19	-0.14	-0.33
Ti	-	-	-	-	0.055	0.013	-	-1.8	-1.8	-1.1
Al	0.091	0.0056	-	-	-	-	0.045	-0.058	-6.3	0.024
N	0.13	0.047	-0.02	0.01	-0.047	-0.53	-0.028	0	0.05	-
O	-0.45	-0.131	-0.021	0.006	-0.04	-0.6	-3.9	0.057	-0.23	-3.1
S	0.06	0.027	-0.0014	0	-0.0022	-0.019	0.013	-	-0.19	0

VITA

Tao Hong obtained B.S. degree in Materials Science from Zhejiang University, Hangzhou, China in 1991. After being a research associate in Qingdao Institute of Chemical Technology for two years, he went to Graduate School of Tsinghua University in Beijing. He got M.S. degree in Materials Physics from Tsinghua University in 1996.

He joined Metal Science Program, Department of Materials Science and Engineering, the Pennsylvania State University as a Ph.D. student in September 1996 in Dr. DebRoy's research group. He passed the candidacy exam in January 1998 and the comprehensive exam in August 2000. He is a member of ASM International (American Society of Metal) and AWS (American Welding Society). He is the author of the following 6 journal papers and several conference publications:

1. T. Hong and T. DebRoy: "Non-isothermal Growth and Dissolution of Inclusions in Liquid Steels", *Metallurgical and Materials Transaction B* (Accepted, in Press).
2. T. Hong and T. DebRoy: "Effects of Time, Temperature, and Steel Composition on Growth and Dissolution of Inclusions in Liquid Steels", *Ironmaking and Steelmaking*, **28**, 450-454, 2001.
3. T. Hong and T. DebRoy: "Time-Temperature-Transformation Diagrams for the Formation and Dissolution of Oxide, Nitride, and Sulfide Inclusions", *Scripta Materialia*, *35*, 847-852, 2001.
4. W. Pitscheneder, T. Hong, T. DebRoy, R. Ebner, K. Mundra, R. Benes: "Experimental and Numerical Investigation of Transport Phenomena in Conduction Mode Weld Pools in Laser Welding", *Welding in the World*, **44**, 25-36, 2000.
5. T. Hong, T. DebRoy, S. S. Babu, and S. A. David: "Modeling of Inclusion Growth and Dissolution in the Weld Pool", *Metallurgical and Materials Transactions B*, **31B**, 161-169, 2000.
6. T. Hong, W. Pitscheneder, and T. DebRoy: "Quantitative Modeling of Motion, Temperature Gyrations, and Growth of Inclusions in Weld Pool", *Science and Technology of Welding and Joining*, **3**, 33-41, 1998.
7. S. S. Babu, S. A. David, T. Hong, and T. DebRoy: "Effect of Fluid Flow on Inclusion Coa.sening in Low Alloy Steel Welds", *Proceeding of the 34th TMS Annual Conference*, 64-69, Oct. 1998, San Diego, California.
8. T. Hong and T. DebRoy: "Oxide Inclusions in the Weld Pool during Submerged Arc Welding of Low Alloy Steel", *Proceeding of the 5th International Conference on Trends in Welding Research*, 123- 127, June 1998, Pine Mountain, Georgia.
9. W. Pitscheneder, T. Hong, T. DebRoy, R. Ebner, K. Mundra, and R. Benes: "Experimental and Numerical Investigation of Transport Phenomena in Conduction Mode Weld Pools", *Proceeding of 4th International Seminar on Numerical Analysis of Weldability*, 3-25, Oct. 1997, Graz, Austria.